

# Ultracoherent soft-clamped mechanical resonators for quantum cavity optomechanics

PhD Thesis  
Yeghishe Tsaturyan



Danish Center for Quantum Optics  
Niels Bohr Institute  
Faculty of Science  
University of Copenhagen  
Denmark

This thesis has been submitted to the PhD School of  
Science at the University of Copenhagen.

**Academic supervisors:** Prof. Eugene Simon Polzik  
Prof. Albert Schliesser

**External referees:** Prof. Adrian Bachtold  
Prof. Eva Weig

**Local referee:** Prof. Peter Lodahl

**Thesis submission:** September 30, 2019

**Thesis defense:** October 23, 2019

# Abstract

Systems based on mechanical resonators are among the most sensitive force probes in existence. The innate ability of mechanical devices to interact with almost any other system through a variety of interaction forces is, at once, a blessing and a curse. Tailoring these interactions is an act of balance and is at the very heart of the research field of cavity optomechanics and, as a result, of the work presented here.

In this thesis, I report on the development of mechanical resonators with exceedingly low internal dissipation, and their application in cavity optomechanics. These devices are based on highly tensioned silicon nitride membranes, whereupon we pattern a phononic crystal structure. Introducing a geometric defect in the central region of this crystal structure allows for spatial localisation of vibrations within the frequency range of the phononic bandgap. These vibrational modes exhibit a distinct departure from regular clamping conditions of a square membrane resonator. Specifically, these resonators, which are attached to silicon substates, do not experience the rigid clamp otherwise present at the interface between a membrane and the underlying substate. Instead, the evanescent decay of the localised vibration modes into the phononic crystal patterned membrane structure constitutes an effective “soft” clamping condition. Using this technique we realise soft clamped membrane resonators with mechanical quality factors in excess of  $10^9$  at moderate cryogenic temperatures. With the highest reported quality factor of  $1.555 \times 10^9$  at 1.28 MHz frequency, these devices are well suited for experiments in quantum optomechanics.

Upon embedding such a device inside a high-finesse optical cavity, we couple the transverse motion of a localised vibrational mode to the cavity field. Due the weak coupling of these mechanical devices to their phonon thermal bath, we observe a strong influence of the radiation pressure back-action force on the resonator motion. Particularly, we demonstrate strong ponderomotive squeezing of light below the vacuum noise level, with  $(-2.89 \pm 0.31)$  dB as the highest degree of measured squeezing. Furthermore, our results suggest that we can indeed prepare these devices close to their motional ground

state. Due to the long coherence time of our mechanical devices, as well as the high detection efficiency, our optomechanical system lends itself for a number of quantum optical protocols, including the generation, storage and tomography of single excitations states.

# Sammenfatning

Systemer baseret på mekaniske resonatorer er blandt de mest følsomme kraft-sensorer der findes. Deres naturlige evne til at vekselvirke med næsten ethvert andet system gennem en række forskellige vekselvirkningskræfter er, på samme tid, en velsignelse og en forbandelse. Nøje tilpasning af disse interaktioner er en balanceakt, og er selve essensen af forskningsfeltet kavitetsoptomekanik, og dermed også af det arbejde, som er præsenteret her.

I denne afhandling rapporterer jeg om udviklingen af mekaniske resonatorer med ekstremt lav intern dissipation, og disses anvendelse i kavitetsoptomekanik. Disse enheder er baseret på stramt udspændte siliciumnitrid membraner, i hvilket vi ætser et fononisk krystalmønster. Indførslen af en geometrisk defekt i den centrale region af det krystalmønster muliggør rumlig lokalisering af vibrationer med frekvenser inden for det fononiske båndgab. Disse vibrationelle tilstande udviser tydelig afvigelse i deres grænsebetingelser fra normalt udspændte kvadratiske membranresonatorer. Konkret udviser disse resonatorer, som er udspændt påsiliciumsubstrater, ikke en rigid fastspænding, der ellers er tilstede i grænsefladen mellem en membranen og det underliggende substrat. I stedet udgr det henfaldende nærfelt (eng. “evanescent field”) af de vibrationelle tilstande i membranstrukturen med det fononisk krystalmønster en effektiv grænsebetingelse svarende til en “blød-fastspænding. Ved brug af denne teknik udvikler vi blødt fastspændte membranresonatorer med mekaniske godheder der overstiger  $10^9$  ved moderate kryogeniske temperaturer. Med den højst rapporterede godhed på  $1.555 \times 10^9$  ved 1.28 MHz frekvens, er disse enheder velegnede til kvanteoptomekaniske eksperimenter.

Ved indlejring af sådan en enhed i en høj-finesse optisk kavitet, kobler vi den transverse bevægelse af en lokaliseret vibrationel tilstand til det optiske felt. Grundet den svage kobling mellem disse mekaniske enheder og deres fononiske bad, observerer vi en stærk påvirkning af lysstrålingstrykkets tilbagekobling på resonatorens bevægelse. Vi viser stærk ponderomotorisk lysklemning under lysets vakuumstøjniveau, med  $(-2.89 \pm 0.31)$  dB værende den højeste grad af lys-klemning vi har målt. Derudover tyder vores resultater på, at vi kan forberede vores mekaniske enheder tæt på deres vibrationelle

grundtilstand. Grundet de lange kohærenstider af vores mekaniske enheder, samt den høje detektionseffektivitet, er vores optomekaniske system velegnet til en række kvanteoptiske protokoller, herunder generering, lagring og tomografi af enkeltexcitationstilstande.

# Acknowledgements

It is quite remarkable how you can spend months on writing pages upon pages of content, and yet, towards the yet, be at a loss for words. I will, nevertheless, attempt to convey the gratitude towards the many people I worked or crossed paths with during the past few years.

First and foremost, I would like to thank my supervisors, Eugene Polzik and Albert Schliesser. The freedom that you gave me to explore and poke my nose into areas that were not always immediately related to our research, particularly at the very onset of my PhD studies, has been one of the single most formative aspects of my time at the Niels Bohr Institute. Your continued guidance, encouragement, advice and criticism. It goes without saying that your combined knowledge and experience has been instrumental to my development as a researcher, and I certainly wouldn't be where I am today without it. But the lessons that I learned from you over the past few years go above and beyond what I initially thought I had signed up for. I will forever be grateful to both of you for that.

Within a week of joining Eugene's group as a master's student, the group was rejuvenated by the human incarnation of enthusiasm – Christoffer Bo Møller. The combination of your dedication and never-ending optimism never ceased to amaze me! Through thick and thin, I couldn't have wished for a better coworker and a friend to share with journey with. Thank you Bo-Dawg!

Across the hallway from the membrane lab, as one of the few PhD students to be found at ridiculously late hours at any given day, was Rodrigo Thomas. Despite the fact that the man was working with atoms, it was evident from the beginning, that, at heart, he belonged to the membrane group. As a result, the almighty entity of “Membrane+Rodrigo” was born. Over the years, Rodrigo has somehow managed to always be there whenever the walls are seemingly collapsing around me. In hindsight, though, it makes sense. Thank you for being there, meu xuxu!

My journey as a young researcher began under the wings of a dear friend and former colleague, William H. P. Nielsen. Your patience, willingness to

share everything and anything that you knew. Your inclusive nature and contagious curiosity. The time we spent working together on the “cryocavity” experiment was one of the most enjoyable periods of my PhD studies. Thank you for that!

I would like to give a particular thanks to Andreas Barg, for his great spirit, otherworldly pebanco-ball skills, as well as calm and reasoned approach, whenever things failed to make any sense whatsoever. To Anders Simonsen, for being a true inspiration – working tirelessly, mostly on his own, and yet finding motivation to push through terribly frustrating cleanroom adventures! Willi Carlsen, a dear friend and part of the original optomechanics team, providing much needed grounding and support! Christoffer Østfeldt, for being that no-nonsense guy, straight to the point and just an all-around cool dude – you shall carry the torch of the bro-lab! Jürgen Appel, for the sheer brilliance and the simple fact that no question is too hard for him to answer. Last, but certainly not least, Senõr Ivan Galinskiy, with whom I shared the past year and a half of Fock state adventures with. For that buzzing electronic brilliance, damn good company and an unhealthy mutual appreciation of shenanigans. It’s been a blast!

As Albert established his own lab, the bifurcation of the membrane lab led to the emergence of two bright stars – Yannick Seis and Junxin Chen. As the original members of the bifurcation, those gentlemen hold a special place in my heart. Gents, you are amazing and I hope our paths will cross again in the future! The group was later enriched by the likes of Massimiliano Rossi (we still have a Juventus game to watch together!), Sampo Saarinen (how do you find those articles?!), David Mason (best road trip partner on a rainy day), Letizia Catalini (those paprika chips are *right* across the street) and Eric Langman (may the in-plane force be with you).

The membrane lab was initially part of a larger “possy”, with esteemed members such as Jean-Baptiste Bèguin (I can still hear those heavy footsteps after a long day of work!), Boris Albrecht (I really shouldn’t say anything – this could go very wrong), Emil Zeuthen (for all the continued support over the years), and Stefan Lund Christensen (for all the invaluable advice at those early stages of the PhD).

Along the way, I have been privileged to co-supervise several brilliant young students. I would particularly like to thank Mads Bjerregaard Kristensen (the string paper will materialise some day, I promise!), Timo Zwettler, Thibault Capelle and Toke Vibel.

At the early stages of my time at the institute, I was fortunate enough to overlap with Luis Guillermo Villanueva and Silvan Schmid. Several of the lessons provided by Guillermo during the crash-course in microfabrication are, to this day, imprinted on my mind. Combined with the continued

guidance from abroad, some of the foundational stones in my knowledge of microfabrication are in place thanks to Guillermo. As for Silvan, I truly couldn't have wished for a better person to learn the basics of dissipation dilution from. With a boundless enthusiasm and always eager to discuss new ideas, knocking on your door to discuss an idea still in the making was a privilege. Thank you both for that!

Outside of confines of the lab, several people deserve a special thanks. First and foremost, I would like to acknowledge the DTU Nanolab cleanroom staff, in particular Karen Birkelund for guiding me through my baby steps in the cleanroom, Thomas Aarøe Anhøj and Elena Khomtchenko for the laughs and voice of reason during lithography related frustrations, and Jonas Michael-Lindhard for the patience as I was working my way through the DRIE machine. Alongside Conny Hjort, Berit Herstrøm, Peixiong Shi, Lean Gottlieb Pedersen, and numerous others, my work in the cleanroom would've been a lot less efficient and enjoyable without your presence. Thank you!

I would like to give a special thanks to Jörg Müller, who, throughout my university studies helped me navigate through various decisions. I owe you a tremendous debt of gratitude for the never ending guidance. Thank you!

Whenever administrative minutiae become unsurmountable, there is no better person to ask than Charlotte Hviid. The number of times Charlotte has saved the day is simply astronomical and I owe a particular debt of gratitude for the administrative support you provided during my time at Harvard.

A special thanks goes to the librarians at the Niels Bohr Institute, Kader Ahmad and previously Lisbeth Dilling, for digging up all those hard-to-find articles. Similarly, to the never-ending help provided by the technical staff, in particular Axel Boisen and Jimmy Hansen for the countless fixes to malfunctioning electronics and last-minute poster printing.

In the larger community of quantum opticians at NBI, I would also like to thank current and former members of the Photonics group, with a special thanks to Tim Schröder, Leonardo Midolo, Hanna Le Jeannic, Camille Papon, and Tommaso Pregnolato. Thank you for adding that little something extra to the spirit of the quantum optics community at NBI!

Finally, I would like to thank my dear family and friends, for supporting and tolerating me throughout this long journey. As cliché as it might sound, this truly wouldn't have been possible without you. To my sister and parents in particular – every bit of my success can be ascribed to your diligent, never-ending support and encouragement. Through ups and downs, through success and failure, I always had you behind me back, ready to catch, should I stumble. As I have said it before and will say it again, every bit of my success is also your. Thank you!



# Published work

## Peer-reviewed journal articles

- [1] David Mason, Junxin Chen, Massimiliano Rossi, **Yeghishe Tsaturyan**, and Albert Schliesser. “Continuous force and displacement measurement below the standard quantum limit”. In: *Nature Physics* 15.8, pp. 745–749 (2019).
- [2] Massimiliano Rossi, David Mason, Junxin Chen, **Yeghishe Tsaturyan**, and Albert Schliesser. “Measurement-based quantum control of mechanical motion”. In: *Nature* 563.7729, pp. 53–58 (2018).
- [3] Andreas Barg, **Yeghishe Tsaturyan**, Erik Belhage, William H. P. Nielsen, Christoffer B. Møller, and Albert Schliesser. “Measuring and imaging nanomechanical motion with laser light”. In: *Applied Physics B* 123.8 (2017).
- [4] Thibault Capelle, **Yeghishe Tsaturyan**, Andreas Barg, and Albert Schliesser. “Polarimetric analysis of stress anisotropy in nanomechanical silicon nitride resonators”. In: *Applied Physics Letters* 110.181106 (2017).
- [5] Christoffer B. Møller, Rodrigo A. Thomas, Georgios Vasilakis, Emil Zeuthen, **Yeghishe Tsaturyan**, Mikhail Balabas, Kasper Jensen, Albert Schliesser, Klemens Hammerer, and Eugene S. Polzik. “Quantum back-action-evading measurement of motion in a negative mass reference frame”. In: *Nature* 547.7662, pp. 191–195 (2017).
- [6] **Yeghishe Tsaturyan**, Andreas Barg, Eugene S. Polzik, and Albert Schliesser. “Ultracoherent nanomechanical resonators via soft clamping and dissipation dilution”. In: *Nature Nanotechnology* 12.8, pp. 776–783 (2017).  
*Note that part of this publication constituted my master’s thesis [1].*

- [7] William H. P. Nielsen, **Yeghishe Tsaturyan**, Christoffer B. Møller, Eugene S. Polzik, and Albert Schliesser. “Multimode optomechanical system in the quantum regime”. In: *Proceedings of the National Academy of Sciences* 114.1, pp. 62–66 (2017).  
*Note that part of this publication constituted my master’s thesis [1].*

## Patent applications

Albert Schliesser, **Yeghishe Tsaturyan**, Eugene S. Polzik, and Andreas Barg. *Mechanical resonator device*. World Intellectual Property Organization, WO 2018/024713 A1 (2018).  
*Note that part of this publication constituted my master’s thesis [1].*

# Contents

Abstract	iii
Sammenfatning	v
Acknowledgements	vii
Published work	xi
List of Figures	xvii
List of Tables	xxi
<b>1 Introduction</b>	<b>1</b>
<b>2 Fundamentals of membrane resonators</b>	<b>5</b>
2.1 Elastic equation of motion for a thin plate . . . . .	5
2.1.1 Effective resonator parameters via Galerkin’s method . . . . .	8
2.2 Dissipation of elastic energy . . . . .	9
2.2.1 Gas damping . . . . .	10
2.2.2 Phonon tunneling losses . . . . .	13
2.2.3 Thermoelastic damping and dissipation dilution . . . . .	14
2.2.4 Surface losses in thin resonators . . . . .	32
2.2.5 Other damping mechanisms . . . . .	37
2.2.6 Damped driven harmonic oscillator . . . . .	39
2.3 Summary . . . . .	41
<b>3 Phononic engineering and soft clamping</b>	<b>43</b>
3.1 Phonon tunneling losses . . . . .	44
3.1.1 Introduction . . . . .	44
3.1.2 Phononic crystal structures in silicon – design rationale	47
3.1.3 Numerical modelling . . . . .	49
3.1.4 Fabrication of shielded membrane resonators . . . . .	52

3.1.5	Characterisation of phononic crystal shielded membrane resonators . . . . .	59
3.2	Soft clamping . . . . .	64
3.2.1	Finite element modelling . . . . .	68
3.2.2	Soft clamped membrane resonators . . . . .	78
3.3	Soft clamped devices for cavity optomechanics . . . . .	89
3.3.1	Second generation – Further from the edge . . . . .	90
3.3.2	Third generation – Opening a second bandgap . . . . .	92
3.4	Summary and outlook . . . . .	96
<b>4</b>	<b>Cavity optomechanics</b>	<b>99</b>
4.1	Basic considerations . . . . .	99
4.2	Hamiltonian description . . . . .	103
4.2.1	Heisenberg-Langevin equations . . . . .	108
4.3	Static optomechanical effects . . . . .	110
4.4	Coherent optomechanical interactions . . . . .	111
4.4.1	Dynamical backaction and sideband cooling . . . . .	112
4.4.2	Optomechanically induced transparency . . . . .	118
4.4.3	Quantum backaction . . . . .	122
4.4.4	Ponderomotive squeezing . . . . .	125
4.5	Mapping to membrane-in-the-middle . . . . .	131
4.5.1	Modal overlap . . . . .	137
4.6	Experimental realisation . . . . .	142
4.6.1	Optomechanical cavity . . . . .	142
4.6.2	Measurement of optomechanically induced transparency	147
4.6.3	Modulation in $2kz_m$ and measurement of $g_0$ . . . . .	150
4.6.4	Role of low-frequency membrane modes . . . . .	154
4.6.5	Cryogenic operation . . . . .	156
4.6.6	Cavity mirror noise . . . . .	157
4.7	Ponderomotive squeezing . . . . .	159
4.7.1	Third generation device . . . . .	161
4.7.2	Second generation device . . . . .	164
4.8	Summary and outlook . . . . .	168
4.8.1	Towards generation of mechanical Fock states . . . . .	168
4.8.2	Exoskeleton mirrors . . . . .	173
4.9	Concluding remarks . . . . .	176
	<b>Bibliography</b>	<b>179</b>
	<b>Appendices</b>	<b>199</b>

<b>A</b>	<b>Fourier analysis</b>	<b>201</b>
A.1	Fourier transforms . . . . .	201
A.2	Power spectral densities . . . . .	202
A.3	Cross spectral densities . . . . .	203



# List of Figures

2.1	Vibrational mode patterns of a square membrane . . . . .	8
2.2	Mechanical quality factor as a function of vacuum pressure . .	12
2.3	Temperature change in a deformed beam . . . . .	15
2.4	Mode curvature of a string . . . . .	22
2.5	Thermoelastic damping model comparison . . . . .	30
2.6	Intrinsic quality factor as a function of thickness . . . . .	34
2.7	Total mechanical quality factor, combining TED, volumetric and surface losses . . . . .	36
3.1	Diatomic chain and its solid state analogy . . . . .	48
3.2	Unit cell and band diagram for a silicon phononic crystal struc- ture . . . . .	50
3.3	Fabrication process flow for silicon phononic crystal shielded membranes . . . . .	53
3.4	Thermal expansion coefficients for silicon and silicon nitride .	55
3.5	Simplified illustrated of the Michelson interferometric setup . .	60
3.6	Driven response of a silicon phononic crystal structure . . . .	62
3.7	Mechanical quality factors for a square membrane at cryogenic temperatures . . . . .	63
3.8	Mode density of a square membrane resonator . . . . .	66
3.9	Profile sketch of a soft clamped membrane . . . . .	67
3.10	COMSOL model mesh of a square membrane . . . . .	68
3.11	Comparison of FEM simulations and analytic calculations of mechanical loss . . . . .	69
3.12	Comparison of FEM simulations and analytic calculations of effective mechanical mass . . . . .	70
3.13	Sketch of a hexagonal honeycomb lattice . . . . .	71
3.14	Band diagrams for an unstressed silicon nitride honeycomb unit cell for varying plate thicknesses . . . . .	72
3.15	Band diagrams of a thin silicon nitride honeycomb unit cell for varying in-plane tensions . . . . .	74

3.16	Simulated band diagrams for stress-redistributed honeycomb unit cell . . . . .	75
3.17	Definition of the defect and vibrational modes of a hexagonal membrane . . . . .	76
3.18	Simulated vibrational modes of a hexagonal-shaped defect within the honeycomb phononic crystal lattice . . . . .	77
3.19	Fabrication process flow for soft-clamped membranes . . . . .	79
3.20	Band diagram and measured vibrational mode spectrum of a soft-clamped membrane . . . . .	81
3.21	Raster measurement of mechanical mode shapes . . . . .	81
3.22	Influence of gas damping and ringdown measurements yielding highest room temperature quality factors . . . . .	83
3.23	Measured quality factors and their frequency scaling . . . . .	84
3.24	Characteristic scaling of the mechanical quality factors for mode A with thickness and lattice constant . . . . .	85
3.25	Normalised curvatures of square and soft clamped membranes . . . . .	86
3.26	Compilation of measured mechanical quality factors . . . . .	86
3.27	Mechanical quality factors under clamped and unclamped conditions . . . . .	87
3.28	Projection of simulated mechanical displacement . . . . .	88
3.29	Influence of elliptical holes around the defect . . . . .	90
3.30	Optical image of the elliptical defect geometry . . . . .	92
3.31	Second generation soft clamped membrane resonators . . . . .	93
3.32	Third generation soft clamped membrane resonators . . . . .	95
3.33	Raster measurement of the radial modes of a third generation soft clamped devices . . . . .	96
4.1	Sketch of a canonical optomechanical system . . . . .	100
4.2	Sketch of an optical cavity probed in transmission . . . . .	102
4.3	Feynman diagrams of optomechanical scattering processes . . . . .	107
4.4	Optical spring and damping . . . . .	114
4.5	Sketch of the Raman-scattering processes . . . . .	117
4.6	Optimal detuning for cooling versus sideband resolution . . . . .	118
4.7	Sketch of optomechanically induced transparency scheme . . . . .	120
4.8	OMIT response features . . . . .	123
4.9	Ponderomotive squeezing dependencies . . . . .	130
4.10	Mean field amplitudes in a membrane-in-the-middle configuration . . . . .	132
4.11	Membrane reflectivity as a function of thickness . . . . .	133
4.12	Sketch of a MIM cavity and optical 2kz tuning. . . . .	135
4.13	Resonance frequency shifts for varying membrane thicknesses . . . . .	136

4.14	MIM modulation of canonical optomechanical parameters . . .	138
4.15	Cross sectional view of optomechanical cavity assembly . . . .	144
4.16	Machined flat, high reflective mirrors . . . . .	144
4.17	Power transmission of flat ATF mirror . . . . .	145
4.18	Tilt and optical alignment imaging of a membrane . . . . .	146
4.19	Optical aperture losses and finesse versus beam waist . . . . .	148
4.20	Cavity detuning and linewidth from broadband driven cavity response . . . . .	149
4.21	Cavity resonance wavelength measurements . . . . .	151
4.22	OMIT measurements . . . . .	152
4.23	Comparison of simulated and measured canonical optomechan- ical parameters . . . . .	153
4.24	Optical cavity mode shape images . . . . .	154
4.25	Spectral composition within the bandgap for varying cavity detunings . . . . .	155
4.26	Vibrational amplitude of low-frequency membrane modes . . .	156
4.27	Empty cavity spectrum . . . . .	159
4.28	Cryogenic characterisation of third generation soft clamped resonator . . . . .	160
4.29	Nonlinear ringdown measurement of a third generation resonator	162
4.30	Power spectral density of output cavity fluctuations . . . . .	163
4.31	Ponderomotive squeezing for varying intracavity powers . . . .	165
4.32	Mirror mode spectrum and spectral composition in the vicinity of the second radial mode . . . . .	166
4.33	Strong ponderomotive squeezing spectra for a second genera- tion soft clamped resonator . . . . .	167
4.34	Exoskeleton mirror . . . . .	174
4.35	Driven response of an exoskeleton mirror and associated band diagram . . . . .	175



# List of Tables

4.1	Modal overlaps localised vibrational modes . . . . .	140
4.2	Modal overlaps lowest vibrational modes . . . . .	141

# Chapter 1

## Introduction

Diving into the history of modern cavity optomechanics is a behemoth of a task, considering its deep routes in quantum optics and solid state physics. Conveying that story is arguably an even greater undertaking, given the intertwined nature of the field. Throughout the thesis I will try to provide an overview of relevant prior work, and how it relates to subject matter. However, before diving into the technical details, a brief contextualisation of the work presented in this thesis is appropriate.

At its core, optomechanics is the study of the interaction between photons (optical or microwave) and motional degrees of freedom. This interaction is mediated by the radiation pressure force, which alters the dynamics of the constituent systems. Engineering the details of this interactions can lead to interesting static, as well as dynamical effects.

The near- and long-term applications of cavity optomechanics are indeed numerous. From prospects of signal conversion between the optical and microwave domains [2], to magnetic-field sensing [3, 4], and tests of gravitationally induced collapse of the mechanical wavefunction [5, 6], the field of optomechanics consists of many parallel trajectories. Since a number of these trajectories involve observation of quantum mechanical effects, one of the key challenges is ensuring that influence of thermal noise on the mechanical degrees of freedom is negligible compared to the disturbance added by the measurement (i.e. measurement back-action [7]). Regardless of the exact trajectory, the vast majority of these paths demand continued improvements of the optical and mechanical sub-systems.

The ability to optimise the optical and mechanical sub-systems individually, before combining them, has made one optomechanical platform particularly popular – namely the *membrane-in-the-middle* system, which consists

of a thin<sup>1</sup> dielectric membrane (slab) placed inside a free-space Fabry-Pérot optical cavity. This optomechanical system, pioneered by the group of Jack Harris [8], emerged in part following the studies by Scott Verbridge and colleagues [9], reporting on surprisingly high mechanical quality factors at room temperature. The use of silicon nitride as the material of choice for electromechanical experiments was not new per se, and priori results included quality factors on the order of a few thousand at room temperature [10] or  $3.5 \times 10^4$  at millikelvin temperatures [11]. However, the results by Verbridge et al. showed  $Q \sim 2 \times 10^5$  at room temperature, which attracted a lot of attention. The group of Jack Harris made use of the fact that thin silicon nitride membranes was a commercially available product, used as vacuum windows for x-ray spectroscopy, among others. These silicon nitride vacuum windows turned out to be exceptionally potent mechanical devices [12], yielding quality factors in excess of  $10^7$  at 300 mK temperatures. Furthermore, embedding them inside a high-finesse optical cavity, resulted in a highly versatile optomechanical system – depending on the location of the membrane within the optical cavity, the experimenters could choose between an optomechanical interaction linear or quadratic in the membrane’s displacement [8]. The fact that this optomechanical system could make use of decades of research in high-finesse free-space optical resonators, combined with the seeming simplicity of the system, unsurprisingly resulted in a tremendous amount of interest in the years to come.

The path from this pioneering piece of work towards an optomechanical system operating in the quantum regime involved several challenges. Among these was the understanding of mechanical dissipation in membrane resonators and developing techniques to ensure reproducibly high quality factors, technical limitations related to cryogenic operation of high-finesse cavities, as well as classical noise of the lasers used in relation to the experiments and thermal noise of the cavity mirrors. Over the past decade these challenges have been addressed to a large extent, allowing for the observation of strong ponderomotive squeezing of light [13, 14], cooling of a vibrational mode of the membrane to the its motional ground state [15–17], quantum feedback control of mechanical motion [17], quantum back-action evading measurements in a hybrid atom-membrane system [18], displacement measurement below the standard quantum limit [19], and so on. This thesis describes some of the developments leading to several of the results outlined above, and is structure as follows:

---

<sup>1</sup>Typically below a few hundred nanometers.

In **Chapter 2** we develop the theoretical toolbox necessary to describe tensioned membrane resonators. In particular, we discuss some of the most important sources of dissipation of elastic energy, with a particular emphasis on the concept of dissipation dilution, which describes the influence of tension on the quality factors of a tensioned resonator – namely the fact that tension “dilutes” mechanical losses. In addition to summarising previous results, a new derivation of dissipation dilution is provided, which suggests that the degree of dilution is temperature dependent. While said dependence is negligible for the membrane devices studied in this thesis, the derivation provides new insights related to dissipation dilution.

**Chapter 3** is dedicated to the description of phononic engineered membrane resonators. After discussing some of the basics of phononic engineering, we describe the concept of *soft clamping* and how phononic crystal patterning of a tensioned membrane resonator can alter the boundary conditions of the vibrational modes, leading to a significant increase in the mechanical quality factors of membrane resonators. Finally, the latest incarnations of soft clamped resonators are described, which provide an improvement of up to 46% in quality factors, compared to the first incarnation.

In **Chapter 4** we summarise basic optomechanical effects, including optomechanically induced transparency and ponderomotive squeezing, and discuss the mapping between the membrane-in-the-middle system and a canonical optomechanical system. Finally, we describe our realisation of the membrane-in-the-middle system and its performance with two different soft clamped resonator geometries. We show that our system is indeed quantum enabled, which is demonstrated by the measurement of strong ponderomotive squeezing of light. Cryogenic measurements of the latest incarnation of soft clamped resonators yield the highest measured quality factor to date. Finally, we discuss future developments, including a proposed solution to the technical noise source related to cavity mirror modes.



# Chapter 2

## Fundamentals of membrane resonators

The aim of this chapter is to establish a common language with regards to mechanical resonators, and develop a toolbox which will later aid us in understanding membranes with more complicated structures. We begin by reviewing the elastic equation of motion for a thin plate in the linear regime, and establishing how effective resonator parameters – spring constant and mass – can be estimated. Since understanding and reducing elastic losses is at the very heart of this thesis, a substantial amount of time will be dedicated to describing some of the more important dissipation mechanisms. The concept of dissipation dilution will be introduced, alongside a derivation of dissipation dilution starting from thermoelastic damping. Here, I find that the dilution factor has an explicit temperature dependence. Accounting for surface and volumetric losses, a region in parameter space is identified where this model can be tested.

### 2.1 Elastic equation of motion for a thin plate

We start by considering the dynamical equation of motion for a thin plate of uniform thickness  $h$  with in-plane forces [20]

$$\begin{aligned} \frac{D_x}{h} \frac{\partial^4 w}{\partial x^4} + \frac{D_y}{h} \frac{\partial^4 w}{\partial y^4} + 2 \frac{D_{xy}}{h} \frac{\partial^4 w}{\partial x^2 \partial y^2} \\ - \sigma_x \frac{\partial^2 w}{\partial x^2} - \sigma_y \frac{\partial^2 w}{\partial y^2} - 2\sigma_{xy} \frac{\partial^2 w}{\partial x \partial y} = -\rho \frac{\partial^2 w}{\partial t^2}, \end{aligned} \quad (2.1)$$

where  $w(x, y, t)$  is the vibration amplitude normal to the midplane of the plate (assumed to be smaller than the plate thickness),  $D_i$  are the flexural

rigidities,  $\sigma_i$  are the in-plane stress components, and  $\rho$  is the material density. The flexural rigidities can be expressed in terms of the Young's moduli and Poisson's ratios as follows

$$D_{i,j} = \frac{E_{i,j}h^3}{12(1 - \nu_j\nu_i)} \quad (2.2)$$

$$D_{xy} = \nu_y D_x + 2\frac{Gh^3}{12}, \quad (2.3)$$

where  $G$  is the shear modulus. Since the material our membranes are fabricated from is isotropic (due to the amorphous nature of the material), the equations above can be simplified assuming  $E_x = E_y = E$ ,  $\nu_x = \nu_y = \nu$  and  $G = E/2(1 + \nu)$ . Simple algebra shows that in this leads leads to  $D_x = D_y = D_{xy} \equiv D$ . Finally assuming an isotropically tensioned plate, with no shear stresses (i.e.  $\sigma_x = \sigma_y \equiv \sigma$  and  $\sigma_{xy} = 0$ ), we arrive at

$$\frac{D}{h} \left\{ \frac{\partial^4 w}{\partial x^4} + \frac{\partial^4 w}{\partial y^4} \right\} - \sigma \left\{ \frac{\partial^2 w}{\partial x^2} + \frac{\partial^2 w}{\partial y^2} \right\} + \frac{2D}{h} \frac{\partial^4 w}{\partial x^2 \partial y^2} = -\rho \frac{\partial^2 w}{\partial t^2}, \quad (2.4)$$

The equation above can of course be written more compactly in terms of the Laplace and biharmonic operators. For the material and device parameters considered in this work<sup>1</sup>, the last term on the left-hand side can be considered as a perturbative term and shown to have negligible effect on the eigensolutions [21].

Upon removing the perturbative term in Eq. (2.4), the equation of motion can be solved by separation of variables for the out-of-plane displacement field (i.e.  $w(x, y, t) = u(t)X(x)Y(y)$ , where  $u(t)$  described the temporal evolution of the field) and assuming clamped boundary conditions ( $w(x, y) = 0$  and  $\partial w/\partial x = \partial w/\partial y = 0$  at all four edges of the plate). The solutions for a clamped square membrane can in fact be constructed from the eigensolutions for a 1D beam [21, 22]. While our main focus is on 2D geometries, it is nevertheless instructive to consider the solutions to the 1D problem, which can be approximated as [21–23]<sup>2</sup>

$$u_m(x) = \begin{cases} v_m(x), & 0 \leq x \leq L/2 \\ (-1)^{m+1}v_m(L - x), & L/2 \leq x \leq L \end{cases} \quad (2.5)$$

$$v_m(x) = \sin(k_x x) + \frac{\lambda k_x L}{2} \left[ \exp\left(\frac{-2x}{\lambda L}\right) - \cos(k_x x) \right], \quad (2.6)$$

<sup>1</sup>While we will return to this in greater detail later on, the relevant quantities for this consideration are:  $E = 270$  GPa and  $h \sim 50$  nm.

<sup>2</sup>To be consistent with the notation of [21], we use  $u_m(x)$  to denote a spatial mode, not to be confused with the aforementioned temporal evolution  $u(t)$  for the out of plane displacement.

where  $k_x = m\pi/L$  ( $m$  indicating the number of antinodes in the vibration pattern and  $L$  being the beam sidelength) and  $\lambda$  being the so-called *dilution factor*<sup>3</sup>, defined as

$$\lambda \equiv \sqrt{\frac{4D}{\sigma h L^2}} = \sqrt{\frac{Eh^2}{3(1-\nu^2)\sigma L^2}}. \quad (2.7)$$

At this point in time, it is worth getting a rough sense of scales. For a typical membrane resonator considered in this work, the thickness is on the order of a few tens of nanometers, while the sidelength is on the order of a few hundred micrometers. This, together with a Young's modulus of  $\sim 270$  GPa and a tensile stress of  $\sim 1$  GPa, gives  $\lambda \sim 10^{-3}$ . This suggests that the second term in Eq. (2.6) is only relevant at the very edges of the beam/membrane. The characteristic length of the exponential decay is  $L_{\text{char}} = \lambda L/2 \approx \sqrt{E/12\sigma} h$ , which for relevant parameters is on the order of a few hundred nanometers. As we will see later in this work, the additional term in Eq. (2.6), which originates from the flexural rigidity terms in the equation of motion (as indicated by the presence of the flexural rigidity in the dilution parameter), can be of paramount importance. However, for now, the observations above suggest that we can omit the second term in Eq. (2.6) and continue our derivation with the simple sinusoidal modeshape.

As such, in it's simplest form the solution to the elastic equation of motion for a thin rectangular plate can be written as [20]

$$w(x, y, t) = u_{mn}(t)\psi_{mn}(x, y) \quad (2.8)$$

$$\approx \underbrace{A_{mn} \sin(\Omega_{mn}t)}_{u_{mn}(t)} \times \underbrace{\sin(mk_x x) \sin(nk_y y)}_{\psi_{mn}(x, y)}, \quad (2.9)$$

where the wavenumbers are defined as  $k_i = \pi/L_i$ ,  $\Omega_{mn}$  is the angular frequency of the vibration and  $A_{mn}$  is the amplitude. Three examples of vibrational mode patterns are shown in Fig. 2.1.

While the dynamics of the plate resonator can be described in detail through Eq. 2.4, as experimentalists we are often times interested in effective parameters describing the resonator at hand (such as an effective spring constant), allowing us write more manageable one-dimensional equations of motion of a point mass. To this end, we employ Galerkin's method [23] in deriving effective resonator parameters.

---

<sup>3</sup>As to why this is the commonly known name for this parameter, we will touch upon later in this chapter.

### 2.1.1 Effective resonator parameters via Galerkin's method

Galerkin's discretization method is a widely used technique in engineering, and belongs to a broader family of weighted-residual methods used in solving partial differential equations [24]. The Galerkin method uses an eigensolution to the differential equation as a test function. Operationally the method involved multiplication of the differential equation with the said test function and integration over entire domain of the resonator [23]. Starting from Eq. (2.4) (now expressed in terms of the Laplace and biharmonic operators, for compactness), we multiply the normalized modeshape  $\psi_{mn}(x, y)$  (see Eq. (2.8)) onto the differential equation and perform volume integration

$$\frac{D}{h} \int \psi_{mn} \nabla^4 w_{mn} \, dV - \sigma \int \psi_{mn} \nabla^2 w_{mn} \, dV = -\rho \int \psi_{mn} \frac{\partial^2 w_{mn}}{\partial t^2} \, dV \quad (2.10)$$

$$u_{m,n} \underbrace{\int \left( \frac{D}{h} \psi_{mn} \nabla^4 \psi_{mn} - \sigma \psi_{mn} \nabla^2 \psi_{mn} \right) \, dV}_{k_{\text{eff}}} = -\ddot{u}_{mn} \rho \underbrace{\int \psi_{mn}^2 \, dV}_{m_{\text{eff}}}, \quad (2.11)$$

where the effective spring constant,  $k_{\text{eff}}$ , and mass,  $m_{\text{eff}}$ , are here defined as

$$m_{\text{eff}} \equiv \rho \int \psi_{mn}^2 \, dV \quad (2.12)$$

$$k_{\text{eff}} \equiv \int \left( \frac{D}{h} \psi_{mn} \nabla^4 \psi_{mn} - \sigma \psi_{mn} \nabla^2 \psi_{mn} \right) \, dV. \quad (2.13)$$

It is worth appreciating that, starting from the more involved elastic equation of motion, we have arrived at the description of simple harmonic motion in Eq. (2.11).

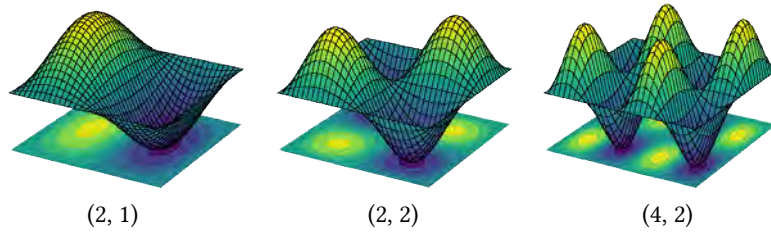


Figure 2.1: Simulated displacement patterns for three different vibrational modes.

The equation for the effective mass, as defined in Eq. ((2.12)) can in fact be written more generally as

$$m_{\text{eff}} \equiv \rho \int \left( \frac{|\mathbf{Q}|}{|\mathbf{Q}|_{\text{max}}} \right)^2 dV, \quad (2.14)$$

where  $\mathbf{Q}$  is the out-of-plane displacement for a given vibrational mode.

With the definition of effective resonator parameters, we see that the differential equation can be masked as an equation of motion for an effective one dimensional resonator. Using Eq. ((2.9)), we can write explicit equations for the effective mass, spring constant, as well as the eigenfrequency, for a rectangular membrane

$$m_{\text{eff}} = \frac{\rho d L_x L_y}{4} = \frac{m_{\text{phys}}}{4} \quad (2.15)$$

$$k_{\text{eff}} = \left( \frac{D}{h} [(mk_x)^2 + (nk_y)^2]^2 + \sigma [(mk_x)^2 + (nk_y)^2] \right) \frac{m_{\text{eff}}}{\rho} \quad (2.16)$$

$$\Omega_{mn} = \sqrt{\frac{k_{\text{eff}}}{m_{\text{eff}}}} = \Omega_{mn}^0 \sqrt{1 + \frac{D}{\sigma h} [(mk_x)^2 + (nk_y)^2]} \quad (2.17)$$

$$\Omega_{mn}^0 = \sqrt{\frac{\sigma}{\rho} [(mk_x)^2 + (nk_y)^2]}. \quad (2.18)$$

Seeing that the second term in Eq. (2.17) scales<sup>4</sup> as  $h^2/L^2$ , this term can be omitted in most cases for typical device parameters. It is worth noting that Galerkin's method has been shown to result in less accurate prediction for resonators operating in the nonlinear regime [24, 25] (i.e. for deformations on the order of or larger than the device thickness). The accuracy can, however, be improved by including more than one mode in the discretization process [25].

## 2.2 Dissipation of elastic energy

As we have seen in the previous section, the equation of elasticity for a plate can be manipulated to take the form of an equation of motion for a simple (undriven) harmonic oscillator, with effective resonator parameters. However, our treatment so far has not considered the fact that the elastic energy, stored in the resonator at hand, eventually dissipates. At the level of the effective one dimensional harmonic oscillator equation, we can introduce a simple damping term proportional to the velocity, i.e.  $\propto m_{\text{eff}} \Gamma_m \dot{z}$ . The

---

<sup>4</sup>By using Eq. (2.2) and the definition of  $k_x/k_y$ .

purpose of this section is to outline the various contributions to elastic energy dissipation and how some can be mitigated.

The total mechanical quality factor,  $Q = 2\pi \frac{W}{\Delta W} \approx \Omega_m / \Gamma_m$ , given by the ratio of the stored and dissipated elastic energies (or mechanical frequency,  $\Omega_m$ , and the dissipation rate,  $\Gamma_m$ , in the low-damping limit), can be divided into two parts – *intrinsic* or *extrinsic* of origin. The exact type of intrinsic and extrinsic sources will typically depend on the specifics of the mechanical resonator at hand, and the environment it “sees”. In our case, the most relevant extrinsic sources of dissipation include gas damping and phonon tunneling losses [26] (also known as anchoring losses), while the relevant intrinsic sources are thermoelastic damping (TED), surface losses and two-level defects (TLS). The sum total of these contributions ultimately determines the quality factor of our devices

$$Q^{-1} = \sum_i Q_i^{-1} = Q_{\text{gas}}^{-1} + Q_{\text{tunnel}}^{-1} + Q_{\text{TED}}^{-1} + Q_{\text{surface}}^{-1} + Q_{\text{TLS}}^{-1} + Q_{\text{other}}^{-1}. \quad (2.19)$$

Other sources of dissipation, of lesser importance/interest for the work at hand, will be discussed at the end of this chapter. In the next few sections we will touch upon the four sources of dissipation mentioned above, starting with gas damping.

### 2.2.1 Gas damping

Loss of elastic energy due to the interaction of a resonator with the surrounding gas molecules is an excellent example of an extrinsic loss mechanism. The exact details of this interaction will typically depend on a number of things – the geometry and surface roughness of the resonator, gas composition, proximity to other objects, temperature, gas pressure, and so on. Broadly speaking, gas damping can be divided into four regimes [23, 27–29]:

- 1) *free molecular*, where the loss of energy to the surrounding gas is negligible compared to other loss mechanisms,
- 2) *molecular* or *ballistic* regime, where elastic energy is dissipated due to momentum exchange with the surrounding (noninteracting) gas molecules,
- 3) *transition* or *crossover* regime, marking the transition from the molecular regime to the Newtonian regime and
- 4) the *continuum* or *Newtonian* regime (also referred to as fluidic or viscous regime), where one has to resort to the Navier-Stokes equations, in order to describe the interaction between the mechanical resonator and the surrounding gas.

It is common practice to distinguish between the various regimes in terms of a dimensionless quantity, the *Knudsen number*,  $Kn$ , defined as the ratio

between the mean free path length of the gas molecules ( $\lambda_f$ ) and the characteristic length scale of the resonator ( $L_c$ )

$$Kn = \frac{\lambda_f}{L_c}. \quad (2.20)$$

The transition between the Newtonian and molecular regime takes place when the mean free path becomes comparable to the characteristic length scale [29],  $0.1 < Kn < 10$ . The mean free path length can be expressed as follows [23, 30]

$$\lambda_f = \frac{k_B T}{\sqrt{2\pi} d^2 p}, \quad (2.21)$$

where  $k_B$  is Boltzmann's constant,  $T$  is the temperature of the gas,  $d$  is the kinetic diameter of the molecule ( $\sim 3.5 \text{ \AA}$  for ambient gas [30]) and  $p$  is the gas pressure. For a characteristic length<sup>5</sup> of  $500 \text{ \mu m}$ , one would anticipate the transition region to be between  $\sim 1 \text{ mbar}$  and  $\sim 10^{-2} \text{ mbar}$  in room temperature settings. Finally, it is worth noting that in the viscous regime the frequency of the resonator changes appreciably as a function of the gas pressure [27, 28]. This dependence is still present in the molecular regime, albeit less pronounced.

For the vast majority of the results presented in this work, we operate deep in the molecular or free molecular regimes. In those cases, the quality factor due to gas damping for a square plate can be derived by considering the momentum exchange between the resonator and the gas molecules on both sides of the resonator [31]. The quality factor can be expressed as

$$Q_{\text{gas}} = Q_D \left( 1 + \frac{L}{d_0} \frac{\beta}{32} \right)^{-1} \quad (2.22)$$

$$Q_D = \frac{\rho h \Omega_{mn}}{4} \sqrt{\frac{\pi}{2}} \sqrt{\frac{RT}{M_m}} \frac{1}{p}, \quad (2.23)$$

where  $d_0$  is the distance between a nearby surface and the membrane,  $L$  is the sidelength of the membrane,  $\beta$  is a geometry-related constant (describing the average travelled distance for a molecule between the plate and the nearby surface [31]),  $R$  is the ideal gas constant,  $M_m$  is the molar mass of the gas and  $p$  is the gas pressure. The second term in Eq. (2.22) is typically referred

---

<sup>5</sup>The notion of ‘‘characteristic length’’ is unfortunately ill-defined, and will depend on the exact geometry of the resonator and its surrounding. If a membrane resonator is in close proximity to another surface, the characteristic length would no longer be the size of the resonator, but rather the gap between the resonator and the nearby surface.

to as *squeeze film damping* (since the air is being “squeezed” out, as the membrane moves towards the nearby surface), and only becomes relevant when the resonator is in close proximity ( $\sim L/50$  for a square membrane, assuming  $\beta = 2/\pi$  [31]) to another surface.

In Fig. 2.2 we see an example of gas damping for a 50 nm thin membrane with 450  $\mu\text{m}$  sidelength. As expected, we see a departure from the  $p^{-1}$  scaling at higher pressures, while the data follows scales in accordance with Eq. (2.23) for lower pressures. The dashed is a plot of Eq. (2.23), with the final  $Q$  as the only fit parameter (i.e.  $(Q_0^{-1} + Q_D^{-1})^{-1}$ ), while the solid line includes a “fudge factor”,  $\alpha$ , to account for pressure differences (i.e.  $Q_D \rightarrow Q_D/\alpha$ ). The fit suggests that the actual pressure, as seen by the membrane, is approximately 35 times higher than is suggested by the pressure gauge, and as a result, that the transition region is around  $p \sim 10^{-2}$  mbar, which roughly agree with the estimate based on the Knudsen number above. More often than not, such a “fudge factor” is required for a quantitative agreement between measurement and data. This will depend on the exact details of the vacuum system, the local environment of the resonator and the proximity of the pressure gauge to the vacuum chamber.

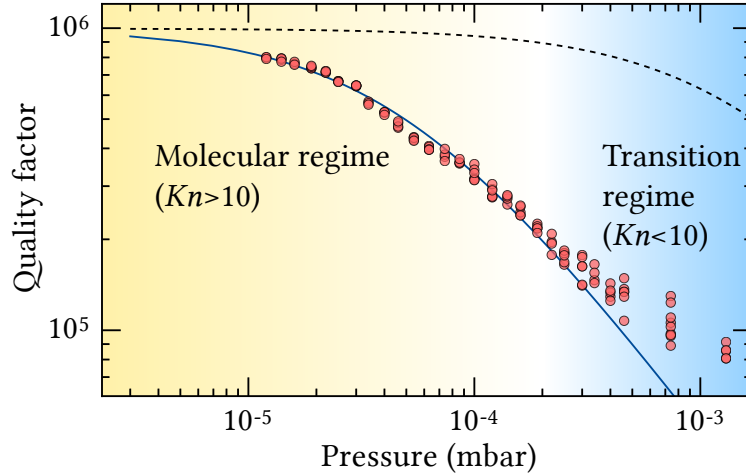


Figure 2.2: Quality factor of a square membrane resonator as a function of vacuum pressure, as read from the pressure gauge. The membrane parameters are:  $L \approx 452 \mu\text{m}$ ,  $h \approx 50 \text{ nm}$ ,  $\sigma \approx 1.14 \text{ GPa}$ . The measurements are of the (2,2) vibrational mode.

Finally, as one might expect, perforating the membrane can reduce the effect of squeeze film damping, since the air molecules now only have to travel from one hole to another [29] (thus resulting in a reduction of  $\beta$ ). While somewhat manageable expressions can be found for certain types of

perforation (e.g. circular holes arranged in a square lattice), one has to resort to numerical simulations for more complex perforations [32]. However, operationally speaking, one can resort to Eq. (2.22) as an estimate for a lower bound.

### 2.2.2 Phonon tunneling losses

Another prime example of an extrinsic loss mechanism is that of phonon tunneling [26], often referred to as anchoring or clamping losses. It refers to the channel of dissipation associated with mounting of the mechanical resonator and, as a result, the eventual dissipation of the stored elastic energy in the mechanical resonator into the supporting structure. A large body of theoretical and experimental work has been devoted to understanding and mitigating this loss mechanisms over the past few decades, and we will return to some of these in the next chapter.

As one might anticipate, the magnitude of this loss mechanisms can be highly dependent on the geometries of the resonator and support structure, and often one has to resort to approximate solutions (for instance, assuming that the support structure is semi-infinite), and eventually numerical simulations. Nevertheless, it is instructive to consider phonon tunneling in general terms, since some of the concepts are integral to finding means to eliminate this loss mechanism. In the following, we limit our discussion to membrane resonators.

The term “phonon tunneling” was initially coined by Ignacio Wilson-Rae [26], and is a general theoretical framework used to describe support-induced losses in nanomechanical resonators. Assuming a weak coupling between the resonator and the underlying support structure, for mechanical quality factor due to phonon tunneling losses can be expressed as follows [33]

$$Q_{\text{tunnel}}^{-1} = \frac{\pi}{2\rho_s\rho_r\omega_r^3} \int_q \left| \int_S d\vec{S} \cdot (\boldsymbol{\sigma}_q^{(0)} \cdot \vec{u}'_R - \boldsymbol{\sigma}'_R \cdot \vec{u}_q^{(0)}) \right|^2 \times \delta(\omega_R - \omega(q)). \quad (2.24)$$

Here,  $i \in R, q$  denote a resonator eigenmode  $R$  and support eigenmode  $q$ . Furthermore,  $\boldsymbol{\sigma}_i$  and  $u_i$  are the stress and displacement fields,  $\rho_i$  the material densities, and  $\omega_R$  and  $\omega(q)$  and the eigenfrequencies of the resonator and the support, respectively. The overlap integral is taken over the contact area  $S$  between the resonator and the support. This expression, albeit quite general, suggests that the mechanical quality factor can be increased by reducing the spatial and/or spectral overlap between the resonator mode(s) and the support modes. In practice, the latter can be achieved by reducing the density

of states of the support (for instance, by decreasing the effective size of the support), while the former can be achieved by choosing different symmetries of the resonator and substrate modes (e.g. by embedding a circular resonator in a square silicon support). But while the specifics of the implementation can vary, reducing the spatial and spectral overlap is a key objective in designing high- $Q$  mechanical resonators. This concept is at the very heart of the devices described in this work.

### 2.2.3 Thermoelastic damping and dissipation dilution

As we turn our attention to internal loss mechanisms, we are inevitably led to the work of Clarence Zener in late 1930's and early 1940's on internal friction in solids. Zener considered transverse vibrations in an isotropic beam, and how the coupling between these vibrations to a temperature field can constitute a mechanism of elastic energy dissipation [34]. His analysis was based on the Thomson effect, which links stress,  $\sigma$ , that a solid is subjected to with a temperature change,  $\Delta T$ , in the solid. Mathematically the Thomson effect can be described as follows for an isotropic solid [35]

$$\Delta T = -\frac{\alpha}{\rho c}\sigma T_0, \quad (2.25)$$

where  $\rho$  is the material density,  $c$  is the specific heat per unit mass,  $T_0$  is the equilibrium temperature, and  $\alpha$  is the coefficient of thermal expansion and, in effect, the coupling coefficient. Assuming a positive coefficient of thermal expansion, an increase in the temperature will be observed upon subjecting the object to a compressive force (i.e.  $\sigma < 0$ ). Zener realised that a similar dynamics is taking place in a beam as it vibrates: the side of the beam which is stretched at a given point in time of the vibration will be cooled down, while the opposite side will heat up (see Fig. 2.3). The resultant temperature gradient across the neutral axis of the beam leads to an irreversible heat transfer, as the system relaxes to equilibrium. This idea was proposed by Zener in his initial work from 1937 [34] and generalised for beams and wires shortly hereafter [36]. Zener's derivation was based on his "standard model" of an anelastic solid (sometimes referred to as the "standard linear solid" model). It is therefore instructive to cover certain aspects of Zener's derivation. Here, we follow the derivation as presented in [37, 38].

#### Zener's model of anelasticity

In the standard theory of elasticity we implicitly assume no time dependence in the stress-strain relation – exerting a force on an object leads to an instan-

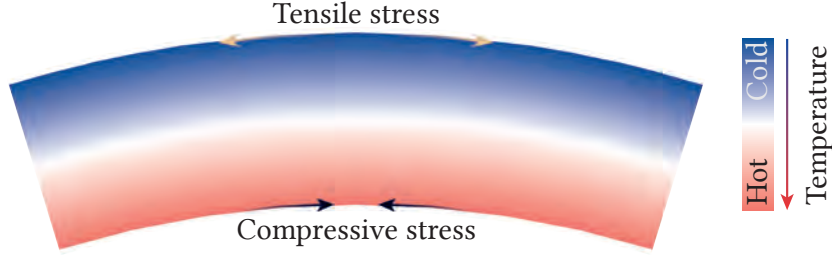


Figure 2.3: Illustration of temperature changes in a deformed beam, assuming a positive coefficient of thermal expansion.

taneous deformation. However, in reality there is a lag between these events. A solid object showing non-instantaneous response to an external force, and no lasting deformation, is known as an *anelastic* solid. This dynamics can be captured by modifying Hooke's law to include time derivatives of stresses and strains

$$\sigma + \tau_\epsilon \dot{\sigma} = E_R(\epsilon + \tau_\sigma \dot{\epsilon}), \quad (2.26)$$

where  $\tau_\epsilon$  ( $\tau_\sigma$ ) is the stress (strain) relaxation time for constant strain (stress), and  $E_R$  is the elastic modulus after all relaxation has occurred. We can solve Eq. (2.26) in Fourier space, re-expressing the stress-strain relation with an effective elastic modulus

$$\sigma = E_R \underbrace{\frac{1 + i\Omega\tau_\sigma}{1 + i\Omega\tau_\epsilon}}_{E_{\text{eff}}} \epsilon. \quad (2.27)$$

By a simple manipulation we find that the effective elastic modulus can be expressed as the sum of an in-phase and an out-of-phase term

$$E_{\text{eff}} = E_R \left[ \frac{1 + \Omega^2\tau_\sigma\tau_\epsilon}{1 + (\Omega\tau_\epsilon)^2} + i \frac{1 + \Omega(\tau_\sigma - \tau_\epsilon)}{1 + (\Omega\tau_\epsilon)^2} \right]. \quad (2.28)$$

The assumption of an imaginary Young's modulus is in and of itself often referred to as *Zener's model*.

Based on this finding, let us take a simplified example and express the stress and strain as harmonic functions of time

$$\epsilon = \epsilon_0 \exp(i\Omega t) \quad (2.29)$$

$$\sigma = \sigma_0 \exp(i\Omega t). \quad (2.30)$$

Expressing the complex Young's modulus,  $\tilde{E} \equiv E_1 + iE_2$ , in polar coordinates, the stress-strain relation can be written as follows

$$\sigma = \underbrace{|\tilde{E}| \epsilon_0 \exp\left(i\Omega t + i \tan^{-1} \frac{E_2}{E_1}\right)}_{\epsilon}, \quad (2.31)$$

where the argument of the complex Young's modulus has been absorbed into the strain field,  $\epsilon$ . We can now calculate the stored and dissipated energies, and hence the mechanical quality factor, using the equations above. The mechanical work done per unit volume per oscillation cycle (i.e. dissipated energy per unit volume per cycle) can be found as follows [39]

$$\Delta W = \int_0^{2\pi/\Omega} \mathcal{R}[\sigma] \mathcal{R}\left[\frac{d\epsilon}{dt}\right] dt, \quad (2.32)$$

where  $\mathcal{R}$  is the real part. The amount of stored energy is found by integration over a quarter oscillation cycle,  $\pi/2\Omega$ ,

$$W = \int_0^{\pi/2\Omega} \mathcal{R}[\sigma] \mathcal{R}\left[\frac{d\epsilon}{dt}\right] dt. \quad (2.33)$$

Thus we arrive at the following result for the quality factor

$$Q^{-1} = \frac{\Delta W}{2\pi W} = \frac{E_2}{E_1}. \quad (2.34)$$

As we can see, in the framework of Zener's model, the quality factor is given by the ratio of the real to imaginary part of the complex Young's modulus. Returning to Eq. (2.28), we can now express the mechanical quality factor by taking the ratio of the real and imaginary parts of  $E_{\text{eff}}$

$$Q_{\text{Debye}}^{-1} = \Delta \frac{\Omega \bar{\tau}}{1 + (\Omega \bar{\tau})^2}, \quad (2.35)$$

where  $\Delta = (\tau_\sigma - \tau_\epsilon)/\tau_\sigma$  (known as "relaxation strength") and  $\bar{\tau} = \sqrt{\tau_\sigma \tau_\epsilon}$ . The quality factor has a Lorentzian form, with a minimum at  $\Omega \bar{\tau} = 1$ . As the naming suggests in Eq. (2.35), dissipation of this form is known as *Debye peaks*. Given the simplicity of the model, it is not surprising that Debye peaks appear in a number of descriptions of dissipation, including two-level systems, which we will touch upon later in this chapter.

In the derivation of thermoelastic damping for a thin beam, Zener arrived at the result in the form of Eq. (2.35), with the relaxation strength and the

characteristic time constant expressed in terms of thermodynamic quantities

$$Q_{\text{TED,Zener}}^{-1} = \Delta_E \frac{\Omega \tau_{\text{TED}}}{1 + (\Omega \tau_{\text{TED}})^2}, \quad (2.36)$$

$$\Delta_E = E \frac{\alpha^2 T_0}{\rho c_p}, \quad (2.37)$$

$$\tau_{\text{TED}} = \frac{h^2 \rho c_p}{\pi^2 k} = \frac{h^2}{\pi^2 D_{\text{th}}}, \quad (2.38)$$

where  $c_p$  is the specific heat capacity,  $k$  is the thermal conductivity, and  $D_{\text{th}} = k/\rho c_p$  is the thermal diffusivity ( $\tau_{\text{TED}}$  is the mean diffusion time across the thickness of the beam). This result was achieved by mode expansion of the temperature field. Zener showed that the dominant contribution (98.6%) is from the first mode, and the resultant quality factor was found to be given by Eq. (2.36). Experimental agreement with the thermoelastic model was found shortly after the proposal. In fact, a few months after his original paper, Zener reported on the quantitative agreement between his thermoelastic model and measurements with glass and metal wires [40].

Separate and apart from the thermoelastic loss model, another aspect of Zener's work has played a key role in experimental physics, particularly over the last few decades – namely the assumption of complex Young's modulus. In the following I will outline the main outcome of these efforts, and how these are intimately related to the work presented in this thesis.

### Dissipation dilution

The first branch of efforts related to the model of anelasticity can be traced back to the early days of LIGO. Among the numerous considerations associated with the design of the gravitational wave detector was the thermal noise of the mirror suspension. In a lengthy report [41] from 1983 compiled by Paul Linsay, Peter Saulson and Rainer Weiss, the authors noted, among others, that the quality factor of the pendulum (consisting of a thin wire suspension and a large mirror) was dominated by the elastic energy stored as gravitational potential energy. The quality factor of the pendulum mode could therefore be approximated as

$$Q \approx Q_{\text{mat}} \frac{E_{\text{grav}}}{E_{\text{elastic}}}, \quad (2.39)$$

where  $Q_{\text{mat}}$  is the intrinsic quality factor of the suspension material (quartz in the case of LIGO), while  $E_{\text{grav}}$  and  $E_{\text{elastic}}$  are the elastic energies stored in the flexure of the wire and as gravitational potential energy, respectively. By

introducing a lossless potential, namely the gravitational field, the amount of stored elastic energy is increased, without increasing the internal friction in the suspension material.

Of course, a bi-product of such a construct is that the quartz wire becomes tensioned, due to the gravitational pull of the mirror attached to the suspension wire. The importance of the tension was first highlighted in the seminal work by Gabriela González and Peter Saulson in 1994 [42]. Here, González and Saulson set out to derive an exact expression for the mechanical quality factor of the pendulum mode, starting from the elastic equation of motion for a tensioned beam<sup>6</sup>. Importantly, the authors did the derivation in the framework of Zener’s model, using a complex Young’s modulus to incorporate material losses (i.e.  $\tilde{E} = E_1 + iE_2$ ). Assuming a displacement modeshape similar to Eq. (2.6), the mechanical quality factor was shown to be given by the following expression [42]

$$Q_n^{-1} = 2\sqrt{\frac{E_1 I}{\sigma L^2}} \left[ 1 + \frac{n^2 \pi^2}{2} \sqrt{\frac{E_1 I}{\sigma L^2}} \right] Q_{\text{int}}^{-1} \quad (2.40)$$

where  $I$  is the area moment of inertia, and  $Q_{\text{int}}^{-1} = E_2/E_1$  is the intrinsic inverse quality factor of the underlying material, given by the ratio of the real and imaginary Young’s moduli. González and Saulson showed that the presence of tension  $\sigma$  “dilutes” the intrinsic losses of the wire. This rather remarkable result was later dubbed *dissipation dilution* [43] and, to this day, plays a key role in gravitational wave interferometers.

More than a decade later, in a rather different context, researchers were studying mechanical dissipation in tensioned silicon nitride strings. In 2006, Scott Verbridge and colleagues reported unexpectedly low dissipation in these microfabricated devices [9], starkly deviating from dissipation in other glassy materials. Unaware of the earlier works of Saulson and colleagues, these results were quite surprising. In an attempt to explain these findings, Silvan Schmid and Christofer Hierold derived an expression for the mechanical quality factor [44] using Zener’s model (i.e. assuming a complex Young’s modulus), finding that

$$Q_n^{-1} = \frac{(n\pi)^2 E}{12 \sigma} \left( \frac{h}{L} \right)^2 Q_{\text{int}}^{-1}. \quad (2.41)$$

---

<sup>6</sup>While the origin of the tension in the case of González and Saulson was due to the gravitational pull of a mirror attached to the wire, the equation of motion based on which the quality factor was derived is the one for a tensioned beam, making the result more general than at first glance.

As we can see, the expression closely resembles the second term of Eq. (2.40) derived by González and Saulson. The discrepancy was later shown to be due to the fact that Schmid and Hierold used a simplified expression for the modeshape (i.e.  $w \propto \sin(k_x x)$ ). However, the prediction of a  $Q$  scaling quadratically with length was incompatible with experiments, where a linear scaling was observed.

A couple of years past, Quirin Unterreithmeier and colleagues took a similar approach as Schmid and Hierold in trying to explain the observed  $Q$ -factors [45]. However, instead of attempting to derive an explicit expression for the quality factor, the stored and dissipated elastic energies were (presumably) derived numerically, showing excellent agreement with experimental data. In passing, the authors noted that “(...) the maximum strain and thus local dissipation occurs near the clamping points (...)”. Shortly after these findings, Schmid reported on a modified derivation of quality factor of a string under flexure [46], which resulted in an expression closely resembling the one by González and Saulson (see Eq. (2.40)). As Schmid pointed out, the additional term in the quality factor, which was missing in his original derivation [44], was due to the concentrated bending at the edges of the string. This was the culmination of several years of work by numerous research groups, resulting in the re-discovery of dissipation dilution and the realisation that tension in a resonator dilutes dissipation.

With growing interest in tensioned silicon nitride resonators for opto- and electromechanics, these considerations were extended to 2D by Pen-Li Yu and colleagues in Cindy Regal’s group [21]. As a stark demonstration of loss concentration near the edges of the membrane, the researchers considered two cases of metallized silicon nitride membranes – one, where the entire membrane was covered by aluminum, and the second case involving metallization everywhere *except* for the edges. Indeed, removing metal in the immediate vicinity of the clamp was shown to boost the mechanical quality factor appreciably. Given the relevance of Yu’s derivation, we will now review some of the main details associated with it.

We start by considering the strain components associated with bending of the plate. Assuming that the deflections of the plate are small compared to the its thickness, we can ignore terms associated with elongation. For a given displacement field of the membrane  $\tilde{w}(x, y, t) = w(x, y)e^{i\Omega t}$ , the oscillating

strains can be written as [21, 47]

$$\tilde{\varepsilon}(t) = \begin{pmatrix} \tilde{\varepsilon}_{xx}(t) \\ \tilde{\varepsilon}_{yy}(t) \\ \tilde{\varepsilon}_{xy}(t) \end{pmatrix} \approx \begin{pmatrix} -z \frac{\partial^2 w}{\partial x^2} \\ -z \frac{\partial^2 w}{\partial y^2} \\ -2z \frac{\partial^2 w}{\partial x \partial y} \end{pmatrix} e^{i\Omega t} = \underbrace{\begin{pmatrix} \varepsilon_{xx} \\ \varepsilon_{yy} \\ \varepsilon_{xy} \end{pmatrix}}_{\varepsilon_0} e^{i\Omega t}. \quad (2.42)$$

Next, the oscillating stresses can be found via the stress-strain relation for a thin plate

$$\tilde{\sigma}(t) = \begin{pmatrix} \tilde{\sigma}_{xx}(t) \\ \tilde{\sigma}_{yy}(t) \\ \tilde{\sigma}_{xy}(t) \end{pmatrix} = \tilde{E} \underbrace{\frac{1}{1-\nu^2} \begin{pmatrix} 1 & \nu & 0 \\ \nu & 1 & 0 \\ 0 & 0 & (1-\nu)/2 \end{pmatrix}}_{\mathbf{M}} \tilde{\varepsilon}(t) = \tilde{E} \mathbf{M} \tilde{\varepsilon}(t), \quad (2.43)$$

where  $\tilde{E} = E_1 + iE_2$  is the complex Young's modulus, following Zener's model of anelasticity. The real part of the oscillating stresses can therefore be written as follows

$$\mathcal{R}[\tilde{\sigma}(t)] = E_1 \mathbf{M} \varepsilon_0 \cos \Omega t - E_2 \mathbf{M} \varepsilon_0 \sin \Omega t. \quad (2.44)$$

Similar to the toy-model in the last section, we can calculate the amount of dissipated elastic energy following Eq. (2.32). The mechanical work done per unit volume per oscillation cycle is found to be given by the following expression [21]

$$\Delta W_{\delta V} = \int_0^{2\pi/\Omega} \mathcal{R}[\tilde{\sigma}^T] \mathcal{R} \left[ \frac{d\tilde{\varepsilon}}{dt} \right] dt = \pi E_2 \varepsilon_0^T \mathbf{M} \varepsilon_0. \quad (2.45)$$

The total loss can thus be estimated by integration of the above equation over the entire volume of the resonator. Using Eqs. (2.42-2.43), the total dissipation can be written as follows

$$\begin{aligned} \Delta W &= \int \Delta W_{\delta V} dV & (2.46) \\ &= \int z^2 dz \iint \frac{\pi E_2(x, y)}{1-\nu^2} \left\{ \underbrace{\left( \frac{\partial^2 w}{\partial x^2} + \frac{\partial^2 w}{\partial y^2} \right)^2}_{\text{mean curvature}} \right. \\ &\quad \left. - 2(1-\nu) \underbrace{\left( \frac{\partial^2 w}{\partial x^2} \frac{\partial^2 w}{\partial y^2} - \left( \frac{\partial^2 w}{\partial x \partial y} \right)^2 \right)}_{\text{Gaussian curvature}} \right\} dx dy, & (2.47) \end{aligned}$$

where, for the sake of generality, we include the spatial dependence of  $E_2$ . Performing the integral from  $z = -h/2$  to  $z = +h/2$  and invoking Green's theorem, it can be shown that the integrated Gaussian curvature is zero for a clamped plate with uniform thickness and constant  $E_2$ , yielding [21]

$$\Delta W = \frac{\pi E_2 h^3}{12(1-\nu^2)} \iint \left\{ \frac{\partial^2 w}{\partial x^2} + \frac{\partial^2 w}{\partial y^2} \right\}^2 dx dy. \quad (2.48)$$

The stored elastic energy can either be calculated similar to Eq. (2.33), or by calculating the maximum kinetic energy

$$W_{\text{kinetic}} = \frac{\rho \Omega^2}{2} \int w(x, y)^2 dV. \quad (2.49)$$

Combining the results of Eqs. (2.47-2.49), and assuming a displacement field given by Eq. (2.6), Yu and colleagues found that the mechanical quality factor for a square membrane could be expressed as follows

$$Q_{mn}^{-1} = \frac{\Delta W}{2\pi W_{\text{kinetic}}} = Q_{\text{int}}^{-1} \lambda \left( 1 + \lambda \frac{(m^2 + n^2)\pi^2}{4} \right), \quad (2.50)$$

$$Q_{\text{int}}^{-1} \equiv \frac{E_2}{E_1} \quad (2.51)$$

where  $\lambda$  is given by Eq. (2.7). By tracking the contribution of the edge-term of the modeshape (cf. Eq. (2.6)) throughout their derivation, they identified the first term as being associated with the clamp. Since the amount of dissipated energy depends on the integrated curvature of the modeshape, it's instructive to look at the spatial dependence of the curvature. In Fig. 2.4 we consider the curvature close to the edge of the membrane, as a function of distance. As we can see, the far dominant contribution is at the clamping point of the membrane, concentrated within a distance of a few hundred nanometers. It is remarkable that for a resonator with a sidelength of several hundred microns, the mechanical dissipation is almost entirely dictated by the losses within a distance of less than a micron. Only for very high mode numbers does the second term in Eq. (2.50) start to play a significant role.

While these derivations are extremely insightful, and will be used extensively in the rest of this work, one thing is arguably lacking for a more complete understanding – namely a clearer interpretation of the intrinsic quality factor, here given by the ratio of the real and imaginary parts of Young's modulus. In the following section this question will be addressed.

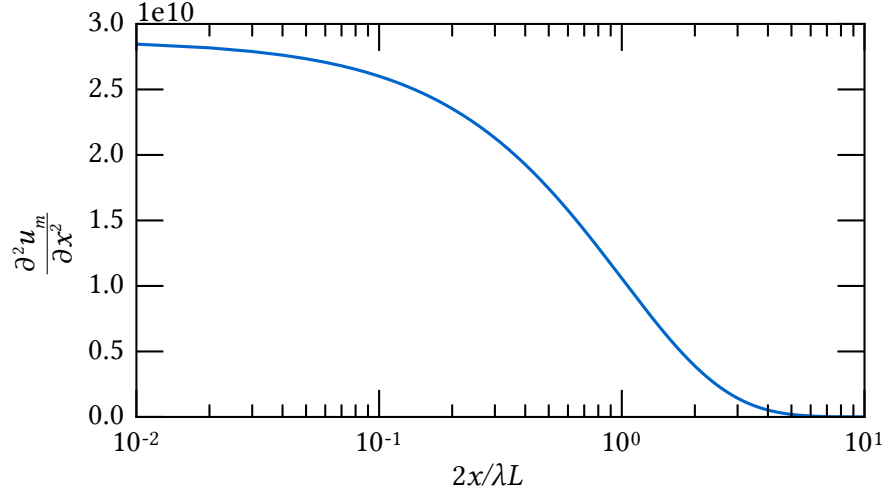


Figure 2.4: Curvature of the fundamental vibrational mode of a string, as a function of position in units of characteristic length,  $L_{\text{char}} = \lambda L/2$ . The normalized displacement field is given by Eq. (2.6). Here,  $L = 500 \mu\text{m}$ ,  $h = 50 \text{ nm}$ ,  $\sigma = 1.27 \text{ GPa}$ ,  $E = 270 \text{ GPa}$ ,  $\nu = 0.27$  and  $L_{\text{char}} \approx 220 \text{ nm}$ .

### Thermoelastic damping in membrane resonators

The first studies of thermoelastic damping in micromechanical resonator came in early 1990's, with Terry Roszhart reporting on measurements of microfabricated cantilever beams from single crystal silicon [48], with beam thicknesses of  $10 \mu\text{m} - 17.5 \mu\text{m}$ . As devices became smaller, thus shifting the product  $\Omega\tau_{\text{TED}}$  closer to unity, researchers became interested in exact solutions of thermoelastic damping<sup>7</sup>. While such derivations were presented by Landau and Lifshitz in the holy book of elasticity [50], and by J. B. Alblas [51], a transparent derivation, alongside an explicit expression for the quality factor, was missing. Inspired by the impressive developments in micro- and nanoelectromechanical systems, Ron Lifshitz and Michael Roukes presented an exact derivation of thermoelastic damping for thin beams [37], where the thermoelastic coupling manifested itself as an additional flexural rigidity in the elastic equations of motion<sup>8</sup>. The quality factor for a beam

<sup>7</sup>This is due to the fact that the accuracy of Zener's model is diminished for smaller values of diffusivity or thicker beams [37, 49].

<sup>8</sup>Very naively one could say that since heating of a beam will result in an increase of the thickness, the thermoelastic coupling will manifest itself as an additional flexural rigidity due the  $D \propto h^3$  scaling.

was found to be given by the following expression

$$Q_{\text{LR}}^{-1} = \Delta_E \left[ \frac{6}{\xi^2} - \frac{6 \sin \xi + \sinh \xi}{\xi^3 \cos \xi + \cosh \xi} \right], \quad (2.52)$$

where  $\Delta_E$  is defined in Eq. (2.37) and  $\xi$  is defined as

$$\xi = h \sqrt{\frac{\Omega \rho c_p}{2k}} = \sqrt{\frac{\pi^2}{2} \Omega \tau_{\text{TED}}}. \quad (2.53)$$

Here we have used Eq. (2.38) to express  $\xi$  in terms of the mean diffusion time  $\tau_{\text{TED}}$ .

A few years later, Andrew Norris and Douglas Photiadis provided a derivation of thermoelastic damping for plate resonators [52], shortly followed by a derivation by Ali Nayfeh and Mohammad Younis [53], which followed an identical path of derivation as Lifshitz and Roukes. Importantly, Nayfeh and Younis considered the effect of in-plane forces, and showed numerically that thermoelastic damping is decreased due to added tension.

Around the same point in time, tensioned nanobeam resonators were receiving a lot of attention due to unexpectedly high mechanical quality factors [9]. Furthermore, Scott Verbridge and colleagues demonstrated that the quality factor could be tuned in-situ by bending the device substrate, thus modifying the tension in the silicon nitride nanobeam [54]. Inspired by these findings, Sandeep Kumar and Aman Haque presented an explicit expression for thermoelastic damping in the presence of a secondary elastic field (i.e. the in-plane tension). Their results were in agreement with the findings of Nayfeh and Younis, in that thermoelastic losses were reduced in the presence of in-plane tension.

As tensioned resonators emerged as promising candidates for cavity optomechanics (particularly following the work in the group of Jack Harris), similar considerations and derivations began to emerge for membrane resonators. The first mentions of thermoelastic damping were by Benjamin Zwickl and colleagues [12], noting that the limit set by thermoelastic damping at 300 K should be  $Q \sim 3 \times 10^{11}$  for millimeter-sized  $\text{Si}_3\text{N}_4$  membranes, which is significantly higher than for untensioned resonators of similar dimensions. Independently, similar estimates were carried out in the group of Jeff Kimble, and while no derivations were published, Dalziel Wilson noted in his thesis that their prediction “(...) is in qualitative agreement with the results of a calculation we’ve been told has been independently carried out by the Yale group” [55]. The derivation leading to the estimate by Zwickl and colleagues was presented a few years later in Zwickl’s dissertation [56], which, to my knowledge, is the first explicit derivation of thermoelastic damping in

tensioned membrane resonators. Zwickl combined the approach presented by Norris and Photiadis [52] with Zener's thermal mode expansion, to arrive at the following result [56]

$$Q_{\text{Zwickl, TED}}^{-1} = \frac{32T_0 h^4 (m^2 + n^2)^{3/2} E^2 \alpha^2}{\pi^3 \sqrt{\rho\sigma} L^3 (1 - \nu)^2 k}. \quad (2.54)$$

The somewhat complicated approach taken by Zwickl, combined with several approximations as part of the derivation, called for a more careful derivation. Srivatsan Chakram and colleagues provided an alternative result [57], closely following the derivations of Lifshitz and Roukes, as well as Neyfeh and Younis

$$Q_{\text{Chakram, TED}}^{-1} = \frac{\Omega_{mn}^2 E^2 \alpha^2 T_0 h^2}{12\sigma^2 c_p (1 - \nu)^2} \left[ \frac{6}{\xi^2} - \frac{6 \sin \xi + \sinh \xi}{\xi^3 \cos \xi + \cosh \xi} \right]. \quad (2.55)$$

The connection between the results of Zwickl and Chakram et al. isn't obvious, and even less so between the result of Zwickl and the result by Lifshitz and Roukes (see Eq. (2.52)). A bit of algebra can, however, shed some light on that. Here, we will be using the approximate equation for the resonance frequency, given by Eq. (2.18), as well as a Taylor expansion of Eq. (2.52) to second order in  $\xi$ , yielding

$$Q_{\text{LR}}^{-1} \approx \Delta_E \frac{\xi^2}{5}. \quad (2.56)$$

Using this approximation, it can be shown that Eq. (2.54) can be re-expressed as follows

$$Q_{\text{Zwickl, TED}}^{-1} = \frac{960}{\pi^6} \lambda^2 \pi^2 (m^2 + n^2) \frac{\xi^2}{5} \Delta_E \quad (2.57)$$

$$\approx \lambda^2 \pi^2 (m^2 + n^2) Q_{\text{LR}}^{-1}, \quad (2.58)$$

where, in the last line, I have inserted the approximate expression for the quality factor by Lifshitz and Roukes (see Eq. (2.56)), and approximated  $960/\pi^6$  to 1 (differing by less than 0.15%). As for the result by Chakram et al., once again using Eq. (2.18) for the approximate resonance frequency, we arrive at

$$Q_{\text{Chakram, TED}}^{-1} = \left( \frac{1 + \nu}{1 - \nu} \right) \frac{\lambda^2 \pi^2 (m^2 + n^2)}{4} Q_{\text{LR}}^{-1}. \quad (2.59)$$

As we can see, the result agrees with the re-arranged expression by Zwickl, up to a numerical factor. More importantly, having re-expressed the results of Zwickl and Chakram, we start seeing a connection between these results

for thermoelastic damping and dissipation dilution (see Eq. (2.50)). The  $\lambda^2$  scaling, which is present in the expression for dissipation dilution, can be found here as well. Since the derivations by Zwickl and Chakram et al. assumed the approximate solution of the displacement field (i.e. Eq. (2.9)), it is conceivable that including the exponential correction of the modeshape close to the clamping points of the membrane will result in a result closely resembling the one from dissipation dilution. I will therefore take a similar approach as in the articles of Lifshitz and Roukes [37] and Neyfeh and Younis [53], but using the full expression for the displacement field of the membrane<sup>9</sup>.

We begin with the thermoelastic linear equation of motion, in the presence of in-plane tension [53]

$$D\nabla^4 w - \sigma h \nabla^2 w + \nabla^2 M^T + N^T \nabla^2 w = -\rho h \frac{\partial^2 w}{\partial t^2}, \quad (2.60)$$

where  $N^T$  and  $M^T$  are the thermal (as indicated by the superscript) axial force and bending moment, defined as

$$N^T = \frac{E\alpha}{1-\nu} \int_{-h/2}^{h/2} \theta(x, y, z, t) dz \quad (2.61)$$

$$M^T = \frac{E\alpha}{1-\nu} \int_{-h/2}^{h/2} z\theta(x, y, z, t) dz. \quad (2.62)$$

Here,  $\theta(x, y, z, t) = T(x, y, z, t) - T_0$  is the relative temperature field. Assuming that  $\Delta_E \ll 1$ , the heat conduction equation can be written as follows

$$k\nabla^2 \theta = \rho c_p \frac{\partial \theta}{\partial t} + \frac{E\alpha T_0}{1-\nu} \frac{\partial}{\partial t} (z\nabla^2 w), \quad (2.63)$$

where  $T$  has been replaced with  $T_0$  in the second term on the right-hand side of the equation. Assuming plane-wave solution for the relative temperature field and no heat flow from the membrane to the ambient across the membrane boundary, the heat equation can be solved, yielding

$$\theta = \frac{E\alpha T_0}{(1-\nu)\rho c_p} \nabla^2 w \left( z - \frac{\sin \tilde{k}z}{\tilde{k} \cos(\tilde{k}h/2)} \right), \quad (2.64)$$

---

<sup>9</sup>I would like to acknowledge Mark Dykman for posing the question of whether dissipation dilution is valid for devices as thin as ours. After some digestion, the derivation that follows is my attempt to answer that question.

where  $\tilde{k}$  is defined as

$$\tilde{k} = (1 + i) \sqrt{\frac{\Omega_m \rho c_p}{2k}} \quad (2.65)$$

$$= (1 + i) \frac{\xi}{h} \quad (2.66)$$

with  $\Omega_m$  being the angular frequency of the resonator, and using the Eq. (2.53) in the last line. Finally, inserting Eqs. (2.64) and (2.65) into the elastic equation of motion yields

$$D^T \nabla^4 w - \sigma h \nabla^2 w = -\rho h \frac{\partial^2 w}{\partial t^2}, \quad (2.67)$$

where  $D^T$  is the modified flexural rigidity, given as

$$D^T = D \left[ 1 + \Delta_E \left( \frac{1 + \nu}{1 - \nu} \right) f(\tilde{k}h) \right] \quad (2.68)$$

$$f(\tilde{k}h) = 1 + \frac{24}{(\tilde{k}h)^3} \left[ \frac{\tilde{k}h}{2} - \tan \frac{\tilde{k}h}{2} \right]. \quad (2.69)$$

Here,  $D$  is the flexural rigidity as defined in Eq. (2.2). This result is rather satisfying, since we have previously tackled equations in the form of Eq. (2.67).

In the previously mentioned derivations of thermoelastic damping [37, 53, 57], the equation of motion was solved in the Fourier domain. Since the second and fourth-order spatial derivatives of simple sinusoidal functions gives the original functions, multiplied with a numerical factor, all spatial dependencies can be eliminated trivially. However, this is not the case for the full solution of the mode profile (cf. Eq. (2.6)). Instead, we will use the Galerkin method to derive the effective mass and spring constant, and finally the angular frequency. Due to the complex functional dependence of the thermoelastic flexural rigidity, the eigenfrequencies will be complex. Since the imaginary part of the eigenfrequency is responsible for the energy decay<sup>10</sup>, we can express the mechanical quality factor as the ratio of real and imaginary parts of the complex angular frequency

$$Q^{-1} = 2 \left| \frac{\mathcal{I}[\Omega]}{\mathcal{R}[\Omega]} \right|. \quad (2.70)$$

<sup>10</sup>Following Eq. (2.9),  $w \propto \exp i\Omega t = \exp(i\Omega_R t) \exp(-\Omega_I t)$ , where  $\Omega_R$  and  $\Omega_I$  are the real and imaginary parts of the angular frequency, respectively. Since the amplitude decay is proportional to  $\exp(-\Gamma_m t/2)$ , this suggests that  $\Gamma_m = 2\Omega_I$ .

Using the expression for the modeshape of a 1D string (cf. Eqs. (2.5-2.6)), we write the normalized displacement field for a square membrane resonator<sup>11</sup>

$$w_{mn}(x, y) = u_m(x)u_n(y). \quad (2.71)$$

Using Galerkin's method, the effective spring constant and effective mass can be expressed as follows

$$m_{\text{eff}} = \rho h \iint w_{mn}^2 \, dx dy \quad (2.72)$$

$$k_{\text{eff}} = \iint \left( D^T \left\{ \frac{\partial^4 w_{mn}}{\partial x^4} + \frac{\partial^4 w_{mn}}{\partial y^4} + 2 \frac{\partial^4 w_{mn}}{\partial y^2 \partial x^2} \right\} w_{mn} - h\sigma \left\{ \frac{\partial^2 w_{mn}}{\partial x^2} + \frac{\partial^2 w_{mn}}{\partial y^2} \right\} w_{mn} \right) dx dy. \quad (2.73)$$

The effective mass for a square membrane was estimated previously (cf. Eq. (2.15)) using the simplified modeshape. Using Eqs. (2.5-2.6) and (2.71), we evaluate the expression for the effective mass, yielding

$$m_{\text{eff}} = \frac{hL^2\rho}{4} (1 + \mathcal{O}(\lambda) + \dots) \approx \frac{hL^2\rho}{4}. \quad (2.74)$$

Given the fact that  $\lambda$  is on the order of  $10^{-3}$  for our resonators, we can safely neglect all but the zeroth-order term<sup>12</sup>, thus recovering the result from Eq. (2.15).

In the limit of  $\lambda m \ll 1$ , the product  $w_{mn} \frac{\partial^4 w_{mn}}{\partial x^4}$  can be approximated as

$$\begin{aligned} \frac{\partial^4 u_m(x)}{\partial x^4} u_m(x) \approx \frac{4m^2\pi^2}{L^4} & \left( \frac{\exp\left[\frac{-4x}{L\lambda}\right]}{\lambda^2} - \frac{\exp\left[\frac{-2x}{L\lambda}\right] \cos\left[\frac{m\pi x}{L}\right]}{\lambda^2} \right. \\ & + \frac{2 \exp\left[\frac{-2x}{L\lambda}\right] \sin\left[\frac{m\pi x}{L}\right]}{m\pi\lambda^3} \\ & \left. + \frac{m^2\pi^2 \sin^2\left[\frac{m\pi x}{L}\right]}{4} \right), \quad 0 \leq x \leq L/2 \end{aligned} \quad (2.75)$$

where the first three terms are dominant close to the membrane edge, while the last term is so elsewhere. Similarly, the product  $w_{mn} \frac{\partial^2 w_{mn}}{\partial x^2}$  can be written

<sup>11</sup>Strictly speaking, this is only true for the special case of equal mode indices, i.e.  $m = n$  [21]. However, the derivation that follows has also been checked using symmetrized mode functions, verifying that the final result also holds for  $m \neq n$ .

<sup>12</sup>It is furthermore worth reminding that the modeshapes used for this derivation are only valid for  $\lambda \ll 1$ .

as

$$\begin{aligned} \frac{\partial^2 u_m(x)}{\partial x^2} u_m(x) \approx \frac{m^2 \pi^2}{L^2} & \left( \exp \left[ \frac{-4x}{L\lambda} \right] - \exp \left[ \frac{-2x}{L\lambda} \right] \cos \left[ \frac{m\pi x}{L} \right] \right. \\ & + \frac{2 \exp \left[ \frac{-2x}{L\lambda} \right] \sin \left[ \frac{m\pi x}{L} \right]}{m\pi\lambda} \\ & \left. + \sin^2 \left[ \frac{m\pi x}{L} \right] \right), \quad 0 \leq x \leq L/2. \end{aligned} \quad (2.76)$$

These approximations significantly simplify the equations one has to deal with. Upon performing the volume integral in Eq. (2.73) and neglecting terms scaling with  $\exp(-1/\lambda)$ , the effective spring constant can be found to be given by the following expression

$$\begin{aligned} k_{\text{eff}} = \frac{\pi^2 D}{4\lambda^2 L^2} & \left\{ 4(1-\lambda)(m^2+n^2) + \lambda \left[ \pi^2 \lambda (m^4+n^4) + 4n^2 \right. \right. \\ & \left. \left. + 2m^2(\pi^2 \lambda (\lambda-1)^2 n^2 + 2) \right] \times \right. \\ & \left. \left( 1 + \left( \frac{1+\nu}{1-\nu} \right) \left( \Delta_E - \frac{6i\Delta_E}{\xi^2} \right) + \left( \frac{1+\nu}{1-\nu} \right) \frac{(6+6i)\Delta_E \tan \left[ \left( \frac{1}{2} + \frac{i}{2} \right) \xi \right]}{\xi^3} \right) \right\}. \end{aligned} \quad (2.77)$$

While somewhat opaque at first glance, a closer look at the imaginary part of the effective spring constant is instructive. Here we find that

$$\begin{aligned} \mathcal{I}[k_{\text{eff}}] = -\frac{\pi^2 D \Delta_E}{4\lambda L^2} & \left( \frac{1+\nu}{1-\nu} \right) \left( 4(m^2+n^2) + \pi^2 \lambda (m^4+n^4) + 2m^2 n^2 \pi^2 \lambda (\lambda-1)^2 \right) \\ & \times \underbrace{\Delta_E \left[ \frac{6}{\xi^2} - \frac{6 \sin \xi + \sinh \xi}{\xi^3 \cos \xi + \cosh \xi} \right]}_{Q_{\text{LR}}^{-1}}. \end{aligned} \quad (2.78)$$

Unsurprisingly we find that the imaginary part of the effective spring constant is proportional to the inverse quality factor derived by Lifshitz and Roukes (cf. Eq. (2.52)). Combining Eqs. (2.74) and (2.77) for the effective mass and the effective spring constant, respectively, the angular frequency can be found. Expanding to first order in  $\Delta_E$  simplifies the equations appreciably, allowing us to calculate the quality factor following Eq. (2.70). One final

Taylor expansion in  $\lambda$  yields the following result

$$Q_{\text{TED}}^{-1} \approx \left( \frac{1+\nu}{1-\nu} \right) Q_{\text{LR}}^{-1} \left\{ \lambda + \lambda^2 \frac{\pi^2(m^2 + n^2)}{4} + \left( \frac{1+\nu}{1-\nu} \right) \frac{\lambda^2 \Delta_E}{2} \left[ 1 + \frac{6 \sin \xi - \sinh \xi}{\xi^3 \cos \xi + \cosh \xi} \right] + \mathcal{O}(\lambda^3) + \dots \right\}. \quad (2.79)$$

While the second term of this expression resembles the results of Zwickl and Chakram, we see that including the corrections to the modeshape at the edges of our resonator has resulted in the emergence of two additional terms – one, which closely resembles the edge term known from “canonical” dissipation dilution calculations (cf. Eq. (2.50)), and an explicitly temperature dependent term (since  $\Delta_E \propto T_0$ ). The latter suggests that the dilution term is in fact temperature dependent. However, since  $\xi \sim \mathcal{O}(10^{-2})$  for thin ( $\sim 10$  nm) membrane resonators, the temperature dependent term will likely be negligible for the devices studied in this thesis. For membrane thicknesses approaching  $1 \mu\text{m}$ , the temperature dependent term could, however, be of importance.

As in dissipation dilution, thermoelastic damping in tensioned resonators has two contributions – one from the sinusoidal modeshape (in agreement with the results of Zwickl and Chakram), and the other originating from the exponential correction at the edges of the resonator. Looking back at the equation for the relative temperature field (cf. Eq. (2.64)), we see that it is proportional to the second order spatial derivative of the displacement field, i.e.  $\theta \propto \nabla^2 w$ . The largest temperature gradients are found in regions with largest curvatures for a given modeshape, which, in our case, happens to be at the clamping points of the resonator. Since the second derivative of the displacement field given by Eq. (2.6) scales as  $(\lambda L)^{-1}$  near the membrane clamp, the dissipation is thus dominated by the large temperature gradients at the clamping points of the resonator (see Fig. 2.4). We can therefore conclude that in order to reduce thermoelastic damping for a given vibrational mode in a tensioned resonator, the curvature of the modeshape has to be reduced accordingly.

As an aside and a testament to “hindsight is 20/20”, let us consider the concept of “modal participation factor”, which was introduced by Douglas Photiadis and colleagues in the early 2000’s [58]. The authors realised that the exact mode profile can play a significant role in the magnitude of thermoelastic damping, and proposed to account for this by a so-called participation factor,  $p_n$ , defined as the ratio of the energy associated with flexure and total modal energy. Thermoelastic damping for given mode  $n$  could then be

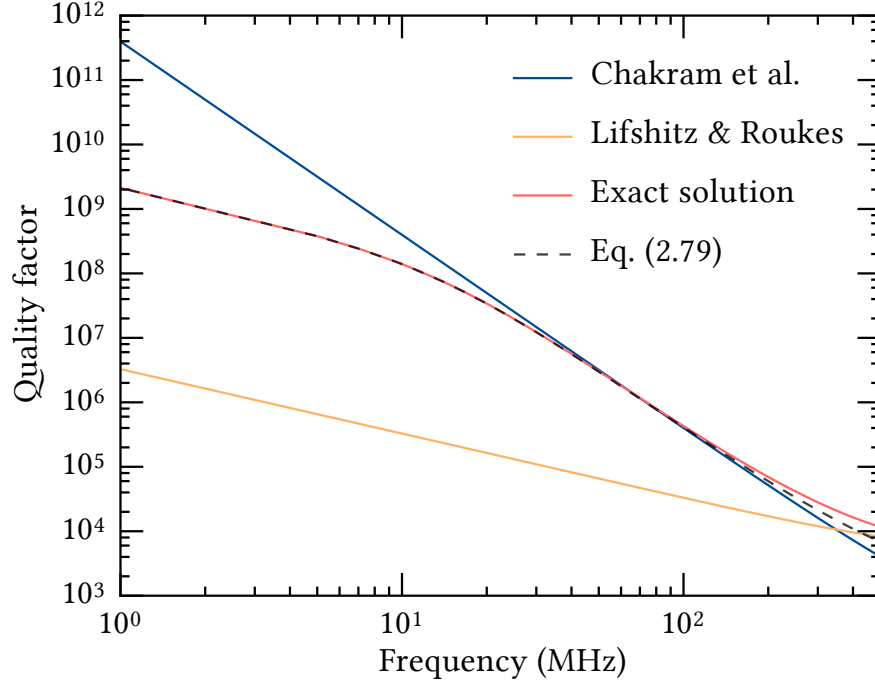


Figure 2.5: Comparison of thermoelastic damping derived in this work with results from Chakram et al. [57] (see Eq. (2.59)), and Lifshitz and Roukes [37] (see Eq. (2.52)). We also compare the approximate solution (dashed) given by Eq. (2.79), and the exact solution (red), estimated numerically from Eqs. (2.74) and (2.77). We assume  $L = 500 \mu\text{m}$ ,  $h = 50 \text{ nm}$ ,  $\sigma = 1.27 \text{ GPa}$ ,  $E = 270 \text{ GPa}$ ,  $\alpha = 2.8 \times 10^{-6} \text{ K}^{-1}$ ,  $T_0 = 294 \text{ K}$ ,  $\nu = 0.27$ ,  $\rho = 3200 \text{ kg m}^{-3}$ ,  $c_p = 656 \text{ Jkg}^{-1}\text{K}^{-1}$  and  $k = 3.2 \text{ Wm}^{-1}\text{K}^{-1}$  (here, I use the same values for CTE, specific heat and thermal conductivity as [56]).

described as  $Q_{\text{n,Zener}}^{-1} = p_{\text{n}} Q_{\text{Zener}}^{-1}$ . A couple of years later, Norris and Photiadis formalised this idea [52], showing that, for an isotropic material, the thermoelastic damping can be expressed as follows<sup>13</sup>

$$Q_{\text{m,Zener}}^{-1} = \left( \frac{1 + \nu}{1 - \nu} \right) \frac{1}{6(1 - \nu^2)} \frac{E_1 h^3 \iint \left( \frac{\partial^2 w}{\partial x^2} + \frac{\partial^2 w}{\partial y^2} \right)^2 dx dy}{\rho \Omega^2 \int w(x, y)^2 dV} \times Q_{\text{Zener}}^{-1}, \quad (2.80)$$

where  $E_1$  is the real part of the complex Young's modulus. As we can see, the numerator corresponds to the surface integral of the mean curvature, while the denominator is the total stored modal energy. This expression looks quite similar to the equations we considered in the context of dissipation dilution

<sup>13</sup>The following expression is based on Eqs. (4.9) and (4.17) in [52], but here I have taken the liberty to express them such that the parallels to previous equations are clearer.

(see particularly Eq. (2.47)). In fact, making the substitution  $E_1 \rightarrow E_2 Q_{\text{Zener}}$  makes the resemblance even clearer. Therefore, in the context of tensioned resonators, the modal participation factor is in essence the inverse of the dilution factor.

Since we have now derived dissipation dilution from “first principles”, its physical origins are clearer than before. Comparing the results for thermoelastic damping (Eq. (2.79)) and dissipation dilution (see Eq. (2.50)), and assuming that the quality factor of our resonator is limited by thermoelastic damping, allows us to express the intrinsic quality factor, previously defined by the ratio of the real and imaginary part of the Young’s modulus, in terms of thermodynamical quantities

$$Q_{\text{int}}^{-1} = \left( \frac{1 + \nu}{1 - \nu} \right) \Delta_E \left[ \frac{6}{\xi^2} - \frac{6}{\xi^3} \frac{\sin \xi + \sinh \xi}{\cos \xi + \cosh \xi} \right]. \quad (2.81)$$

In the limit of  $\xi \ll 1$  this expression simplifies to

$$Q_{\text{int}}^{-1} \approx \left( \frac{1 + \nu}{1 - \nu} \right) \Delta_E \frac{\xi^2}{5} = \left( \frac{1 + \nu}{1 - \nu} \right) \frac{h^2 \Omega_m E \alpha^2 T_0}{10k}, \quad (2.82)$$

where we have Taylor expanded Eq. (2.81) to second order in  $\xi$ , and substituted the expressions for  $\xi$  and  $\Delta_E$  (see Eqs. (2.37-2.53)).

Finally, of high relevance for this work is the case of cryogenic operation of thin membrane resonators. As it turns out, the mean-free path length of thermal phonons in tensioned silicon nitride resonators is on the order of  $\sim 30$  nm at 10 K [59]. As we will see later, some of the experiments in this thesis are focused around cryogenic operation with membrane thicknesses on the order of 10 nm. In this regime the heat transfer transitions from diffusive to ballistic. As suggested by Lifshitz and Roukes [37], and later shown numerically by Kiselev and Iafrate [60], the characteristic time constant  $\tau$  (given by Eq. (2.38) in the diffusive regime) transitions from  $\tau \propto h^2$  (as in Zener’s model for thermoelastic damping) to  $\tau \propto h$ . Since we have previously seen that  $\xi \propto \sqrt{\tau_{\text{TED}}}$  (see Eq. (2.53)), this suggests that in the ballistic regime we can expect a scaling of  $\xi \propto \sqrt{h}$ .

Naïvely one could say that since the explicitly temperature dependent term ( $\mathcal{O}(\lambda^2 \Delta_E)$ ) in Eq. (2.79) is small compared to the first two terms, the dilution factor is mostly unchanged as a function of temperature –  $\lambda$  only depends on temperature via the temperature dependence of Young’s modulus, Poisson’s ratio and the tension. However, seeing that the mean-free path length exceeds  $\sim 30$  nm at liquid helium temperatures [59], it is unclear

whether the foundational equations of our thermoelastic damping model still hold. In the ballistic regime the temperature becomes non-local and hence nonlocal terms could arise in our heat equation. To my knowledge the generalisation of Fourier’s law of heat conduction to the ballistic regime is a topic of ongoing research and the interested reader is referred to a recent publication by Hua et al. [61] outlining the current state of affairs. It can therefore not be ruled out that for the thinnest devices presented in this work there is indeed a (minor) deviation from the “canonical” dissipation dilution model at liquid helium temperatures.

Looking back at the expression for the intrinsic  $Q$  in the limit of small  $\xi$  (cf. Eq. (2.82)), the result suggests that one can expect a  $Q_{\text{int}} \propto h^{-2}$  scaling with thickness. While this suggests that shrinking the device thickness down is highly favorable, another dissipation mechanism starts to play a significant role at these length scales – namely losses due to surface impurities and/or roughness. This source of dissipation has been shown to play a significant role at sub-micron length-scales [62–64] and will be discussed in the following section.

#### 2.2.4 Surface losses in thin resonators

It is an experimental fact that an increase in the surface-to-volume ratio of a mechanical device is accompanied by a reduction of its mechanical quality factor. Surfaces are prone to contamination, as well as physical and chemical damage during the fabrication process, so it is not surprising that losses at the surfaces of a resonator are greater than in the bulk. Early studies of silicon nitride cantilevers by Kevin Yasumura and colleagues showed that below a thickness of  $\sim 1 \mu\text{m}$ , the quality factor scaled linearly with the device thickness [62], approaching a plateau for thicker devices, which is ascribed to volumetric (bulk) losses.

We can explain this in broad strokes within the framework of Zener’s model, and by dividing the imaginary part of Young’s modulus into two parts – one responsible for surface related dissipation, and one for the bulk

$$\tilde{E} = E_1 + i \underbrace{[E_{2,\text{vol}} + E_{2,\text{surf}} (\delta(z - h) + \delta(z))]}_{E_2}, \quad (2.83)$$

where a Dirac delta function appears in conjunction with  $E_{2,\text{surf}}$ , to signify its role being limited to the surface only (here we assume that the device midplane is at  $z = h/2$  with surfaces at  $z = 0$  and  $h$ , whereas at Eq. (2.48) the midpoint was  $z = 0$ ). As we saw in the derivation of dissipation dilution,

the total dissipated elastic energy scales with  $\Delta W \propto \int z^2 E_2 dz$  (see Eq. (2.47)). Using the expression above for the complex Young's modulus we find that

$$\Delta W \propto \int z^2 [E_{2,\text{vol}} + E_{2,\text{surf}}\delta(z - h)] dz \times \iint (\text{curvatures}) dx dy \quad (2.84)$$

$$\propto \left( \frac{h^3}{3} E_{2,\text{vol}} + h^2 E_{2,\text{surf}} \right) \times \iint (\text{curvatures}) dx dy \quad (2.85)$$

$$\propto \left( E_{2,\text{vol}} + \frac{3E_{2,\text{surf}}}{h} \right) \times \frac{h^3}{3} \iint (\text{curvatures}) dx dy. \quad (2.86)$$

In the last line we have factored out  $h^3/3$ , to ensure the correct scaling for the next step of our calculation. Recalling that the quality factor can be written as the product of the dilution factor and the ratio of the real and imaginary parts of the Young's modulus (see Eq. (2.50)), we can express the mechanical quality factor as

$$Q_m = D(\lambda) \frac{E_1}{E_{2,\text{vol}} + \frac{3E_{2,\text{surf}}}{h}} \quad (2.87)$$

$$= D(\lambda) \left( \underbrace{\frac{E_{2,\text{vol}}}{E_1}}_{Q_{\text{vol}}^{-1}} + \underbrace{\frac{3E_{2,\text{surf}}}{E_1 h}}_{Q_{\text{surf}}^{-1}} \right)^{-1}, \quad (2.88)$$

where  $D(\lambda)$  is the overall dilution factor for a given geometry. As we can see,  $Q_{\text{surf}}$  scales linearly with the device thickness  $h$ , as it has been observed experimentally.

An extensive literature study was recently carried out by Silvan Schmid and Luis Guillermo Villanueva, where the authors considered the intrinsic mechanical quality factor of silicon nitride devices for a variety of geometries (membranes, strings and cantilevers), as a function of device thickness [64]. Spanning two orders of magnitude in thickness, a clear trend was shown to emerge – surface losses were dominant below  $h \sim 100$  nm, and the intrinsic quality factor saturated around  $Q_{\text{int}} \sim 2.8 \times 10^4$  above  $\sim 1$   $\mu\text{m}$  device thickness. In Figure 2.6 the best fit of  $Q_{\text{int}}^{-1} = Q_{\text{vol}}^{-1} + Q_{\text{surf}}^{-1}$  is shown from the study of Villanueva and Schmid, alongside a 60% confidence interval (originating from the uncertainties in the device dimensions and the tensile stresses of the devices). The values found in this study were as follows

$$Q_{\text{vol}} = 28000 \pm 2000 \quad (2.89)$$

$$Q_{\text{surf}} = [(6 \pm 4) \times 10^{10} \text{ m}^{-1}] \times h, \quad (2.90)$$

while in the surface-dominated regime the quality factor was found to be  $Q_{\text{surf}} \approx (5.7 \times 10^{10} \text{ m}^{-1}) \times h$ . These values will be used extensively in this work, as we try to estimate the mechanical quality factors of various membrane geometries.

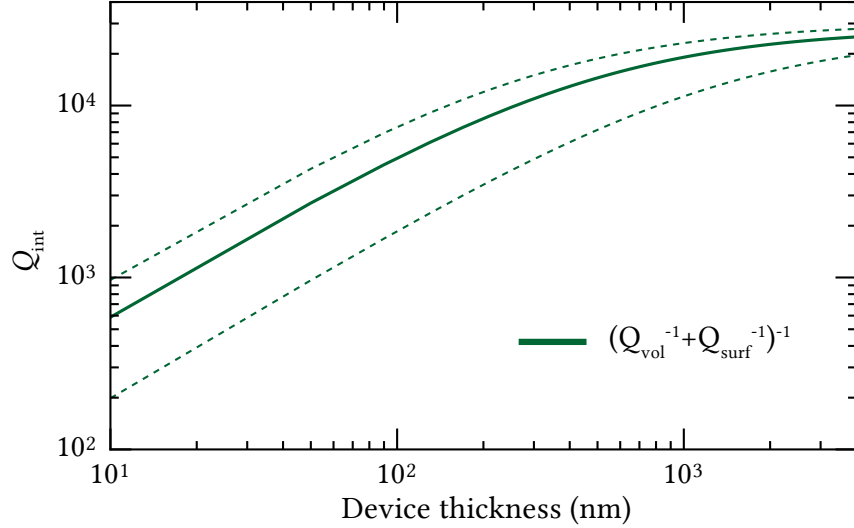


Figure 2.6: Intrinsic quality factor as a function of device thickness, assuming a surface and volumetric quality factor given by Eqs. (2.90) and (2.89) (following Villanueva and Schmid [64]).

While in fundamental research we are mainly interested in the best possible performance of a mechanical device, in the context of practical sensors it can be advantageous to realise devices which are accurately described using easily accessible material data. As we saw in relation to thermoelastic damping, one can in principle predict the mechanical quality factor entirely based on thermodynamic and elastic quantities. On the other hand, estimating  $Q_{\text{vol}}$  and  $Q_{\text{surf}}$  necessitates careful measurements with varying device dimensions, which can be cumbersome. Thus it could be of interest to recognise a parameter regime where the mechanical quality factor is dominated by thermoelastic damping, rather than surface and bulk losses. A more sinister, albeit more honest, reason to identify such a regime is that it would allow us to verify the theoretical predictions for thermoelastic damping.

As we have seen, upon introducing tension in a resonator, the intrinsic dissipation will be diluted as follows

$$Q_{\text{m}} = D(\lambda)Q_{\text{int}} = D(\lambda) (Q_{\text{vol}}^{-1} + Q_{\text{surf}}^{-1})^{-1}, \quad (2.91)$$

where the dilution factor  $D(\lambda)$  is given by Eq. (2.50) as

$$D(\lambda) = \left( \lambda + \lambda^2 \frac{(m^2 + n^2)\pi^2}{4} \right)^{-1}. \quad (2.92)$$

In Fig. 2.7 we consider the total quality factor (of the fundamental vibrational mode) for square silicon nitride membrane resonators in room temperature settings

$$Q_{\text{m,tot}} = Q_{\text{TED}}^{-1} + D(\lambda)^{-1} (Q_{\text{vol}}^{-1} + Q_{\text{surf}}^{-1}), \quad (2.93)$$

where we use the values for  $Q_{\text{vol}}$  and  $Q_{\text{surf}}$  obtained by Villanueva and Schmid (see Eqs. (2.89-2.90)). As shown in Fig. 2.7, the total quality factor is dominated by surface and volumetric losses below device thicknesses of  $\sim 100$  nm, while thermoelastic damping plays the dominant role for thicker devices. Initially, the quality factor is independent of the thickness. This is due to the fact that  $Q_{\text{int}} \propto h$ , while  $\lambda \propto h$ , resulting in a thickness-independent quality factor in the surface-dominated regime. For thicknesses above  $\sim 1 \mu\text{m}$ , the dilution factor grows, resulting in a dip in the overall quality factor.

Since we are interested in using high-stress silicon nitride, we need to consider one limitation – namely the fact that above a thickness of  $\sim 400$  nm the silicon nitride film starts cracking [65]. While this is not a “hard limit” and can be mitigating by structuring of the silicon nitride film in the vicinity of the resonator [65], we use this as an “upper bound” for our current consideration. Fig. 2.7 suggests that studying thermoelastic damping should be possible for smaller device dimensions (i.e.  $L \lesssim 250 \mu\text{m}$ ).

### Reduction of surface losses

Seeing that surface losses are the dominant source of dissipation in thin membrane resonators, it is worthwhile investigating options to reduce this source. Additionally, by doing so one could access the thermoelastic damping limited regime for smaller thicknesses, making it easier to probe this damping mechanism. In the context of silicon cantilevers, Yasumura and colleagues showed that heat treatment of samples in a nitrogen environment can result in a 4-fold enhancement of the mechanical quality factor [62]. Heat treatments can remove surface adsorbates, release spurious strains in the devices, remove  $\text{SiO}_2$  layers arising from oxidation of the silicon surface, and so on. Other studies have shown  $Q$  improvements of more than an order of magnitude as a result of annealing in ultra-high vacuum (UHV) [66], and subsequently a steady reduction of the  $Q$ , as contaminants gradually latch

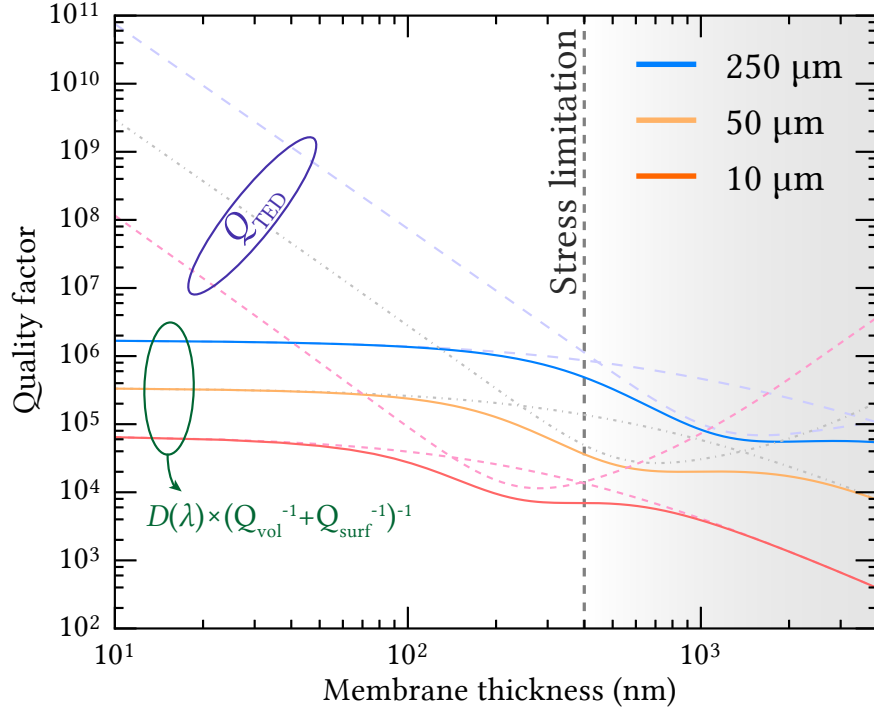


Figure 2.7: Solid lines show the total mechanical quality factor, combining thermo-elastic damping (dashed and highlighted with an ellipse), as well as volumetric and surface losses (dashed and annotated). The material stress limitation is indicated by the black dashed line. The individual curves correspond to membrane sidelengths of 10  $\mu\text{m}$ , 50  $\mu\text{m}$  and 250  $\mu\text{m}$  and are indicated by different colours. Here, we have assumed  $\sigma = 1.27$  GPa,  $E = 270$  GPa,  $\alpha = 2.8 \times 10^{-6}$   $\text{K}^{-1}$ ,  $T_0 = 294$  K,  $\nu = 0.27$ ,  $\rho = 3200$   $\text{kg m}^{-3}$ ,  $c_p = 656$   $\text{J kg}^{-1} \text{K}^{-1}$  and  $k = 3.2$   $\text{W m}^{-1} \text{K}^{-1}$ .

on to the device surfaces. Finally, it has been demonstrated that modifying the surface chemistry can improve the performance of mechanical devices. For instance, exposing the surfaces of silicon cantilevers to atomic hydrogen results in chemically inert surfaces [67], due to a reduction of the number of dangling bonds and thus the reactivity of the surface. This can, among others, reduce the oxidation rate, which causes additional dissipation in silicon resonators [67]. Diamond resonator, on the other hand, perform best with oxygen termination [68].

Unfortunately, when it comes to silicon nitride, there are no in-depth studies of the effects of surface treatment on mechanical performance. Recently, Silvan Schmid and colleagues demonstrated the effect of oxygen plasma on the mechanical  $Q$ 's of silicon nitride membrane resonators [69]. The oxygen

plasma oxidises the silicon nitride surface, and the resultant silicon oxynitride has a compressive stress, resulting in almost 50% reduction of the overall membrane tension. The effect on the intrinsic quality factors are appreciable (up to  $\sim 40\%$  reduction), suggesting that the oxidized layer is more lossy, compared to pristine silicon nitride. Finally, it is conceivable that heat treatments of silicon nitride in vacuum will result in a reduction of surface adsorbates. As for surface passivation, I am currently not aware of efforts in this direction.

### 2.2.5 Other damping mechanisms

As we are wrapping up the topic of dissipation, we consider one final loss mechanism that is of relevance for the type of resonators described in this work. While it is not central to this thesis, a general overview is nevertheless warranted.

#### Two-level systems

An important question in the context of sensing and cavity optomechanics is the temperature dependence of the mechanical quality factor. Assuming operation in thermoelastic damping limited regime, which was discussed in the previous section, one could in principle predict the temperature dependence of the quality factor using Eq. (2.81) and knowledge of the temperature dependence of the coefficient of thermal expansion, thermal conductivity and the specific heat capacity. However, since our devices will, for the most part, only be a few tens of nanometers thick, surface losses will be dominant (see Fig. 2.7). In this regime, we need to describe the temperature dependence by other means.

As it turns out, dissipation in resonators based on amorphous materials is effectively universal at cryogenic temperatures, and the agreement is not only qualitative, but also quantitative, showing little dependence on the chemical composition of the resonator material [70]. Following measurements by Zeller and Pohl of thermal conductivity and specific heat in vitreous<sup>14</sup> SiO<sub>2</sub>, selenium and germania [71], Phillips [72], as well as Anderson, Halperin and Varma [73], proposed a tunneling model to explain the observations by Zeller and Pohl. The model assumes a distribution of defect states, each with two equilibrium positions. Describing each of these defects as an effective particle in a double-well potential, the researchers could accurately describe the observations of Zeller and Pohl. Importantly, Anderson and colleagues pointed

---

<sup>14</sup>Also referred to as fused silica or fused quartz.

out that one should anticipate attenuation of ultrasonic phonons, due to their interaction with the two-level systems (TLS). This idea was explored further by Jäckle [74], predicting that the attenuation should scale as  $T^3$  at low temperatures (below 1 K), which was confirmed experimentally shortly hereafter by Hunklinger and colleagues [75].

The attenuation of elastic waves is due to the coupling of two-level defect states within the material and the strain fields,  $\epsilon$ , described by the so-called deformation potential,  $\gamma = 1/2(\partial\Delta/\partial\epsilon)$  [76, 77]. As mentioned before, a defect state is represented as a particle in a double-well potential with an asymmetry  $\Delta$  and energy barrier height  $V$ . Above liquid helium temperatures, the particle can move over the potential barrier via multi-phonon processes, where phonons originating from the mechanical mode of interest contribute to this excitation. The elastic energy is dissipated upon the subsequent decay of the excited defect state. The internal friction due to this relaxation process can to a very good approximation be described as [76]

$$Q_{\text{rel,TLS}}^{-1} = \frac{\gamma^2}{\rho v^2 k_B T} \int_{-\infty}^{\infty} d\Delta \int_0^{\infty} P(\Delta, V) \text{sech}^2\left(\frac{\Delta}{2k_B T}\right) \frac{\Omega\tau}{1 + \Omega^2\tau^2} dV, \quad (2.94)$$

where  $P(\Delta, V)$  is the distribution of energies  $V$  and  $\Delta$ ,  $v$  is the velocity of sound. We recognise the last part of the integral as a Debye peak (see Eq. (2.35)). The relaxation rate between the two wells of the potential can be described by Arrhenius' law

$$\tau^{-1} = \tau_0^{-1} \cosh\left(\frac{\Delta}{2k_B T}\right) \exp\left(-\frac{V}{k_B T}\right). \quad (2.95)$$

Assuming a Gaussian distribution for  $\Delta$ , and a ‘‘modified’’ Gaussian distribution [77] for the energy barrier  $V$  (i.e.  $g(V) \propto (V/V_0)^{-\xi} \exp(-V^2/2V_0^2)$ , where  $\xi < 1$ ), the inverse quality factor is found to be

$$Q_{\text{rel,TLS}}^{-1} = \mathcal{C} \Phi\left(\frac{\sqrt{2}k_B T}{\Delta_C}\right) \frac{1}{k_B T} \int_0^{\infty} \left(\frac{V}{V_0}\right)^{-\xi} \times \exp\left(-\frac{1}{2}\frac{V^2}{V_0^2}\right) \frac{\Omega\tau_0 \exp(V/k_B T)}{1 + \Omega^2\tau_0^2 \exp(2V/k_B T)} dV, \quad (2.96)$$

with  $\Phi$  being the error function. The remaining parameters are found by fitting the above model to the data. Below liquid helium temperatures (more specifically, below  $\sim 1$  K), the particle in the double-well potential can no longer hop between the wells via thermal excitation, but rather through quantum mechanical tunnelling [77].

Seeing that silicon nitride is an amorphous material, a behaviour similar to silica is anticipated. Indeed, Faust et al. [78] first reported evidence of two-level defect states in silicon nitride string resonators, by considering the temperature dependence of two vibrational modes of the device as a function of temperature. The authors found that the low-temperature ( $< 100$  K) behaviour can be accurately described by the relaxation model presented by Vacher et al. [77], where the TLS parameters agreed with those for silica to within 30%. Importantly, this was observed in a prestressed structure, suggesting that the presence of tension in the resonator does not affect the coupling between the resonator mode and the two-level defect states.

It is interesting to note that a few years prior to this publication, Jian-sheng Wu and Clare C. Yu proposed a modified TLS model as an explanation for the observed low mechanical dissipation in stressed silicon nitride resonators [79]. Among the possible explanations was dissipation dilution<sup>15</sup>, but also the possibility of pre-tension modifying the tunnel barrier height  $V_0$  or the deformation potential  $\gamma$ . The modified TLS model predicted, among others, a stress-dependent thermal conductivity and specific heat. This was later studied by Hossein Ftouni and colleagues [59], finding that the thermal properties of the silicon nitride are not stress dependent. This provides some confidence in the results presented previously on thermoelastic damping (particularly, Eq. (2.79)).

### 2.2.6 Damped driven harmonic oscillator

Our derivations up to this point have focused on the origins of dissipation in tensioned membrane resonators, as well as touched upon the mapping from a two-dimensional resonator to an effective 1D (point-mass) oscillator undergoing simple harmonic motion (cf. (2.11)). Combining these, alongside a generic driving force  $F_{\text{ext}}$ , leads us to the well-known equation for a damped harmonic oscillator

$$\frac{\partial^2 q}{\partial t^2} + \Gamma_m \frac{\partial q}{\partial t} + \Omega_m^2 q = \frac{F}{m_{\text{eff}}}, \quad (2.97)$$

where  $\Gamma_m = \Omega_m/Q_m$  and  $q$  is the displacement field of a particular vibrational mode of the resonator. We can solve this equation in a straightforward

---

<sup>15</sup>In fact, this publication is how we became aware of work on dissipation dilution preceding the findings of Silvan Schmid, Quirin Unterreithmeier, and others within our field of research.

fashion in the Fourier domain<sup>16</sup>

$$q(\Omega) = \chi_m(\Omega)F(\Omega), \quad (2.98)$$

$$\chi_m(\Omega) = \frac{m_{\text{eff}}^{-1}}{\Omega_m^2 - \Omega^2 - i\Omega\Gamma_m}. \quad (2.99)$$

Here we have defined the mechanical susceptibility,  $\chi_m$ , describing the response of the mechanical mode to an external driving force. In our case, a very relevant driving force is the thermal Langevin force. Following the fluctuation-dissipation theorem, the auto-correlation of the thermal force can be written as [80]

$$\langle F_{\text{th}}(t)F_{\text{th}}(t + \tau) \rangle = 2m_{\text{eff}}\Gamma_m k_B T \delta(\tau). \quad (2.100)$$

This result holds in the limit of  $k_B T \gg \hbar\Omega$  (i.e. high-temperature limit) and under the assumption that the correlation time of the bath is significantly shorter than all other relevant time scales (i.e. Markovian limit). Following the Wiener-Khinchin theorem, the (single-sided) power spectral density of the Langevin force can be written as

$$S_{F_{\text{th}}F_{\text{th}}}(\Omega) = 2 \int_{-\infty}^{\infty} \langle F_{\text{th}}(0)F_{\text{th}}(\tau) \rangle e^{-i\Omega\tau} d\tau \quad (2.101)$$

$$= 4m_{\text{eff}}\Gamma_m k_B T. \quad (2.102)$$

Minimising the influence of the Langevin force noise is often a key objective in mechanical sensor design and optimisation, and is at the heart of this work. The equation above suggests that this can be achieved via three different paths – reduction of resonator mass, dissipation rate and temperature.

Using Eq. (2.98) in conjunction with the above result, the power spectral density of the displacement can be expressed as

$$S_{qq}(\Omega) = |\chi_m(\Omega)|^2 S_{F_{\text{th}}F_{\text{th}}}(\Omega) \quad (2.103)$$

$$= \frac{4\Gamma_m k_B T m_{\text{eff}}^{-1}}{(\Omega_m^2 - \Omega^2)^2 + (\Omega\Gamma_m)^2}. \quad (2.104)$$

For Fourier frequencies close to the mechanical resonance, the displacement power spectral density simplifies to a simple Lorentzian lineshape

$$S_{qq}(\Omega) \approx \frac{k_B T}{m_{\text{eff}}\Omega_m^2} \frac{\Gamma_m}{(\Omega_m - \Omega)^2 + (\Gamma_m/2)^2}. \quad (2.105)$$

---

<sup>16</sup>Following our definition of the Fourier transform,  $\mathcal{F}[\dot{q}] = -i\Omega q(\Omega)$ .

Invoking Parseval’s theorem, the mean-squared displacement can be found by integration of the displacement power spectral density

$$\langle q^2 \rangle = \int_{-\infty}^{\infty} S_{qq}(\Omega) \frac{d\Omega}{2\pi} = \frac{k_B T}{m_{\text{eff}} \Omega_m^2}. \quad (2.106)$$

As we can see, the temperature of the vibrational mode can be estimated by integration of the power spectral density. Conversely, knowing the bath temperature, resonance frequency and effective mass can be used to calibrate vibrational spectra in absolute displacement units. While the latter will not be of relevance for the results presented here, the connection between the displacement PSD and the mode temperature will be invoked later in this work.

## 2.3 Summary

As we conclude this chapter, let us summarise some of the key points that will be of relevance for the work at hand, as well as future research. We saw the value of Galerkin’s method from the get go (see Section 2.1.1), as it allows us to define effective resonators parameters starting from the elastic equations of motion. In particular the definition of effective mass will be employed in the following chapters, both as a figure of merit for the mechanical devices, and in relation to estimating the light-mechanical coupling strength in cavity optomechanics.

After reviewing two of the most prominent extrinsic sources of dissipation for our mechanical devices, a substantial part of the chapter focused on thermoelastic damping, in particular its connection to dissipation dilution. Starting from the thermoelastic equations of motion, and using Galerkin’s method, we derived an explicit expression for thermoelastic damping, valid for highly tensioned membrane resonators. We found that the stress-dependent prefactor closely resembles the “canonical” dilution factor [21]. However, this derivation provided two new insights. Firstly, we found that the dilution factor is in fact temperature dependent, albeit weakly for thin and highly stressed resonators. Secondly, since the equations of motion upon which the derivation is based on are potentially invalid for thin resonators in low temperature settings, we are led to the conclusion that the standard model for dissipation dilution is not necessarily valid for our devices at cryogenic temperatures. This is a particularly interesting question to explore in the future.

While the derivation of thermoelastic damping presented in this chapter provides us with an explicit expression for the mechanical quality factor,

which only depends on the elastic and thermal properties of the resonator material, surface related losses are in fact the dominant source of dissipation for the device dimensions considered in this thesis. However, we identify a region in the parameter space, where the contribution of thermoelastic damping is dominant. Realising and characterising membrane devices that span this region of the parameter space would potentially allow us to verify the validity of the model.

For the following chapters, however, we will solely focus on the geometric dependence of the dilution factor.

# Chapter 3

## Phononic engineering and soft clamping

Having established some theoretical groundwork, we now move our attention to the experimental aspects of developing high- $Q$  mechanical resonators. Specifically, we will focus on the use of phononic crystal structures in suppressing phonon tunneling losses in membrane resonators. The underlying design considerations are outlined, particularly in light of their designated use in quantum optomechanical experiments.

In the second half of the chapter the concept of *soft clamping* is presented, which allows for a significant reduction of the internal dissipation in membrane resonators. Starting from a phononic crystal slab akin to the one discussed in relation to phonon tunneling losses, we consider the evolution from a thick to a thin plate, and how the introduction of in-plane tension affects the properties of the phononic bandgap structure. The device fabrication and characterisation are outlined, and the fingerprints of soft clamping are identified based on the measurements. Finally, building upon the basics of soft clamping, three additional devices and their design rationale are presented.

Note that the following chapter includes results which constituted part of my master's thesis [1]. Figures reprinted or reproduced from the master's thesis will be acknowledged accordingly in figure captions.

## 3.1 Phonon tunneling losses

### 3.1.1 Introduction

Anchor losses, clamping losses, radiation losses, mounting losses, phonon tunneling losses, and so on – the devil goes by many names. All these terms refer to one and the same loss mechanism, namely loss of elastic energy into the support of the resonator. Studies of this loss mechanism can be found in numerous fields of research within physics and engineering, and can be traced several decades back in time. Here, I will outline select examples, drawing parallels to research in our own field of optomechanics. As an aside, it is worth mentioning that not all applications of mechanical resonators necessarily benefit from extremely high quality factors and thus small bandwidths. A prime example is mechanical transducers, where the resonator bandwidth has to be comparable to the signal bandwidth (either intrinsically or externally, by dampening the resonator motion). These applications nevertheless demand careful study of anchor losses, in the interest of reproducibility.

Among the various solutions to reduce dissipation due to anchor losses one can find common threads. A common technique is suspension of the resonator at the nodal points of the mode of interest [81]. The so called “free-free” design found it’s way to our research field [82], where a careful study of anchor losses was conducted using the phonon tunneling approach, which we touched upon in the previous chapter. This theory, developed by Ignacio Wilson-Rae [26], provides a general framework to describe anchor losses in suspended beam and membrane-like resonators. Due to it’s relevance for the work at hand, the term phonon tunneling will be adapted in this work, over the multitude of other names for the same loss mechanism.

Another technique involves structuring of the region around the resonator (e.g. etching trenches/mesas), in order to realise acoustic<sup>1</sup> reflectors. Examples can be found both for surface acoustic waves (SAWs) [83], as well as suspended mechanical structures [84]. Similar techniques have been adapted in optomechanical devices, including silicon nitride membranes [85], where the corrugations in the silicon substrate act as acoustic reflectors. In a similar vein, nested structures, where the inner-most part is the resonator of interest, while the outer structure acts as a mechanical low-pass filter, have shown to reduce the influence of phonon tunneling losses in torsional res-

---

<sup>1</sup>While there is not a clearly established terminology within our field (or the literature for mechanical resonators in general) when it comes to referring to bulk waves in solid objects, in this work I will refer to pressure waves in fluids as *acoustic* waves, while waves propagating in solids will be referred to as *elastic* waves.

onators [86, 87], as well as membrane resonators [88]. Yet another approach is using beams of particular length as suspension, which provides an acoustic impedance mismatch between the resonator and its support [89]. A similar approach was adapted by Tobias Kippenberg’s group in realising microdisk resonators with low mechanical dissipation [90]. These devices also included another layer of impedance mismatch, namely due to the difference in the material of the microdisk resonator (silica) and its support (silicon). Similar to optics, the interface between two materials results in an impedance mismatch, where part of the (elastic) wave is reflected<sup>2</sup>.

Finally, another method to reduce phonon tunneling losses, similarly adapted from optics, involves acoustic/elastic Bragg reflectors. Shortly after the pioneering work by Eli Yablonovitch and coworkers in 1991 [91], introducing photonic crystals as we know them, two research groups [92, 93] published their results on the acoustic analogy of photonic crystals – *phononic crystal structures*. Here the idea is quite similar: by periodically modulating the acoustic (elastic) potential, acoustic (elastic) excitations with wavelengths comparable to the periodicity of the underlying structure interfere destructively<sup>3</sup>, thus creating phononic bandgaps (sometimes referred to as stop bands) – regions in frequency, where acoustic (elastic) waves are not allowed to propagate and any excitation within the frequency range of the bandgap is exponentially suppressed. Similar to the theory of electrons in periodic potentials, the eigensolutions in a phononic crystal structures are Bloch waves [94],  $\psi_{n\mathbf{k}}(\mathbf{r}) = \exp(i\mathbf{k} \cdot \mathbf{r})u_{n\mathbf{k}}(\mathbf{r})$ , where  $u_{n\mathbf{k}}(\mathbf{r})$  is a function with the periodicity of the crystal lattice. Inside a phononic bandgap the wavevectors  $\mathbf{k}$  become imaginary, thus resulting in an exponential decay of an excitation created within the stop band. In essence, due to Bragg interference<sup>4</sup> spectral regions that forbid elastic wave propagation emerge. As one can imagine,

---

<sup>2</sup>In contrast to optics, however, vacuum does not support elastic wave propagation. As such, the ultimate impedance mismatch can be achieved upon levitating a mechanical resonator – this being one of the main points of attraction in levitated optomechanics.

<sup>3</sup>More precisely, when the lattice constant  $a$  is comparable to half the phonon wavelength.

<sup>4</sup>It should be mentioned, that phononic bandgaps can not only emerge due to Bragg interference, as described here, but also by the existence of internal resonances within the unit cells of the crystal structure. This was demonstrated by Ping Sheng and coworkers in year 2000 [95], where a matrix of lead balls covered with a layer of silicon rubber was shown to have phononic bandgaps, despite the fact that the lattice constant was two orders of magnitude smaller than the relevant wavelength at which the stop band was observed. Roughly speaking, this mechanisms relies on elastic waves being trapped in local “cavities”, before they are radiated away. Since this is not of relevance for this work, this topics – albeit exciting on its own – will not be discussed further.

scatterers can either be defined purely geometrically (e.g. by periodic corrugation or perforation of a slab of material), or by periodic modulation of the material parameters, and thus the speed of sound. The latter can be achieved in a multitude of ways, but a simple example is arranging steel rods in a periodic fashion, and filling the gaps with epoxy.

Some of the main advantages of phononic crystal structures for vibration isolation applications were already pointed out by Bahram Djafari-Rouhani and colleagues in their original paper from 1993 [92]:

*“A complete acoustic gap or a **low density of states** should have important consequences for the suppression of zero-point motion and for the localization of phonons, and may lead to improvements in transducers and in the creation of a **vibrationless environment**.”.*

While the various approaches for vibration isolation described above can reduce phonon tunneling losses, many of them have one or both of the following challenges: 1) losses can be sensitive to the exact positioning of the immediate support structure (e.g. suspension beams in the free-free resonator design) and 2) the suspension structure has its own vibrational modes, thus “contaminating” the vibrational spectrum with more modes. Phononic crystal structures, on the other hand, offer means to define a spectral region with no vibrations, other than the ones designed by the experimenter.

Unsurprisingly, this was realised by researchers within our field, and the first devices were introduced by the group of Oskar Painter in 2009 [96]. The so-called *optomechanical crystals* combined photonic and phononic crystal structures, allowing for co-localisation of photons and phonons in a corrugated silicon slab, and thus strong light-matter coupling. It should be mentioned, that a few years prior to this, Martin Maldovan and Edwin Thomas proposed a 2D structure for such co-localisation [97]. These publications sparked tremendous interest in microfabricated devices based on artificial crystals within optomechanics.

Focusing onto efforts to reduce phonon tunneling losses within our sub-community working with membranes, the first systematic experimental studies of phonon tunneling loss were conducted by Dalziel J. Wilson [98]. Here, the quality factors of square silicon nitride membrane resonators were studied for different mounting conditions, ultimately concluding that the highest  $Q$ 's were observed for minimal contact between the membrane chip and the environment (i.e. small glue droplets at three of the corners of the silicon chip). Similar conclusions were reached by other research groups working with these mechanical devices. While minimising the contact makes perfect sense, this solution has several drawbacks: 1) such mounting conditions are difficult to

reproduce, 2) the thermal contact between the resonator and the environment is reduced, which is disadvantageous for experiments in cryogenic settings and 3) the membrane resonator can hybridise with the substrate modes, which can lead to a “contaminated” vibrational spectrum. These concerns eventually lead to the implementation of phononic crystal structures in the area surrounding the membrane resonators. This was initially realised in the group of Cindy Regal, as well as our in Copenhagen, and showed the potential of such structuring for cavity optomechanics [99, 100]. In the following section, we consider some of the main features of such structures, design considerations and device performance.

### 3.1.2 Phononic crystal structures in silicon – design rationale

Let us outline a “plan of attack” for suppressing phonon tunneling losses in membrane resonators. Simple analytic examples from solid state physics, such as vibrations in a periodic diatomic chain consisting of atoms with alternating masses, can give us initial clues at the very onset of our journey. Without going through the details of these examples (see [101, 102] for the calculations of vibrations in 1D atomic chains with alternating masses), the main points can be summarised as follows: a phononic bandgap can emerge in a lattice with alternating masses, and the width of the bandgap will depend on the ratio of these masses. In close analogy, one can envision a beam, where the width is modulated periodically (see sketch in Fig. 3.1).

Unfortunately, analytics can only get us so far, and in order to evaluate actual structures, we need to resort to numerical simulations. This is done using a commercial software solution based on the finite element method (FEM) – COMSOL Multiphysics. In the software the elastic equations of motion are solved numerically for an arbitrary geometry, allowing us to find the eigensolutions for complex mechanical structures.

This brings us to the topic of design rationale. We begin by constraining the parameter space, based on experimental requirements and practical ease:

- Since our goal is to use these devices in optomechanical experiments, we need to operate in a frequency range where technical noise sources are negligible. One of these sources of noise is our laser and, for the lasers used in our quantum optical experiments, classical amplitude and phase noise becomes negligible, compared to vacuum noise fluctuations, above  $\sim 1$  MHz [17]. Therefore, design a structure with a phononic bandgap above this frequency is preferable for our experiments.

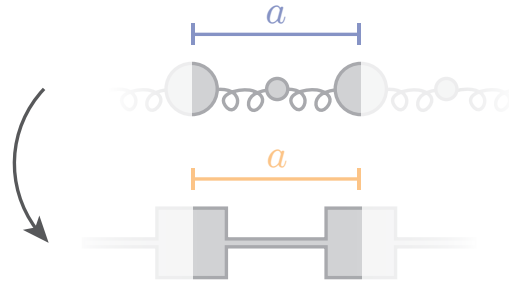


Figure 3.1: Sketch of a diatomic chain, consisting of a string of alternating point masses connected with springs, and in analogy to that, a beam with modulated width.

- To make use of established microfabrication techniques, our phononic support structure will be based on silicon.
- As mentioned previously, in order for a bandgap to emerge at a certain frequency, the lattice constant of our artificial crystal structure has to be comparable to half the wavelength of the elastic wave. Based on the density and Young's modulus of silicon [103], we can estimate the speed of sound for transverse wave in silicon to be  $v_t \sim \sqrt{E/\rho} \sim 6000$  m/s [104]. As such, for a bandgap to emerge at a frequency of  $f_c \sim 2$  MHz, the lattice constant  $a$  has to be on the order of  $v_t/2f_c \sim 1500$   $\mu\text{m}$ . Typically, the thickness of the slab has to be comparable to the lattice constant, in order to have a substantial bandgap [105,106]. Since wafers with 350  $\mu\text{m}$  and 500  $\mu\text{m}$  thickness are readily available inside our cleanroom facility, we choose the thicker one of the two in the interest of matching wafer thickness to lattice constant.
- A slab of silicon with a phononic crystal structure etched into it will of course have its own vibrational modes. To avoid the lowest order modes being excited by technical (e.g. acoustic) noise inside the laboratory, we would like to keep the fundamental resonance frequency of our phononic crystal structure above 10 kHz. Using Eq. (2.17) we can estimate what this would correspond to in terms of overall size of the crystal structure. Disregarding the presence of the holes in the silicon slab, we find that a crystal lattice with  $\sim 16$  mm sidelength is our pain threshold. Assuming a lattice constant of  $\sim 1500$   $\mu\text{m}$  based on our previous estimate, this would correspond to  $\sim 5$  unit cells on each side of a membrane, embedded in the center of such a crystal structure.
- The crystal structure of choice will be etched into the silicon wafer

using a process known as deep reactive ion etching (DRIE) (more on this later). While very high aspect ratios (i.e. ratio between etch depth and feature size) can be achieved using DRIE [107], we choose to be conservative in our choice of critical dimensions within our structure and fix the narrowest dimension to  $100\ \mu\text{m}$  (i.e. an aspect ratio of 5 for a  $500\ \mu\text{m}$  thick silicon wafer).

In fact, the second to last point was proven to be an issue for the initial phononic crystal structures developed in our group [100]. Here, the collective motion of the crystal structure was too large to allow for stable operation of a cavity optomechanical system [108]. As a result, 2D phononic crystal structures were developed during my PhD studies.

Last, but certainly not least, we get to the choice of the "microscopic" structure of our phononic crystal support structure. In our case, this choice was based on previous work from the group of Oskar Painter, showing that 2D phononic crystal structures based on a periodic array of cross-like holes result in large phononic bandgaps [109, 110].

### 3.1.3 Numerical modelling

We now briefly touch upon some of the basic numerical modelling techniques that we use in designing mechanical resonators based on phononic crystal structures. With the design rationale described in the previous section, as well as a choice of a crystal structure in place, the very first step is to identify the centre frequency and size of the phononic bandgap. This typically involves computing band diagrams, which are obtained by simulating the eigenvalues of a periodic structure as a function of the Bloch wavevector. In practice, we start with a single unit cell of the crystal structure and apply Bloch-Floquet periodic boundary conditions on the outer-most surfaces of the unit cell, along the directions of the crystal periodicity. This is shown in Fig. 3.2, where each pair of shaded areas indicates the use of a periodic boundary condition. Since we are interested in the response of the periodic crystal structure to incident waves of different wavevectors, the  $x$ - and  $y$ -components of the wavevector are swept across the first Brillouin zone, computing the eigenfrequencies of the periodic structure for each value of the wavevector. As we plot the eigenvalues versus the wavevector, we obtain band diagrams similar to those that we have been exposed to in solid state physics. With growing interest in phononic crystal structures, COMSOL now provides excellent examples and basic models on how to calculate band diagrams in periodic crystal structures [111]. The resultant band diagram for our particular structure is shown in Fig. 3.2. As we can see,

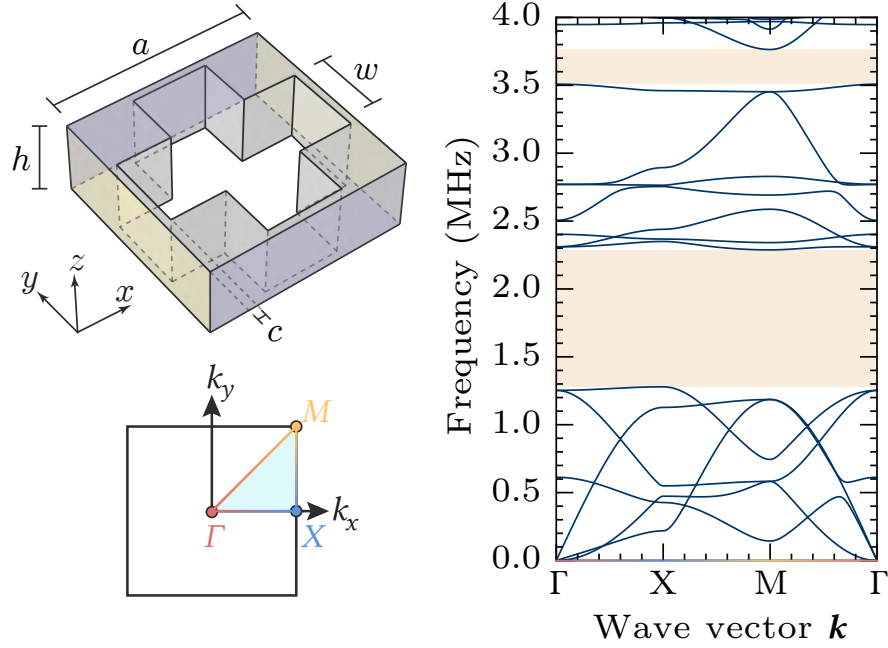


Figure 3.2: Simulated band diagram for a silicon phononic crystal structure. Top left shows the unit cell of a cross-structure phononic crystal. Highlighted are the pairs of surfaces (yellow along  $x$ -direction and blue along  $y$ -direction) upon which Bloch-Floquet periodicity is imposed. Bottom left shows the equivalent first Brillouin zone of the unit cell. The simulated band diagram is shown on the right. Here we use  $a = 1350 \mu\text{m}$ ,  $h = 500 \mu\text{m}$ ,  $w = 513 \mu\text{m}$  and  $c = 50 \mu\text{m}$ . The material parameters are the default values provided by COMSOL, where  $\rho = 2329 \text{ kg/m}^3$ ,  $E = 170 \text{ GPa}$  and  $\nu = 0.28$ .

the structure does not support vibrational modes in the frequency range between  $\sim 1.25 \text{ MHz}$  and  $\sim 2.25 \text{ MHz}$ , and yet again at higher frequencies. This process can be repeated for varying parameters of the unit cell, in order to maximise the bandgap and/or its centre frequency, depending on the experimental requirements. In this case, the optimisation was simply done by varying the hole width  $w$  (see unit cell in Fig. 3.2) and unit cell size  $a$ , while maintaining the same critical dimensions  $c$  and plate thickness.

Typically, implementing such a model in COMSOL is not a particularly challenging task, in part because of an established toolbox, often provided by COMSOL itself. However, paying attention to meshing (i.e. discretisation) of the crystal structure can be of importance and alleviate unpleasant surprises. First, as it relates to phononic bandgap simulations, it is important to ensure a matching mesh on the periodic boundary condition. Failing to do so can result in seemingly realistic, but in reality incorrect band diagrams. Of

broader relevance is the question of mesh density and what constitutes a good mesh. In most cases, we discretise our geometry into triangles and tetrahedrons, which COMSOL does using Delauney triangulation [112]. However, meshing a geometry with regions significantly smaller than the overall dimensions of the entire geometry can result in “flat” triangles and tetrahedra in said regions. Such discretisation can lead to numerical inaccuracies in our simulation results [113] and should therefore be avoided. One could therefore use the presence of equilateral triangles and absence of “flat” triangles and tetrahedra as a gauge for the mesh quality. This often times provides a sufficiently fine mesh density from the get go. Ultimately, convergence tests are a helpful path forward, where multiple simulations are performed using the same geometry, but with an increasing amount of mesh elements. Combined with the canonical “5-8 mesh elements per wavelength” recommendation from COMSOL [114], these guidelines can be utmost helpful in constructing robust numerical models.

Once the unit cell geometry has been identified and verified to support a large phononic bandgap, the next step is typically to design a device based on the underlying crystal structure, with an embedded defect supporting a membrane resonator. In our case, the overall size of the structure is largely limited by the considerations regarding the fundamental resonance frequency of the entire phononic crystal structure (cf. Section 3.1.2). We are thus bounded from above in size, but how many unit cells are actually needed in order to render phonon tunneling losses negligible? This question can be addressed within the framework of phonon tunneling, as demonstrated by Garret Cole and colleagues [82]. Alternatively, one can employ a more straightforward (yet computationally heavy) approach by using *perfectly matched layers* (PML), which are domains within the simulation acting as perfect absorbers of elastic waves. This technique is often used in assessing anchor losses of mechanical resonators [115, 116] and is well suited for complex geometries. Therefore, we adapt this approach in addressing the question regarding the minimum number of unit cells. Surprisingly, we find that even for a single unit cell the radiation loss limited quality factor for the (2, 2) mode of a square membrane ( $h = 100$  nm) is approximately  $10^{11}$ , while two unit cells result in a radiation loss limited  $Q$  of  $\sim 10^{13}$  and, finally,  $\sim 2 \times 10^{13}$  for three unit cells. While these numbers might seem excessive, this is not particularly uncommon when assuming a perfect crystal structure (even one consisting of a single unit cell). However, as recently reported by MacCabe et al. [117], imperfections in the crystal structure can lead to a significant reduction of the radiation loss limited  $Q$ . Therefore, we base our choice on similar studies and land upon a lower bound of 3 unit cells.

### 3.1.4 Fabrication of shielded membrane resonators

With the geometry in place, we move our focus to the fabrication process. Throughout this section the reader is referred to Fig. 3.3 for an overview and some detail will be provided about the basics of microfabrication. The interested reader is referred to [118] for a comprehensive overview of microfabrication basics.

The process starts with the selection of double-side polished (DSP) silicon wafers. We use wafers provided by Okmetic, with  $\langle 100 \rangle$  crystal orientation ( $0.0 \pm 0.5^\circ$  off-orientation) and  $500 \pm 15 \mu\text{m}$  thickness. The wafers are transferred to a low-pressure hot-wall furnace [118], where amorphous silicon nitride is deposited on the surface of the silicon wafers. This process is known as low-pressure chemical vapor deposition (LPCVD), and takes place by injecting ammonia (80 sccm  $\text{NH}_3$ ) and dichlorosilane (20 sccm  $\text{SiH}_2\text{Cl}_2$ ) in the gas phase into the deposition chamber. The reaction takes place at high temperatures (typically  $\sim 780^\circ\text{C}$ ) and 200 mTorr pressure, resulting in a thin film of stoichiometric silicon nitride ( $\text{Si}_3\text{N}_4$ ), where *stoichiometric* typically refers to a 3/4 ratio of silicon to nitrogen), as well as hydrogen ( $\text{H}_2$ ) and hydrogen chloride ( $\text{HCl}$ ) in gaseous form as reaction byproducts<sup>5</sup>. Upon completion of the process, the wafers are cooled down. Due to a difference in rate of contraction of silicon and silicon nitride, the deposited thin film becomes tensioned, described by the integrated difference in the coefficients of thermal expansion of the two materials [119]

$$\sigma_{\text{th}} = \frac{E_{\text{Si}_3\text{N}_4}}{1 - \nu_{\text{Si}_3\text{N}_4}} \int_{T_{\text{dep}}}^{T_{\text{room}}} (\alpha_{\text{Si}} - \alpha_{\text{Si}_3\text{N}_4}) dT, \quad (3.1)$$

where  $E_{\text{Si}_3\text{N}_4}$  and  $\nu_{\text{Si}_3\text{N}_4}$  are the Young's modulus and Poisson's ratio of silicon nitride (assumed to be constant as a function of temperature),  $T_{\text{dep}}$  is the deposition temperature,  $T_{\text{room}}$  is the final (room) temperature, and  $\alpha_{\text{Si}}$  and  $\alpha_{\text{Si}_3\text{N}_4}$  are the coefficients of thermal expansion (CTE) of silicon and silicon nitride, respectively. We can estimate the thermal contribution to the film stress using values for CTE from literature. While values for silicon are readily found [120], the thermal expansion coefficient for LPCVD silicon nitride is harder to come across. A comparison of measurements for LPCVD nitride up to  $400^\circ\text{C}$  [121] and data originating from plasma deposited silicon nitride and spinel-type (crystalline) silicon nitride [122] shows fair agreement in the overlapping temperature range, suggesting that we can use the data from [122] for our estimate. As shown in Fig. 3.4, the thermal expansion

---

<sup>5</sup>These can be embedded in the deposited thin film and have an effect on the mechanical quality factor [78].

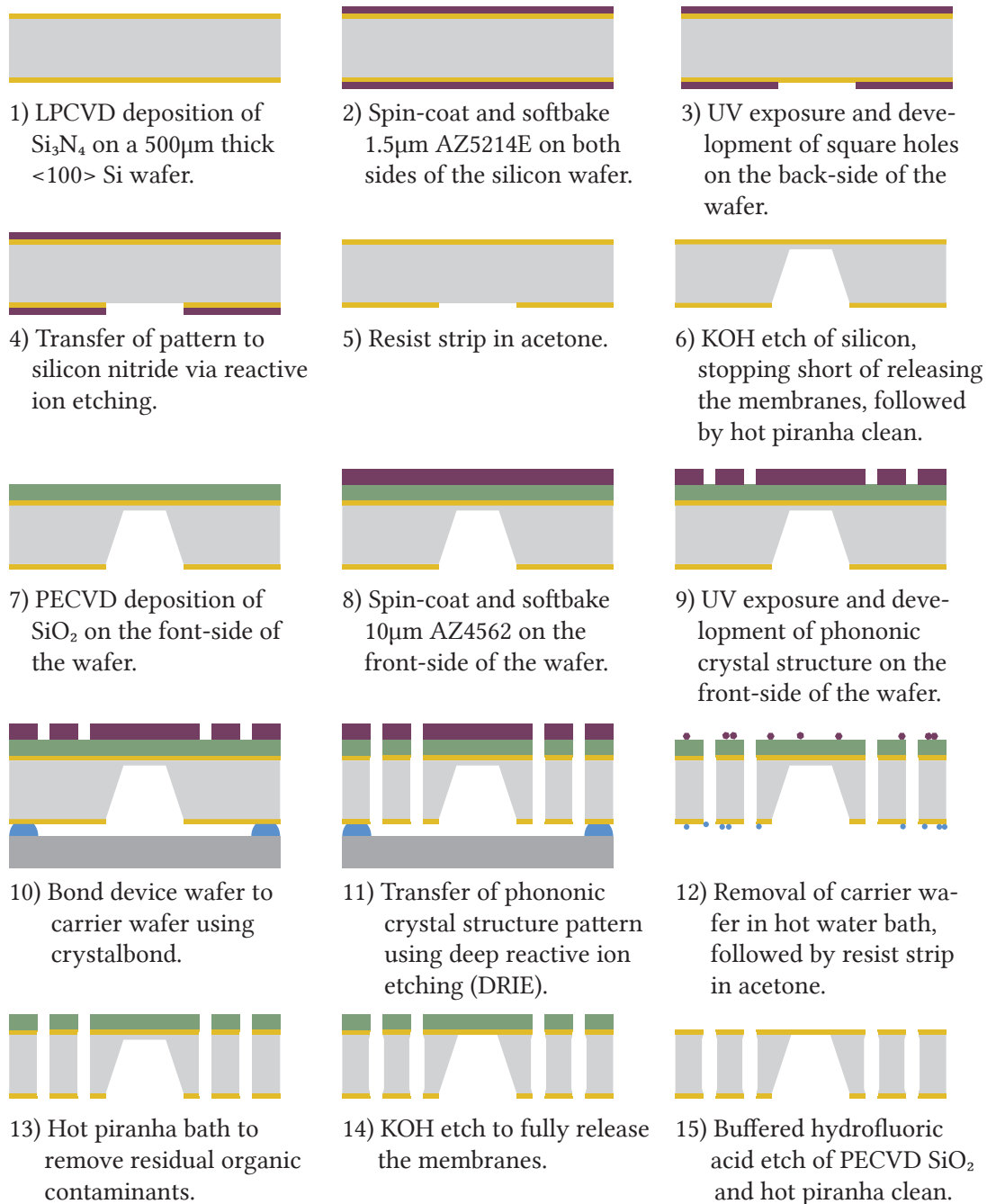


Figure 3.3: Process flow for silicon phononic crystal shielded membrane resonators. The various materials are colour coded as follows: silicon (light grey), silicon nitride (orange), photoresist (purple), PECVD  $\text{SiO}_2$  (green), crystalbond (blue), carrier wafer (dark grey).

coefficient of silicon is lower than the CTE of silicon nitride, meaning that silicon nitride contracts *slower* than silicon, resulting in compressive stress in the thin film. Integrating the difference in CTEs in the temperature range 300 K to 1050 K suggests that the thermal contribution to the overall stress of the silicon nitride film is  $\sim 100$  MPa. Similar estimates found in the literature suggest that depending on the deposition method of the thin film, the thermal stress contribution can be either compressive [119] or tensile [123]. But whether tensile or compressive, it is typically found to be on the order of  $\sim 100$  MPa.

Once the silicon nitride film has been deposited, we can measure the overall tension in the film by measuring the bow of the wafer with and without the thin film. In practice, this involves a (reference) measurements of the wafer curvature, with the silicon nitride thin film on both sides of the wafer, followed by removal of the film from one side only and a repeated measurement of the curvature. The measurement is done using Bruker's Dektak XTA® stylus profiler. Knowing the curvature before and after removal, as well as material parameters of the substrate, allowed us to calculate the stress of the remaining silicon nitride film following this expression [125]

$$\sigma = \frac{E_{\text{Si}}}{6(1 - \nu_{\text{Si}})} \frac{t_{\text{Si}}^2}{t_{\text{Si}_3\text{N}_4}} \left( \frac{1}{R_{\text{post}}} - \frac{1}{R_{\text{pre}}} \right), \quad (3.2)$$

where  $E_{\text{Si}}$  and  $\nu_{\text{Si}}$  are the Young's modulus and Poisson's ratio of silicon (dependent on the crystal orientation),  $t_{\text{Si}}$  ( $t_{\text{Si}_3\text{N}_4}$ ) is the thicknesses of the silicon wafer (silicon nitride thin film), and  $R_{\text{post}}$  ( $R_{\text{pre}}$ ) is the measured curvature after (before) the removal of the thin film. Using this technique we have measured the *tensile* stress of 105.5 nm silicon nitride to be  $1273 \pm 24$  MPa. Combined with our estimate of stress due to the mismatch of CTEs we therefore conclude that the dominant contribution of stress is not thermal of origin. Indeed, the consensus in the literature is that the tension in deposited thin films is predominantly intrinsic of nature (i.e. related to the deposition conditions) and that the films are already tensioned at elevated temperatures. Understanding the exact details of this dynamics is still actively being studied [126]. The origin of the stress can be explained by a mechanism known as *crystallite coalescence* [127], which suggests that the initial growth happens in small patches (crystallites), and as the islands grow bigger, they spontaneously snap together, which can result in stretching (tensioning) of the film. The details of this process will depend on a number of things, including deposition surface. As such, determining the stresses of deposited thin films is a non-trivial exercise and in practice means that one should measure these, for instance using the wafer bow technique.

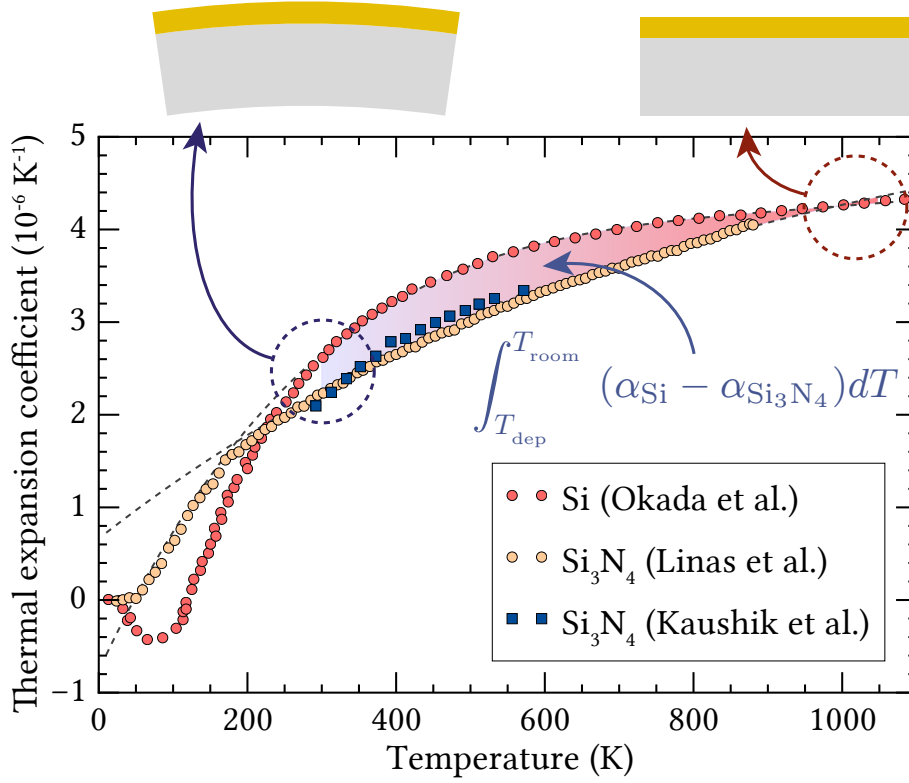


Figure 3.4: Thermal expansion coefficients for silicon nitride [121,122] and silicon [120] as a function of temperature. The values have been extracted digitally using WebPlotDigitizer [124]. The values from [122] originate from plasma deposited silicon nitride and spinel-type (crystalline) silicon nitride, while the values from [121] are for LPCVD silicon nitride. The shaded area represents the thermal contribution to the stress of silicon nitride. The dashed lines are fits to the extracted data from Linan et al. and Okada et al. in the relevant temperature range (300 K and 1050 K). On the top a cross-section view of the wafer curvature at elevated temperatures and room temperature is shown (the curvature originating from thermal stresses only). The depicted wafer (top left) curvature corresponds to a compressive film stress.

Following the deposition of silicon nitride, we proceed with **Step 2 and 3** of the process (cf. Fig. 3.3). Here, the pattern for the square holes, which in the end will define the size and placement of the membranes on the silicon wafer, is transferred lithographically onto the said wafer. We begin by baking out the wafer on a hotplate (or in a dedicated furnace) at 150 °C, in order to remove moisture, followed by application of hexamethyldisilazane

(HMDS) in the gas phase, in order to improve the adhesion of photoresist to the wafer. A thin layer ( $1.5 \mu\text{m}$ ) of positive photoresist (i.e. a photosensitive polymer, where the polymer chains are broken upon illumination with UV light) is spin coated onto both sides of the wafer, with a 60 s softbake at  $90^\circ\text{C}$  after each coating. The latter results in evaporation of the solvent in the photoresist and solidifies the polymer. The wafer is transferred to a mask aligner, where a photomask<sup>6</sup> is used to transfer a pattern (in this case, a matrix of square holes) onto the photoresist. Once illuminated, the polymer chains in the exposed regions have been broken and can be removed chemically (i.e. developed). In this case, we use diluted TMAH (AZ 726 MIF developer) to develop the wafer, followed by a rinse in deionized (DI) water. The combination of spin coating, baking, exposure and, finally, development, will henceforth be referred to as the "lithographic step".

Upon completion of the lithographic step, our wafer is covered on both sides with photoresist, with square openings in the photoresist, and thus access to the silicon nitride, on one of the sides (referred to as the *back-side*) only. In **Step 4 and 5** of the process (cf. Fig. 3.3) we transfer this pattern to the silicon nitride on the back-side of the wafer, using dry etching (more specifically, reactive ion etching (RIE) or inductively coupled plasma etching (ICP)). Here, a fluorine gas (consisting of  $\text{CF}_4$  and  $\text{H}_2$ ) is ionized and accelerated towards the sample. The silicon nitride is gradually etched away, thus exposing the silicon underneath. The photoresist, which was used to protect the rest of the silicon nitride, is subsequently removed in an acetone bath with sonication.

The square openings in the silicon nitride are now used to remove the silicon between the back-side of the wafer and the front-side. This is done chemically, using potassium hydroxide (KOH), which etched silicon anisotropically, resulting in characteristic pyramid-formed "craters" in the silicon (see **Step 6** in Fig. 3.3). For a given square opening in the silicon nitride of sidelength  $L$ , the resultant sidelength of the square a distance  $d$  away from the opening will be  $L - \sqrt{2}d$ . As such, if the sidelength of the square previously etched in the silicon nitride is  $1200 \mu\text{m}$  and we etch all the way through the wafer, the size of the opening on the front-side will be  $\sim 492 \mu\text{m}$ . Since the etch rate of silicon in KOH is significantly higher than the one for silicon nitride<sup>7</sup>, the en-

---

<sup>6</sup>In this case, a photomask is a large piece of glass with a thin layer of chromium, where parts of the chromium have been removed, thus blocking light everywhere, except for the regions where the metal has been removed.

<sup>7</sup>This ratio, often referred to as *selectivity*, is better than 1:80000 – i.e.  $> 80000$  nm silicon is removed for every nanometer of silicon nitride etched in the same amount of time. More specifically, the etch rate of silicon along the  $\langle 100 \rangle$  direction in KOH at  $80^\circ\text{C}$  is  $\sim 1.3 \mu\text{m}/\text{min}$ , while the etch rate of stoichiometric silicon nitride is  $\sim 1 \text{ nm}/\text{hr}$ .

tire wafer is submerged into the chemical solution and etched for  $\sim 6$  hours. The etch is stopped slightly short of removing all of the silicon between the opening and the silicon nitride of the front-side, which would "release" the membrane. This is done to provide mechanical stability for the subsequent fabrication steps. Finally, in order to remove organic residues from the KOH etch, the wafer is cleaned in a hot piranha solution, which consists of a 4:1 mixture of sulfuric acid ( $\text{H}_2\text{SO}_4$ ) and hydrogen peroxide ( $\text{H}_2\text{O}_2$ ).

After the KOH etch, the to-be silicon nitride membranes are supported from below by a thin ( $\sim 10 \mu\text{m}$ ) silicon layer, but are exposed on the front side of the wafer. Since the subsequent steps in the process involve some risk of contamination and/or damaging of the silicon nitride film, we deposit a thin layer ( $0.3-0.5 \mu\text{m}$ ) of silicon dioxide ( $\text{SiO}_2$ ) using plasma-enhanced chemical vapor deposition (PECVD) in **Step 7** of the process. With a deposition rate of approximately  $100 \text{ nm/min}$ , this process only takes a few minutes and provides extra protection for the to-be membrane surface.

With both membrane surfaces being protected (with silicon from below, and silicon dioxide from above), we move to **Steps 8-11** of the process (cf. Fig. 3.3), where the phononic crystal pattern is defined on the front-side of the wafer and subsequently transferred to the silicon wafer. We begin with yet another lithographic step, by coating the front-side of the wafer with a thick ( $\sim 10 \mu\text{m}$ ) layer of positive photoresist (AZ® 4562). Prior to this the wafer has once again been baked out and coated with HMDS. A thick layer of polymer is needed in order to withstand approximately 1 hour of dry etching in the following steps of the process. Upon exposure and development, a matrix of the phononic crystal pattern of our choice is defined in the polymer layer on the front-side of the wafer. The wafer is now ready to be dry-etched, in order to transfer the phononic crystal pattern into the silicon. However, since we intend to etch all the way through the wafer, there is a risk of contaminating and/or damaging the ceramic electrode<sup>8</sup> in the etching chamber (the wafer is clamped to the electrode during the etch process). In order to avoid this, we need to attach our device wafer to a plane silicon wafer (henceforth referred to as *carrier* or *dummy* wafer). Since the dry etch process generates heat, the wafers in the process chamber are typically cooled from the back side using helium gas. Therefore, we need to make sure that upon attaching our device wafer to the carrier wafer, a decent thermal link is maintained. This is done using a mounting wax (adhesive) known as *crystalbond*. Resembling a square candle, crystalbond is solid at room temperature, melts at elevated temperatures (typically above  $60 \text{ }^\circ\text{C}$ ), and can either water- or acetone-soluble. For process compatibility reasons,

---

<sup>8</sup>Referred to as Thick Dielectric Electro Static Chuck (TDESC).

we choose the water soluble option. We heat our carrier wafer to  $\sim 70$  °C on a hotplate and apply a thin layer of crystalbond at the surface of the silicon wafer by hand. To avoid trapped air pockets underneath the to-be membranes, instead of a uniform layer of crystalbond,  $\sim 1$  cm wide strips of crystalbond are applied across the carrier wafer. Upon doing so, the device wafer is placed on top of the carrier wafer, and the sandwich of the two wafers, with crystalbond between them, is removed from the hotplate, in order to cool down and for the crystalbond to solidify. Once cooled down, the wafer sandwich is moved to the reaction chamber of a deep reactive ion etcher (DRIE). We are using the SPTS Pegasus system by SPTS Technologies Ltd., which allows processing of 4" silicon wafers using the Bosch plasma etch process. In short, the Bosch process alternates between a nearly isotropic etch of the silicon (using primarily sulfur hexafluoride,  $\text{SF}_6$ , alongside oxygen,  $\text{O}_2$ ), followed by polymer deposition (a so-called *passivation* layer, which uses octafluorocyclobutane gas,  $\text{C}_4\text{F}_8$ ), which protects the sidewalls, allowing for highly anisotropic etching of silicon, resulting in nearly vertical etch profiles. This etch process is rather "violent", which is why, in steps 6 and 7 we ensured to protect the membrane from both sides. With an etch rate of  $\sim 10$   $\mu\text{m}/\text{min}$  in silicon, the process takes approximately an hour at 0 °C and results in a complete transfer of the phononic crystal structure into the silicon wafer.

We are now entering the final stretch of the process. In **Step 12** of the process we wish to remove the carrier wafer. This is done in two steps. First, the wafer sandwich is placed onto a hotplate set to 80 °C, in order to soften the crystalbond, and the device wafer is carefully removed from the carrier. To remove the bulk of the crystalbond, the wafer is placed into a 90 °C water bath with agitation. The combination of wafer and heat efficiently removes the majority of crystalbond from the device wafer. The wafer is finally transferred to a room temperature water rinse, and is left for an hour or more. Lastly, the photoresist on the front-side of the wafer, which is partially burnt after the long dry etch, is removed by placing it into acetone overnight. While the vast majority of crystalbond and photoresist is removed in the hot water bath and acetone bath, there are still some minor residues remaining on the device wafer. In **Step 13** these are removed using a hot piranha solution.

With the phononic crystal etched into the silicon wafer, we are now ready to fully release the membranes in a short ( $\sim 10$  min) KOH etch in **Step 14**. Unavoidably, the vertical sidewalls are also etched during the KOH etch, but due to the brevity of the etch and hence the relatively small change in dimensions, compared to the simulated geometry, this is not a major concern for the performance of the device. Finally, in **Step 15** of the process we

remove the protective SiO<sub>2</sub> layer using buffered hydrofluoric acid etch (BHF) and clean the device wafer once more in a piranha solution, thus concluding the fabrication process.

### 3.1.5 Characterisation of phononic crystal shielded membrane resonators

One of the first and simplest measurement we can do with newly fabricated microresonators is coherently driving the resonator at some frequency and looking at the response of the resonator at that exact frequency. Depending on the specifics of the measurement, we can either use a piezoelectric transducer to launch elastic waves and thus excite the resonator, or an amplitude modulated diode laser, which excited the resonator directly. The response of the resonator is measured interferometrically. Here, we use a balanced Michelson interferometer to do so (see [128] for more details on our setup). A simplified sketch of our interferometric setup is shown in Fig. 3.5.

The primary light source in our setup is a Nd:YAG solid state laser<sup>9</sup>, operating at 1064 nm wavelength. The light is split between the *reference arm* and the *probe arm* of the interferometer using a half-wave plate ( $\lambda/2$ ) and a polarizing beam splitter (PBS). The light in the probe arm is coupled into a single mode fiber, at the output of which we place the membrane resonator we wish to characterise. More specifically, the probe beam is guided through a fiber to a *probe head*, which, in essence, is a portable optical setup consisting of a fiber coupler, lenses, a translation stage, and a CCD camera. The membrane resonator is placed either inside a large vacuum chamber, which can accommodate 4" silicon wafers, as well as individual samples, reaching pressures down to 10<sup>-8</sup> mbar, or a flow cryostat<sup>10</sup> with a base pressure at room temperature of  $\sim 10^{-5}$  mbar. Importantly, the probe head used in conjunction with the flow cryostat includes a 50 $\times$  microscope objective<sup>11</sup> and a motorised translation stage. As we will see later in this chapter, this allows for measurements of mode displacement profiles.

The light which is reflected from the membrane will be phase modulated due to the membrane motion. Upon reflection, light is coupled back into the fiber and recombined with light from the reference arm on a PBS. At the output of a (lossless) Michelson interferometer we expect to see the power

---

<sup>9</sup>Mephisto Ultra-Narrow Linewidth DPSS Laser by Coherent Inc.

<sup>10</sup>Microstat Hi-Res by Oxford Instruments.

<sup>11</sup>50 $\times$  Mitutoyo Plan Apo NIR Infinity Corrected Objective.

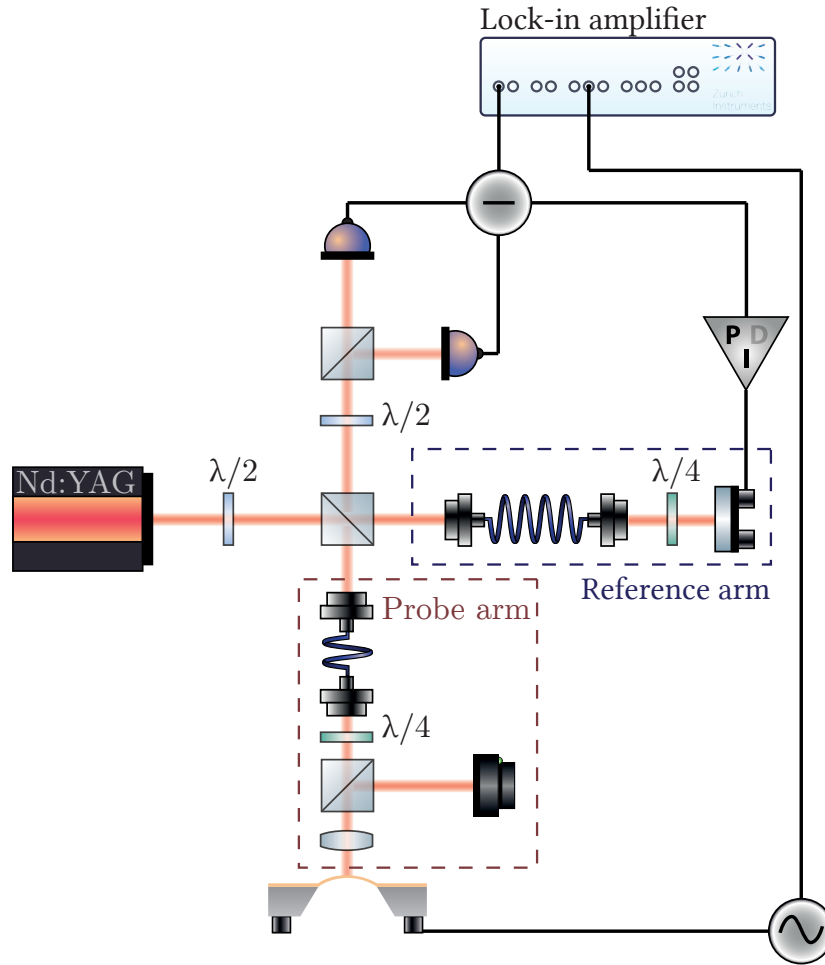


Figure 3.5: Simplified illustration of the Michelson interferometric setup. Light from the laser is split between the *probe* and *reference* arms of the interferometer, where in the latter a piezo-mounted mirror is used to stabilise the relative path length difference of the two interferometer arms. The mechanical resonator is placed inside a vacuum chamber (not shown here) in the probe arm, and a CCD camera is used for sample imaging. Light reflected from both interferometer arms is recombined on a polarising beam splitter, and subsequently detected using a balanced photodetector. The output signal of the photodetector is split between an analyser (here shown as a lock-in amplifier) and a PI-controller, used in locking the interferometer at a particular point of the interference fringe.

depend on the optical path length difference  $\Delta L$  as follows

$$\frac{P_{\text{out}}}{P_{\text{in}}} = \frac{1 - \cos(2k\Delta L)}{2}, \quad (3.3)$$

where  $k$  is the wavenumber. The output signal is most sensitive to small fluctuations in the path length difference when the phase difference  $\Delta\phi = 2k\Delta L$  equals  $\pi(2n - 1)/2$  (where  $n$  is an integer). As such, the mirror in our reference arm is mounted on a piezoelectric transducer, which is used to stabilise the path length difference to  $\Delta L = \lambda(2n - 1)/8$  using a proportional-integral (PI) feedback loop with a bandwidth of  $\sim 2.5$  kHz. Since the light from the two interferometer arms are orthogonally polarised immediately after the PBS where they are re-combined, a half-wave plate rotates the polarisation by  $45^\circ$ , before splitting the light on a PBS. This ensures that light reflected from the probe and reference arms are evenly distributed between the two output ports of the polarising beam splitter. We use a balanced detection scheme, which ensures common noise rejection (e.g. laser amplitude noise, acoustic noise, etc.). Once the interferometer is locked, the output signal of our detector (Thorlabs PDB420C-AC) is sent to a spectrum analyzer and/or lock-in amplifier, where fluctuations in the signal at the relevant Fourier frequencies are analysed.

Our strategy for characterising the silicon phononic crystal structures is as follows. We mount a single sample inside one of our vacuum chambers on top of a piezo, with the probe light focused either on the membrane, the silicon defect or the outer frame of the chip. Using a vector network analyser (VNA), or a lock-in amplifier, the piezo is driven at different frequencies, while monitoring the response of the device at said frequency at the output of the interferometer. As we sweep the drive tone across the expected frequency region of the phononic bandgap, we expect to see a different response at different positions of the membrane chip. More specifically, the motion in the central part of the phononic crystal structure is expected to be smaller within the frequency range of the phononic bandgap, compared to the displacement outside the crystal structure. This behaviour is shown in Fig. 3.6, where the driven responses, averaged over ten locations on the frame or the defect, are compared, showing  $> 20$  dB suppression of vibrations over a frequency range of  $\sim 2$  MHz. Importantly, the measurement shows not only suppressed vibrational amplitude, but also a sparse mode spectrum, with the peaks found inside the bandgap being ascribed to localised modes of the silicon defect, in the centre of which the membrane is placed. We note that the size of the observed bandgap is larger than the simulated structure in Fig. 3.2. This is largely due to the fact that the sidewalls of our phononic crystal structure are etched during the final release (cf. 3.1.4), thus reducing the critical dimension from  $100 \mu\text{m}$ , as initially designed, down to  $\sim 75 \mu\text{m}$  (here we assume a 10 minute KOH etch with an etch rate of  $1.25 \mu\text{m}/\text{min}$ ). This results in a larger mass mismatch within our phononic crystal structure, and hence a larger

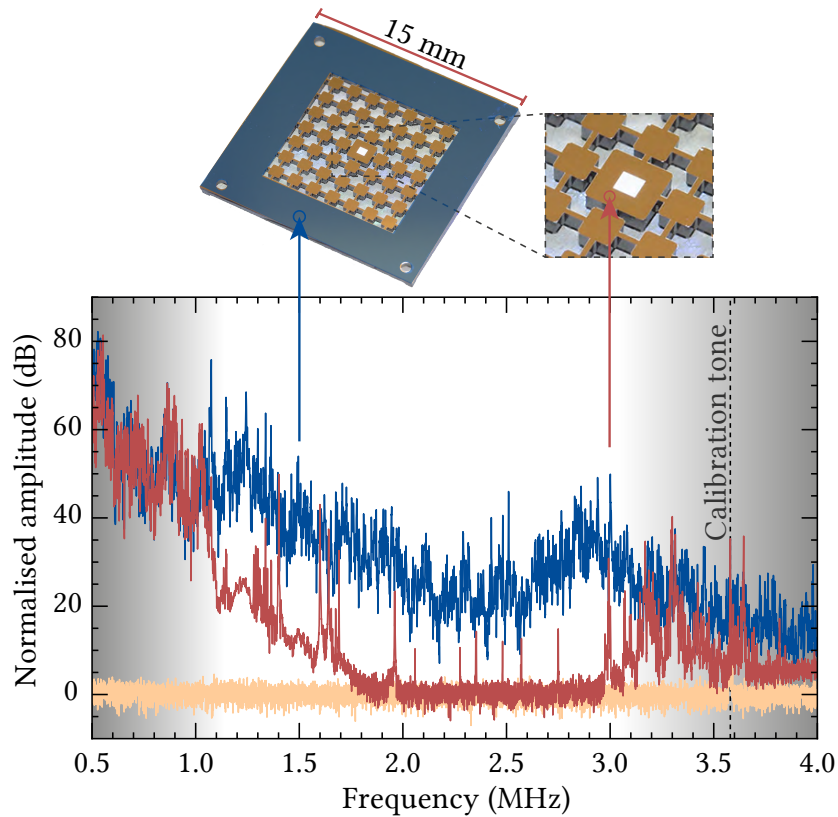


Figure 3.6: Driven response of a silicon phononic crystal structure, normalised to the shotnoise. Each curve is an average of ten measurements at different positions of the frame (blue) or the defect (red). An RF tone at 3.58 MHz is sent onto the piezo of the reference arm and is used to account for power drifts among these individual sweeps. The white square in the central part of the defect is the silicon nitride membrane. Figure is adapted from [1] and [14].

bandgap.

The measurements shown in Fig. 3.6 are helpful in identifying regions in frequency where the phononic crystal suppresses vibrations. However, as we can see, our measurement sensitivity is insufficient to resolve the degree of suppression between 2 MHz and 3 MHz. Furthermore, the mapping between the degree of suppression and quality factors of the membrane modes is non-trivial. Hence, a direct assessment of the quality factors is needed, in addition to the driven measurements shown above.

This is done using a ringdown technique, where the individual membrane modes are excited by a resonant drive (either using a piezo or an amplitude

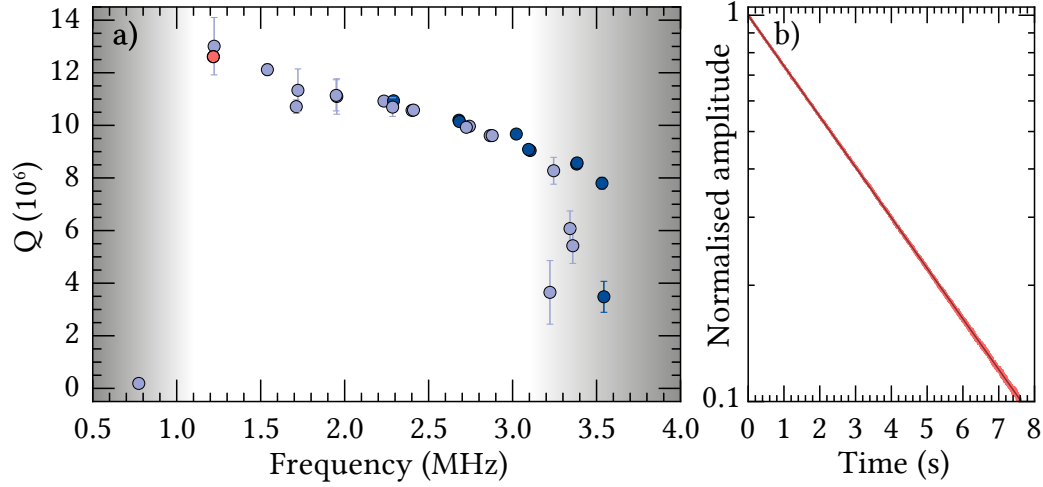


Figure 3.7: a) Mechanical quality factors for a 60 nm thin silicon nitride membrane at cryogenic temperatures. The shaded areas indicate regions of frequency outside of the bandgap (cf. Fig. 3.6). Light blue circles indicate modes where both mode indices are lower than 3, while opposite applies for the dark circles. The membrane sidelength is  $\sim 544 \mu\text{m}$ . b) Ringdown measurement for the red datapoint in a). Here, the mechanical frequency is  $\Omega_m = 2\pi \times 1.218 \text{ MHz}$  and the measured quality factor is  $Q = (12.61 \pm 0.04) \times 10^6$ . Figure a) is adapted from [1] and [14].

modulated light source). Upon turning the drive off, the mode amplitude decays according to

$$q(t) = q_0 \sin(\Omega_m t + \phi) e^{-\Gamma_m t/2}, \quad (3.4)$$

where  $q_0$  is the initial amplitude and  $\Gamma_m$  is the energy decay rate. Since we mostly care about the time evolution of the envelope of the amplitude decay (i.e.  $e^{-\Gamma_m t/2}$ ) the detected signal is analysed using a lock-in amplifier, where the demodulated signal at the mechanical frequency yields the decay envelope. Upon fitting an exponential function and recalling that  $Q_m = \Omega_m/\Gamma_m$ , the quality factor can be estimated. Typically, this is repeated several times and the average of the individual estimates is the quality factor we ultimately quote.

In Fig. 3.7b we see an example of one such ringdown measurement, performed at cryogenic temperatures, alongside a broader overview of measured quality factors for thirty vibrational modes of the membrane (Fig. 3.7a). As we can see, the membrane modes inside the phononic bandgap have comparable mechanical quality factors and are monotonically decreasing in magnitude as a function of frequency. On the contrary, modes outside of the bandgap

show deviation from this trend and a larger spread in  $Q$ -factors is seen. This can be understood in terms of modal overlap between the membrane and support structure, which has a significantly denser mode spectrum outside of the bandgap (cf. Fig. 3.6). Furthermore, in Fig. 3.7a we differentiate between vibrational modes with mode indices  $m \vee n < 3$  and others, since it has previously been pointed out that the latter category is more susceptible to phonon tunneling losses [64]. While the vast majority of modes within our phononic bandgap belong to this category, no such trend can be seen for our samples.

As we have now seen, phononic crystal engineering is a powerful tool in suppressing and eliminating dissipation due to phonon tunneling. Having done so, the dominant source of dissipation is no longer extrinsic, but intrinsic in nature. As we touched upon in the previous chapter, surface loss is the main source of dissipation in thin silicon nitride resonators, and is subsequently diluted due to the presence of tension in the thin film. Therefore, if we wish to improve the mechanical quality factors of our devices (for a given temperature), we can either reduce the intrinsic dissipation (e.g. by modifying the surface chemistry or using a different material for the mechanical resonator) or by improving the degree of dilution. The latter is the path we have chosen to pursue and will be the focus for the remainder of this chapter.

## 3.2 Soft clamping

The curvature at the edges of a membrane resonator dictate its mechanical quality factor. This, in short, is one of the main conclusions from dissipation dilution, discussed in the previous chapter. Broadly speaking, the boundary conditions of our resonators essentially dictate that the membrane has to be in a horizontal position at the edges, leading to significant bending and hence dissipation. The quality factor for a square resonator was found to be given by the following expression

$$Q_{mn}^{-1} = Q_{\text{int}}^{-1} \left( \lambda + \lambda^2 \frac{(m^2 + n^2)\pi^2}{4} \right), \quad (3.5)$$

where the first term in the parentheses is due to the curvature at the membrane edges. Given the fact that  $\lambda \sim 10^{-3}$  for our devices, the second term  $\mathcal{O}(\lambda^2)$  is negligible and hence the quality factor simply scales inversely with  $\lambda$ . Seeing that  $\lambda \propto \sqrt{Eh^2/\sigma L^2}$ , the degree of dilution can be improved in a three<sup>12</sup> different ways: a) choosing a material with a significantly lower

---

<sup>12</sup>As we saw in the previous chapter, surface related losses scale linearly with thickness, which happens to cancel out the thickness scaling due to dissipation dilution. Therefore,

Young's modulus b) increasing the tension in the silicon nitride resonators (for instance mechanically, by bending the silicon chip [54], rapid thermal annealing [129], or choosing a different substrate material [130]) or c) increasing the sidelength of the membrane resonator. Since for most standard materials the yield stress is proportional to the Young's modulus, it is not very likely that we can find a material which can provide us a significantly lower Young's modulus, while preserving a high yield strength. Further, since the dilution term scales with the square root of Young's modulus, this does not seem like a viable option. Similarly, since the yield strength of LPCVD silicon nitride is approximately  $\sigma_y = 6.4$  GPa [131], increasing the tension in our resonators would result in approximately two-fold improvement of the dilution factor, due to the square root scaling. Finally, we can consider the option of increasing the size of our resonator. This approach was taken by Chakram et al. [57], where mechanical quality factors of 50 million were measured using large ( $\sim (5 \text{ mm})^2$ ) silicon nitride membranes, and showing  $Qf$ -products of 100 THz at  $f \approx 2.7$  MHz.

While we could increase the dilution factor by scaling the lateral dimensions of our devices up, this approach opens a different can of worms: by doing so we not only increase the effective mass of the resonator ( $m_{\text{eff}} \propto L^2$ ), thus reducing the optomechanical interaction strength, but also increase the density of membrane modes at higher frequencies, making it increasingly harder to separate between the different vibrational modes of the membrane resonator. Using the expression for the mechanical resonance frequency (see Eq. (2.18)) and treating the mode indices as continuous variables, it can easily be shown that the approximate number of modes  $N$  per unit frequency is given as

$$\frac{dN}{df} = 2\pi f L^2 \frac{\rho}{\sigma}. \quad (3.6)$$

In Fig. 3.8 the calculated mode density is plotted for a membrane of comparable dimensions to the device studied by Chakram et al. [57]. At the frequency with the highest measured  $Qf$ -product, the mode density is almost 1 per kilohertz. With a decoherence rate of  $\Gamma_{\text{dec}} = k_B T / \hbar Q \approx 2\pi \times 130$  kHz at room temperature, it is evident that using such vibrational modes in quantum optomechanical experiments is not feasible.

---

we do not gain in dilution by reducing the resonator thickness.

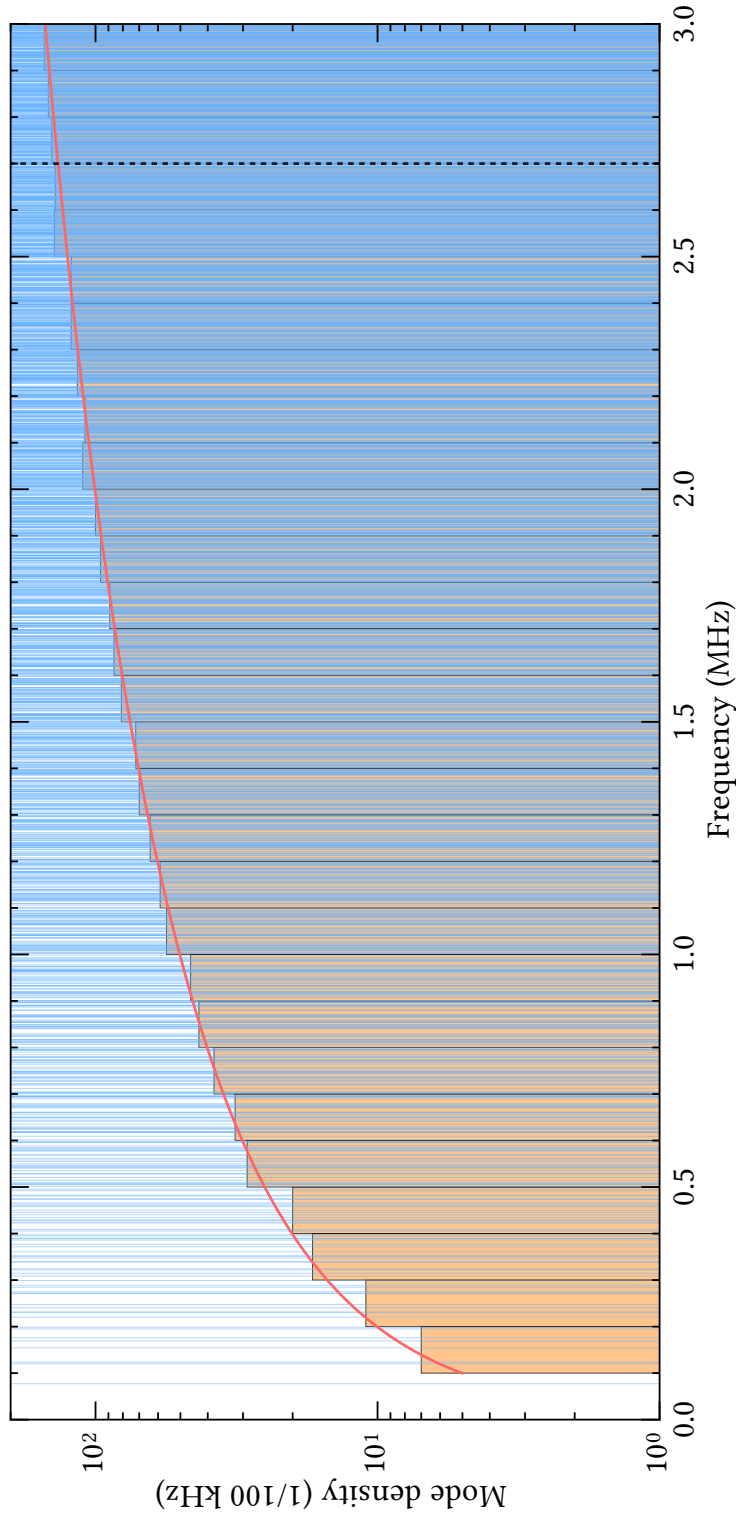


Figure 3.8: Calculated mode density of a  $5 \times 5.25 \text{ mm}^2$  square silicon nitride membrane, with 1 GPa tensile stress. We have introduced a 5% difference in the sidelength of the resonator, in order to lift the mode degeneracy and elucidate our point. Vertical (blue) lines indicate calculated eigenfrequencies, histogram (yellow) indicates the number of modes per 100 kHz, while the envelope (red) curve is the analytically calculated mode density in Eq. (3.6). The dashed vertical line at 2.7 MHz indicates the frequency at which  $Q \times f \sim 100 \text{ THz}$  was measured in [57]. Figure is adapted from [132].

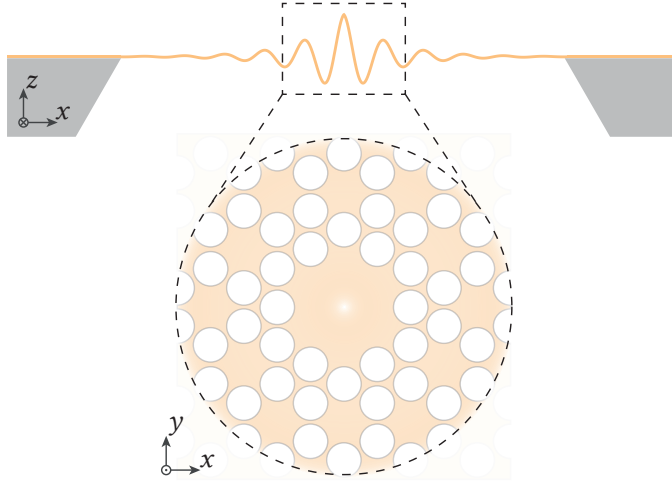


Figure 3.9: Profile sketch of a soft clamped membrane, illustrating the gradual transition of a localised vibration into the phononic crystal structure (bottom), which acts as a “soft” clamping region.

Seeing that the only viable option of increasing the dilution factor is a double-edged sword, we turn our attention back to expression for dissipation dilution, as we look for an alternative solution. It is evident that eliminating the “hard clamp” at the edges of our resonators would result in a much more favourable  $Q \propto \lambda^{-2}$  scaling. Remarkably, this can be achieved by phononic crystal patterning of the membrane resonator, as opposed to the structuring of the substrate, discussed earlier in this chapter. By introducing a defect in the membrane (see Fig. 3.9), we can localise vibrational modes in the central region of our device. The fact that the isolation structure (i.e. the phononic crystal structure) and the resonator have comparable stiffnesses<sup>13</sup>, the localised vibrational modes decay gradually into the “soft” clamping region (i.e. the phononic crystal structure), and have negligibly small amplitudes at the interface of the membrane structure and the supporting silicon substrate. Since the localised vibrational modes no longer “see” the rigid clamp, their integrated curvatures are significantly reduced and hence the degree of dilution is dramatically enhanced. This essentially amounts to elimination of the  $\mathcal{O}(\lambda)$  in dissipation dilution, leaving us with the more favourable  $\mathcal{O}(\lambda^2)$  term. *The technique of eliminating the rigid clamp by phononic crystal engineering is what we call “soft clamping”.* In the following sections we will go through the various steps of the design process, as well as device

<sup>13</sup>Stiffness being the ability of a membrane structure, subject to an external force, to resist deformation. For thin plates, the stiffness is dominated by the in-plane tension, rather than flexural rigidity, which becomes negligible due to the  $D \propto h^3$  scaling.

characterisation.

### 3.2.1 Finite element modelling

#### Simulation of mechanical $Q$ 's and effective masses

Simulating the mechanical properties of our soft clamped devices is a key part of the design process. In most phononic crystal structures the geometry is decoupled from the intrinsic properties of the resonator. However, in our case the stress distribution is strongly coupled to the geometry. Therefore, it isn't obvious that our "geometric intuition" will always be true – moving or scaling a set of holes in our structure could lead to a non-trivial redistribution of the stress, and the resulting mode properties could be opposite to what we had intended with said geometric perturbation. As such, we need to develop a set of numerical tools, which will aid us in optimising our devices.

We will use a plain square membrane as our test case, comparing simulated and analytic values of the effective masses and quality factors, which are the two primary quantities we are interested in extracting from our simulations. In COMSOL we will be using the Structural Mechanics module to perform eigenfrequency analysis of the membrane resonator, and estimate said quantities by manipulating the simulated displacement fields – by integration, differentiation, or both. The effective mass is estimated in COMSOL using Eq. (2.14). The quality factor is estimated by the ratio of the kinetic energy given by Eq. (2.49), and the dissipated energy expressed in terms

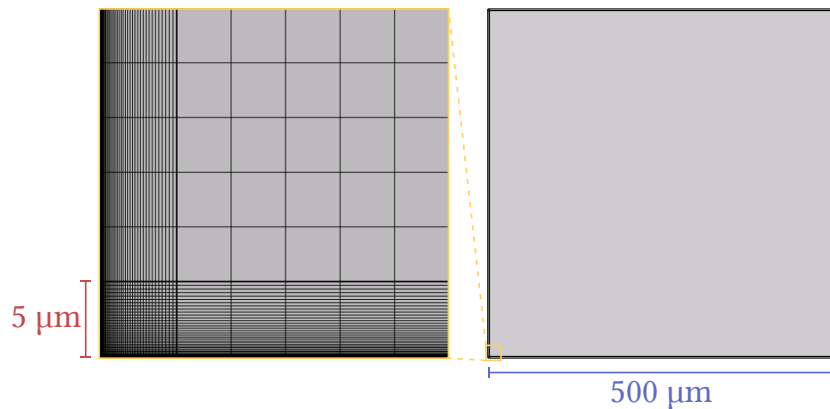


Figure 3.10: COMSOL model of a  $500 \mu\text{m} \times 500 \mu\text{m}$  square silicon nitride membrane. The geometry includes a  $5 \mu\text{m}$  frame, which is used for dense meshing near the membrane edges. Fixed boundary conditions are applied at the four surfaces of the square membrane (i.e. at the clamping points).

of the second order derivatives of the displacement field (cf. Eq. (2.48)). Anticipating a large curvature around the membrane edges, we mesh the a region of  $5 \mu\text{m}$  around the circumference of the membrane extra densely (see Fig. 3.10).

In Fig. 3.11b such a comparison of the quality factors is shown for a square membrane resonator of  $100 \text{ nm}$  thickness and  $500 \mu\text{m}$  sidelength. We have once again introduced a small degeneracy ( $0.1\%$ ), in order to break the degeneracy in our simulation. As shown in the figure inset, the simulated quality factor agrees with the analytic estimate to within  $10\%$ . Comparing the stored and dissipated energies from our simulation with theory suggests that the discrepancy is due to our estimate of the dissipated energy. The few percent discrepancy is likely due to the imperfect meshing at the membrane edges. However, since the simulations of soft clamped membranes do not involve such large curvatures, the slight discrepancy in the simulated values for a square membrane is perfectly acceptable.

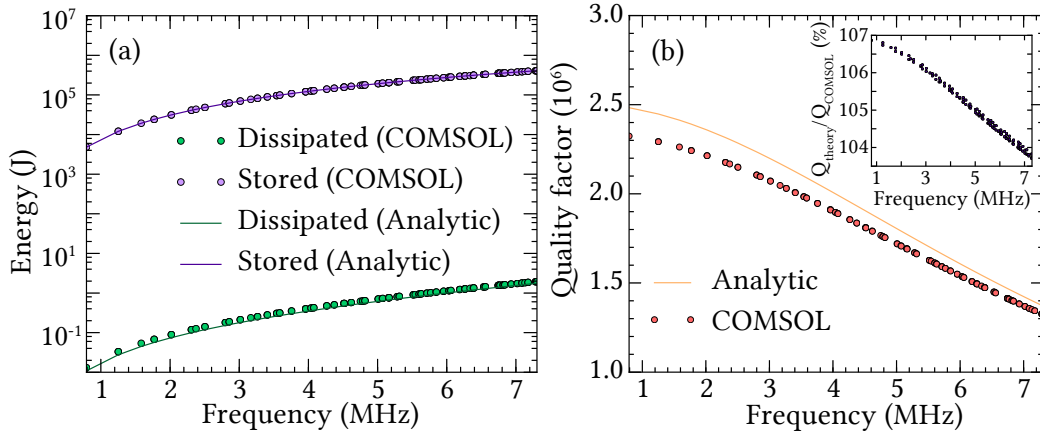


Figure 3.11: Comparison of simulated (a) energies and (b) quality factors with analytic values for a  $100 \text{ nm}$  thin silicon nitride membrane with  $500 \mu\text{m}$  sidelength and  $1 \text{ GPa}$  tensile stress. The inset of figure (a) shows the ratio of the simulated and analytic values, suggesting that the COMSOL simulation agrees with the theoretical values to within  $10\%$ .

Finally, we compare the simulate effective masses with theoretical values (see Fig. 3.12). Here, the agreement is better than  $0.5\%$  and only slight deviations are seen for higher order vibrational modes. If necessary, this could be improved with a denser mesh. With this, we are now confident that we can accurately simulate the two most important quantities for device optimisation, and are ready to move on to simulations related to soft clamped membranes.

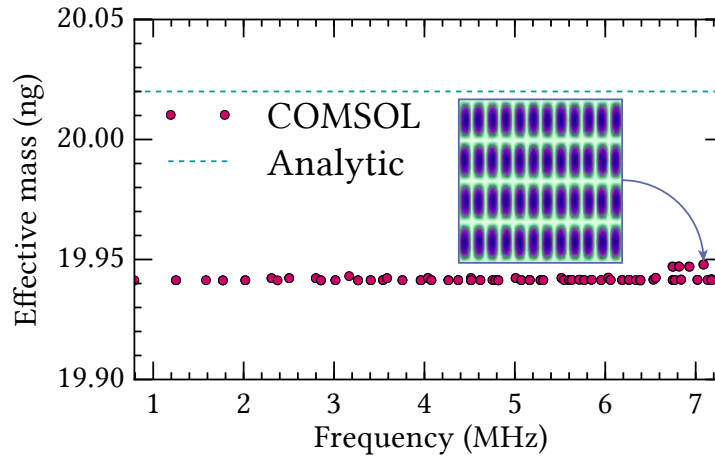


Figure 3.12: Simulated (circles) and analytic (dashed) values of the effective mass for a 100 nm thin and 500  $\mu\text{m}$  wide membrane resonator with 1 GPa tensile stress. Across the entire range, the agreement with the theoretical value is better than 0.5%. Slight deviation is seen for higher order modes (example of one of these modes is shown in the inset).

### Phononic bandgaps in thin, tensioned films

At a first glance it might seem obvious that periodic perforation of a thin silicon nitride membrane will result in a phononic bandgap. However, as mentioned earlier in this chapter, slabs with periodic perforation typically exhibit large bandgaps when the plate thickness is comparable to the lattice constant. In an earlier study by Khelif et al. [105] it was indeed shown that the ratio of thickness to lattice constant is a key parameter for the existence, as well as the overall size, of the bandgap. A year later Mohammadi and colleagues compared the properties of square and honeycomb lattice phononic crystal structures [106], etched into a thin silicon slab. The honeycomb lattice was shown to support a larger relative bandgap, as compared to the square lattice. Interestingly, the honeycomb lattice was furthermore shown to exhibit a richer bandgap structure as a function of the plate thickness, with complete phononic bandgaps emerging even for thicknesses more than 3 times the lattice constant. These observations render the honeycomb lattice an interesting candidate for our purposes.

Starting with a unit constituent of a honeycomb lattice, we consider the evolution of the band diagram, as the ratio of thickness to lattice constant is reduced. Our starting point is a rectangular unit cell (see Fig. 3.13a), with lattice constant  $a = \sqrt{3} \times 100 \mu\text{m}$  and hole radius  $r = 0.45 \times a/\sqrt{3}$ .

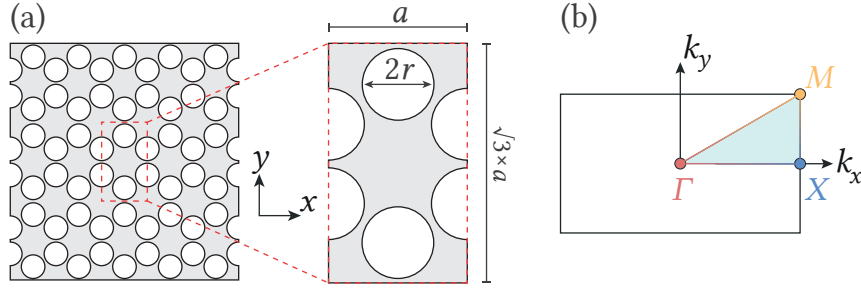


Figure 3.13: (a) Sketch of a unit cell of the hexagonal honeycomb lattice and (b) the corresponding first Brillouin zone.

Bloch-Floquet periodicity is imposed on the boundaries along the  $x$ - and  $y$ -directions, and the wavevector  $k$  is swept across the first Brillouin zone (see Fig. 3.13b). At first we consider an unstressed membrane where the only restoring force is its flexural rigidity. Banddiagrams for thicknesses between  $100 \mu\text{m}$  and  $1 \mu\text{m}$  are shown in Fig. 3.14. For  $100 \mu\text{m}$ , we see a complete bandgap between  $\sim 16 \text{ MHz}$  and  $\sim 24 \text{ MHz}$ . As the thickness-to-lattice constant ratio becomes smaller, we see a reduction and eventually closure of the bandgap. Furthermore, as the unit cell becomes thinner, the flexural rigidity reduces and more bands with flexural polarisation start populating lower frequencies, ultimately resulting in a tightly packed forest of flexural bands. While this is in no way surprising, we notice something interesting – namely a sub-group of bands that remain almost stationary as we vary the thickness over two orders of magnitude. Upon closer inspection we find that these bands correspond to in-plane motion (see inset of vibrational modeshapes in Fig. 3.14) of the perforated structure. In order to establish direct mechanical coupling between in- and out-of-plane modes of our structure, some sort of symmetry breaking along the  $z$ -direction is needed (e.g. non-uniform plate thickness or external electrostatic potential). Furthermore, in an actual device a non-zero spatial and spectral overlap between the in-plane and out-of-plane modes would be necessary (similar to the requirement in the phonon tunneling framework). Seeing that the group velocity of the in-plane modes (i.e. the slope of the vibrational bands corresponding to in-plane motion) is significantly larger than for the flexural bands, it is therefore conceivable that in-plane modes will be sparsely located at lower frequencies in an actual device. It is therefore a fair assumption that low-frequency flexural modes will not couple to in-plane motion in an actual device.

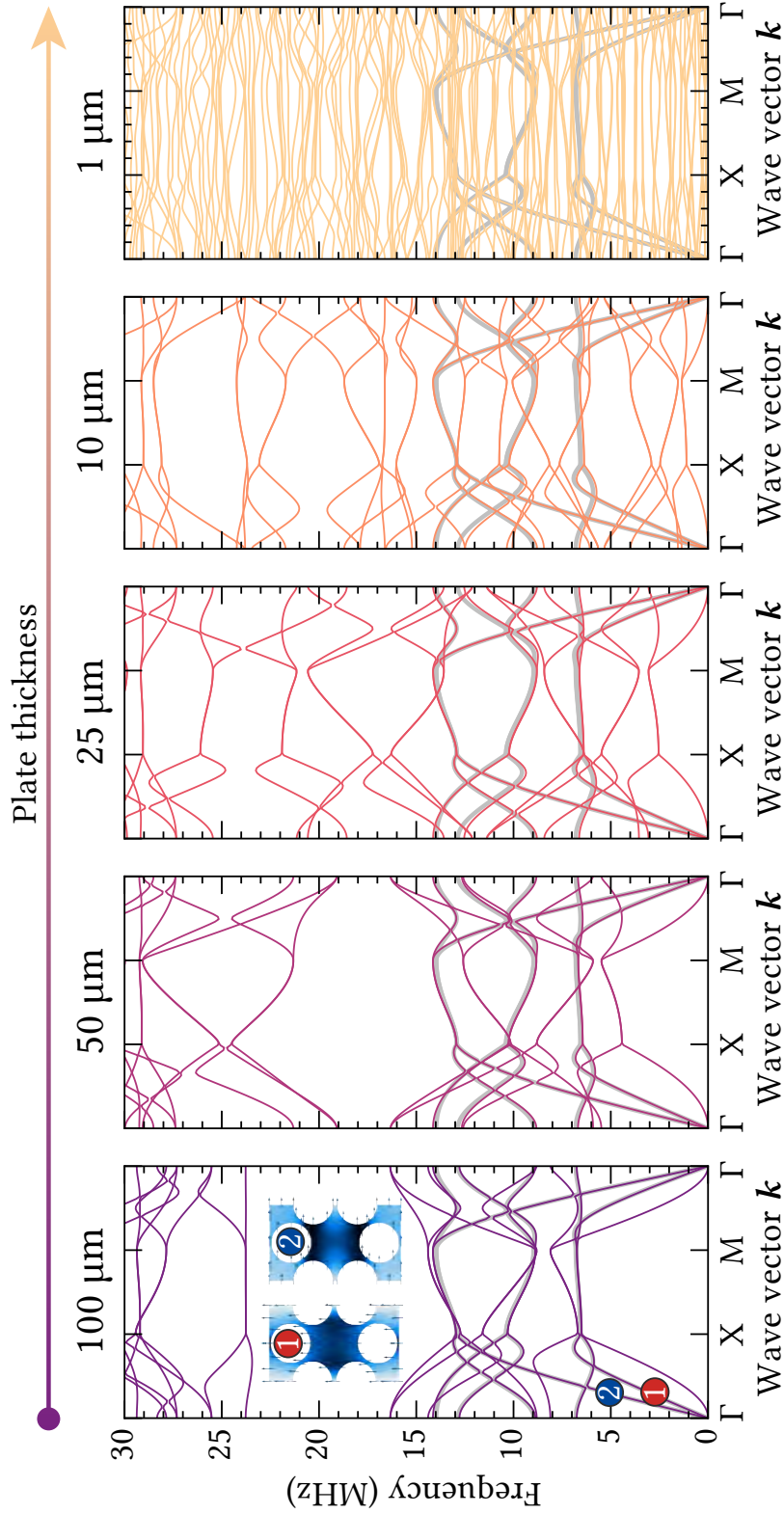


Figure 3.14: Band diagrams for a honeycomb lattice in silicon nitride, with lattice constant  $a = \sqrt{3} \times 100 \mu\text{m}$  and hole radii  $r = 0.45 \times a/\sqrt{3}$ . The thickness of the unit cell (see inset, left-most figure, or Fig. 3.13) is varied from left to right, with the respective thicknesses indicated above each band diagram. In gray is shown a band diagram simulation for in-plane modes ( $100 \mu\text{m}$  thickness), by imposing the boundary condition  $z = 0$  at the top-surface of the unit cell. The same band diagram is shown in all five plots. The inset in the left-most figure shows the modeshape of the two lowest bands with in-plane polarisation.

With these things in mind, combined with the fact that the reduced stiffness of the phononic crystal structure can be compensated for by introducing an in-plane force, we consider the evolution of the band diagram, as we increase the tension in the phononic crystal structure. Here, the thickness of the crystal structure is 100 nm. As shown in Fig. 3.15, starting from a 10.24 kHz wide quasi-bandgap for 2.5 MPa pre-stress, the bandgap increases in size and moves up in frequency, as we increase the tension. The center frequency has a square-root scaling with the pre-tension, which is consistent with the previous calculations (cf. Eq. (2.18)). For the maximum value of the initial stress, comparable to the pre-stress in our deposited silicon nitride thin films, we see an appreciable quasi-bandgap at  $f_c = 1439.24$  kHz. Furthermore, as shown in Fig. 3.15, the *relative* bandgap size (i.e. ratio of bandgap size,  $\Delta f$ , to center frequency,  $f_c$ ) increases by approximately 4% (14.93% to 18.47%) from 2.5 MPa to 1250 MPa. The absolute values for the center frequency and span of the quasi-bandgaps are  $f_c = \{68.62, 205.05, 643.18, 1439.24\}$  kHz and  $\Delta f = \{10.24, 36.79, 117.65, 265.86\}$  kHz.

Thus far we have not discussed the fact that the stress distribution in a perforated membrane structure is not uniform. In fact, in order to accurately simulate the phonon dispersion, an additional step is required in our band diagram simulations. Assuming an initial stress along the  $x$ - and  $y$ -directions of the membrane, a steady-state analysis is performed in COMSOL. The new equilibrium distribution shows concentrations of stress in narrow region and relaxation elsewhere. This stress distribution is subsequently used as the initial condition for the eigenfrequency analysis, where we once again impose Bloch-Floquet periodicity. In order to demonstrate the importance of this additional step, we compare a band diagram for a unit cell with a uniform stress distribution, to a band diagram where the stress redistribution in the unit cell is accounted for. As shown in Fig. 3.16, the dispersion relation assuming homogeneous (incorrect) stress distribution results in bands with significantly higher frequencies, compared to the band diagram where stress concentration and relaxation is accounted for. The average stress over the unit cell is approximately 796.1 MPa, corresponding to a 36.3% reduction from the 1.25 GPa pre-stress assumed in this simulation.

Beyond the importance of accounting for the stress redistribution, in order to accurately predict the location and size of bandgaps in these structures, this comparison furthermore suggests that the spatial modulation of the propagation speed (which is proportional to the square root of tension) does not play a crucial role in defining the size of the quasi-bandgap. Instead, mass contrast (broadly speaking, one can think of the “small-mass-big-mass” picture) and stiffness are the key parameters. Since the latter scales linearly

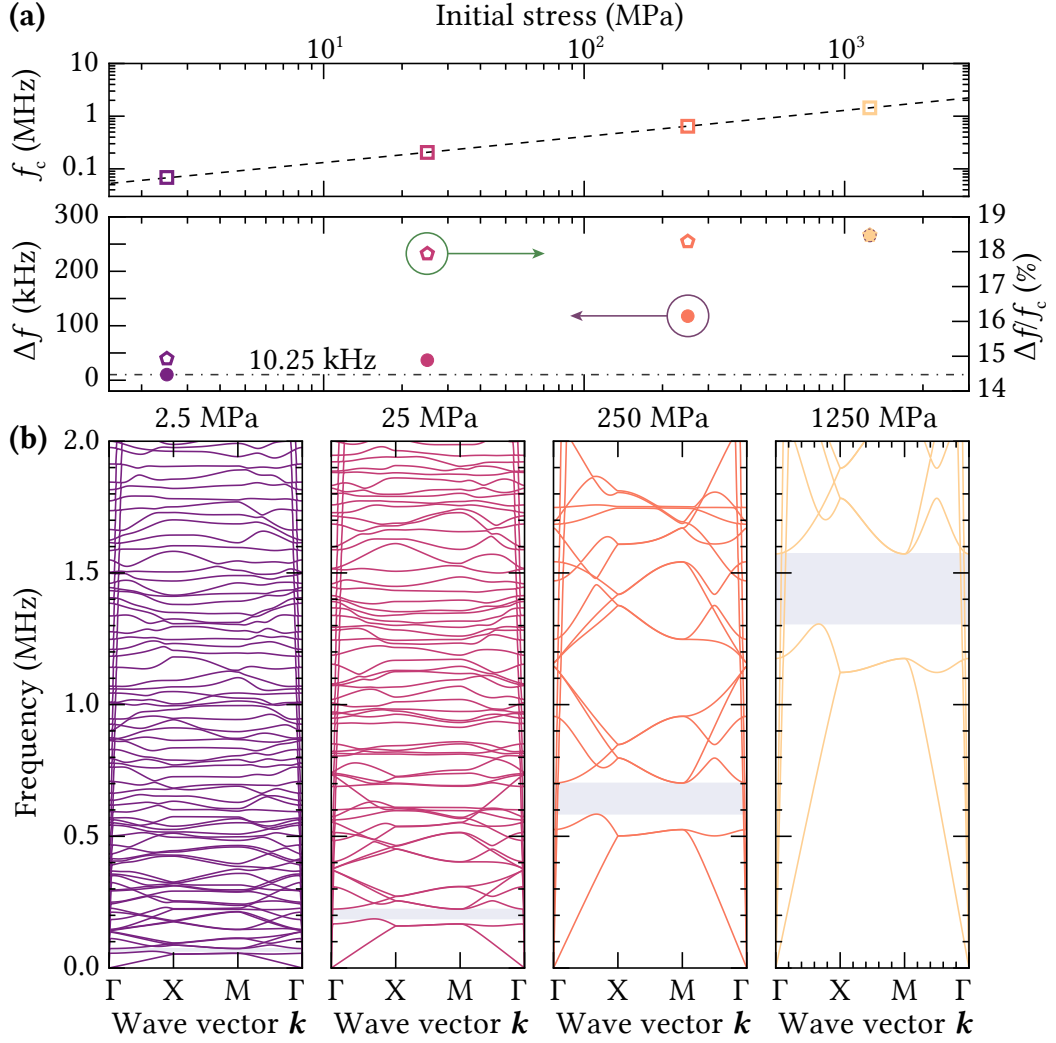


Figure 3.15: Band diagram simulations for varying in-plane tension in a honeycomb lattice ( $a = \sqrt{3} \times 100 \mu\text{m}$ ,  $r = 0.45 \times a/\sqrt{3}$  and  $h = 100 \text{ nm}$ ). a) The relative and absolute size, as well as the center frequency, of the quasi-bandgap as a function of initial stress. Here, pentagons and circles correspond to the relative and absolute bandgap sizes, respectively. The dashed line (top) corresponds to a fit of  $f_c(\sigma) = a\sqrt{\sigma} + b$ , with  $a = 40.61 \text{ kHz}/\sqrt{\text{MPa}}$  and  $b = 2.77 \text{ kHz}$ . b) The corresponding band diagrams.

with tension<sup>14</sup>, it is important to maintain a high average value of stress across the entire membrane structure. For instance, the average value of the

<sup>14</sup>Writing the stiffness (spring constant) as  $k_{\text{eff}} = m_{\text{eff}}\Omega_{\text{m}}^2$ , with  $m_{\text{eff}}$  being the effective mass, and recalling that  $\Omega_{\text{m}} \propto \sqrt{\sigma}$  (cf. Eq. (2.18)), we see that  $k_{\text{eff}} \propto \sigma$ .

von Mises stress in the unit cell shown in Fig. 3.16 is approximately 796 MPa, slightly shy of 40% lower than in the unit cell with uniform 1250 MPa stress distribution. If we naively rescale the frequency of the upper bands for the unit cell with uniform stress distribution with said percentage, we find that these bands should be closer to 1667 kHz, instead of 2617 kHz. This roughly agrees with the simulated frequency of the upper band edge in the case of redistributed stress in the unit cell. Therefore, in order to realise large quasi-bandgaps in our structures, we need to have a large mass contrast, as well as a high average stress. Unfortunately, while the former can be achieved by increasing the ratio of hole radii to lattice constant, this would necessarily lead to a reduction of tension in the large regions of the phononic crystal structure and potentially an overall decrease of the bandgap size.

As an aside, let us once again consider the inhomogeneous stress distribution in Fig. 3.16. While it is evident that the stress in the narrow regions will be higher than elsewhere, the choice of von Mises stress as the metric might seem unclear or perhaps arbitrary. As mentioned before, the yield strength

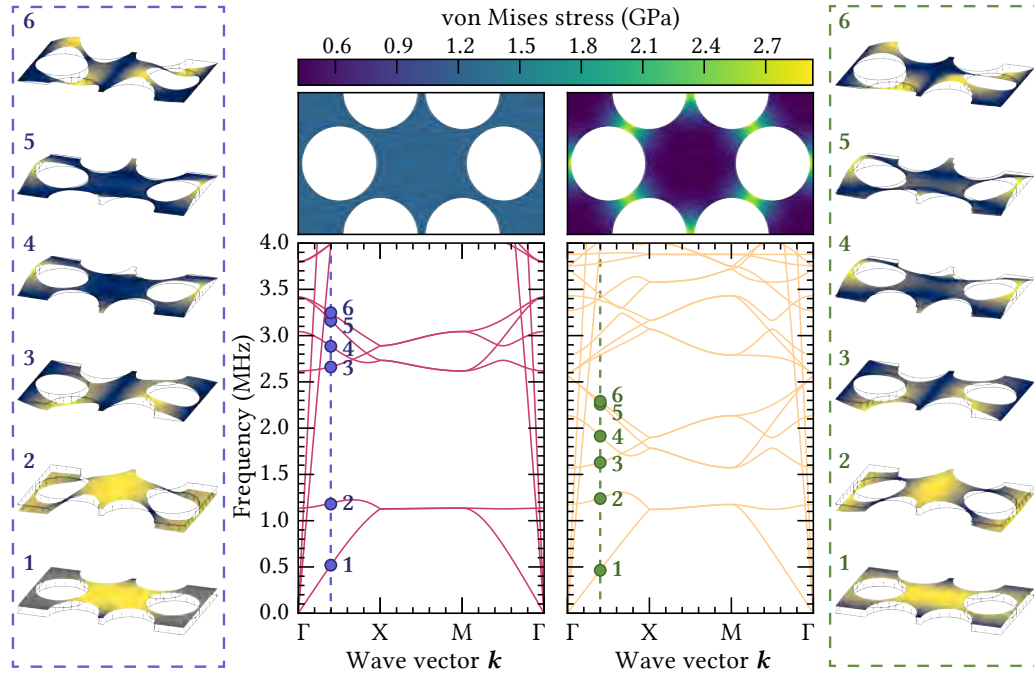


Figure 3.16: Simulated band diagrams assuming a uniform 1.25 GPa stress distribution (top left) and redistributed stress (top right) in the unit cell, alongside the corresponding band diagrams (bottom). The modeshapes of the first six bands for wavenumber  $k_x = 0.4 \times \pi/a$  are shown on the far left and right with the color map indicating their absolute displacement value.

of silicon nitride is approximately  $\sigma_y = 6.4$  GPa [131], which is merely five times higher than the initial stress of LPCVD silicon nitride. Therefore, as we begin to perforated such a highly stressed film, we need to keep track of the tension, in order to avoid reaching yield stress and thus plastic deformation. The von Mises stress [133] is a commonly used quantity in mechanical engineering to predict yielding of a materials, and in the relevant case of plane stresses can be expressed as [134]

$$\sigma_v = \sqrt{\sigma_{11}^2 + \sigma_{22}^2 + 3\sigma_{12}^2 - \sigma_{11}\sigma_{22}}, \quad (3.7)$$

where  $\sigma_{ij}$  are the principal stresses in the material. For instance, in the case of a thin plate with  $\sigma_{11} = \sigma_{22} = \sigma$  and  $\sigma_{12} = 0$ , the von Mises stress equals  $\sigma_v = \sigma$ . The von Mises yield criterion, expressed in terms of the von Mises stress, simply states that yielding will occur when the von Mises stress equals the yield stress, i.e.  $\sigma_v = \sigma_y$ . Therefore, in our simulations of stress distribution in soft clamped resonators, we use the von Mises stress as the relevant metric.

Lastly, we need to introduce a defect within our artificial crystal lattice, in order to localise vibrational modes within the phononic crystal. One of the simplest defect geometries can be realised by translation of six holes within the crystal structure, resulting in a hexagonal-shaped defect (see Fig. 3.17a). Before simulating the vibrational mode of this structure, it is worth considering the vibrational modes of a simple hexagonal-shaped membrane. Shown in figure 3.17 are the first ten vibrational mode patterns of such a

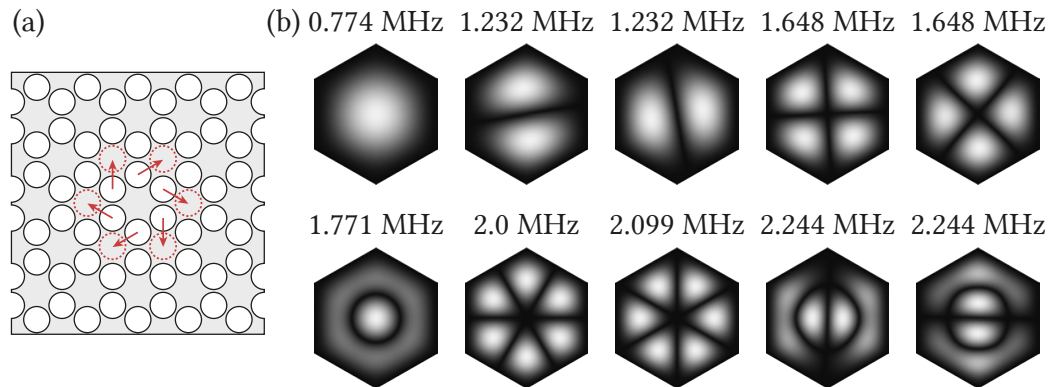


Figure 3.17: a) Sketch of a honeycomb lattice, with red arrows representing translational of holes and dashed circles indicating the new positions of the holes. b) Vibrational mode patterns of a hexagonal silicon nitride membrane with  $350 \mu\text{m}$  sidelength,  $100 \text{ nm}$  thickness and  $1.25 \text{ GPa}$  tensile stress.

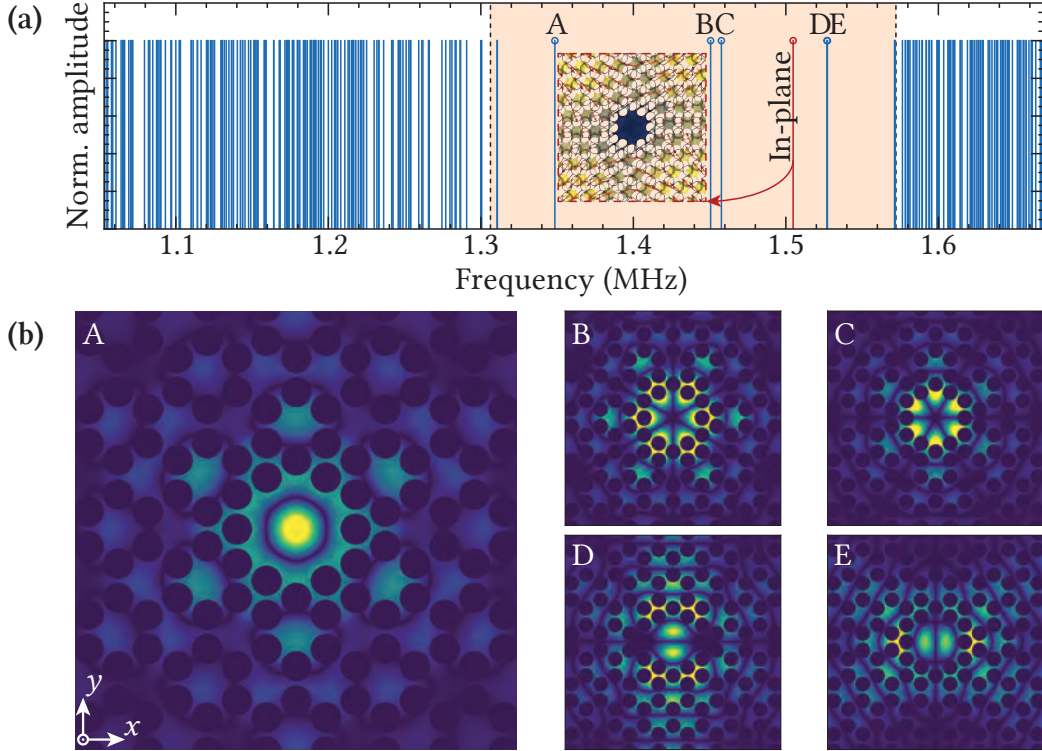


Figure 3.18: Simulated vibrational modes of a hexagonal-shaped defect within the honeycomb phononic crystal lattice. a) Spectral composition of vibrational eigenmodes, where each vertical line corresponds to an eigenmode of the phononic crystal structure. The filled (orange) area corresponds to the predicted bandgap from a unit cell simulation (cf. Fig. 3.15). Within the bandgap we find five localised modes with transverse polarisation, as well as an in-plane “pinch” mode (see inset). b) The vibrational mode patterns of the five modes highlighted in the spectrum. Figure b) is reproduced from [1] and [132].

membrane. Seeing that the membrane is near-circular, it is unsurprising that the vibrational mode shapes closely resemble the radial and azimuthal modes of a circular plate [20].

We now consider the vibrational mode patterns for the proposed defect geometry in Fig. 3.17a. An eigenfrequency analysis of the perforated membrane structure, with lattice constant  $a = \sqrt{3} \times 100 \mu\text{m}$ ,  $r = 0.45 \times a/\sqrt{3}$  and 1.25 GPa pre-tension, confirms the existence of a phononic bandgap. Within the anticipated frequency range of the quasi-bandgap (cf. Fig. 3.15a) we see an absence of modes, except for a small handful (see Fig. 3.18a). These are five localised transverse vibrational modes, as well as a in-plane “pinch”

mode of the entire membrane structure. As we can see, the modes A-E correspond to the second row of mode patterns in Fig. 3.17. We therefore conclude that the fundamental-like mode A in Fig. 3.18 correspond to the second radial mode of the hexagonal-like defect. As anticipated the modes evanescently decay into the “soft” clamping region, which is the phononic crystal structure. The following two sections will focus on the fabrication process and importantly the mechanical performance of these devices.

### 3.2.2 Soft clamped membrane resonators

#### Fabrication process

While the geometry of soft clamped devices differs appreciably from the silicon phononic crystal structures discussed in the first section of this chapter, the fabrication processes have several parallels. As such, certain parts of the fabrication process for soft clamped membrane will be covered superficially, and the reader is referred to the description of the silicon phononic crystal fabrication process in Section 3.1.4. Throughout this section, the reader is referred to figure 3.19, for an overview of the process flow.

Unsurprisingly, **Step 1** of the process involves deposition of stoichiometric silicon nitride on 500  $\mu\text{m}$  thick 4” silicon wafers with  $\langle 100 \rangle$  crystal orientation. In contrast to the silicon phononic crystal structures, there is no apparent reason for choosing this particular wafer thickness, other than compatibility with existing experimental assemblies designed for the silicon phononic crystal based devices. We proceed with a photolithographic step (**Step 2-3**), in order to define square openings on the back-side of the wafer. This involves spin-coating 1.5  $\mu\text{m}$  AZ® MIR™ 701 (positive photoresist) at 4600 rpm, followed by a 60 s softbake at 90°C, UV exposure, post-exposure bake<sup>15</sup> (PEB) and, finally, development. Following 60 s PEB at 110°C, the photoresist is developed in diluted TMAH, thus exposing square regions of the silicon nitride film underneath the photoresist. Similar to the silicon phononic crystal fabrication, we use reactive ion etching in **Step 4** to etch the silicon nitride in the exposed regions of the wafer. The photoresist is then stripped away in **Step 5** using acetone or NMP (1-Methyl-2-pyrrolidone) Remover 1165. We repeat **Steps 2-5**, in order to define the phononic crystal structure on the

---

<sup>15</sup>Since the critical dimensions in our phononic crystal structures can be on the order of a few micrometers, a post-exposure baking step is employed to smoothen out the inhomogeneously exposed photoresist, originating from the standing-wave pattern formed inside the photoresist during UV exposure. For more details, the reader is referred to the application notes provided by the photoresist manufacturer [135].

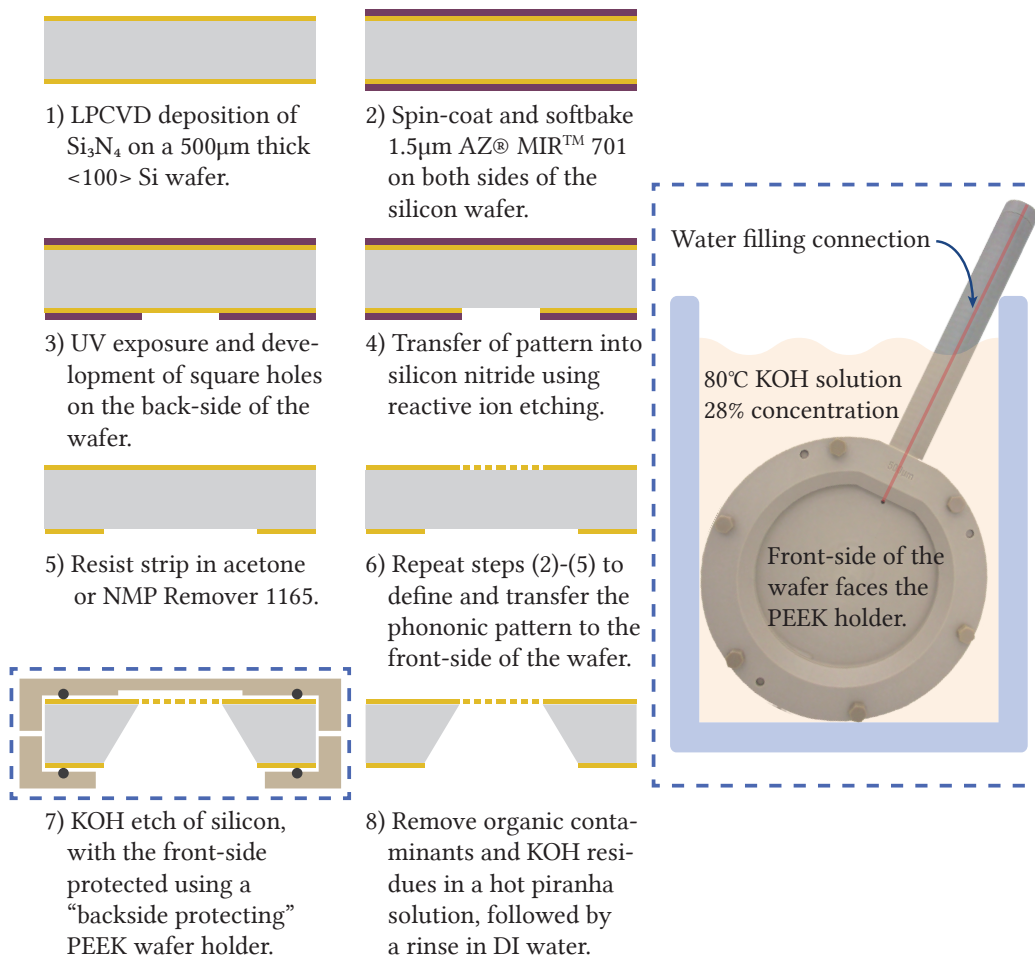


Figure 3.19: Process flow for the fabrication of soft-clamped membrane resonators. The inset shows the backside protecting holder used in the second to last step of the process.

front-side of the wafer. At this point, the wafer has a matrix of square holes on the back-side, and a corresponding matrix of phononic crystal patterns on the front side.

As with silicon phononic crystal shielded membranes, the soft clamped membranes are released in **Step 7** in a KOH solution at  $80^\circ\text{C}$ . The wafer is placed inside a PEEK (polyetheretherketone) backside protecting holder<sup>16</sup>, which ensures that the KOH solution only attacks the back-side of the wafer, thus protecting the phononic crystal pattern throughout the 6 hour etch. The holder is tightened with screws (see Fig. 3.19 for a picture of the holder), and

<sup>16</sup>Tandem4 wafer holder with backside protection from AMMT GmbH.

the front-side of the wafer is sealed using a set of EPDM o-rings<sup>17</sup>. Following the etch, the backside protecting holder is rinsed in DI water and the wafer is subsequently removed. While in liquid, the wafer is handled with utmost care, to avoid rupturing the perforated membrane structure. Finally, in **Step 8** the wafer is cleaned using a hot piranha solution (cf. Section 3.1.4), rinsed in DI water, and dried in air in a clean environment. The wafer with membranes is subsequently placed inside a vacuum chamber, in order to be characterised, or, alternatively, broken into individual devices, before doing so.

### Initial characterisation of soft clamped membranes

We begin with an interferometric measurement of a soft clamped membrane, akin to the measurements described in Section 3.1.5. In contrast to the silicon phononic crystal structures, the effective masses of the soft clamped membrane modes are sufficiently low to allow us to measure the Brownian motion of the membrane structure, thus avoiding driven measurements, which tend to be more time consuming.

One such measurement is shown in Fig. 3.20, alongside a simulated band diagram for the corresponding device dimensions. The displacement spectrum is an average of several spectra taken in a square region in the central part of the defect. As we can see, within the frequency range of 1.41 – 1.68 MHz, only a handful of modes are found, while outside this frequency window we observe a dense mode spectrum. Comparing the measured mode spectrum with the simulated band diagram of a unit cell strongly suggests that the observed depletion of modes is evidence of the phononic bandgap. In fact, the spectral location of said window agrees with our simulation to within 2%.

Next, we wish to identify the modes within the phononic bandgap. In order to do so, we perform a *raster-scan* of the membrane device. As previously mentioned, our interferometric setup includes a probe head with a motorised translation stage, as well as a 50× microscope objective, which allows us to focus the probe light down to a spot diameter of 2 μm. This allows us to raster-scan the probe beam across the surface of the membrane over a rectangular grid in an automated fashion, extracting calibrated displacement spectra at each position of the grid. In post-processing we extract the displacement of each one of the five modes identified in Fig. 3.20, thus constructing 2D displacement maps for said modes. In figure 3.21 these displacement maps are shown for the modes within the apparent phononic

---

<sup>17</sup>EPDM o-rings are the most suitable sealing material for KOH and TMAH etching. Alternatives include FFMP, albeit at a significantly higher cost.

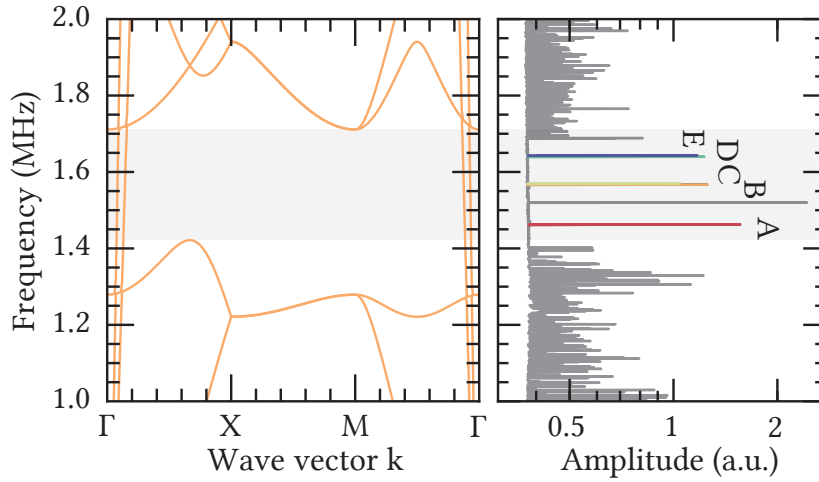


Figure 3.20: Simulated band diagram (left) and measured mechanical mode spectrum (right) for the geometry shown in Fig. 3.18. The shaded area indicates the simulated bandgap, the position and size of which is in good agreement with the measurement. The five localised modes inside the bandgap are labeled according to the naming in Fig. 3.18. The unlabeled peak at  $\sim 1.5$  MHz is a calibration tone. Here, the lattice constant is  $a \approx \sqrt{3} \times 92.58 \mu\text{m}$ . Figure is reproduced from [1] and [132].

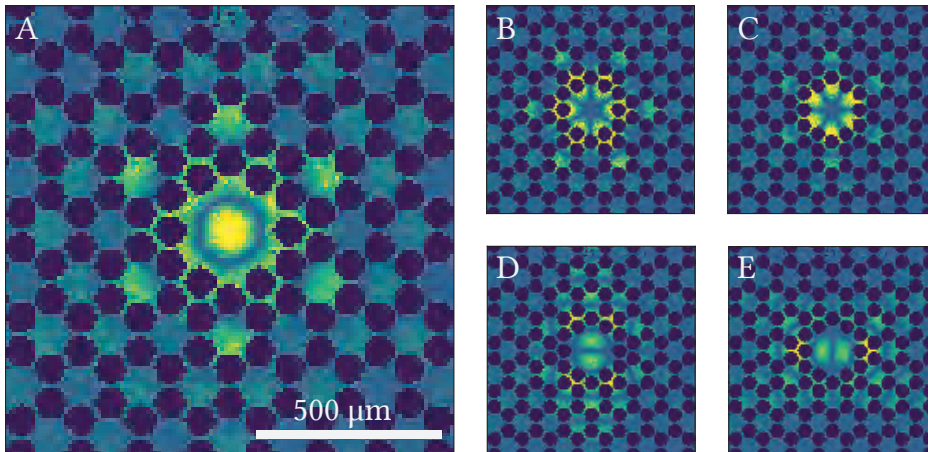


Figure 3.21: Measured vibrational mode patterns of the localised defect modes, obtained via a raster measurement. We see excellent agreement with the simulated modeshapes (see Fig. 3.18b). Figure is reproduced from [1] and [132].

bandgap. We see an excellent agreement with the simulated modeshapes (cf. Fig. 3.18b). Outside of the defect the localised modes decay quickly with increasing distance, as expected within a phononic bandgap.

### Evidence of soft clamping

Having verified some of the key design features of our devices, we now wish to address the question whether our approach has indeed eliminated the effect of the rigid clamp. Recalling that  $\lambda \propto L^{-1}$  and  $f_{mn} \propto L^{-1}$ , we can express the quality factor for a square membrane resonator as

$$Q_{mn}^{-1} = aQ_{\text{int}}^{-1} \left( f_{mn} + bf_{mn}^2 \frac{(m^2 + n^2)\pi^2}{4} \right), \quad (3.8)$$

where  $a$  and  $b$  are constants. If our devices indeed render losses due to the rigid clamp negligible, this will equate to eliminating the first term in the above equation, and hence we would anticipate a  $Q \propto f_{mn}^{-2}$  scaling. Since the quasi-bandgap only spans a few hundred kilohertz in frequency, this effect will not be sufficiently pronounced within the bandgap<sup>18</sup>. Hence, we choose to fabricate and characterise samples with varying size, by rescaling the entire membrane geometry. This ensures a fixed relative position of the modes within the bandgap, as well as a constant stress distribution within the membrane resonators. Each wafer contains four series of  $N = 10$  samples, where the lattice constants of the samples are scaled from  $a_{\text{min}} = \sqrt{3} \times 50 \mu\text{m}$  to  $a_{\text{max}} = \sqrt{3} \times 200 \mu\text{m}$ , with a multiplicative factor of  $(a_{\text{max}}/a_{\text{min}})^{1/(N-1)} \approx 1.1665$ .

We begin by placing a wafer of soft clamped membranes with  $h \approx 35 \text{ nm}$  inside a large vacuum chamber<sup>19</sup>, with a base pressure of  $10^{-8} \text{ mbar}$ . The vacuum pressure is measured immediately outside the chamber using an ion gauge<sup>20</sup>. For the resonator with the highest mechanical  $Qf$  – *product* we consider the pressure dependence of the quality factor. By performing ring-down measurements for varying vacuum pressures, we observe a  $Q \propto p^{-1}$  scaling at higher pressures (see Fig. 3.22a), in agreement with Eq. (2.22). At a pressure of approximately  $1.85 \times 10^{-7} \text{ mbar}$  we measure a quality factor of  $Q = (214 \pm 2) \times 10^6$  at  $f_{\text{E}} = 777 \text{ kHz}$  for mode E<sup>21</sup> on one of the samples on the wafer. Fitting  $Q = (Q_0^{-1} + Q_{\text{D}}^{-1})^{-1}$  to our data, where  $Q_{\text{D}}^{-1} \propto p$  (cf.

<sup>18</sup>Not to mention the fact that the degree of dilution is different for the localised modes.

<sup>19</sup>The wafer is placed on top of a teflon piece, and firmly clamped around the edges with a teflon ring, tightened with a set of screws.

<sup>20</sup>Pfeiffer PKR 251 Compact FullRange™ Gauge.

<sup>21</sup>Here, the uncertainty in the quality factor is from the standard deviation of several ringdown measurements of the same mode.

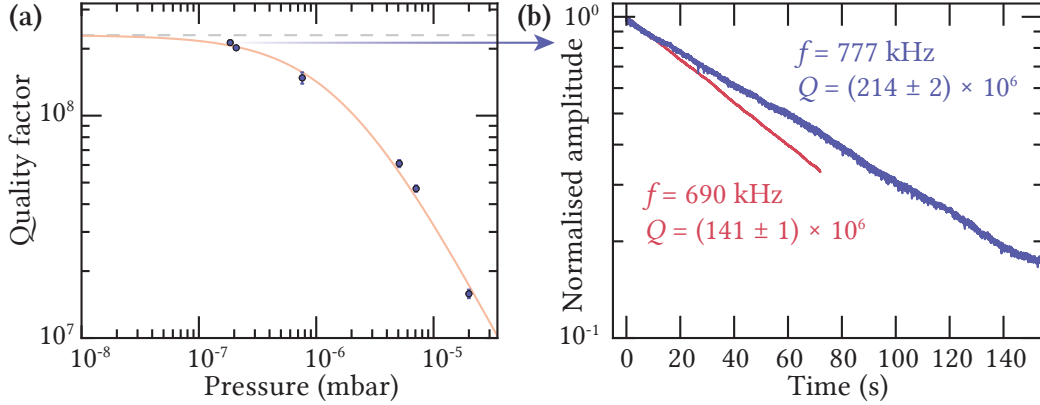


Figure 3.22: a) Mechanical quality factor of mode E as a function of vacuum pressure. The quality factor is gas damping limited down to  $\sim 10^{-7}$  mbar. A ringdown measurement corresponding to the highest quality factor is shown on the right. b) Ringdown measurements of modes A (red) and E (blue) from two different membrane resonators, both with lattice constants  $a = \sqrt{3} \times 200 \mu\text{m}$ . Figure b) is reproduced from [1] and [132].

Eq. (2.22)), we find a saturation level of  $Q_0 = 230 \times 10^6$ , suggesting that gas damping contributes less than 10% in our measurements of the quality factors. Fig. 3.22b shows a representative ringdown measurements for this sample, alongside the highest measured quality factor for the fundamental-line mode (A), yielding  $Q = (141 \pm 1) \times 10^6$  at  $f_A = 690$  kHz.

We now consider measurements of all five localised modes of our membrane structures from multiple membrane resonators with 35 nm silicon nitride thickness. In figure 3.23 the quality factors and  $Qf$ -products for all samples and modes are shown. Following our discussion from above (cf. Eq. (3.8)), we anticipate a  $Q \propto f^{-1}$  scaling for a rigidly clamped resonator, and  $Q \propto f^{-2}$  scaling for a soft clamped boundary condition. As a guide to the eye, these scalings are shown in Fig. 3.23. As we can see, our data adheres to the  $Q \propto f^{-2}$  line, strongly suggesting that all five localised modes are softly clamped, despite the fact that they are embedded in rectangular shaped membranes. As further confirmation we observe a  $Q \times f \propto f^{-1}$ . By eliminating the hard clamping condition, we have thus reduced the integrated curvature due to this clamping region, leading to an apparent enhancement of the mechanical quality factors.

In addition to the observed  $Q \propto f^{-2}$  scaling, the standard theory of dissipation dilution further suggests that we should anticipate a distinct scaling with thickness, as well as pre-tension. Assuming a soft clamped boundary condition, standard theory of dissipation dilution (cf. Eq. (2.50)) suggests

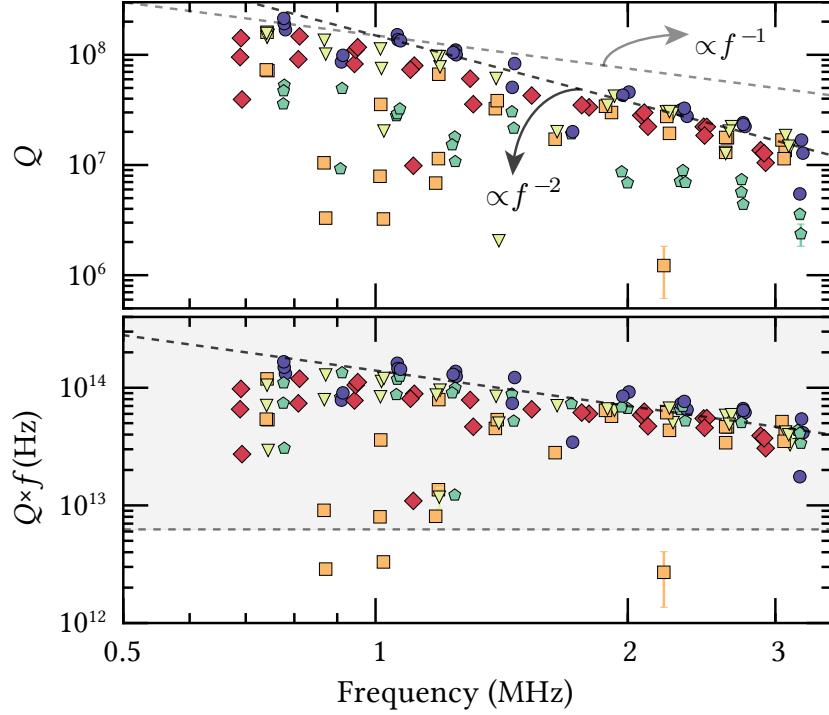


Figure 3.23: Measured quality factors (top) and  $Qf$ -products (bottom) for membranes of thickness  $h = 35$  nm. The membrane geometry is scaled from  $a_{\min} = \sqrt{3} \times 50 \mu\text{m}$  to  $a_{\max} = \sqrt{3} \times 200 \mu\text{m}$ . The observed  $f^{-2}$  frequency scaling of the  $Q$ -factors and  $f^{-1}$  for the  $Qf$ -products is indicative of a soft clamping condition. The colours indicate the localised vibrational modes seen in Fig. 3.20. The dashed horizontal line (bottom) indicates the  $Qf \approx 6$  THz required for a quantum coherent oscillation at room temperature. Figure is adapted from [1] and [132].

that  $Q \propto \lambda^{-2}$  for a soft clamped resonator mode, and hence the quality factor can be written as

$$Q_{m,\text{soft}}^{-1} = \eta_m \frac{E h^2}{\bar{\sigma} a^2} Q_{\text{int}}(h)^{-1}, \quad (3.9)$$

where  $\eta_m$  is a mode- and geometry-dependent numerical pre-factor,  $a$  is the lattice constant, and  $\bar{\sigma}$  is the pre-stress. Recalling that the intrinsic quality factor is thickness dependent [64] (cf. Section 2.2.4), the quality factor will in fact scale *linearly* with thickness below a few of hundred nanometers. To further corroborate the hypothesis of  $Q$ -enhancement by soft clamping, we have fabricated samples with varying thicknesses,  $h = \{35, 66, 121, 240\}$  nm. The samples are prepared in exact same fashion and using the exact same

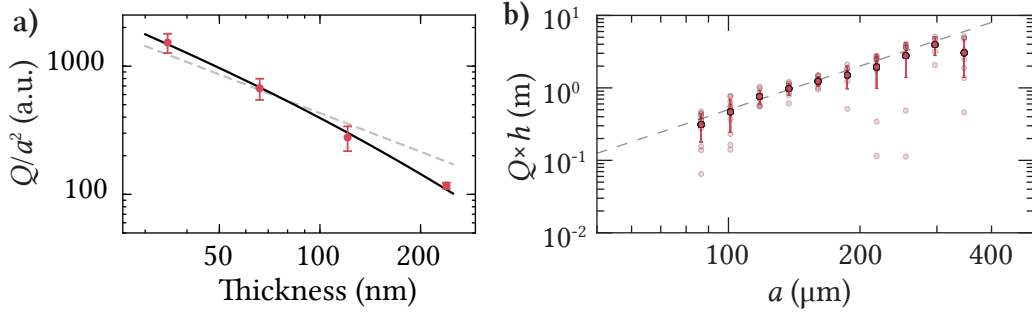


Figure 3.24: Characteristic scaling of the mechanical quality factors for mode A with a) membrane thickness  $h$ , and b) lattice constant  $a$ . The solid line in a) accounts for volumetric, as well as surface losses, while the dashed line shows the scaling due to surface losses only. Consistent with the results from Villanueva et al. [64], we see a deviation for the largest membrane thickness. b) The dashed line indicates  $a \propto a^2$  scaling, consistent with dissipation dilution in the absence of a rigid clamp. Figure is reproduced from [1] and [132].

photolithographic mask as the samples in Fig. 3.23, with the exception of a different initial deposition thickness. For each of the five localised modes we now consider the scaling of the quality factor with the lattice constant and with thickness. In Fig. 3.24 we present the rescaled quality factors as a function of device thickness and lattice constant. All of the localised modes exhibit a  $Qh \propto a^2$  scaling (Fig. 3.24, bottom row), as well as  $Qa^{-2} \propto h$  scaling (Fig. 3.24, middle row). Expectedly, our data shows poor agreement with the linear thickness scaling for  $h = 240$  nm (see dashed line in Fig. 3.24, middle row). Including (thickness independent) volumetric losses in our fit model (i.e.  $Q_{\text{int}}^{-1} = Q_{\text{vol}}^{-1} + Q_{\text{surf}}(h)^{-1}$ , where  $Q_{\text{surf}}(h) \propto h$ ), we see good agreement across all five modes.

Drawing on our experience with square membrane resonators (see Section 3.2.1), we now seek to verify our hypothesis of soft clamping by a direct comparison of simulated and measured quality factors. For each of the localised eigenmodes, we compute the maximum kinetic energy following Eq. (2.49), as well as the dissipated energy given by Eq. (2.48).

In Fig. 3.25 we compare the normalised curvatures,  $|(\partial_x^2 + \partial_y^2)w_A(x, y)|/W_{\text{kin}}^{\text{max}}$ , of mode A and the fundamental mode of a  $327.2 \mu\text{m} \times 327.2 \mu\text{m}$  square membrane. The lateral dimensions of the membrane are chosen in order to match the fundamental frequency of the square resonator with the resonance frequency of mode A (the lattice constant of the crystal structure being  $a \approx \sqrt{3} \times 92.587 \mu\text{m}$ ). This comparison reveals the advantage of soft clamping over a rigid clamping condition of the membrane resonator: the curvature

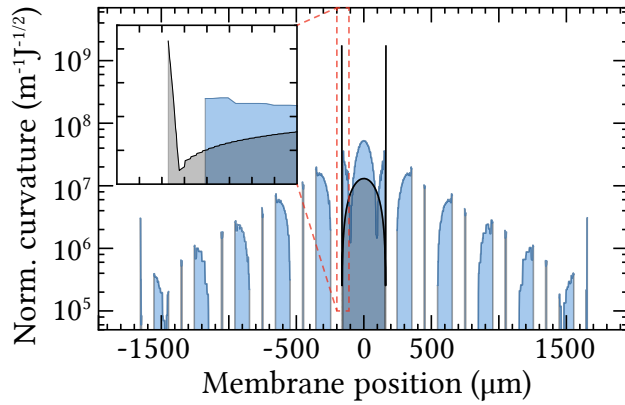


Figure 3.25: Normalised curvatures of the fundamental mode of a square membrane (grey) and a soft clamped resonator (blue). For the soft clamped resonator, the curvature is evaluated along the  $y$ -axis ( $x = 0$ , see Fig. 3.18). The dimensions of the square membrane resonators are chosen such that the eigenfrequencies of the vibrational modes for the two structures are the same. Figure is reproduced from [1] and [132].

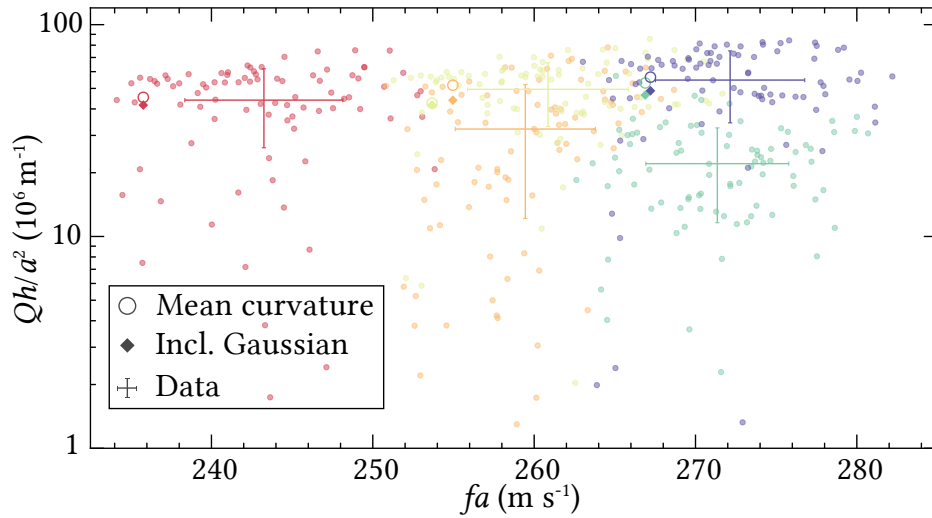


Figure 3.26: Compilation of measured mechanical quality factors for 85 soft clamped devices with thicknesses  $h = \{35 \text{ nm}, 66 \text{ nm}, 121 \text{ nm}\}$ . Here, the quality factors are normalised to  $a^2/h$ , following the observed scalings in Fig. 3.24. Simulated values for the  $Q$ -factors are plotted alongside the data, where empty circle indicates integration of the mean curvature only, while diamonds indicate integration including Gaussian curvature. Figure is adapted from [1] and [132].

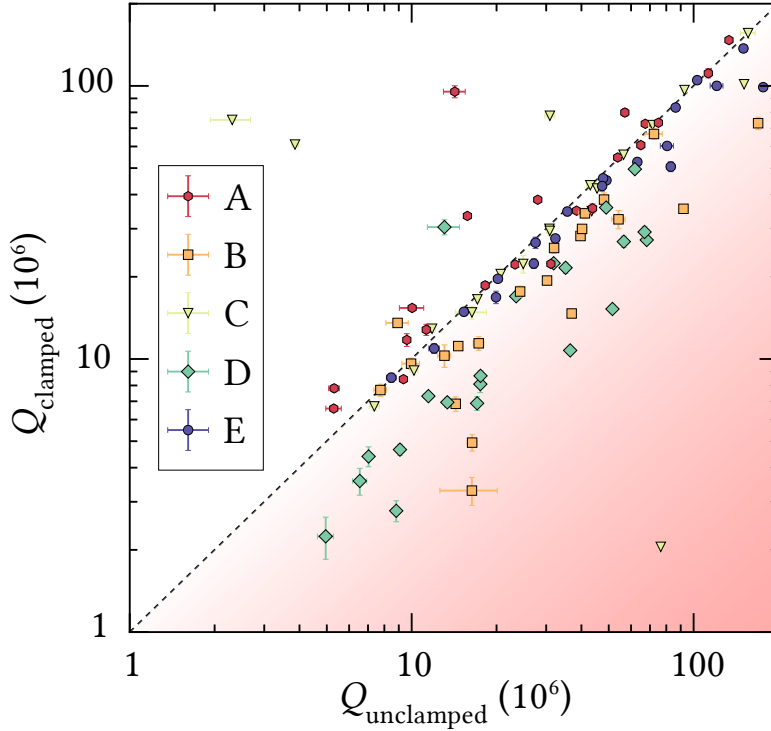


Figure 3.27: Comparison between mechanical quality factors under clamped or non-clamped conditions. The data consists of membranes with thicknesses  $h = \{35 \text{ nm}, 65 \text{ nm}\}$ . Strong deviation of datapoints from the diagonal like are indicative of residual phonon tunneling loss. As we can see, mode D shows systematically worse performance under clamped conditions.

in the clamping region is more than two orders of magnitude larger for the square membrane, compared to our perforated membrane resonator.

Assuming  $Q_{\text{int}}(h = 66 \text{ nm}) = 3750$  (cf. Section 2.2.4), we estimate the diluted quality factors for the five modes to be  $\{Q_A, Q_B, Q_C, Q_D, Q_E\} = \{20.72, 23.65, 19.44, 24.23, 25.80\} \times 10^6$ . Upon including the Gaussian curvature in our estimates of the dissipate elastic energy (cf. Eq. (2.47)), the resultant  $Q$ 's are  $\{\tilde{Q}_A, \tilde{Q}_B, \tilde{Q}_C, \tilde{Q}_D, \tilde{Q}_E\} = \{19.05, 20.08, 19.09, 21.24, 22.25\} \times 10^6$ . This suggests that the integrated mean-field curvature accounts for the majority of the elastic energy loss. Normalising these values according to the observed geometrical scaling, we now compare our simulations with normalised quality factors  $Q \times h/a^2$  for all measured devices with  $h = \{35, 66, 121\}$  nm. Data for 425 modes across 85 samples is presented in Fig. 3.26. Remarkably, the mean values of the measured quality factors are in quantitative agreement with simulations for the majority of localised modes.

Beyond a small ( $< 2\%$ ) discrepancy in the simulated resonance frequen-

cies, which we ascribe to small disagreements between the geometry and material parameters of the simulated and fabricated devices, we observe a significantly lower measured quality factor for mode D, as compared to the simulated values. A somewhat smaller, discrepancy is furthermore seen for mode B. In order to explain these observations, we perform complimentary measurements on a subset of samples, where the wafers with  $h = \{35, 66\}$  nm silicon nitride thickness are not clamped around the edges. Rather, the wafers are placed inside the vacuum chamber under their own gravitational weight. The motivation for such a series of measurements is to assess the role of phonon tunneling losses. Across 21 samples, we measure the quality factors without clamping,  $Q_{\text{unclamped}}$ , followed by measurements on the same samples with the wafer firmly clamped, yielding  $Q_{\text{clamped}}$ . As we can see in Fig. 3.27, the mechanical quality factors of mode D consistently degrade upon clamping. To a lesser extent we see a similar trend for mode B. This suggests that the discrepancies in the simulated and measured quality factors seen in Fig. 3.26 can be ascribed to residual radiation loss.

COMSOL simulations can further aid in explaining the discrepancy for mode D. Indeed, mode D has the largest amplitude at the silicon frame, as shown by in Fig. 3.28. We thus attribute the increased loss of this particular mode under clamped conditions, see Fig. 3.27, to be due to phonon tunneling.

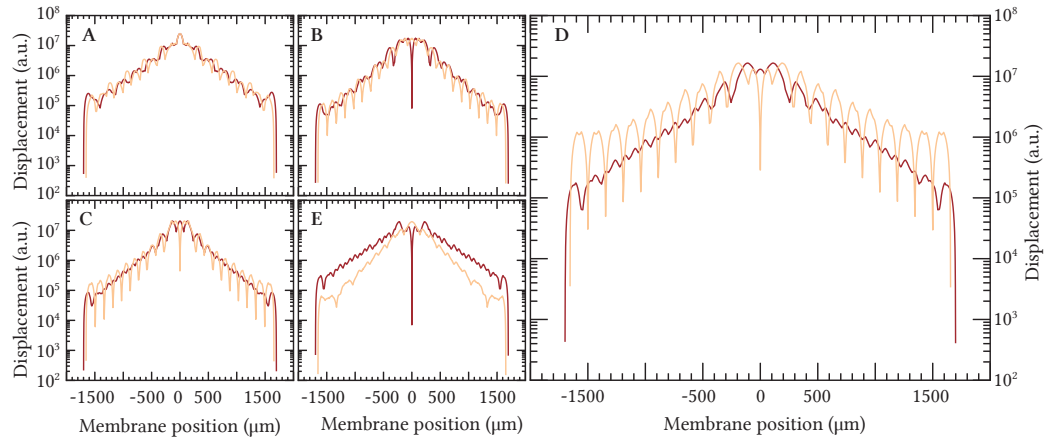


Figure 3.28: Projection of the simulated mechanical displacement onto the  $x$ - and  $y$ -axes, shown as the red and orange lines, respectively. The inset label letters indicate the defect mode illustrated in Fig. 3.18. The  $y$ -axis projection of mode D (far right) shows much larger displacement at the edge of the phononic structure than any other mode. This figure is reproduced from [1] and [132].

### 3.3 Soft clamped devices for cavity optomechanics

With the concept of soft clamping on solid theoretical and experimental footing, we now turn our attention to applications of soft clamped devices, specifically in relation to research projects in cavity optomechanics pursued by the groups of Albert Schliesser and Eugene S. Polzik at the Niels Bohr Institute. The following section will therefore touch upon three concrete examples of soft clamped devices, designed and optimised for, but certainly not limited to, specific experimental pursuits.

The specific geometry presented in the previous section (i.e. defect geometry and ratio of hole radii to lattice constant) will, for the sake of simplicity, be referred to as the *first generation* single-defect soft clamped membranes. While these devices are evidently capable of providing high mechanical quality factors, other factors need to be accounted for in the context of cavity optomechanics. First and foremost, in the context of cavity optomechanics, it is evident that the fundamental-like localised mode of our soft clamped membranes is the better choice among the five localised modes, despite the higher quality factors observed for mode E). This can be seen from the following consideration. Firstly, with the maximum amplitude of mode A being in the centre of the defect (cf. 3.21), the optical beam spot is far away from the perforated regions, which could lead to scattering of light and hence optical losses within our cavity. Second, the Gaussian-like mode profile of mode A will provide us with an appreciable mode-overlap with the optical Gaussian beam, leading to a larger optomechanical interaction strength. Combined with a lack of neighbouring localised vibrational modes, these considerations render mode A as the best choice for single-mode cavity optomechanics. Thus our focus henceforth will be on mode A.

However, one of the potential shortcomings of said mode can be found in the spectral composition of the first generation devices: specifically its proximity to the band edge (cf. Fig. 3.20). Anticipating a threefold increase in the mechanical quality factor upon cryogenic cooling to  $\sim 10$  K, the decoherence rate for the best performing device from the previous section (see Fig. 3.22 for mode A) is estimated to  $\Gamma_{\text{dec}} = n_{\text{th}}\Gamma_{\text{m}} \approx 2\pi \times 493$  Hz. As we will see in the next chapter, this roughly corresponds to the width of the mechanical resonance, as we optically cool the mechanical mode of interest to a mean occupancy of  $\bar{n} = 1$ . With the mean occupancy scaling inversely with the decoherence rate, the latter will in practice be on the order of several kilohertz for a resonance close to the motional ground state. Including the fact that sideband cooling in the unresolved sideband regime is accompa-

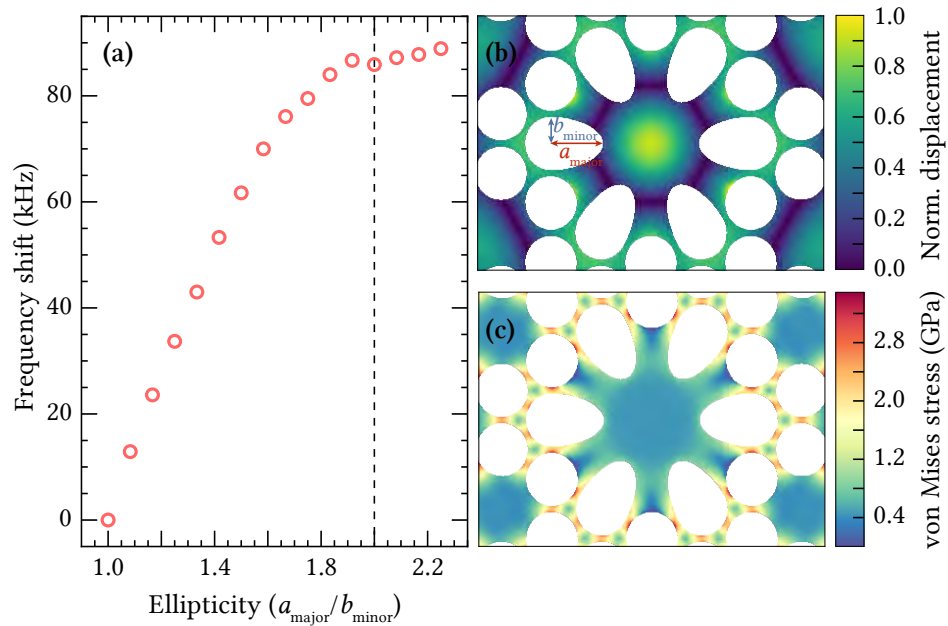


Figure 3.29: The holes around the defect are modified to be elliptical. Increased ellipticity a) increases the fundamental defect mode frequency, b) confines the mode further to the centre of the defect, and c) modifies the stress distribution, leading to regions of very low tensile stress.

nied by a spring-softening and hence reduction of the resonance frequency of the mode of interest, we see that the proximity of mode A to the lower band edge can potentially be problematic, as we seek to exploit the low mechanical loss of our soft clamped membranes in quantum optomechanical experiments. Therefore our first modification to the existing geometry will be in an attempt to increase the frequency separation between the fundamental-like mode and the lower band edge, while preserving the high mechanical quality factor.

### 3.3.1 Second generation – Further from the edge

Pushing the resonance frequency of the fundamental-like mode up can in principle be done in several ways – from modification of the holes in the existing defect geometry, or further perforation, to thinning of the membrane in the central region. While some require new fabrication steps (the last example being one), others are straightforward to implement. Here, two examples will be considered – one, which allows for wide tuneability, yet degrades the mechanical quality factor, and another, with moderate tuneability, yet improved mechanical performance.

The first approach we consider is one where holes surrounding the defect are modified. In order to increase the resonance frequency of the fundamental-like mode with respect to the band edge, the effective size of the defect has to be reduced. We do so by replacing a subset of circular holes within the defect with semi-elliptical holes. In Fig. 3.29 we consider a simulation of the frequency tuning as a function of ellipticity, here defined as the ratio of the semi-major and semi-minor axis,  $\epsilon = a_{\text{major}}/a_{\text{minor}}$ , alongside a simulation of the stress distribution within the defect and the displacement field of the fundamental-like mode for  $\epsilon = 2$ . For said ellipticity the simulated frequency shift is  $\sim 86$  kHz.

At a first glance, this geometry seems rather promising – the frequency shift is appreciable and the modeshape closely resembles that of mode A from the previous section. However, a close inspection of an actual device (see Fig. 3.30) of this type reveals a major issue: regions of the defect, close to the semi-elliptical holes, are seemingly sagging. As we take a closer look at our simulated stress distribution (cf. Fig. 3.29c), we find that in these regions the tensile stress is as low as 5 MPa. Combined with the fact that the fundamental-like mode has an appreciable displacement in these regions (cf. Fig. 3.29b), it is not surprising that the measured mechanical quality factors with these devices are on the order of a few millions.

It is worth considering why this particular geometry failed its purpose. Looking at the stress distribution within the defect in Fig. 3.29c, we realise that the elliptical holes effectively “shield” the region with stress relaxation from in-plane forces in the vertical and horizontal directions<sup>22</sup>. It is therefore important to ensure that the tensile stress “reaches” each and every corner and crevice of our structures.

With these observations at hand, we now consider a geometry which isn’t plagued by the issues described above. By introducing a set of holes with small radii  $r_{\text{minor}}$  within our defect, this can in fact be achieved. To avoid stress relaxation akin to the example above, these holes are strictly circular and placed at a distance  $R_{\text{minor}}$  from the center

$$R_{\text{minor}} = \frac{a}{\sqrt{3}} + r_{\text{major}} - r_{\text{minor}}, \quad (3.10)$$

where  $r_{\text{major}}$  ( $r_{\text{minor}}$ ) is the radius of the main (secondary) holes within the membrane structure. Similar to the first generation devices,  $r_{\text{major}} = 0.45 \times a/\sqrt{3}$ . This particular choice of  $R_{\text{minor}}$  ensures that the spacing between the

---

<sup>22</sup>It can be helpful to think of the stress distribution as a flow of a liquid in the negative of our devices (i.e. where holes are solid pillars, and regions with material are absent). The regions between the semi-elliptical holes (think, pillars) would experience low flow rates, while narrow regions would be exemplified by high flow rates.

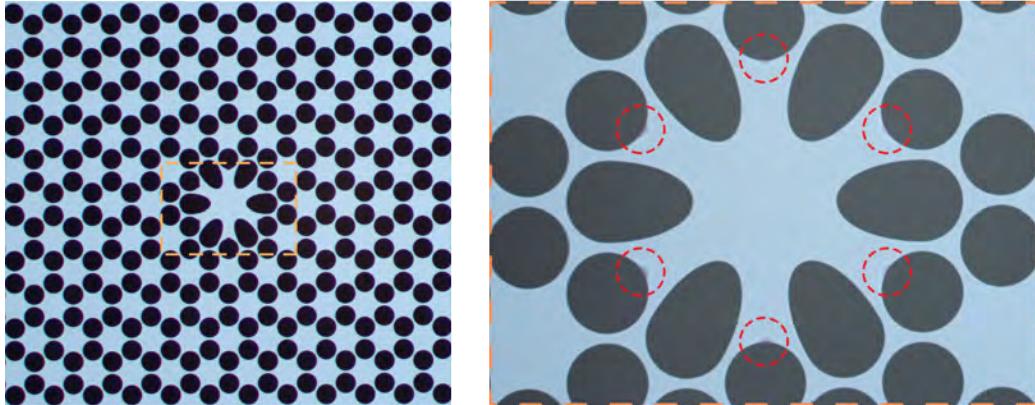


Figure 3.30: Optical image of a membrane where the holes around the defect have been modified to be elliptical. The dashed red circles mark regions of very low tensile stress, where the membrane is sagging. Figure is adapted from [1] and [132].

smaller holes and the existing holes in the defect is the same as the tether widths within the crystal structure (see inset in Fig. 3.31).

We now consider how the resonance frequency, effective mass, stored and dissipated elastic energies, and finally the mechanical quality factor, depend on the radius of the secondary holes. Fig. 3.31 shows the simulated values for said quantities, for a device with  $h = 20$  nm and lattice constant  $a \approx \sqrt{3} \times 109.053$   $\mu\text{m}$ . Since our primary focus is shifting the frequency of the fundamental-like mode away from the band edge, we first consider the resonance frequency of the mode as a function of  $r_{\text{minor}}$  (cf. Fig. 3.31, bottom). The largest frequency shift is predicted for  $r_{\text{minor}}/r_{\text{major}} = 0.55$ . Note that for the same lattice constant and pre-tension, a first generation device has a fundamental resonance frequency of  $\sim 1.195$  MHz. With a resonance frequency of  $\sim 1.224$  MHz for  $r_{\text{minor}}/r_{\text{major}} = 0.55$ , this amounts to a  $\sim 28.6$  kHz frequency difference. For this ratio of secondary to primary hole radii we calculate a  $\sim 33\%$  increase in the effective mass and  $\sim 5.5\%$  increase in the mechanical quality factor. While this isn't particularly favourable from a force sensing point of view, which scales with the ratio  $m_{\text{eff}}/Q_{\text{m}}$ , as we will see in the next chapter, the increase in the effective mass is not of significant importance in the context of cavity optomechanics.

### 3.3.2 Third generation – Opening a second bandgap

Looking back at the vibrational mode patterns of our soft clamped resonators, we see that only the fundamental-like mode has an anti-node at the centre of

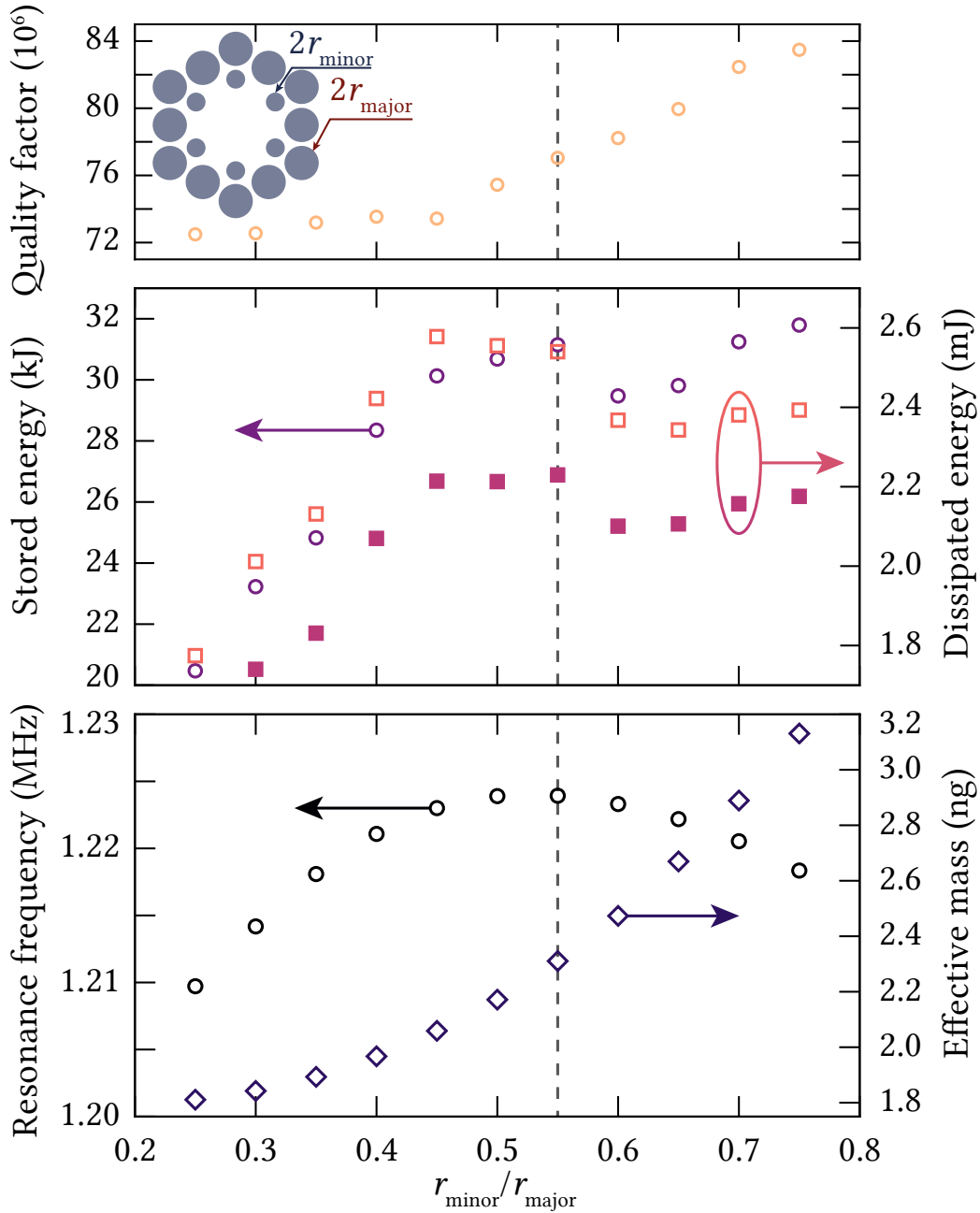


Figure 3.31: Simulations of second generation membrane resonators. We consider the various parameters of relevance, as a function of the relative size between the primary and secondary holes. The addition of secondary holes in the defect leads to a shift in the resonance frequency of the fundamental-like mode, this increasing the frequency separation between the mode and the band edge. Furthermore, we see an increase in the effective mass, as well as the  $Q$ -factor, for increasing values of  $r_{\text{minor}}/r_{\text{major}}$ . The dashed vertical line emphasises the geometry which leads to the largest frequency shift. We use the following parameters for these simulations:  $\sigma = 1.17$  GPa,  $a \approx \sqrt{3} \times 109.053 \mu\text{m}$ ,  $h = 20$  nm.

defect. This, among others, means that an optical probe placed in the centre of our structure will have little to no coupling to the other localised modes. However, having a soft clamped device where more than one localised mode couples strongly to an optical could be of interest for certain optomechanical experiments. One could, of course, displace the optical probe in the  $xy$ -plane, but this would result in a result coupling between the optical field and the fundamental-like mode, and potentially introduce optical losses associated with diffraction and/or absorption due to the holes in the membrane. Therefore, we wish to modify our existing membrane structure, in order to localise a second vibrational mode with a radial pattern. This, however, requires introducing a second bandgap at higher frequencies.

Looking back at Fig. 3.16, we make two observations. First, from a somewhat superficial point of view, we note that the band structure for the two band diagrams looks very similar. The lack of stress redistribution seemingly “stretches” the band diagram along the frequency axis. Second, for the band diagram of a unit cell with a uniform stress distribution we notice a small(er) bandgap at higher frequencies. Combining these two observations we realise that a second bandgap can potentially be opened up, if the average stress within the unit cell can be increased. This can in fact be achieved by decreasing the hole radii of the phononic crystal structure. In Fig. 3.32 we consider the evolution of the band structure, as we change the hole radii  $r = r_{\text{fac}} \times a/\sqrt{3}$ , where  $r_{\text{fac}}$  is varied from 45% (i.e.  $r_{\text{fac}} = 0.45$ ) to 37%. Alongside each band diagram we furthermore show the average von Mises stress in the unit cell, normalised to the initial (unrelaxed) stress. As we can see, the relative stress increases as we reduce the hole radii, and the second bandgap gradually opens up. However, for the smallest radii in Fig. 3.32 we see a substantial reduction in the size of the first bandgap. Hence, we choose  $r_{\text{fac}} = 0.41$  as our target for the hole radii.

The defect geometry for these structures is largely based on the insights from the second generation soft clamped devices. In fact, only a slight modification is needed in order to localise a second radial mode in the newly opened phononic bandgap. For  $r_{\text{minor}}/r_{\text{major}} = 0.45$ , we find that the second bandgap contains a radial mode. In Fig. 3.33 we show a raster measurement of the two radial localised modes, alongside a power spectral density obtained in our optomechanical cavity, which will be discussed in the next chapter.

In addition to the emergence of a second bandgap and a second radial mode, simulations suggest that with this new structure we should anticipate a rather favourable improvement in the mechanical quality factor of the first localised radial mode. Assuming  $h = 20$  nm,  $\sigma = 1.17$  GPa and  $a \approx \sqrt{3} \times 109.053$   $\mu\text{m}$ , we find that the third generation structures should provide a 46% improvement over the second generation devices. More specif-

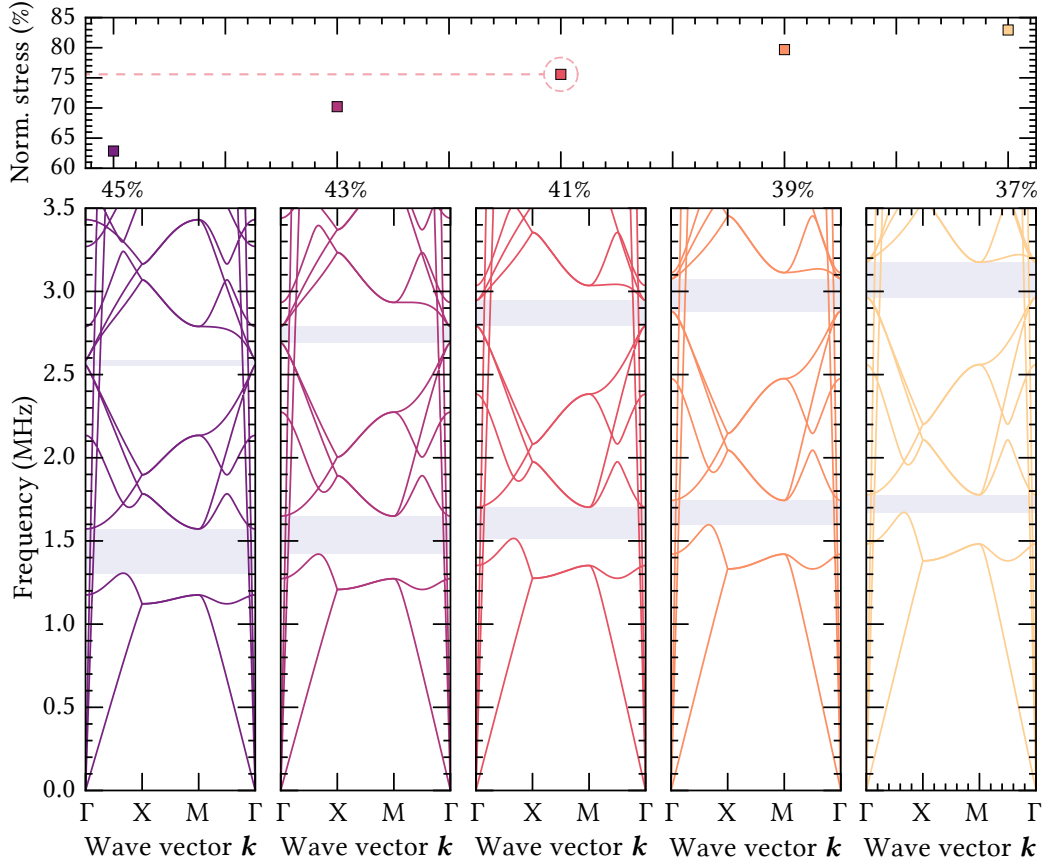


Figure 3.32: Evolution of band structure as a function of decreasing hole radii  $r = r_{\text{fac}} \times a/\sqrt{3}$ , where  $r_{\text{fac}}$  is shown as percentage, spanning from 45% to 37%. The shaded areas indicate the first and second quasi-bandgaps. The top figure shows the average von Mises stress normalised to the initial (unrelaxed) stress, which is  $\sigma = 1.25$  GPa.

ically, for the same choice of thickness, pre-tension and lattice constant, we simulate a mechanical quality factor of 71.21 M for the first generation devices, 76.82 M for the second generation devices and 111.86 M for the third generation. As we will see in the following chapter, at cryogenic temperatures third generation resonators can reach mechanical quality factors approaching 1.6 B at  $\sim 1.25$  MHz frequencies, amount to a  $Qf$ -product of  $1.99 \times 10^{15}$  Hz, which, to my knowledge, is the highest  $Qf$ -product for any silicon nitride mechanical resonator reported to date.

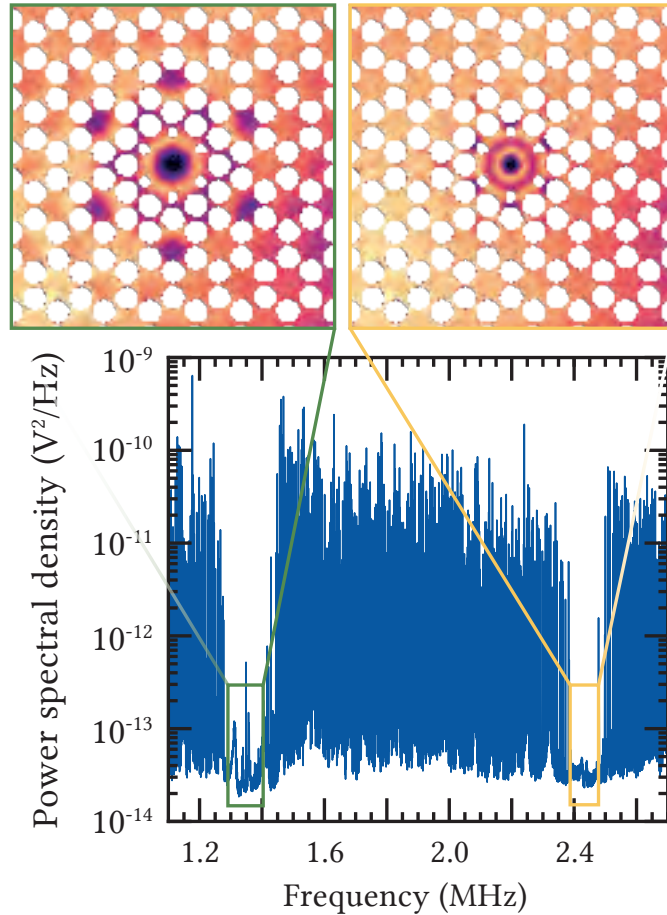


Figure 3.33: Raster measurement of a third generation soft clamped resonator, showing the vibrational patterns of the two radial modes. The power spectral density shows an overview of the broadband spectral response.

### 3.4 Summary and outlook

As we have seen in this chapter, the combination of phononic bandgap engineering and dissipation dilution can lead to significant improvements in mechanical resonator performance. Importantly, this combination not only leads to a reduction of radiative losses (i.e. phonon tunneling), as was the case for the silicon phononic crystal shielded resonators discussed in the first part of this chapter, but also of *internal* dissipation, associated with bending in the clamping regions of membrane resonators. The elimination of the hard clamp can be identified by the  $f^{-2}$  scaling of the mechanical quality factors, as well as the  $Q \propto h^{-1}$  thickness scaling, which is absent in regular membrane resonators. Furthermore, numerical simulations of the mechanical

quality factor, which involves integration of the mode curvature, were seen to be in excellent agreement with measurements.

Building on these findings, two new resonator geometries were presented towards the end (i.e. second and third generation soft clamped devices). With application in cavity optomechanics in mind, second generation resonators aim to increase the frequency separation between the band edge and the resonance frequency of the localised radial mode, while third generation resonators are found to be promising candidates for cavity optomechanics, not the least in light of the projected improvement in  $Q$  slightly shy of 50%. The following chapter aims to corroborate on this, as we study the performance of second and third generation soft clamped devices in the quantum regime.



# Chapter 4

## Cavity optomechanics with soft clamped resonators

Thus far our focus has been on the improvement of the mechanical performance of our membrane resonators. In doing so, we have reduced the coupling to the thermal bath, thus lowering the bar for overwhelming this (undesirable) coupling with one that we can tailor – namely the coupling to an optical bath. This chapter will describe our implementation of a cavity optomechanical system, which harnesses the hard-earned improvements in the mechanical domain.

We will first discuss the theoretical aspects of cavity optomechanics, and how the behaviour of a membrane-in-the-middle system is mapped onto the canonical description of an optomechanical system. Moving forward, the experimental details of our implementation will be discussed, including limitations due to classical noise sources. Strong ponderomotive squeezing, alongside ground-state cooling, is demonstrated in a multimode optomechanical system. Finally, we discuss improvements of our current optomechanical system in the context of heralded single phonon generation. A new method is developed in realising phononic crystal shielded mirrors, which could enable quantum optomechanical experiments in room temperature settings.

### 4.1 Basic considerations

In Fig. 4.1 the so-called *canonical optomechanical system* is depicted as a Fabry-Pérot with a harmonically suspended end-mirror. The optomechanical interaction is mediated by the radiation pressure force. The exerted force on the suspended mirror alters its motion, which, in turn, changes the resonance condition of the optical cavity and thus the intracavity photon number  $\langle \hat{n} \rangle$ ,

and ultimately the magnitude of the exerted force.

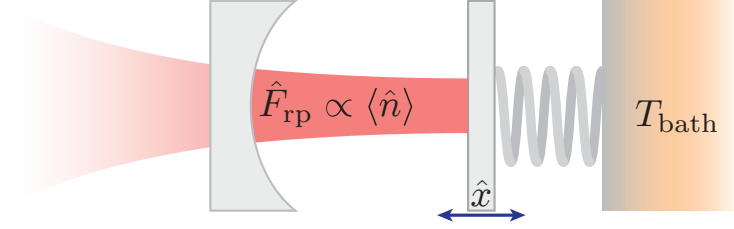


Figure 4.1: Sketch of a canonical optomechanical system, consisting of a Fabry-Pérot, where one of the end-mirrors harmonically suspended, depicted by a spring. The radiation pressure, which is proportional to the intracavity photon number  $\langle \hat{n} \rangle$ , exerts a force on the end-mirror, resulting in a change of the cavity resonance and thus a light-motion coupling.

Following this line of thought a bit further, we consider the effect of this coupling on the intracavity optical field  $\hat{a}$ . The harmonic motion of the suspended mirror modulates the intracavity field amplitude at a frequency  $\Omega_m$ , which, roughly speaking, can be written as  $a \propto \sin(\Omega_m t) \sin(\omega_L t)$ . Simple trigonometry tells us that the optical field will obtain components (i.e. *sidebands*) at frequencies  $\omega_L \pm \Omega_m$ . If the input optical field is off-resonant<sup>1</sup>, the sidebands will inevitably be imbalanced due to the non-flat spectral response of the cavity resonance. Placing our input field below the cavity resonance, will tilt this imbalance towards the sideband  $\omega_L + \Omega_m$ . The excess energy  $\hbar\Omega_m$  is in fact originating from the suspended mirror, and, as these photons eventually leak out of the cavity, they carry away this excess energy, thus reducing the stored elastic energy of the mirror. This rather handwaving description already describes one of the key features originating from the optomechanical coupling – namely the fact that the motion of a mechanical resonator, which interacts with a cavity field via the radiation pressure force, can be dampened by the presence of light.

The fact that the cavity resonance is shifted due to mirror displacement can also be seen as follows. The resonance condition of a Fabry-Pérot cavity is simply  $n\lambda/2 = L$ , where  $L$  is the cavity length and  $\lambda$  is the wavelength of light. Hence, the (angular) resonance frequencies of the cavity can be expressed as  $\omega_c = 2\pi nc/2L$ , where  $n$  is an integer. Allowing for small excursions in the overall cavity length,  $L \rightarrow L + x$ , the resonance frequency to

<sup>1</sup>Here, we assume that the mechanical frequency is comparable to the spectral width of the optical cavity resonance.

first order in  $x$  can be expressed as

$$\omega_c = \omega_{c,0} + x \underbrace{\left. \frac{d\omega_c}{dx} \right|_{x=0}}_G, \quad (4.1)$$

where  $\omega_{c,0}$  is the equilibrium resonance frequency (i.e.  $x = 0$ ). The quantity  $G \equiv d\omega_c/dx$  signifies the optical frequency shift per displacement.

Moving towards a Hamiltonian description of our system, we recall that quantisation of the optical field yields the following Hamiltonian describing the energy [136]

$$\hat{H} = \hbar\omega_c \left( \underbrace{\hat{a}^\dagger \hat{a}}_{\hat{n}} + \frac{1}{2} \right), \quad (4.2)$$

where  $\hat{a}$  ( $\hat{a}^\dagger$ ) is the optical annihilation (creation) operator, and  $\hat{n} = \hat{a}^\dagger \hat{a}$  is the so-called number operator, the expectation value of which quantifies the average number of intracavity photons,  $\bar{n}_{\text{cav}}$ . Assuming quantisation of the mirror motion (i.e.  $x \rightarrow \hat{x}$ ), and using the expression for the cavity resonance shift from Eq. (4.1), we find that

$$\hat{H} = \hbar(\omega_{c,0} + G\hat{x}) \left( \hat{a}^\dagger \hat{a} + \frac{1}{2} \right), \quad (4.3)$$

$$\hat{H} = \hbar\omega_c \hat{a}^\dagger \hat{a} + \hbar G \hat{x} \hat{a}^\dagger \hat{a}, \quad (4.4)$$

where, in the last line, we have neglected the contribution due to zero-point energy and replaced  $\omega_{c,0}$  with  $\omega_c$  to simplify the notation. While the first part is the bare Hamiltonian of the optical field, the second term describes the optomechanical interaction. It thus follows that the radiation pressure force is simply

$$\hat{F}_{\text{rp}} = -\frac{\partial \hat{H}}{\partial \hat{x}} = -\hbar G \hat{a}^\dagger \hat{a}. \quad (4.5)$$

Unsurprisingly the magnitude of the radiation pressure force depends on the photon population inside the optical cavity. Simply put, one of the main objectives in (quantum) optomechanics is to realise a system where the interaction due to the radiation pressure force outweighs the thermal Langevin force.

Before moving to a more general description of the optomechanical interaction, let us review some of the key characteristics of a simple Fabry-Pérot

cavity. Here, we consider an optical cavity, consisting of two mirrors (see Fig. 4.2). Often we will refer to the two available points of entry for light into the cavity as *ports*. As we shall see later in this chapter, in our experimental setup the cavities are driven from one port, while the second is used for detection purposes. The cavity mirrors are associated by a set of complex quantities, namely the amplitude transmissivities  $t_i$  and reflectivities  $r_i$ . The cavity length<sup>2</sup>  $L$  defines the round-trip time of photons within our optical resonator,  $\tau = 2L/c$ , where  $c$  is the speed of light. The inverse of the round trip time is the so-called *free-spectral range* (FSR) and quantifies the frequency spacing of cavity resonances

$$\text{FSR} = \frac{c}{2L}. \quad (4.6)$$

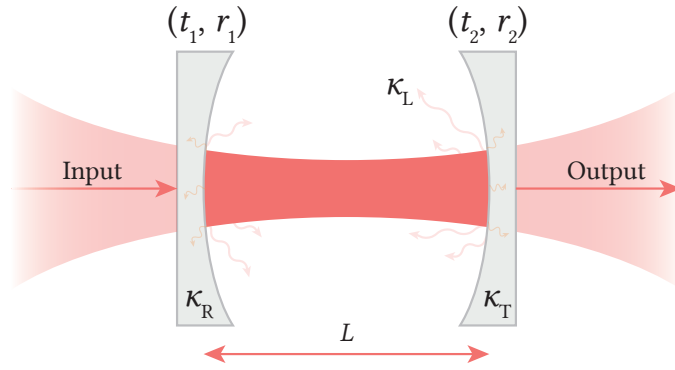


Figure 4.2: Sketch of an optical cavity probed in transmission, with the relevant quantities defined. The rates of  $\kappa_{R,T}$  signify the rate of loss via the two ports of the cavity, while  $\kappa_L$  is the rate of loss. The subscript “R” is short for reflective (port), whilst the subscript “T” is short for transmissive (port).

The round-trip time can furthermore be thought of as an attempt-rate of the individual photons at escaping the optical cavity through either of the mirrors. We therefore define transmission rates through both ports as follows

$$\kappa_R = \frac{|t_1|^2}{\tau}, \quad \kappa_T = \frac{|t_2|^2}{\tau}. \quad (4.7)$$

<sup>2</sup>More specifically, the optical path length, defined as  $\text{OPL} \equiv nL$ , where  $n$  is the refractive index of the medium occupying the space between the two mirrors. However, since our experiments are performed in vacuum, the optical path length equals the physical length of the optical resonator.

The total optical loss rate is thus  $\kappa = \kappa_R + \kappa_T + \kappa_L$ , where the last term accounts for losses through experimentally inaccessible ports (e.g. scattering and absorption). Anticipating a mechanical resonator being embedded inside such an optical cavity, it is important to consider through which port the light preferentially exits through – after all, the light that escapes the confines of our optical cavity carries valuable information about the state of our mechanical resonator. Thus, in our experiments the input mirror is highly reflective (hence the subscript  $R$  in  $\kappa_R$ , see Fig. 4.2), while the output mirror has a significantly lower reflectivity. In quantifying the fraction of light escaping the optical cavity through a desirable port we define the *cavity outcoupling efficiency*

$$\eta_c = \frac{\kappa_T}{\kappa}. \quad (4.8)$$

Finally, combining the expression for FSR with the (total) cavity decay rate  $\kappa$ , yield a unitless quantity known as *finesse*

$$\mathcal{F} = 2\pi \frac{\text{FSR}}{\kappa} = \frac{2\pi}{\mathcal{L}}, \quad (4.9)$$

where  $\mathcal{L}$  denotes the total losses within the cavity (scattering, absorption and transmission).

With this, we move to a rigorous description of the optomechanical interaction.

## 4.2 Hamiltonian description

Our starting point is the Hamiltonian formulation of the canonical optomechanical system, as provided by Law [137]

$$\hat{H} = \hat{H}_{\text{opt}} + \hat{H}_{\text{mech}} + \hat{H}_{\text{int}} + \hat{H}_{\text{drive}}, \quad (4.10)$$

$$\hat{H}_{\text{opt}} = \hbar\omega_c \left( \hat{a}^\dagger \hat{a} + \frac{1}{2} \right), \quad (4.11)$$

$$\hat{H}_{\text{mech}} = \frac{\hat{p}^2}{2m_{\text{eff}}} + \frac{1}{2}m_{\text{eff}}\Omega_m^2 \hat{x}^2, \quad (4.12)$$

$$\hat{H}_{\text{int}} = \hbar G \hat{x} \hat{a}^\dagger \hat{a}, \quad (4.13)$$

$$\hat{H}_{\text{drive}} = i\hbar\sqrt{\kappa_R} \left( \bar{s}_{\text{in}} \hat{a}^\dagger e^{-i\omega_L t} - \bar{s}_{\text{in}}^* \hat{a} e^{i\omega_L t} \right), \quad (4.14)$$

where  $\omega_c$  is the cavity resonance frequency,  $\hat{x}$  and  $\hat{p}$  are the mechanical position and momentum operators,  $G = d\omega_c/d\hat{x}$  quantifies the optical resonance

frequency shift per displacement, and  $\bar{s}_{\text{in}} = P_{\text{in}}/\hbar\omega_L$  is the normalised amplitude of the drive field. To recognise the interaction term from Eq. (4.4). This Hamiltonian description assumes that the scattering of photons from the cavity mode associated with  $\omega_c$  into other optical modes is negligible, which holds in the case of  $\Omega_m \ll \text{FSR}$ . This indeed holds in our system, where  $\Omega_m \sim 2\pi \times 1 \text{ MHz}$ , while the free-spectral range is on the order of 100 GHz.

The “dimensionfull” and dimensionless mechanical position and momentum operators are defined as

$$\hat{x} = x_{\text{zpf}}(\hat{b}^\dagger + \hat{b}), \quad \hat{p} = ip_{\text{zpf}}(\hat{b}^\dagger - \hat{b}), \quad (4.15)$$

$$\hat{Q} := \frac{1}{\sqrt{2}}(\hat{b}^\dagger + \hat{b}), \quad \hat{P} := \frac{i}{\sqrt{2}}(\hat{b}^\dagger - \hat{b}), \quad (4.16)$$

where  $\hat{b}^\dagger$  ( $\hat{b}$ ) is the phononic creation (annihilation) operator, and the zero-point motion and zero-point momentum of the mechanical oscillator are defined as

$$x_{\text{zpf}} = \sqrt{\frac{\hbar}{2m_{\text{eff}}\Omega_m}}, \quad p_{\text{zpf}} = \sqrt{\frac{\hbar m_{\text{eff}}\Omega_m}{2}}. \quad (4.17)$$

It is commonplace to define the cavity frequency shift in terms of the zero-point motion of the mirror

$$g_0 := Gx_{\text{zpf}}. \quad (4.18)$$

This is the so-called *single-photon optomechanical coupling rate* and is a key parameter in quantifying the strength of the optomechanical interaction. The exact form of this coupling rate for our membrane-in-the-middle system will be discussed later in this chapter.

Regrettably, the single-photon coupling rate is usually small compared to other rates in the optomechanical cavity (particularly the decoherence rate,  $n_{\text{th}}\Gamma_m$ , and the cavity decay rate,  $\kappa$ ). Hence the vast majority of optomechanical experiments operate in a regime of strong laser driving. Here, the interaction Hamiltonian can be linearised by expressing the cavity field in terms of a constant amplitude,  $\bar{a}$ , alongside small fluctuations

$$\hat{a}(t) = \bar{a} + \delta\hat{a}(t). \quad (4.19)$$

Here,  $\bar{a}$  is the mean field, and it holds that  $\langle\hat{a}\rangle = \bar{a}$ . The linearised interaction Hamiltonian, in terms of the dimensionless position operator, can thus be

expressed as follows

$$\hat{H}_{\text{int}}^{\text{lin}} = \hbar g_0 \hat{Q}(\bar{a} + \delta\hat{a})^\dagger(\bar{a} + \delta\hat{a}) \quad (4.20)$$

$$= \hbar g_0 \hat{Q}(|\bar{a}|^2 + \bar{a}^* \delta\hat{a} + \bar{a} \delta\hat{a}^\dagger + \delta\hat{a} \delta\hat{a}^\dagger). \quad (4.21)$$

The first term is in essence a static force on the mechanical resonator, which simply shifts its equilibrium position such that  $\hat{x} \rightarrow \hat{x} - \hbar G \bar{a}^2 / m_{\text{eff}} \Omega_{\text{m}}^2$ , while the last term is neglected since the optical fluctuations are assumed to be small to first order. Finally, without loss of generality, we assume that  $\bar{a} = \bar{a}^*$ , allowing us to express the linearised interaction Hamiltonian

$$\hat{H}_{\text{int}}^{\text{lin}} = \hbar g_0 \hat{Q} \bar{a} (\delta\hat{a} + \delta\hat{a}^\dagger). \quad (4.22)$$

As an aside, with the definition of the cavity field in Eq. (4.19), we see that  $\bar{n}_{\text{cav}} = \langle \hat{a}^\dagger \hat{a} \rangle = |\bar{a}|^2$ . Inspired by Eq. (4.22), we define the *light enhanced optomechanical coupling* rate as

$$g := |\bar{a}| g_0 = \sqrt{\bar{n}_{\text{cav}}} g_0 \quad (4.23)$$

Before deriving the equations of motion for light and mechanics, we make a final simplification to our optomechanical Hamiltonian. The operators for the optical and mechanical fields in Eq. (4.10) are in fact time dependent, where the former evolves at optical frequencies, i.e.  $\delta\hat{a} \propto e^{i\omega_c t}$ . Seeing that we are interested in the fluctuations of light at the mechanical frequency, it is reasonable to transform the Hamiltonian to a reference frame rotating at the laser frequency, where the relevant frequency is now the detuning between the cavity resonance frequency and the drive frequency,  $\Delta = \omega_L - \omega_c$ . This is done by the unitary transformation [136]

$$\tilde{H} = \hat{U}^\dagger \hat{H} \hat{U} + i\hbar \frac{d\hat{U}^\dagger}{dt} \hat{U}, \quad (4.24)$$

where the operator  $\hat{U}$  is defined as follows

$$\hat{U} = e^{-i\hat{H}_0 t/\hbar}, \quad \text{with } \hat{H}_0 = \hbar\omega_L \hat{a}^\dagger \hat{a}. \quad (4.25)$$

Using the Hadamard lemma<sup>3</sup> the linearised Hamiltonian in the rotating frame can be expressed as

$$\begin{aligned} \tilde{H}_{\text{lin}} = & -\hbar \bar{\Delta} \delta\hat{a} \delta\hat{a}^\dagger + \hbar \Omega_{\text{m}} \hat{b}^\dagger \hat{b} + \hbar g (\delta\hat{a}^\dagger + \delta\hat{a}) (\hat{b}^\dagger + \hat{b}) \\ & + i\hbar \sqrt{\kappa_{\text{R}}} (\bar{s}_{\text{in}} \delta\hat{a}^\dagger - \bar{s}_{\text{in}}^* \delta\hat{a}), \end{aligned} \quad (4.26)$$

<sup>3</sup>For two operators,  $\hat{A}$  and  $\hat{B}$ , the Hadamard lemma can be written as follows [138]:

$$e^{\hat{A}} \hat{B} e^{-\hat{A}} = \hat{B} + [\hat{A}, \hat{B}] + \frac{1}{2!} [\hat{A}, [\hat{A}, \hat{B}]] + \frac{1}{3!} [\hat{A}, [\hat{A}, [\hat{A}, \hat{B}]]] + \dots$$

where the detuning and the mechanical displacement have been redefined as follows

$$\hat{x} \rightarrow \hat{x} - \bar{x} = \hat{x} - \frac{\hbar G \bar{a}^2}{m_{\text{eff}} \Omega_m^2} \quad (4.27)$$

$$\bar{\Delta} = \Delta + G \bar{x} = \Delta + \frac{\hbar G^2 \bar{a}^2}{m_{\text{eff}} \Omega_m^2}. \quad (4.28)$$

We have furthermore discarded terms that do not depend on  $\delta \hat{a}$  or  $\hat{b}$ , since these do not alter the dynamics of the optomechanical system.

Finally, it is instructive to consider temporal dependence of the interaction Hamiltonian. Following Eq. (4.26) the interaction part of the linearised Hamiltonian can be expressed as

$$\tilde{H}_{\text{int}}^{\text{lin}} \propto \delta \hat{a}^\dagger \hat{b}^\dagger e^{i(\bar{\Delta} - \Omega_m)t} + \delta \hat{a} \hat{b} e^{-i(\bar{\Delta} - \Omega_m)t} + \delta \hat{a}^\dagger \hat{b} e^{i(\bar{\Delta} + \Omega_m)t} + \delta \hat{a} \hat{b}^\dagger e^{-i(\bar{\Delta} + \Omega_m)t}. \quad (4.29)$$

The first two terms describe a two-mode squeezing interaction [136], while the last two terms are equivalent to a beam-splitter (“swap”) interaction. Importantly, we can control which of the two processes is more pronounced, simply by changing the detuning. For instance, assuming a blue-detuned laser  $\bar{\Delta} = +\Omega_m$  we see that the first two terms in Eq. (4.29) are time-independent, while the beam-splitter terms are oscillating at a frequency of  $\pm 2\Omega_m$ . Within the rotating frame approximation, rapidly oscillating terms average out to zero. Hence, assuming  $2\Omega_m \gg \kappa$  (i.e. resolved sideband regime), this choice of detuning renders the beam-splitter interaction negligible. Conversely, for  $\bar{\Delta} = -\Omega_m$ , the beam-splitter interaction becomes the dominant one. Viewing each of the terms above as a Raman process (i.e. inelastic scattering of photons), we consider two examples of particular relevance for this work. Within the beam-splitter interaction, we first consider the scenario where  $\Omega_m \gg \kappa$ . Operating at a detuning of  $\bar{\Delta} = -\Omega_m$ , the scattering process  $\delta \hat{a} \hat{b}^\dagger$ , which annihilates a pump photon and creates a phonon excitation, is off-resonant. The resonant process,  $\delta \hat{a}^\dagger \hat{b}$ , leads to creation of photons with higher energy, at the expense of removing energy from the mechanical resonator. This scattering process is represented as a Feynman diagram in Fig. 4.3a and corresponds to laser cooling of mechanical motion.

If we instead consider operation in a regime where  $\Omega_m$  is comparable to the cavity linewidth  $\kappa$ , both processes  $-\delta \hat{a} \hat{b}^\dagger$  and  $\delta \hat{a}^\dagger \hat{b}$  will inevitably take place. A representative scattering process in this regime is shown in Fig. 4.3b, where a phonon excitation recombines with a pump photon,  $\omega_L$ , to create a blue-detuned photon. In fact, the two output photons in Fig. 4.3b

are entangled and, as we will see later in this chapter, manifests itself as *ponderomotive squeezing* upon detection [139]. Importantly, this combined process only plays a significant role if the red sideband photon,  $\omega_L - \Omega_m$ , as well as the mechanical excitation, do not decay between the first and second scattering processes. One could say that this requirement is in fact embedded in the definition of the *quantum cooperativity*, which, broadly speaking, describes the ratio of good (i.e. coherent scattering) and bad (i.e. optical and mechanical losses) processes

$$C_q := \frac{4g^2}{(\bar{n}_{\text{th}} + \frac{1}{2})\Gamma_m\kappa}, \quad (4.30)$$

where  $\bar{n}_{\text{th}}$  describes the mean phonon occupancy of the thermal bath, described by the Boltzmann distribution

$$\bar{n}_{\text{th}} = \frac{1}{e^{\hbar\Omega_m/k_B T_{\text{bath}}} - 1} \approx \begin{cases} k_B T_{\text{bath}}/\hbar\Omega_m, & (k_B T_{\text{bath}} \gg \hbar\Omega_m) \\ e^{-\hbar\Omega_m/k_B T_{\text{bath}}}, & (k_B T_{\text{bath}} \ll \hbar\Omega_m) \end{cases} \quad (4.31)$$

where  $T_{\text{bath}}$  is the bath temperature. Since our experiments are typically performed at  $\Omega_m \sim 2\pi \times 1$  MHz and  $T_{\text{bath}} \sim 10$  K, it holds for the exponent in that  $\hbar\Omega_m \ll k_B T_{\text{bath}}$ , which allows us to use the approximation  $\bar{n}_{\text{th}} \approx k_B T_{\text{bath}}/\hbar\Omega_m$  to estimate the bath occupancy. For said parameters the mean bath occupancy is therefore  $\bar{n}_{\text{th}} \approx 210 \times 10^3$ . As such, we tend to ignore the additional half thermal quanta in the denominator of Eq. (4.30). As we will see later in this chapter, the quantum cooperativity is a quantity frequently emerging in equations quantifying “quantumness” in optomechanical experiments, with the (soft) threshold being at  $C_q \geq 1$ .

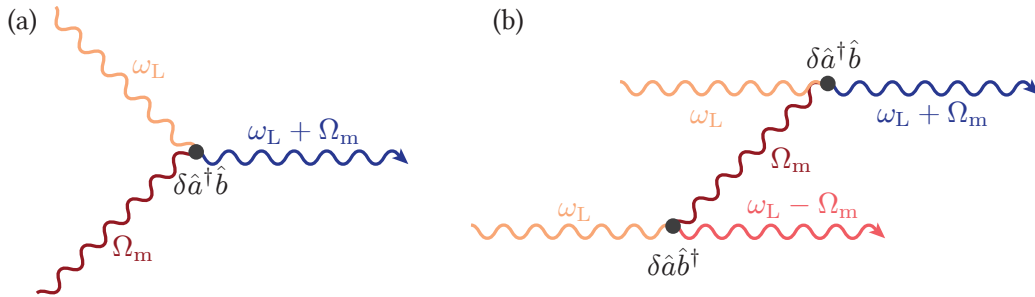


Figure 4.3: Feynman diagram of optomechanical scattering processes involving a phonon (red) of frequency  $\Omega_m$  and a photons from a pump field (yellow) of frequency  $\omega_L$ . (a) Beam-splitter interaction. (b) Two-mode squeezing optomechanical interaction.

### 4.2.1 Heisenberg-Langevin equations

From classical mechanics we are familiar with the Hamiltonian equations, which provide us with the equations of motion for the generalised position and momentum. Dissipation is often times included in an ad-hoc fashion, by adding a velocity dependent damping term. In the quantum domain, the unitary time evolution of an operator can be described via Heisenberg's equation [140], which reads  $d\hat{A}/dt = i [\hat{H}, \hat{A}] / \hbar + \partial\hat{A}/\partial t$ . However, adapting the naïve approach from classical mechanics by adding a damping term proportional to velocity leads to inconsistencies, such as commutation relations decaying in time.

Fortunately, dissipation can be adequately accounted for within the Heisenberg-Langevin framework, where the system under investigation is coupled to a large ensemble of harmonic oscillators (often referred to as a *heat bath* or *reservoir*). Given the size of the reservoir, the system has a negligible effect on the bath dynamics, while the system dynamics is indeed affected by the presence of the bath. Energy dissipated from the system is captured by this system-bath coupling. Furthermore, as a result of the fluctuation-dissipation theorem, the coupling to this bath results in a fluctuating force acting on the system operators. These so-called “noise terms” ultimately ensure that the commutation relations are conserved. In-depth discussions of the quantum Langevin framework can be found in [138, 141, 142].

Within the first Markov approximation, assuming a memory-less reservoir (or, equivalently, a frequency-independent system-bath coupling), and the rotating wave approximation, the Heisenberg-Langevin equation for an arbitrary system operator  $\hat{O}$  can be expressed as follows [138, 142]

$$\frac{d\hat{O}}{dt} = \frac{1}{i\hbar} [\hat{O}, \hat{H}_{\text{sys}}] - [\hat{O}, \hat{S}^\dagger] \left( \frac{\gamma}{2} \hat{S} + \hat{f} \right) + [\hat{O}, \hat{S}] \left( \frac{\gamma}{2} \hat{S}^\dagger + \hat{f}^\dagger \right), \quad (4.32)$$

where  $\hat{H}_{\text{sys}}$  is the system Hamiltonian,  $\hat{S}$  is the system operator that couples to the heat bath, and  $\hat{f}$  is the forcing term (i.e. the noise term) acting on the system, as a result of the system-reservoir coupling. However, typically the forcing term is expressed in terms of an input noise operator.

Using the Hamiltonian given by Eq. (4.10), in conjunction with a transformation to the rotating frame of the laser drive (cf. Eq. (4.24)), we arrive

at the following set of quantum Langevin equations

$$\dot{\hat{a}} = \left( i\Delta - \frac{\kappa}{2} - iG\hat{x} \right) \hat{a} + \sqrt{\kappa_R} \bar{s}_{\text{in}} + \sqrt{\kappa} \hat{a}_{\text{in}}, \quad (4.33)$$

$$\dot{\hat{x}} = \frac{\hat{p}}{m_{\text{eff}}}, \quad (4.34)$$

$$\dot{\hat{p}} = -m_{\text{eff}}\Omega_m^2 \hat{x} - \hbar G \hat{a}^\dagger \hat{a} - \Gamma_m \hat{p} + \hat{F}_{\text{th}}, \quad (4.35)$$

where  $\hat{a}_{\text{in}}$  is the light input noise operator and  $\hat{F}_{\text{th}}$  is the thermal force operator (i.e. the forcing term). The light input noise operator fulfils the following commutation and correlation relations

$$[\hat{a}_{\text{in}}(t), \hat{a}_{\text{in}}^\dagger(t')] = \delta(t - t'), \quad (4.36)$$

$$\langle \hat{a}_{\text{in}}(t) \hat{a}_{\text{in}}^\dagger(t') \rangle = (\bar{n} + 1) \delta(t - t'), \quad (4.37)$$

$$\langle \hat{a}_{\text{in}}^\dagger(t) \hat{a}_{\text{in}}(t') \rangle = \bar{n} \delta(t - t'), \quad (4.38)$$

where  $\delta(\tau)$  is the Dirac delta function, and  $\bar{n}$  is the mean thermal occupation of the optical field, described by the Boltzmann distribution (see Eq. (4.31)).

At room temperature an optical field at a wavelength of 852 nm has a mean thermal occupation of  $\bar{n} \approx 3.6 \times 10^{-25}$ . Thus, the correlations for an optical field can be simplified to  $\langle \hat{a}_{\text{in}}(t), \hat{a}_{\text{in}}^\dagger(t') \rangle = \delta(t - t')$  and  $\langle \hat{a}_{\text{in}}^\dagger(t), \hat{a}_{\text{in}}(t') \rangle = 0$ .

As for the thermal force operator, its (symmetrised) autocorrelation function is given by [143]

$$\frac{1}{2} \langle \hat{F}(t) \hat{F}(t') + \hat{F}(t') \hat{F}(t) \rangle = m_{\text{eff}} \Gamma_m k_B T \frac{d}{dt} \coth \left( \frac{\pi k_B T}{\hbar} (t - t') \right). \quad (4.39)$$

Noting that  $\partial_x \coth x = -1/\sinh^2 x$ , it is evident that the correlation function is rapidly decaying for time scales larger than  $\tau = \hbar/k_B T$ . In our case the time scale we need to compare this to is the mechanical decay time. Seeing that we can realise mechanical resonators with quality factors in excess of  $10^8$  in room temperature settings, the decay time  $\Omega_m/Q_m \sim 16$  s is significantly longer than  $\hbar/k_B T \approx 2.5 \times 10^{-14}$  s. Thus we can safely assume a memoryless thermal bath, resulting in a simplified correlation function

$$\frac{1}{2} \langle \hat{F}(t) \hat{F}(t') + \hat{F}(t') \hat{F}(t) \rangle = 2m_{\text{eff}} \Gamma_m k_B T \delta(t - t'). \quad (4.40)$$

Ultimately we are interested in studying the fluctuations of the optical field leaving the cavity. Within the quantum Langevin formalism the output field can be described in terms of the vacuum input field to that port  $\hat{a}_{\text{in}}$ , as well as the intracavity field emerging from the port as

$$\hat{a}_{\text{out}} = \hat{a}_{\text{in}} - \sqrt{\eta_c \kappa} \hat{a}, \quad (4.41)$$

where we have included the outcoupling efficiency as defined in Eq. (4.8). Detection inefficiencies,  $\eta_{\text{det}}$ , can be described by an additional beamsplitter placed at the output of the cavity. The two inputs of this hypothetical beamsplitter are the vacuum fluctuations and the field exiting the cavity,  $\hat{a}_{\text{out}}$ . The modified output field can thus be described as follows

$$\hat{a}_{\text{out}} = \sqrt{\eta_{\text{det}}} (\hat{a}_{\text{in}} - \sqrt{\eta_c \kappa} \hat{a}) + \sqrt{1 - \eta_{\text{det}}} \hat{a}_{\text{vac}}, \quad (4.42)$$

where  $\hat{a}_{\text{vac}}$  obeys a similar set of commutation and correlation relations as Eqs. (4.36-4.37). With the quantum Langevin equations of motion, as well as the input-output relation, we are in a position of describing some of the most important optomechanical effects relevant for this work.

### 4.3 Static optomechanical effects

Using the quantum Langevin formalism introduced above, we will now consider the only static optomechanical effect, which is of experimental relevance for this work, namely *static optical bistability*. As we saw in section 4.2, a consequence of the radiation pressure interaction is a shift in the equilibrium position of the suspended mirror. It is therefore conceivable that multiple stable points emerge, as we increase in amount of intracavity optical power. Indeed, this was one of the first radiation pressure effects to be observed by Dorsel and colleagues [144], in a system truly resembling the canonical optomechanical system – a Fabry-Pérot cavity, where one of the end-mirrors was suspended by two tungsten wires.

Our interest in this effect is mainly due to the limitations it imposes on the highest achievable value for quantum cooperativity. Starting with the equations of motion given by Eqs. (4.33-4.35), we consider the steady state solutions for the intracavity and displacement fields in a mean-field approximation (i.e.  $\langle \hat{a}_{\text{in}} \rangle = \langle \hat{F}_{\text{th}} \rangle = 0$ ,  $\langle \hat{a} \rangle = \bar{a}$  and  $\langle \hat{x} \rangle = \bar{x}$ )

$$\bar{a} = \frac{\sqrt{\kappa_{\text{R}}} \bar{s}_{\text{in}}}{-i(\Delta - G\bar{x}) + \kappa/2} \quad (4.43)$$

$$\bar{x} = -\frac{\hbar G}{m_{\text{eff}} \Omega_{\text{m}}^2} |\bar{a}|^2. \quad (4.44)$$

Inserting the expression for the static displacement into the intracavity field results in a third-order polynomial. Thus, for a sufficiently large intracavity field more than one stable solutions emerge. This can be illustrated by plotting the absolute square of the intracavity field as a function of the static displacement,  $\hat{x}$ . Evidently, Eq. (4.43) represents a Lorentzian, while Eq.

(4.44) is a line with slope  $-m_{\text{eff}}\Omega_m^2/\hbar G$ . When this slope exceeds the largest slope of  $|\bar{a}|^2$  given by Eq. (4.43), the optomechanical system enters a bistable regime.

Using Eq. (4.43) it can be shown that the largest slope for Lorentzian is at a detuning  $\bar{\Delta}_{\text{onset}} = \pm\kappa/2\sqrt{3}$ , where we are only interested in the negative (red-detuned) solution<sup>4</sup>. Finally, equating the slope of Eq. (4.43) (evaluated at  $\bar{\Delta}_{\text{onset}} = -\kappa/2\sqrt{3}$ ) to the slope of Eq. (4.44), we find the following condition for the onset of bistability

$$|\bar{s}_{\text{in}}|^2 \geq \frac{m_{\text{eff}}\Omega_m^2\kappa^3}{3\sqrt{3}G^2\hbar\kappa_{\text{R}}}. \quad (4.45)$$

Following Eq. (4.43), the intracavity field at this detuning is  $|\bar{a}|^2 = 3\kappa_{\text{R}}|\bar{s}_{\text{in}}|^2/\kappa^2$ . Using the fact that  $g_0 = Gx_{\text{zpf}}$ , alongside the definition of zero-point motion in Eq. (4.17), the condition for bistability can be written as follows

$$n_{\text{cav}}^{\text{onset}} \geq \frac{m_{\text{eff}}\Omega_m^2\kappa}{\sqrt{3}G^2\hbar} = \frac{\Omega_m\kappa}{2\sqrt{3}g_0^2}. \quad (4.46)$$

Combined with Eq. (4.30), we are now in a position to estimate the maximum quantum cooperativity at the onset of static bistability for a localised mode of a soft clamped membrane resonator, while keeping track of the parameters from Eq. (4.46) (indicated by a tilde)

$$C_q^{\text{onset}} = \frac{2}{\sqrt{3}} \frac{g_0^2}{\tilde{g}_0^2} \frac{\tilde{\Omega}_m}{n_{\text{th}}\Gamma_m} \quad (4.47)$$

$$\approx \frac{2}{\sqrt{3}} \frac{\tilde{m}_{\text{eff}}\tilde{\Omega}_m^2}{m_{\text{eff}}\Omega_m^2} \frac{\hbar}{k_{\text{B}}T} Q \times \Omega_m = \frac{2}{\sqrt{3}} \frac{\tilde{k}_{\text{eff}}}{k_{\text{eff}}} \frac{\hbar}{k_{\text{B}}T} Q \times \Omega_m, \quad (4.48)$$

where in the last line we have used the approximation  $n_{\text{th}} \approx \hbar\Omega_m/k_{\text{B}}T$  (cf. Eq. (4.31)). This result suggests that the highest attainable quantum cooperativity for an optomechanical system is dictated by the  $Qf$ -product of the mode of interest and the lowest spring constant in the system,  $\tilde{k}_{\text{eff}} = \tilde{m}_{\text{eff}}\tilde{\Omega}_m^2$ . As we will see later in this chapter, this is an important consideration for our optomechanical system.

## 4.4 Coherent optomechanical interactions

Moving towards dynamical effects we anticipate in our experimental endeavours, we now provide a theoretical treatment of a few key optomechanical effects – dynamical backaction and sideband cooling, optomechanically induced transparency and ponderomotive squeezing.

<sup>4</sup>Note, that here we refer to the detuning, which includes the static displacement.

### 4.4.1 Dynamical backaction and sideband cooling

Arguably the most exciting optomechanical effects arise from the fact that the mechanical motion affects the intracavity field, which, in turn, modifies the dynamics of the mechanical resonator. This is referred to as *dynamical backaction* and is briefly summarised in this section.

We begin by writing the linearised Heisenberg-Langevin equations for the field fluctuations (cf. Eq. (4.26))

$$\delta\dot{\hat{a}} = \left( i\bar{\Delta} - \frac{\kappa}{2} \right) \delta\hat{a} - iG\bar{a}\hat{x} + \sqrt{\kappa_R}\delta\bar{s}_{\text{in}} + \sqrt{\kappa}\delta\hat{a}_{\text{in}}, \quad (4.49)$$

$$\dot{\hat{x}} = \frac{\hat{p}}{m_{\text{eff}}}, \quad (4.50)$$

$$\dot{\hat{p}} = -m_{\text{eff}}\Omega_m^2\hat{x} - \hbar G\bar{a}(\delta\hat{a}^\dagger + \delta\hat{a}) - \Gamma_m\hat{p} + \hat{F}_{\text{th}}. \quad (4.51)$$

Since we are merely interested in the effect of the radiation pressure interaction on the mechanical response, we neglect the input terms in Eqs. (4.49) and (4.51), and treat the field fluctuations as complex quantities, rather than quantum mechanical operators (i.e.  $\delta\hat{a} \rightarrow \delta a$  and  $\delta\hat{a}^\dagger \rightarrow \delta a^*$ ). In the Fourier domain the solutions to the light and mechanical fields can be expressed as follows<sup>5</sup>

$$\delta a(\Omega) = \frac{-iG\bar{a}}{-i(\bar{\Delta} + \Omega) + \kappa/2} x(\Omega), \quad \delta a^*(\Omega) = \frac{iG\bar{a}}{i(\bar{\Delta} - \Omega) + \kappa/2} x(\Omega), \quad (4.52)$$

$$\underbrace{m_{\text{eff}}(\Omega_m^2 - \Omega^2 - i\Omega\Gamma_m)}_{\chi_m^{-1}(\Omega)} x(\Omega) = \underbrace{-\hbar G\bar{a}(\delta a^*(\Omega) + \delta a(\Omega))}_{\delta F_{\text{rp}}(\Omega)}. \quad (4.53)$$

We recognise the left-hand side of Eq. (4.53) as the product of the inverse (bare) mechanical susceptibility (cf. Eq. (2.99)) and the mechanical displacement, while the right-hand side corresponds to the radiation pressure force fluctuations,  $\delta F_{\text{rp}}(\Omega)$ . The radiation pressure force alters the response of the mechanical resonator, resulting in an effective mechanical susceptibility

$$\chi_{\text{eff}}^{-1}(\Omega) := \chi_m^{-1}(\Omega) + \chi_{\text{opt}}^{-1}(\Omega), \quad (4.54)$$

$$\chi_{\text{opt}}^{-1}(\Omega) = \frac{4g^2 m_{\text{eff}} \Omega_m}{\kappa} \left( \frac{\kappa/2}{(\bar{\Delta} + \Omega) + i\kappa/2} + \frac{\kappa/2}{(\bar{\Delta} - \Omega) - i\kappa/2} \right) \quad (4.55)$$

$$= 4g^2 m_{\text{eff}} \Omega_m \frac{\bar{\Delta}}{\bar{\Delta}^2 + (\kappa/2 - i\Omega)^2}, \quad (4.56)$$

where in the second to last line we have used the relation  $\hbar G^2 \bar{a}^2 = 2m_{\text{eff}} \Omega_m g^2$ . In extension of our definition of an effective susceptibility, we can define an

<sup>5</sup>Here,  $\delta a^*(\Omega)$  corresponds to  $\mathcal{F}[\delta a^*(t)]$ .

effective mechanical frequency,  $\Omega_{\text{eff}}$ , and damping,  $\Gamma_{\text{eff}}$ ,

$$\chi_{\text{eff}}^{-1}(\Omega) = m_{\text{eff}} (\Omega_{\text{eff}}^2 - \Omega^2 + i\Omega\Gamma_{\text{eff}}) \quad (4.57)$$

$$\Gamma_{\text{eff}}(\Omega) = \frac{\mathcal{I}[\chi_{\text{eff}}^{-1}(\Omega)]}{m_{\text{eff}}\Omega} \quad (4.58)$$

$$\Omega_{\text{eff}}(\Omega) = \sqrt{\Omega^2 + \frac{\mathcal{R}[\chi_{\text{eff}}^{-1}(\Omega)]}{m_{\text{eff}}}}. \quad (4.59)$$

The explicit dependence on the Fourier frequency suggests that the exact values for these effective quantities will depend on the range of frequencies within the optical density of states that is being sampled by the mechanical resonator. Assuming  $\kappa \gg \Gamma_{\text{eff}}$  (corresponding to a uniform density of optical states within the effective linewidth of the mechanical resonator), as well as  $\Omega_{\text{eff}}/\Omega_{\text{m}} \ll 1$ , Eqs. (4.58-4.59) can be evaluated at  $\Omega = \Omega_{\text{m}}$

$$\Gamma_{\text{opt}} := \Gamma_{\text{eff}}(\Omega_{\text{m}}) - \Gamma_{\text{m}} \quad (4.60)$$

$$\delta\Omega_{\text{m}} := \Omega_{\text{eff}}(\Omega_{\text{m}}) - \Omega_{\text{m}} \approx \Omega_{\text{m}} \left( 1 + \frac{1}{2} \frac{\mathcal{R}[\chi_{\text{eff}}^{-1}(\Omega_{\text{m}})]}{m_{\text{eff}}\Omega_{\text{m}}^2} \right) - \Omega_{\text{m}} \quad (4.61)$$

$$= \frac{1}{2} \frac{\mathcal{R}[\chi_{\text{eff}}^{-1}(\Omega_{\text{m}})]}{m_{\text{eff}}\Omega_{\text{m}}}, \quad (4.62)$$

where in Eq. (4.61) we have Taylor expanded  $\Omega_{\text{eff}}(\Omega_{\text{m}})$  to first order in  $\mathcal{R}[\chi_{\text{eff}}^{-1}(\Omega_{\text{m}})]/m_{\text{eff}}\Omega_{\text{m}}^2$ . The resultant expressions for the *optical spring* effect (i.e. optically induced frequency shift) and *optomechanical damping* are thus

$$\delta\Omega_{\text{m}} = g^2 \left( \frac{\bar{\Delta} + \Omega_{\text{m}}}{(\bar{\Delta} + \Omega_{\text{m}})^2 + (\kappa/2)^2} + \frac{\bar{\Delta} - \Omega_{\text{m}}}{(\bar{\Delta} - \Omega_{\text{m}})^2 + (\kappa/2)^2} \right) \quad (4.63)$$

$$\Gamma_{\text{opt}} = 2g^2 \left( \frac{\kappa/2}{(\bar{\Delta} + \Omega_{\text{m}})^2 + (\kappa/2)^2} + \frac{\kappa/2}{(\bar{\Delta} - \Omega_{\text{m}})^2 + (\kappa/2)^2} \right). \quad (4.64)$$

Looking back at Eq. (2.106) and performing a similar integral with the optically modified mechanical susceptibility (see Eq. (4.57)) yields

$$\langle x^2 \rangle = \int_{-\infty}^{\infty} |\chi_{\text{eff}}(\Omega)|^2 S_{F_{\text{th}}F_{\text{th}}}(\Omega) \frac{d\Omega}{2\pi} \approx \frac{k_{\text{B}}T_{\text{eff}}}{m_{\text{eff}}\Omega_{\text{eff}}^2}, \quad (4.65)$$

where we have defined an *effective mode temperature* as

$$T_{\text{eff}} = \frac{\Gamma_{\text{m}}}{\Gamma_{\text{opt}} + \Gamma_{\text{m}}} T. \quad (4.66)$$

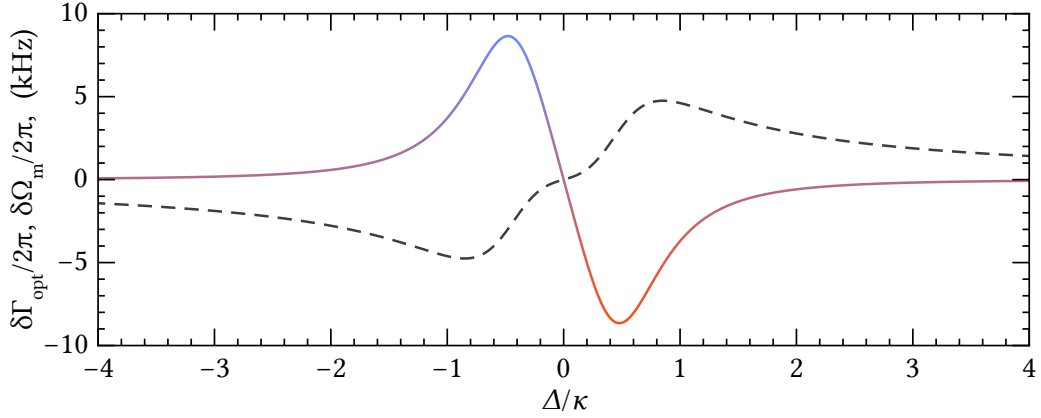


Figure 4.4: Example of the optical spring (dashed,  $\delta = \delta\Omega_m$ ) and damping (solid,  $\delta = \Gamma_{\text{opt}}$ ) for experimentally relevant parameters. For negative detunings the resonator experiences spring softening, while positive detunings result in spring hardening. The latter regime is, however, often times inaccessible experimentally, since the accompanying negative damping leads to amplification of the mechanical motion (for  $\Gamma_{\text{opt}} \gg \Gamma_m$ ) and hence parametric instability.

Hence, the light induced damping of the mechanical mode not only leads to a spectral broadening of the mode, but also a reduction of its temperature. While our treatment is purely classical, this result nevertheless captures the essence of laser cooling and is of particular interest for this work. With this in mind, we seek to find the optimal detuning for which the optically induced broadening is at its largest. Using Eq. (4.64) we find that that the optical broadening is largest for the following detunings

$$\bar{\Delta}^{\text{optimal}} = -\frac{1}{2\sqrt{3}}\sqrt{4\Omega_m^2 - \kappa^2 + 2\sqrt{\kappa^4 + 4\kappa^2\Omega_m^2 + 16\Omega_m^4}} \quad (4.67)$$

$$\approx \begin{cases} -\Omega_m, & \Omega_m \gg \kappa \text{ (resolved sideband regime)} \\ -\kappa/\sqrt{12}, & \Omega_m \ll \kappa \text{ (unresolved sideband regime)} \end{cases}. \quad (4.68)$$

Using these results, we consider two approximations which are particularly helpful in our experimental considerations. First, we consider the optical damping rate in the *resolved sideband* regime (i.e.  $\kappa \ll \Omega_m$ ). Taylor expanding Eq. (4.64) to lowest order in  $\kappa/\Omega_m$  and evaluating at  $\bar{\Delta} = -\Omega_m$  following the above result, we obtain

$$\Gamma_{\text{opt}} \approx \frac{4g^2}{\kappa}. \quad (4.69)$$

Assuming  $\Gamma_{\text{opt}} \gg \Gamma_{\text{m}}$ , we can express the quantum cooperativity (cf. Eq. (4.30)) in terms of the optical broadening

$$C_q \approx \frac{\Gamma_{\text{opt}}}{\bar{n}_{\text{th}}\Gamma_{\text{m}}}. \quad (4.70)$$

In a similar fashion one can re-express Eq. (4.66) in terms of the quantum cooperativity. Assuming  $\Gamma_{\text{opt}} \gg \Gamma_{\text{m}}$  and using the high-temperature approximation  $\bar{n} \approx k_{\text{B}}T/\hbar\Omega_{\text{m}}$  (cf Eq. (4.31)) we find that

$$T_{\text{eff}} \approx \frac{\hbar\Omega_{\text{m}}}{k_{\text{B}}C_q} \quad \rightarrow \quad \bar{n}_{\text{eff}} \approx \frac{1}{C_q}, \quad (4.71)$$

where we have defined an effective mean occupancy  $\bar{n}_{\text{eff}} \approx k_{\text{B}}T_{\text{eff}}/\hbar\Omega_{\text{m}}$ . This result, originating from a purely classical analysis, suggests that in order to reach a mean occupancy lower than unity, we require  $C_q > 1$ . In fact, a full quantum treatment of the problem yields the same result in the resolved sideband regime.

Lastly, let us consider the probability,  $P_n$ , of finding a vibrational mode with a certain mean occupancy in a particular energy eigenstate  $|n\rangle$ . Following [136] we write

$$P_n = \frac{\bar{n}^n}{(1 + \bar{n})^{n+1}}. \quad (4.72)$$

The probability of finding a particular vibrational mode in its motional ground state  $|0\rangle$  is hence  $P_0 = 1/(1 + \bar{n})$ , which suggests that for a mean occupancy of  $\bar{n} = 1$  the mode can be found in its motional ground state 50% of the time. The term ‘‘ground state cooling’’ within the field of cavity optomechanics refers to achieving a mean phonon occupancy below unity, which, in turn, requires  $C_q > 1$ .

Going from a classical to a quantum mechanical description of radiation pressure cooling can be done in two different ways. Starting from the equations of motion (cf. Eqs. (4.49-4.51)) one could calculate the expectation value of the phononic number operator in the Fourier domain,  $\langle \hat{b}^\dagger \hat{b} \rangle$ , thus finding an explicit expression for the mean phonon occupancy. A detailed derivation following this approach can be found in the doctoral dissertation of Cheng Yang [145]. Alternatively, a scattering picture can be adapted, where transition rates between phononic states are calculated using Fermi’s golden rule. Here, we follow this approach as presented in [138, 146, 147].

The average phonon number,  $\bar{n}$ , can be expressed in terms of the probabilities  $P_n$  given by Eq. (4.72) as  $\bar{n} = \sum_{n=0}^{\infty} P_n n$ . Since we are considering a system

where the mechanical resonator couples to two different reservoirs – an optical and a thermal – a change in the mean occupancy can either originate from a thermal process or a Raman-scattering process, akin to those discussed in relation to Fig. 4.3. The rate of change of the average phonon number can therefore be written as the difference of upwards going transitions (i.e. phonons entering from the thermal reservoir and optomechanical scattering processes  $\propto \delta\hat{a}\hat{b}^\dagger$ ) and downwards going transitions (i.e. phonons dissipating into the thermal reservoir and optomechanical scattering processes  $\propto \delta\hat{a}^\dagger\hat{b}$ )

$$\dot{\bar{n}} = (\bar{n} + 1)(A^+ + A_{\text{th}}^+) - \bar{n}(A^- + A_{\text{th}}^-), \quad (4.73)$$

where  $A^\pm$  are the light-mediated transition rates (see Fig. 4.5 for a sketch), while  $A_{\text{th}}^\pm$  are the thermal transition rates. The respective transitions are driven by the radiation-pressure and Langevin forces, and in accordance with Fermi's Golden rule the transition rates are proportional to the density of states associated with said forces at the relevant Fourier frequencies. The thermal transition rates can be expressed as follows [138]

$$A_{\text{th}}^+ = \frac{x_{\text{zpf}}^2}{\hbar^2} S_{FF}(-\Omega_m), \quad A_{\text{th}}^- = \frac{x_{\text{zpf}}^2}{\hbar^2} S_{FF}(\Omega_m) \quad (4.74)$$

$$S_{FF}(-\Omega_m) = 2m_{\text{eff}}\Gamma_m\hbar\Omega_m\bar{n}, \quad S_{FF}(\Omega_m) = 2m_{\text{eff}}\Gamma_m\hbar\Omega_m(\bar{n} + 1), \quad (4.75)$$

where  $S_{FF}$  is the power spectral density of the Langevin force. The resultant transition rates are thus  $A_{\text{th}}^+ = \bar{n}_{\text{th}}\Gamma_m$  and  $A_{\text{th}}^- = (\bar{n}_{\text{th}} + 1)\Gamma_m$ . Similarly the light-mediated transition rates can be expressed as [147]

$$A^\pm = \frac{x_{\text{zpf}}^2}{\hbar^2} S_{F_{\text{rp}}F_{\text{rp}}}(\Omega = \mp\Omega_m) = g_0^2 S_{NN}(\Omega = \mp\Omega_m) \quad (4.76)$$

$$S_{NN}(\Omega) = \bar{n}_{\text{cav}} \frac{\kappa}{(\bar{\Delta} + \Omega)^2 + (\kappa/2)^2} \quad (4.77)$$

where  $S_{F_{\text{rp}}F_{\text{rp}}}(\Omega)$  is the power spectral density of the radiation pressure force (cf. Eq. (4.5)). Comparing the optical density of states in Eq. (4.77) to Eq. (4.64) the expression for the optical damping rate, we see that

$$\Gamma_{\text{opt}} = A^- - A^+. \quad (4.78)$$

Having established a connection between the mean phonon occupancy and the optical damping rate in Eq. (4.71) (i.e. larger damping equals lower occupation), this result comes as no surprise – the transition rate  $A^-$  removes excitations from our mechanical resonator, and for  $A^- \gg A^+$ , the damping rate is positive, leading to an overall reduction of the mean occupancy.

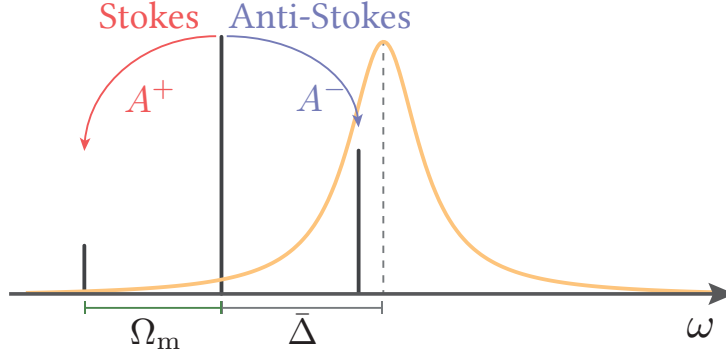


Figure 4.5: Sketch of the Raman-scattering processes. Sidebands scattered at  $\pm\Omega_m$  from a probe field (black) detuned by  $\bar{\Delta}$  from cavity resonance (dashed black line).

Combining these results, we can solve Eq. (4.73) in the steady-state, yielding the following expression for the mean phonon occupancy

$$\bar{n}_{\text{final}} = \frac{\Gamma_{\text{opt}}\bar{n}_{\text{min}} + \Gamma_m\bar{n}_{\text{th}}}{\Gamma_{\text{opt}} + \Gamma_m} \quad (4.79)$$

$$\bar{n}_{\text{min}} = -\frac{(\bar{\Delta} + \Omega_m)^2 + (\kappa/2)^2}{4\bar{\Delta}\Omega_m}. \quad (4.80)$$

The minimum occupancy  $\bar{n}_{\text{min}}$  is merely a consequence of imperfect sideband resolution. Only for  $\Omega_m \gg \kappa$  is the Stokes sideband (originating from the process associated with the  $A^+$  transition rate) strongly suppressed by the optical cavity. The expression for the final occupancy is simplified in the resolved sideband regime

$$\bar{n}_{\text{final}} \approx \bar{n}_{\text{min}} + \frac{1}{C_q}, \quad (4.81)$$

where we have used Eq. (4.70) in order to express the occupancy in terms of the quantum cooperativity. As we can see, even for an infinitely large quantum cooperativity, the lowest attainable mean occupancy is given by  $\bar{n}_{\text{min}}$ . This limit is often referred to as the *backaction* or *Doppler* limit, and only very recently was it reached in an optomechanical experiment [16].

There are, however, techniques that allow for *sub-Doppler cooling*. These involve, among others, cooling by injection of squeezed light [148], cooling by measurement [149, 150], feedback cooling [17], Stokes sideband suppression by optomechanically induced transparencies [151], and cooling by teleportation in hybrid systems [152].

Due to the importance of the backaction limit as it pertains to laser cooling, let us consider the optimal detuning, as we seek to minimise  $\bar{n}_{\min}$

$$\bar{\Delta}_{\bar{n}_{\min}}^{\text{optimal}} = -\sqrt{\frac{\kappa^2}{4} + \Omega_m^2} \approx \begin{cases} -\Omega_m, & \Omega_m \gg \kappa \text{ (resolved sideband)} \\ -\kappa/2, & \Omega_m \ll \kappa \text{ (unresolved sideband)} \end{cases}. \quad (4.82)$$

In the resolved sideband regime the optimal detuning coincides with the optimal detuning previously derived in relation to the optical damping rate (cf. Eq. (4.68)). In the unresolved sideband regime, however, the results differ, which can be ascribed to the fact that in Eq. (4.82) we seek to maximise the asymmetry between the Stokes and anti-Stokes sidebands. But while  $\bar{\Delta} = -\kappa/2$  might not be the optimal detuning for broadening, in practice one often has an abundance of optical power and can compensate for the reduced optical damping rate by simply increasing the input power. In Fig. 4.6 a comparison between the optimal detunings following Eqs. (4.68) and (4.82) is shown.

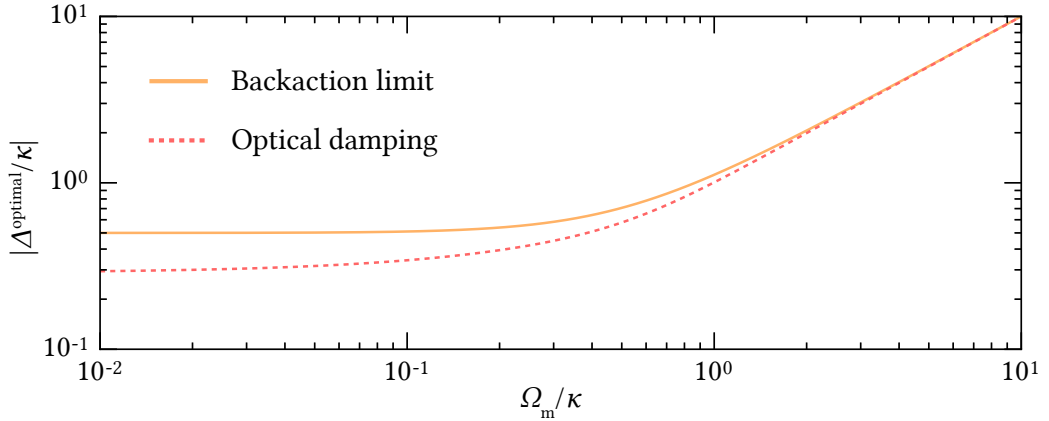


Figure 4.6: Comparison of optimal detuning based on the backaction limit Eq. (4.68) (solid) and optical damping rate Eq. (4.82) (dashed).

#### 4.4.2 Optomechanically induced transparency

To say that electromagnetically induced transparency (EIT) [153] is a well-known effect in atomic physics would be an understatement. With numerous applications spanning from motional ground state cooling of atoms [154, 155], slow light [156] and storage of light pulses [157], to single-atom optical transistors [158], EIT is widely used in atomic physics. The effect can be

observed in optical media with a Raman transition, upon probing it with two phase-coherent laser beams. A window of transparency for the one of the beams emerges once the frequency difference of the two beams matches the Raman transition.

EIT is often realised in atomic media exhibiting a three-level  $\Lambda$ -scheme. As we will see shortly, such a level structure can also be realised in optomechanical systems, leading to the emergence of *optomechanically induced transparency* (OMIT). This idea was initially proposed by A. Schliesser in his doctoral thesis [159], and shortly hereafter demonstrated experimentally [160]. In the context of this thesis, we employ this technique as a means of measuring key system parameters – namely cavity linewidth,  $\kappa$ , and the cavity detuning with respect to the laser frequency,  $\bar{\Delta}$ . Here we follow a similar derivation as presented in [14].

As in atomic physics, the input to our system is a strong pump (control) field, with a small modulation which constitutes the probe field. When the difference frequency of the probe and control fields matches a Raman transition of the optomechanical system, a transparency window is expected to emerge. In our case, the Raman transition is none other than the mechanical resonance transition. In effect, when the weak probe field overlaps spectrally with a mechanical sideband originating from Raman scattering processes involving the strong control field, we see an interference effect, which manifests itself as a window of transparency for the probe field.

In contrast to a “canonical” EIT experiment, we inject two probe beams symmetrically around the strong control field, into the cavity. This is merely a consequence of how we perform the measurement – in order to preserve phase coherence between the control and probe fields, we use an electro-optic modulator (EOM) to generate sidebands at a frequency  $\pm\Omega_p$  relative to the carrier. A sketch of the relevant  $\Lambda$  level scheme is depicted in Fig. 4.7. We will return to the experimental details of the underlying measurement later in this chapter.

Our starting point is the set of linearised equations of motion, given by Eqs. (4.49-4.51). Since the effect we wish to study is classical in nature, we take the expectation values of said equations, thus discarding the quantum noise operators (i.e.  $\langle \delta \hat{a}_{\text{in}} \rangle = \langle \hat{F}_{\text{th}} \rangle = 0$ ). Similar to Section 4.4.1 we write the solutions in the Fourier domain

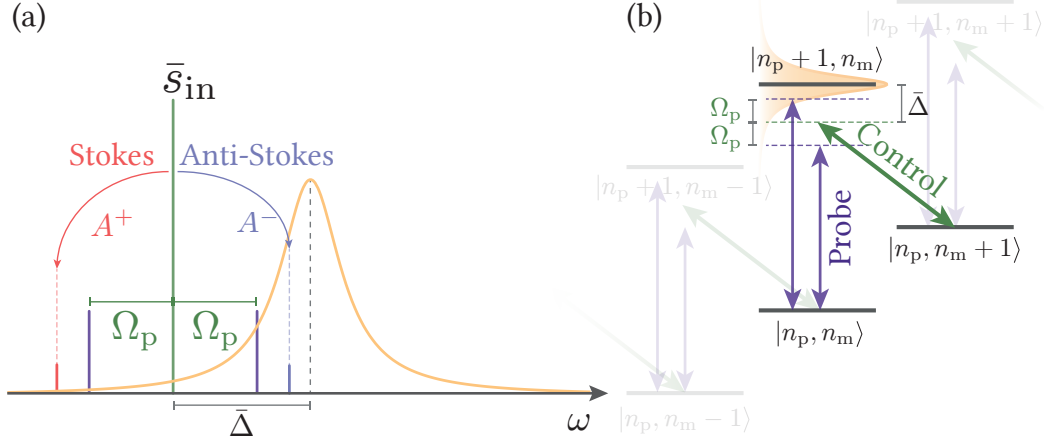


Figure 4.7: Sketch of OMIT. To the left the probe tones are seen at  $\pm\Omega_p$  from the control field  $\bar{s}_{\text{in}}$  (green). To the right the level structure of the optomechanical system is shown. The detuned control field addresses the Stokes sideband transition, annihilating a phonon and generating a photon. A given energy level is given by the mechanical and optical occupations,  $n_m$  and  $n_p$  respectively.

$$\delta a(\Omega) = (-iG\bar{a}x + \sqrt{\kappa_R}\delta\bar{s}_{\text{in}})\chi_c(\Omega), \quad (4.83)$$

$$\delta a^*(\Omega) = (iG\bar{a}x + \sqrt{\kappa_R}\delta\bar{s}_{\text{in}}^*)\chi_c^*(-\Omega) \quad (4.84)$$

$$x(\Omega) = -\hbar G\bar{a}(\delta a(\Omega) + \delta a^*(\Omega))\chi_m(\Omega), \quad (4.85)$$

where we have defined the optical susceptibility  $\chi_c(\Omega)$  as follows

$$\chi_c(\Omega) := \frac{1}{-i(\bar{\Delta} + \Omega) + \kappa/2}. \quad (4.86)$$

As previously mentioned, we assume the intracavity field to be real. In order to fulfil this requirement, the physically irrelevant phase of the intracavity field is absorbed into the phase of input field. Following Eq. (4.43) and assuming  $G = 0$ , we find that

$$\bar{s}_{\text{in}} = \frac{-i\bar{\Delta} + \kappa/2}{\sqrt{\kappa_R}}\bar{a} = \frac{-i\bar{\Delta} + \kappa/2}{\sqrt{\bar{\Delta}^2 + \kappa^2/4}}|\bar{s}_{\text{in}}| = e^{-i\theta_{\text{in}}}|\bar{s}_{\text{in}}|, \quad (4.87)$$

where  $\theta_{\text{in}} = \text{atan}(-2\bar{\Delta}/\kappa)$ . Similar to the definition of mechanical position and momentum operators, we now define the optical amplitude and phase quadratures in terms of the creation/annihilation operators

$$X := \frac{1}{\sqrt{2}}(\hat{a}^\dagger + \hat{a}), \quad Y := \frac{i}{\sqrt{2}}(\hat{a}^\dagger - \hat{a}). \quad (4.88)$$

Combined with Eq. (4.87) we can now write a general relation between the fluctuations of the quadrature operators and the creation/annihilation operators, assuming that the mean field is rotated by a phase angle  $\theta$

$$\begin{pmatrix} \delta\hat{a} \\ \delta\hat{a}^\dagger \end{pmatrix} = \underbrace{\frac{1}{\sqrt{2}} \begin{pmatrix} e^{-i\theta} & ie^{-i\theta} \\ e^{i\theta} & -ie^{i\theta} \end{pmatrix}}_{\mathbf{M}_\theta} \begin{pmatrix} \delta\hat{X} \\ \delta\hat{Y} \end{pmatrix}. \quad (4.89)$$

Our input field is thus converted into amplitude modulation inside the cavity,  $\delta X$ , if it fulfils the following relation

$$\delta\bar{s}_{\text{in}} = \frac{i}{\sqrt{2}} \frac{-i\bar{\Delta} + \kappa/2}{\sqrt{\bar{\Delta}^2 + \kappa^2/4}} \delta X = \frac{i}{\sqrt{2}} \frac{|\chi_c(0)|}{\chi_c(0)} \delta X, \quad (4.90)$$

$$\delta\bar{s}_{\text{in}}^* = -\frac{i}{\sqrt{2}} \frac{i\bar{\Delta} + \kappa/2}{\sqrt{\bar{\Delta}^2 + \kappa^2/4}} \delta X = -\frac{i}{\sqrt{2}} \frac{|\chi_c(0)|}{\chi_c^*(0)} \delta X, \quad (4.91)$$

where we have used Eq. (4.86) for the optical susceptibility. Solving Eqs. (4.83-4.85) for  $\delta a + \delta a^*$ , and inserting Eqs. (4.90-4.91), yields

$$\delta a(\Omega) + \delta a^*(\Omega) = \frac{C(\Omega)}{1 - M(\Omega)}, \quad (4.92)$$

$$C(\Omega) := \sqrt{\kappa_R} \left( \chi_c(\Omega) \frac{i}{\sqrt{2}} \frac{|\chi_c(0)|}{\chi_c(0)} - \chi_c^*(-\Omega) \frac{i}{\sqrt{2}} \frac{|\chi_c(0)|}{\chi_c^*(0)} \right) \delta X, \quad (4.93)$$

$$M(\Omega) := 2ig^2 m_{\text{eff}} \Omega_m \chi_m(\Omega) (\chi_c(\Omega) - \chi_c^*(-\Omega)). \quad (4.94)$$

Evidently, the cavity response has two distinct contributions –  $C(\Omega)$ , which only depends on the optical susceptibilities, and  $M(\Omega)$ , which is directly dependent on the optomechanical coupling and the mechanical susceptibility. The latter also entails that the cavity response is only modified close to the resonance frequency of the mechanical resonator. In Fig. 4.8a the full response function,  $C(\Omega)/(1 - M(\Omega))$ , is plotted, alongside the response for zero optomechanical coupling. At the mechanical frequency the cavity response is distorted and a Fano resonance [161] arises, which is a known interference effect to arise in systems where a discrete state interacts with a continuum of states. In our case, the former originates from the discrete mechanical resonance spectrum, while the latter is provided by the optical radiation field. Furthermore, since the relative phase of the cavity susceptibility changes below and above the resonance, the narrowband response due to the mechanical resonance changes, depending on its resonance frequency (see Fig. 4.8c).

In practice, we perform these types of measurements in the cavity transmission by direct detection. The detected photocurrent is proportional to

$\hat{a}^\dagger \hat{a}$ , which, upon linearisation (i.e.  $\hat{a} \rightarrow \bar{a} + \delta \hat{a}$ ), yields a photocurrent  $\propto \bar{a}(\delta \hat{a}^\dagger + \delta \hat{a})$ . Hence, our detected signal is simply

$$\delta X_{\text{det}}(\Omega) = \sqrt{\kappa_{\text{T}}} (\delta a(\Omega) + \delta a^*(\Omega)). \quad (4.95)$$

Despite the fact that the input and output coupling rates,  $\kappa_{\text{R}}$  and  $\kappa_{\text{T}}$ , are present in these equations, in practice they do not matter – a simple normalisation procedure renders them quite irrelevant. The details of our measurements procedure will be described later in this chapter.

### 4.4.3 Quantum backaction

Thus far we have avidly ignored the quantum noise terms in our equations of motion. As we saw in Section 4.4.1, the radiation pressure drives the mechanical oscillator. In the following section we consider the impact of including said noise terms.

Following our definitions of the optical and mechanical quadrature operators (cf. Eqs. (4.16) and (4.88)), the linearised equations of motion (see Eqs. (4.49-4.51)) can be expressed as follows

$$\delta \dot{\hat{X}} = -\frac{\kappa}{2} \delta \hat{X} - \bar{\Delta} \delta \hat{Y} + \sqrt{\kappa} \delta \hat{X}_{\text{in}}, \quad (4.96)$$

$$\delta \dot{\hat{Y}} = -\frac{\kappa}{2} \delta \hat{Y} + \bar{\Delta} \delta \hat{X} + 2g \hat{Q} + \sqrt{\kappa} \delta \hat{Y}_{\text{in}}, \quad (4.97)$$

$$\dot{\hat{Q}} = \Omega_{\text{m}} \hat{P}, \quad (4.98)$$

$$\dot{\hat{P}} = -\Gamma_{\text{m}} \hat{P} - \sqrt{2\Gamma_{\text{m}}} \hat{P}_{\text{in}} - \Omega_{\text{m}} \hat{Q} - 2g \delta \hat{X}, \quad (4.99)$$

where the mechanical noise operator  $\hat{P}_{\text{in}}$  has been defined following [138] in terms of the Langevin force operator as follows

$$\hat{P}_{\text{in}} := \frac{x_{\text{zpf}}}{\hbar \sqrt{\Gamma_{\text{m}}}} \hat{F}_{\text{th}}. \quad (4.100)$$

The equations of motion can now be cast in matrix form

$$\underbrace{\begin{pmatrix} \delta \dot{\hat{X}} \\ \delta \dot{\hat{Y}} \\ \dot{\hat{Q}} \\ \dot{\hat{P}} \end{pmatrix}}_{\mathbf{\dot{v}}} = \underbrace{\begin{pmatrix} -\kappa/2 & -\bar{\Delta} & 0 & 0 \\ \bar{\Delta} & -\kappa/2 & 2g & 0 \\ 0 & 0 & 0 & \Omega_{\text{m}} \\ 2g & 0 & -\Omega_{\text{m}} & -\Gamma_{\text{m}} \end{pmatrix}}_{\mathbf{M}} \underbrace{\begin{pmatrix} \delta \hat{X} \\ \delta \hat{Y} \\ \hat{Q} \\ \hat{P} \end{pmatrix}}_{\mathbf{v}} + \underbrace{\begin{pmatrix} \sqrt{\kappa} \delta \hat{X}_{\text{in}} \\ \sqrt{\kappa} \delta \hat{Y}_{\text{in}} \\ 0 \\ \sqrt{2\Gamma_{\text{m}}} \hat{P}_{\text{in}} \end{pmatrix}}_{\mathbf{F}_{\text{in}}}. \quad (4.101)$$

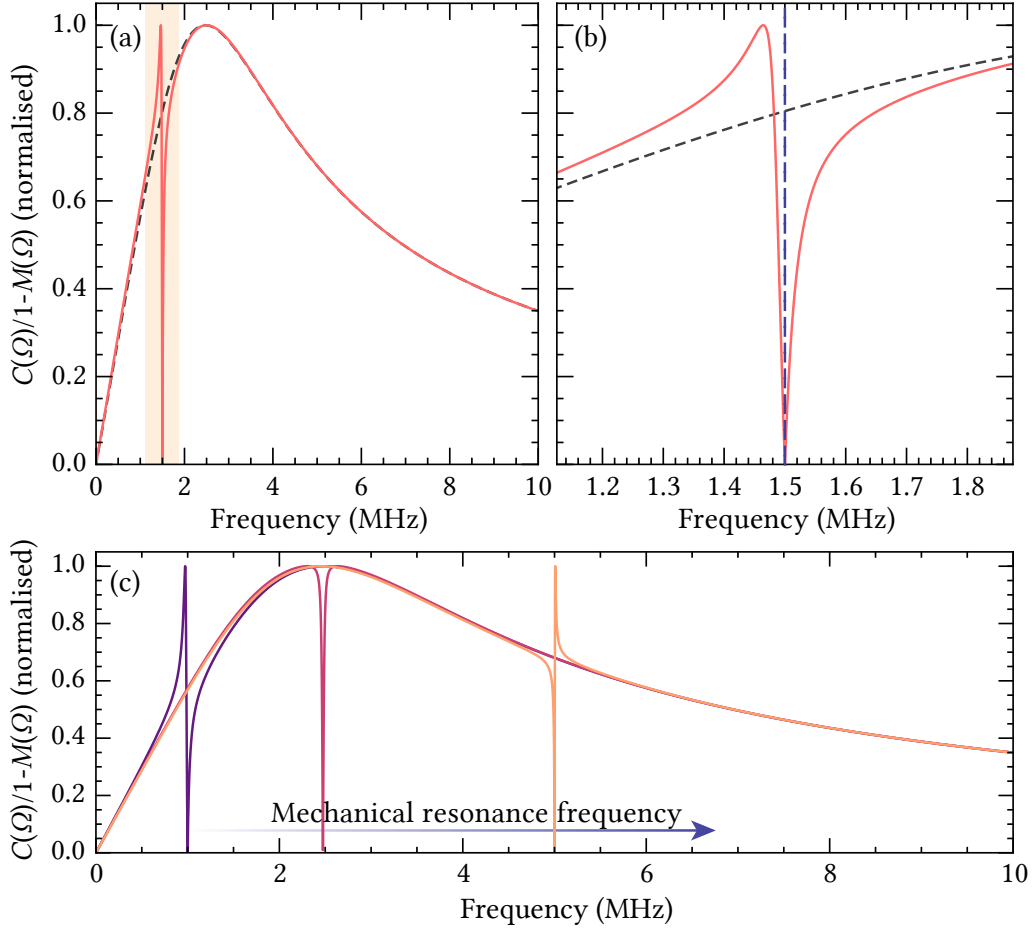


Figure 4.8: OMIT response following Eq. (4.92). Figures (a) and (b) depict the full response (solid), as compared to the bare response, described by the function  $C(\Omega)$  (cf. Eq. (4.93)). The dashed-dotted line in (b) indicates the mechanical resonance frequency. Here, the relevant parameters are:  $\kappa = 2\pi \times 3.5$  MHz,  $\Omega_m = 2\pi \times 1.5$  MHz,  $g = 2\pi \times 0.2$  MHz, and  $\bar{\Delta} = -\kappa/2$ . Figure (b) is a close-up view of the OMIT feature (shaded area in (a)). c) For the same cavity parameters, the full OMIT response is shown for varying mechanical frequencies,  $\Omega_m = 2\pi \times \{1, 2.475, 5\}$  MHz.

We solve this equation in the Fourier domain, followed by a matrix inversion,

yielding

$$\mathbf{V}(\Omega) = -(\mathrm{i}\Omega\mathbf{1} + \mathbf{M})^{-1}\mathbf{F}_{\mathrm{in}}(\Omega) = \mathbf{L}(\Omega)\mathbf{F}_{\mathrm{in}}(\Omega), \quad (4.102)$$

$$\mathbf{L}(\Omega) = \frac{\tilde{\chi}_{\mathrm{eff}}(\Omega)}{\kappa} \begin{pmatrix} 2v\tilde{\chi}_{\mathrm{m}}^{-1}(\Omega) & 2u\tilde{\chi}_{\mathrm{m}}^{-1}(\Omega) & L_{13} & 4gu \\ -u\left(\frac{8g^2}{\Delta} + 2\tilde{\chi}_{\mathrm{m}}^{-1}(\Omega)\right) & 2v\tilde{\chi}_{\mathrm{m}}^{-1}(\Omega) & L_{23} & 4gv \\ 4gv & 4gu & L_{33} & \kappa \\ -4\mathrm{i}g\Omega v/\Omega_{\mathrm{m}} & -4\mathrm{i}g\Omega u/\Omega_{\mathrm{m}} & L_{43} & -\mathrm{i}\kappa\Omega/\Omega_{\mathrm{m}} \end{pmatrix}. \quad (4.103)$$

Here we have defined modified effective and mechanical susceptibilities,  $\tilde{\chi}_{\mathrm{eff}}(\Omega)$  and  $\tilde{\chi}_{\mathrm{m}}(\Omega)$ , alongside cavity response functions  $v(\Omega)$  and  $u(\Omega)$

$$\tilde{\chi}_{\mathrm{eff}} := \chi_{\mathrm{eff}}(\Omega)m_{\mathrm{eff}}\Omega_{\mathrm{m}}, \quad \tilde{\chi}_{\mathrm{m}}(\Omega) := \chi_{\mathrm{m}}(\Omega)m_{\mathrm{eff}}\Omega_{\mathrm{m}}, \quad (4.104)$$

$$u(\Omega) := \frac{-2\bar{\Delta}}{4\bar{\Delta}^2 + (\kappa - 2\mathrm{i}\Omega)^2}\kappa, \quad v(\Omega) := \frac{\kappa - 2\mathrm{i}\Omega}{4\bar{\Delta}^2 + (\kappa - 2\mathrm{i}\Omega)^2}\kappa, \quad (4.105)$$

where  $\chi_{\mathrm{eff}}$  is the effective susceptibility defined in Eq. (4.54). Finally, note that since the displacement operator doesn't have an explicit input noise term, the entire third column of  $\mathbf{L}(\Omega)$  is redundant and has thus been omitted.

Using Eq. (4.103) the solution to the (dimensionless) displacement field is therefore

$$\hat{Q}(\Omega) = \tilde{\chi}_{\mathrm{eff}} \left( \underbrace{\sqrt{2\Gamma_{\mathrm{m}}}\hat{P}_{\mathrm{in}}}_{\text{thermal}} + \underbrace{\frac{4g}{\sqrt{\kappa}} \left[ v(\Omega)\delta\hat{X}_{\mathrm{in}} + u(\Omega)\delta\hat{Y}_{\mathrm{in}} \right]}_{\text{quantum backaction}} \right), \quad (4.106)$$

In addition to the Langevin forcing term, the mechanical resonator is also driven by the light fluctuations. The forcing term involving the granularity of light is also known as *quantum backaction* and can lead to a wealth of interesting quantum optomechanical phenomena.

Following our definition of the optical quadrature operators, in conjunction with Eq. (4.37), the field correlators in the Fourier domain are

$$\langle \delta\hat{X}_{\mathrm{in}}^\dagger(\Omega)\delta\hat{X}_{\mathrm{in}}(\Omega') \rangle = \langle \delta\hat{Y}_{\mathrm{in}}^\dagger(\Omega)\delta\hat{Y}_{\mathrm{in}}(\Omega') \rangle = \frac{2\pi}{2}\delta(\Omega - \Omega') \quad (4.107)$$

$$\langle \delta\hat{X}_{\mathrm{in}}^\dagger(\Omega)\delta\hat{Y}_{\mathrm{in}}(\Omega') \rangle = -\langle \delta\hat{Y}_{\mathrm{in}}^\dagger(\Omega)\delta\hat{X}_{\mathrm{in}}(\Omega') \rangle = \frac{2\pi\mathrm{i}}{2}\delta(\Omega - \Omega'). \quad (4.108)$$

With this we can now derive the (symmetrised) power spectral density of the

displacement field, finding

$$\bar{S}_{QQ} = |\tilde{\chi}_{\text{eff}}|^2 \left( \bar{S}_{FF}^{\text{th}} + \bar{S}_{FF}^{\text{qba}} \right), \quad (4.109)$$

$$\bar{S}_{FF}^{\text{th}} = 2\Gamma_m(\bar{n}_{\text{th}} + 1/2), \quad (4.110)$$

$$\bar{S}_{FF}^{\text{qba}} = g^2\kappa \left( |\chi_c(\Omega)|^2 + |\chi_c(-\Omega)|^2 \right), \quad (4.111)$$

where  $\bar{S}_{FF}^{\text{th}}$  and  $\bar{S}_{FF}^{\text{qba}}$  are the thermal and quantum backaction force noise, respectively. In practice the thermal Langevin force often times masks quantum mechanical signatures of a mechanical resonator. The relative contribution of quantum backaction noise to thermal force noise is therefore an imperative quantity to improve. In the resolved and unresolved sideband regimes it can be shown that

$$\frac{\bar{S}_{FF}^{\text{qba}}}{\bar{S}_{FF}^{\text{th}}} \approx \begin{cases} C_q, & \Omega_m, \bar{\Delta} \ll \kappa \text{ (unresolved sideband)} \\ C_q \left( \frac{1}{2} + \frac{1}{2} \left( \frac{\kappa}{4\Omega_m} \right)^2 \right) & \Omega_m \gg \kappa \text{ and } \bar{\Delta} = -\Omega_m \text{ (resolved sideband)} \end{cases}, \quad (4.112)$$

where  $C_q$  is the quantum cooperativity given by Eq. (4.30). We can therefore interpret the quantum cooperativity as the relative contribution of Langevin force noise to quantum backaction noise. These contributions evidently equilibrate for  $C_q \gtrsim 1$ .

As we have already seen, one of the consequences of  $C_q > 1$  is motional ground state cooling. We will now describe another optomechanical effect which becomes accessible in this regime, namely ponderomotive squeezing.

#### 4.4.4 Ponderomotive squeezing

Looking back at our equations of motion (4.96-4.99), we turn our attention to the light quadratures. As we can see, when  $\bar{\Delta} = 0$ , the (direct) coupling between the amplitude and phase quadratures of light vanishes. This comes as no surprise, since the first derivative of the cavity response is zero on resonance. However, the light quadratures remain coupled due to the optomechanical coupling. As seen in Eq. (4.99), the momentum of the mechanical resonator couples to the amplitude fluctuations of light. The position-momentum coupling subsequently results in a displacement of the mechanical resonator (cf. Eq. (4.98)), which imprints itself on the phase quadrature of light due to the fact that  $\delta\hat{Y} \propto 2g\hat{Q}$  (cf. Eq. (4.97)). Evidently, an optomechanical system imparts an amplitude dependent phase shift on light, which suggests that it can be thought of as an effective Kerr

medium (i.e. a dispersive medium with a  $\chi^{(3)}$  nonlinearity). This was indeed realised early on by Pierre Meystre and colleagues [162], pointing out that there is in fact a one-to-one correspondence between an optical cavity with a suspended mirror and a Kerr medium.

Coincidentally, later the same year Richard Slusher and coworkers reported on the first observation of squeezing of light below the vacuum noise level using the Kerr nonlinearity of Na atoms inside an optical resonator [163]. The fact that a medium with a  $\chi^{(3)}$  nonlinearity can lead to non-classical correlations between the light quadratures, resulting in a reduction of fluctuations below the shot noise level, had been proposed a few years before by Horace Yuen and Jeffrey Shapiro [164]. But despite a tremendous amount of interest in realising a “quantum noise eater”, particularly in view of its potential in relation to the gravitational wave detectors [165], doing so involved numerous difficulties. The interested reader is referred to the excellent (and rather entertaining<sup>6</sup>) paper by Marc Levenson and Robert Shelby, appropriately entitled “Experimentalists’ Difficulties in Optical Squeezed State Generation” [166], as well as the review paper by Daniel Walls [167].

In the years following the publication of Slusher, a number of new systems successfully demonstrated squeezing below the shot noise level. Importantly, the most potent among these were  $\chi^{(2)}$  nonlinearity-based systems, which, to date, hold the record for the largest observed squeeze factor of 15 dB [168]. The reason for the success of these systems is primarily due to the fact that the  $\chi^{(2)}$  nonlinearities are typically larger than the  $\chi^{(3)}$  nonlinearities. However, as pointed out by Holico and colleagues [169], the  $\chi^{(2)}$  nonlinearity leads to squeezing at a different frequency compared to the pump laser frequency. This contributed to the continued interest in developing “quantum noise eaters” using Kerr media.

Unfortunately, the low third-order nonlinearity posed a challenge – in order to achieve appreciable squeezing, a substantial amount of light needed to be used. But this was accompanied by additional losses, due to Brillouin scattering in fibers or spontaneous emission for atomic systems [169, 170]. This led researchers to explore other options, among which was the optical cavity with a harmonically suspended mirror. First theorised by Hilico et al. [169], and later put on more solid theoretical footing by Mancini et al. [171] and Fabre et al. [170], a squeezer based on an optomechanical system was deemed a promising alternative to other candidates. Due to the motional origin of squeezing, the method was termed *ponderomotive squeezing*, echoing

---

<sup>6</sup>Starting with the first challenge of “figuring out what the theorists are talking about”, and ending with the difficulty of “proving that we aren’t crazy”, this paper provides a relatable overview of some of the earlier challenges in generating squeezed light.

the language used by Braginsky and Manukin [172].

Despite the optimism of Stefano Mancini and Paolo Tombesi in 1994, stating that “the up-to-date technology is mature enough to obtain an optomechanical control of the quantum fluctuations” [171], it took experimentalists almost 20 years to observe ponderomotive squeezing in an optomechanical system. Brooks et al. [173] first reported on percent level squeezing of light in a Fabry-Pérot based system, where the collective motion of an ultracold  $^{87}\text{Rb}$  atomic ensemble acted as the mechanical resonator. Shortly hereafter, Safavi-Naeini et al. [174] reported squeezing at a level of a few percent in a silicon-based optomechanical crystal. The rather modest amount of squeezing observed in the experiment by Brooks et al. [173] was due to detection of a less favourable quadrature angle, while Safavi-Naeini et al. [174] ascribed the low level of squeezing to the thermal noise of higher-order mechanical modes. Later the same year Thomas Purdy and colleagues reported on substantial improvement over the previous results, demonstrating ponderomotive squeezing of  $-1.7 \pm 0.2$  dB in a membrane-in-the-middle based system [13]. In 2016 our own group demonstrated further improvement in this direction, by using silicon phononic crystal shielded membrane resonators embedded in a high-finesse Fabry-Pérot cavity. With  $-2.4$  dB squeezing below the shot noise level [14], this remains one of the largest reported amount of sub shot noise squeezing in an optomechanical system. Using a very similar cavity, with an improved outcoupling efficiency, Christoffer B. Møller recently demonstrated  $-(3.3 \pm 0.2)$  dB ponderomotive squeezing [175].

In order to aid us in interpreting and analysing the data presented later in this chapter, we seek to develop the theoretical framework for modelling of ponderomotive squeezing. Here, we closely follow the approach from Nielsen et al. [14]. Starting from Eqs. (4.96-4.97), we write the solution for the amplitude quadrature fluctuations in the Fourier domain

$$\delta\hat{X}(\Omega) = \frac{4g\hat{Q}}{\kappa}u(\Omega) + \frac{2}{\sqrt{\kappa}}\left(v(\Omega)\delta\hat{X}_{\text{in}} + u(\Omega)\delta\hat{Y}_{\text{in}}\right). \quad (4.113)$$

Inserting the solution for the displacement field given by Eq. (4.106) yields

$$\begin{aligned} \delta\hat{X}(\Omega) = & \left(\frac{16g^2u(\Omega)}{\kappa}\tilde{\chi}_{\text{eff}} + 2\right)\frac{1}{\sqrt{\kappa}}\left[v(\Omega)\delta\hat{X}_{\text{in}} + u(\Omega)\delta\hat{Y}_{\text{in}}\right] \\ & + \frac{4gu(\Omega)}{\kappa}\tilde{\chi}_{\text{eff}}\sqrt{2\Gamma_{\text{m}}}\hat{P}_{\text{in}}. \end{aligned} \quad (4.114)$$

Assuming perfect detection efficiency for the sake of simplicity, and using

the input-output relation given by Eq. (4.42)<sup>7</sup>, the output field is found

$$\begin{aligned} \delta\hat{X}_{\text{out}}(\Omega) = & - \left( \frac{16g^2uv}{\kappa} \tilde{\chi}_{\text{eff}} + 2v - 1 \right) \delta\hat{X}_{\text{in}} - \left( \frac{16g^2u^2}{\kappa} \tilde{\chi}_{\text{eff}} + 2u \right) \delta\hat{Y}_{\text{in}} \\ & - \frac{4gu}{\sqrt{\kappa}} \tilde{\chi}_{\text{eff}} \sqrt{2\Gamma_{\text{m}}} \hat{P}_{\text{in}}. \end{aligned} \quad (4.115)$$

Finally, we calculate the symmetrised power spectral density<sup>8</sup> of the amplitude quadrature fluctuations, finding

$$\begin{aligned} \bar{S}_{XX}^{\text{out}} = & \underbrace{1}_{\text{shot noise}} + \underbrace{\left( \frac{16g^2}{\kappa} \right)^2 |\tilde{\chi}_{\text{eff}}|^2 |u(u+v)|^2}_{\text{quantum backaction}} + \underbrace{\frac{16g^2}{\kappa} |\tilde{\chi}_{\text{eff}}|^2 |u|^2 4\Gamma_{\text{m}} \left( \bar{n}_{\text{th}} + \frac{1}{2} \right)}_{\text{thermal force noise}} \\ & + \underbrace{\frac{32g^2}{\kappa} \text{Re} [\tilde{\chi}_{\text{eff}} u (2u^2 + 2v^2 - v)]}_{\text{correlations}}. \end{aligned} \quad (4.116)$$

While the first three terms are comprised of absolute squares and are thus strictly positive, the last term can in principle become negative close to the mechanical resonance frequency, leading to a reduction of fluctuations below the shot noise level.

To garner intuition for ponderomotive squeezing, we consider the influence of detection inefficiency. Optical losses, whether inside the cavity or outside, inevitably lead to admixing of vacuum fluctuations into our signal, thus washing out the correlations created within our optomechanical cavity. Combined with the assumption of a fast cavity (i.e.  $\kappa \gg |\bar{\Delta}|, \Omega_{\text{m}}$ ) and high (classical) cooperativity limit, we find that the measured fluctuations  $\bar{S}_{XX}^{\text{meas}}$  is bounded from below by

$$\bar{S}_{XX}^{\text{meas}} \gtrsim \left( 1 - \frac{\Gamma_{\text{opt}}}{\Gamma_{\text{opt}} + \bar{n}_{\text{th}}\Gamma_{\text{m}}} \right) \eta + (1 - \eta) \quad (4.117)$$

$$\approx 1 - \frac{C_q}{C_q + 1} \eta, \quad (4.118)$$

where in the last line we have used the resolved-sideband approximation for  $\Gamma_{\text{opt}}$  in conjunction with Eq. (4.70). For ideal detection efficiency, the amount of ponderomotive squeezing is determined solely by the quantum cooperativity. This bound furthermore suggests that for moderately high values of

<sup>7</sup>It follows directly from said relation that  $\delta\hat{X}_{\text{out}}(\Omega) = \delta\hat{X}_{\text{in}}(\Omega) - \sqrt{\kappa} \delta\hat{X}(\Omega)$ .

<sup>8</sup>Note that we have multiplied the PSD with a factor 2, resulting in the shot noise level being 1, rather than 1/2, as one would anticipate from our definition of the light quadratures.

quantum cooperativity the amount of squeezing can largely be described by the detection efficiency alone. Put differently, for a significantly broadened mechanical mode the bath temperature plays a negligible role in the amount of observed ponderomotive squeezing and is almost solely determined by the detection efficiency. This observation will be of importance later in this work.

In Fig. 4.9 we evaluate the full model for ponderomotive squeezing for experimentally relevant parameters, while varying three parameters of interest – number of thermal phonons, cavity detuning and detection efficiency. Firstly, we see that the amount of squeezing is only weakly dependent on the thermal occupancy of the bath. Only for a bath occupancies of  $\bar{n}_{\text{th}} = 5 \times 10^5$  and  $\bar{n}_{\text{th}} = 10^6$  (corresponding to  $C_q \approx 6.8$  and  $C_q \approx 3.4$ ) do we start seeing a discernible departure from the minimum amount of squeezing. It is furthermore worth noting that the effect of an increase in the thermal occupancy shifts the squeezing curve upwards – both the peak value, as well as the minimum value. While not surprising, given the way the bath occupancy appears in Eq. (4.116), it can be helpful in identifying anomalies in measurements.

Next, despite the fact that we assume a detection efficiency of  $\eta = 50\%$  in the top left figure, the largest amount of ponderomotive squeezing is not  $\sim 0.5$ , as one would naïvely anticipate from Eq. (4.117). However, as we reduce the detuning (top right plot in Fig. 4.9), the feature becomes narrower, due to a reduced amount of backaction cooling, but more importantly, it slowly approaches the bound of  $\sim 0.5$ . This is indeed compatible with the expectation from the scattering picture discussed earlier (cf. Section 4.2). More specifically, the calculated ponderomotive squeezing spectra in Fig. 4.9) assume  $\Omega_m = 2\pi \times 1.475$  MHz and  $\kappa = 2\pi \times 2.95$  MHz. Since ponderomotive squeezing is indicative of entanglements between Stokes- and anti-Stokes sidebands [139], it is therefore necessary to have a small detuning for this specific choice of cavity linewidth and sideband resolution, in order to avoid a large asymmetry in the scattering rates of the two processes. In the unresolved sideband regime the requirement is slightly different – here, a larger detuning is more favourable, since it ensures a more pronounced mixing between the light quadratures. This can be show by further simplifying the correlation term in Eq. (4.116). In the fast cavity (i.e.  $\kappa \gg |\bar{\Delta}|, \Omega_m$ ) and high cooperativity regime we find that

$$\bar{S}_{XX}^{\text{out}} \approx 1 - \frac{16\bar{\Delta}}{\kappa} \frac{4g^2}{\kappa} \text{Re}[\tilde{\chi}_{\text{eff}}] + \left(\frac{8\bar{\Delta}}{\kappa}\right)^2 \frac{4g^2}{\kappa} |\tilde{\chi}_{\text{eff}}|^2 \left(\frac{4g^2}{\kappa} + \bar{n}_{\text{th}}\Gamma_m\right). \quad (4.119)$$

Indeed, the output field fluctuations increase for larger detunings. However, for the results presented in this work, we rely on the numerical simulations presented in Fig. 4.9 as a guide and source of intuition.

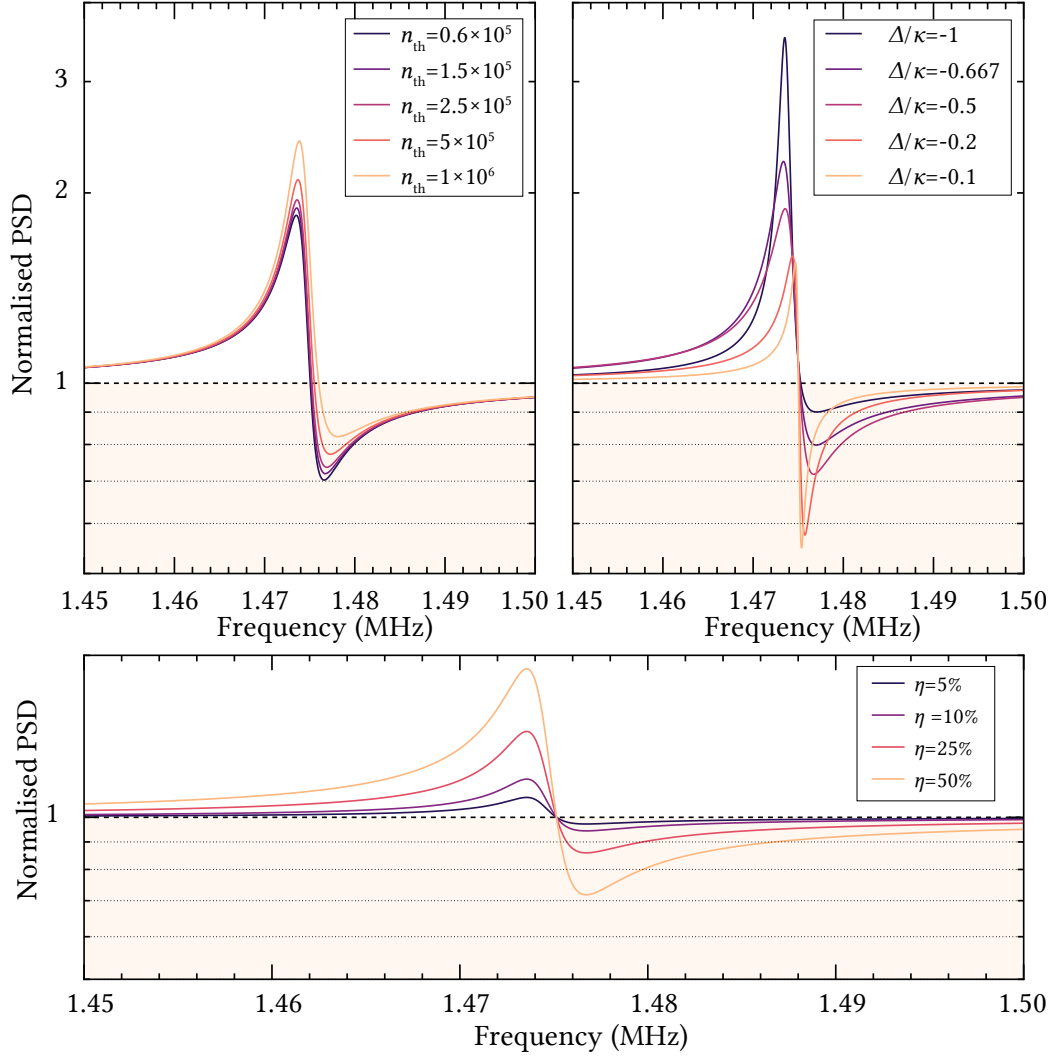


Figure 4.9: Ponderomotive squeezing dependence on thermal occupancy (top left), cavity detuning (top right) and detection efficiency (bottom). For all three plots we use the following parameters:  $\kappa = 2\pi \times 2.95$  MHz,  $\Omega_{\text{m}} = 2\pi \times 1.475$  MHz,  $g = 2\pi \times 50$  kHz, and  $\Gamma_{\text{m}} = 2\pi \times 1$  mHz. For the top row we have assumed a detection efficiency of  $\eta = 50\%$ , while in the top right and bottom figures the bath temperature is set to 10 K.

With this, we move to the final ingredient in understanding our optomechanical system – namely establishing a mapping between the canonical system and the membrane-in-the-middle configuration.

## 4.5 Mapping to membrane-in-the-middle

The theoretical considerations thus far have been rather generic and could be applied to most optomechanical systems operating in the dispersive coupling regime. The final piece of the puzzle is understanding the unique features of a membrane-in-the-middle optomechanical system, and identifying how certain parameters are mapped from this specific system to a generic optomechanical system.

One of the virtues of the MIM configuration is its simplicity – a high-finesse Fabry-Pérot cavity, with a thin dielectric slab placed between the mirrors. This, to a large extent, allows for the optimisation of the individual constituents of the system, before putting it all together. This system has been studied extensively – theoretically, as well as experimentally – since its conception in the research group of Jack Harris in 2008 [176]. The most common method of describing the specificities of the MIM configuration is using the transfer matrix formalism. This method allows for the calculation of some of the key parameters as a function of membrane position within the cavity – cavity resonance shift, optomechanical coupling rate, outcoupling efficiency, and so on. Here, we follow the treatment as described in [14, 55, 176].

The relevant configuration for the work at hand is shown in Fig. 4.10, where the electric field amplitudes  $A_i$  of the traveling waves are specified. For simplicity, the electric field amplitudes are assumed to be plane waves. This is a good approximation when the Rayleigh length  $z_R$ , which in practice is set by the cavity geometry, is much longer than the cavity length  $L$ . For our system the optical beam waist is approximately  $w_0 \approx 45 \mu\text{m}$ , which amounts to a Rayleigh length of  $z_R = \pi w_0^2 / \lambda \approx 7.5 \text{ mm}$  at a wavelength of  $\lambda = 852 \text{ nm}$ . Since our cavity length is  $\sim 2.5 \text{ mm}$  long, the aforementioned approximation would appear borderline. However, previous studies in our group have shown good agreement between experimental data and predictions from this simple transfer matrix model [14, 17], suggesting that the approximation is sufficiently accurate for our purposes.

Since the dielectric slab (i.e. the membrane) is semi-transparent, the left and right sub-cavities of the optical resonator are coupled. The coupling strength is dictated by the relative lengths of the two sub-cavities, as well as the reflectivity and transmissivity of a dielectric slab. The latter

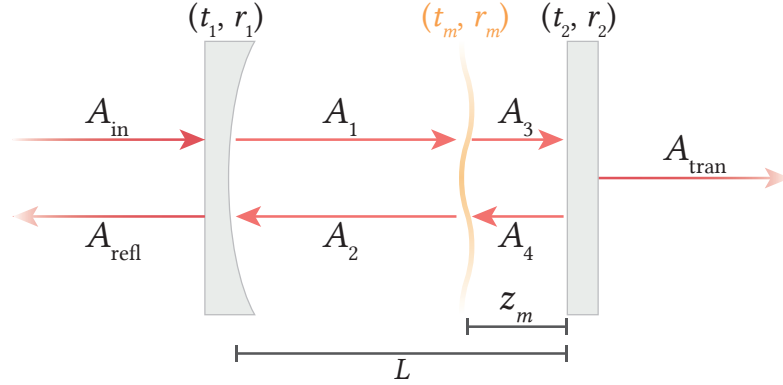


Figure 4.10: Mean field amplitudes in a membrane-in-the-middle configuration. The cavity is driven from one side only with the input field  $A_{\text{in}}$ , and light is collected in transmission. The (amplitude) reflection and transmission coefficients of the membrane and the mirrors,  $(t_i, r_i)$ , as well as the distance of the membrane from the flat mirror,  $z_m$ , are specified.

are given by the following set of equations

$$r_m = \frac{(n^2 - 1) \sin(knh)}{2in \cos(knh) + (n^2 + 1) \sin(knh)}, \quad (4.120)$$

$$t_m = \frac{2n}{2in \cos(knh) + (n^2 + 1) \sin(knh)} \quad (4.121)$$

where  $n$  and  $h$  are the refractive index and thickness of the dielectric, respectively, and  $k$  is the wavenumber of the incident light field. For  $knh \ll 1$ , the power reflectivity can be expressed as

$$|r_m|^2 \approx (n^2 - 1)^2 \left( \frac{kh}{2} \right)^2. \quad (4.122)$$

A comparison of the exact and approximate solutions is shown in Fig. 4.11, where the power reflectivity is shown as a function of thickness. As we can see, the approximate solution is valid up to  $h \sim 25$  nm. Also, note that for the experimentally relevant thickness of  $h = 15$  nm the reflectivity is merely 2.64%.

We can now write a system of equations describing the field amplitudes<sup>9</sup>

<sup>9</sup>More specifically, the field amplitude fluxes.

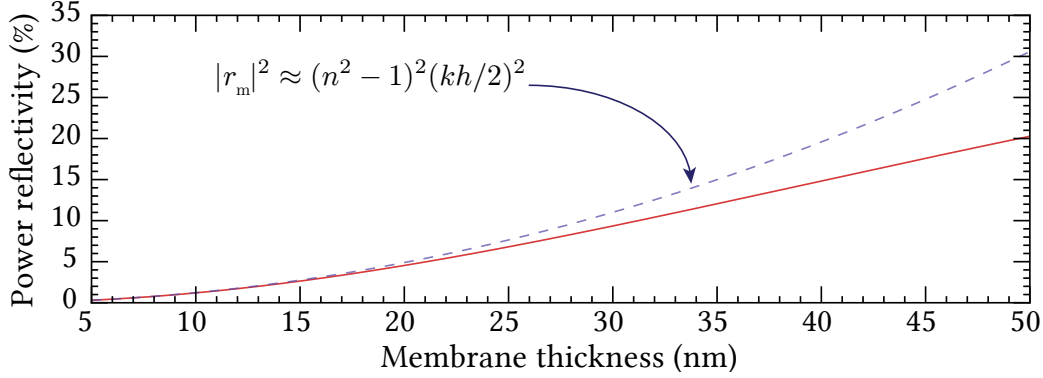


Figure 4.11: Membrane (power) reflectivity as a function of thickness, assuming  $n = 2$  and  $\lambda = 852$  nm, reflecting typical experiment conditions. The solid line is evaluated using Eq. (4.120), while the dashed line is valid for  $knh \ll 1$ .

in our system

$$A_1 = it_1 A_{\text{in}} + r_m A_2 e^{ik(L-z_m)}, \quad (4.123)$$

$$A_2 = r_m A_1 e^{ik(L-z_m)} + it_m A_4 e^{ikz_m}, \quad (4.124)$$

$$A_3 = it_m A_1 e^{ik(L-z_m)} + r_m A_4 e^{ikz_m}, \quad (4.125)$$

$$A_4 = r_2 A_3 e^{ikz_m}, \quad (4.126)$$

$$A_{\text{trans}} = it_2 A_3 e^{ikz_m} \quad (4.127)$$

While these equations are straightforward to solve numerically, the analytic expressions are less illuminating. However, an approximate solution for the MIM cavity resonances can be derived, assuming a lossless cavity, where the mirror reflectivities are much larger than that of the membrane. Following [55, 176], the resonance condition can be found to be

$$|r_m| \cos(2k_{\text{res}} z_m) = \cos(k_{\text{res}}(L-h) - \arg(|r_m|)), \quad (4.128)$$

where  $k_{\text{res}}$  is a resonant wavenumber. Assuming that the cavity resonances are close to those of a bare (empty) cavity, we can further approximate this expression. This is a fair assumption, seeing that the reflectivity of a silicon nitride membrane is only a few percent at the relevant thicknesses (cf. Fig. 4.11). We find that

$$(k_{0,n} - k_{\text{res}})L \approx -|r_m| \sin(2k_{0,n} z_m), \quad (4.129)$$

where  $k_{0,n}$  is the bare cavity resonant wavenumber, with the subscript  $n$  accounting for the fact that we are not working with the first resonance of the

cavity. As we can see, the membrane position modulates the resonance frequency of the cavity. Importantly, it does so periodically, with a periodicity of  $2k_{0,n}z_m$ . Furthermore, it worth noting that in our system  $k_{0,n} - k_{\text{res}}$  is always negative, since the optical path length can only increase by embedding a (thin) dielectric medium inside the cavity.

This result is important for our particular realisation of the MIM configuration. Due to practical reasons, which we will touch upon shortly, our cavity length, as well as the membrane position,  $z_m$ , as in fact fixed. Therefore, the only remaining knob we can turn is the wavelength of light. Since the cavity resonances are discretely spaced, the *relative* position of the membrane with respect to the standing wave will differ from resonance to resonance. In Fig. 4.12 a rough illustration of this process is shown. Broadly speaking, one can think of this process as follows – since the laser is resonant with the cavity when an integer multiple of half wavelength equal the cavity length, going from resonance to resonance corresponds to adding (removing) a “bubble” of the optical standing wave. In doing so, we change the relative position of the membrane with respect to the standing wave, which leads to a slight shift of the cavity resonance in agreement with Eq. (4.129). Therefore, in our everyday language, the question “Where is the membrane with respect to the standing wave?” is replaced by “Where are we in  $2kz$ ?”.

Fig. 4.12 also illustrates an important detail of practical importance, namely that not all membrane locations are equally favourable. For instance, placing the membrane in the middle of the cavity would only provide access to the nodal and anti-nodal points of the standing wave, thus limiting tuneability of the system.

Returning to Eqs. (4.128) and (4.129), we now consider the resonance frequency shift for varying  $k_{0,n}$ , which is treated as a continuous variable for illustrative purposes. Importantly, we fold the computed resonance frequencies back into  $2\pi$  (i.e.  $\text{mod}(2kz_m, 2\pi)$ ). In Fig. 4.13 we compare the frequency shifts for varying membrane thicknesses. As one might have expected, the frequency shifts are modest compared to the free spectral range (here, 60 GHz) for thin membranes, but already for a thickness of 50 nm the frequency shift compared to the bare cavity resonance is approximately a third of the FSR. Furthermore, we see a deviation of the solutions found via Eq. (4.129) for large thicknesses, which is consistent with the fact that said approximation assumes small frequency shifts with respect to the bare cavity resonances. However, for the membrane thicknesses relevant for this work, the sinusoidal approximation of Eq. (4.129) provides sufficient accuracy.

Finally, returning to the field equations (4.123-4.127), we seek to calculate the  $2kz$ -modulation of three key parameters – namely the cavity linewidth, optomechanical coupling rate, and finally the outcoupling efficiency. While

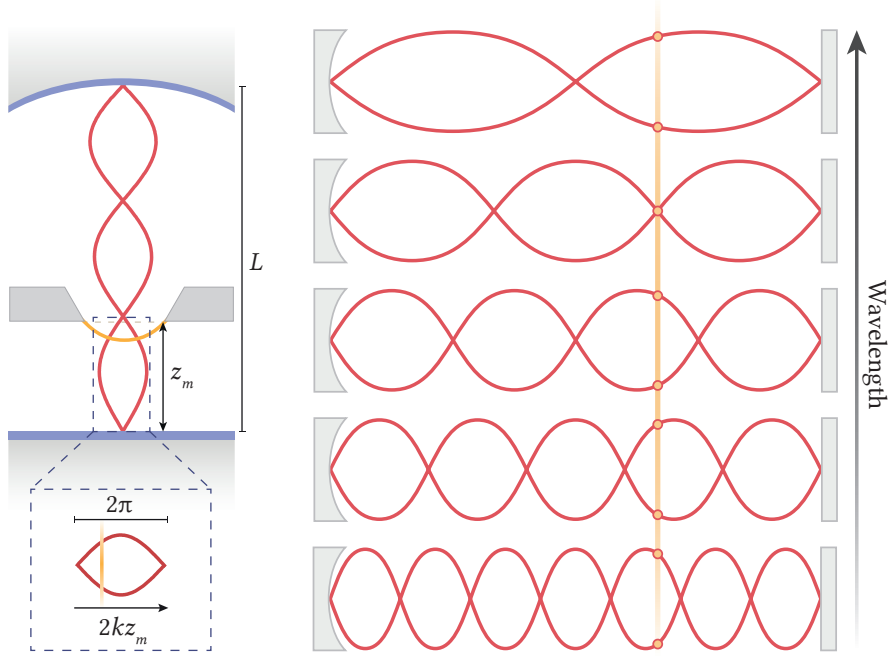


Figure 4.12: Left: Sketch of a Fabry-Pérot cavity in a plano-concave configuration, with an embedded dielectric membrane (yellow). The optical path length within the cavity, and hence the resonance frequency, depend on the relative position of the dielectric slab to the optical standing wave (the optical “bubble”), which is described by the quantity  $2kz_m$  following Eq. (4.129). Right: An illustration of how the relative membrane position changes with respect to the standing wave for difference cavity resonances.

the cavity linewidth is not necessary in order to establish a mapping between our MIM configuration and a canonical optomechanical system, it nevertheless provides valuable insight and reference point for experimental endeavours.

Firstly, starting with a fixed cavity length and membrane position, we find cavity resonances numerically by computing the transmitted cavity field for varying wavenumbers. Upon identifying the cavity resonances, we vary the wavenumber in the immediate vicinity of each resonance<sup>10</sup>, and fitting a Lorentzian to extract the cavity linewidth.

While in a canonical optomechanical system the suspended mirror experiences a radiation pressure force from one side only, this is certainly not the case for our configuration. Due to the fact that our membrane divides the

<sup>10</sup>More specifically  $\pm 5$  full-width half maxima (FWHM), where the FWHM is estimated from the bare cavity FSR and mirror transmissivities,  $|t_1|^2$  and  $|t_2|^2$ .

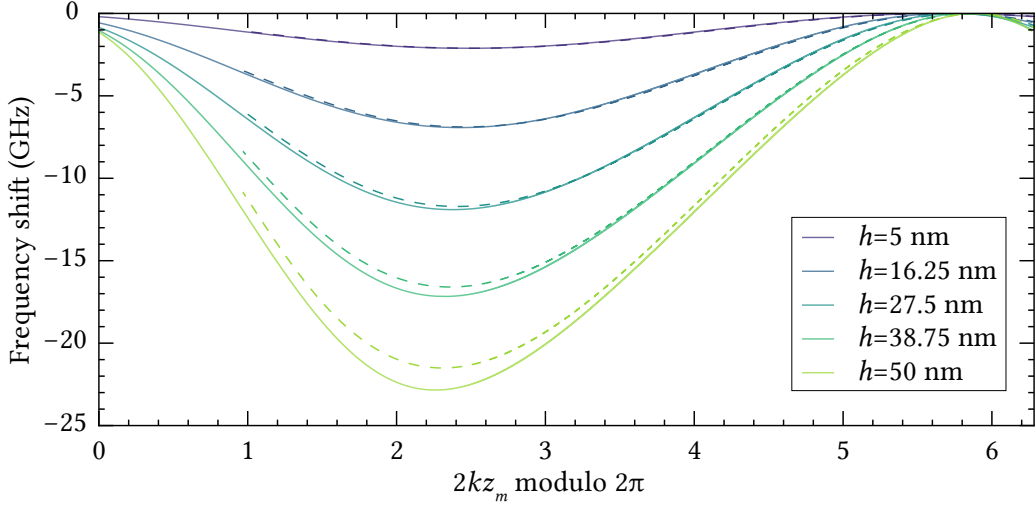


Figure 4.13: Resonance frequency shift dependence on membrane thickness, as a function of  $2kz_m$ . The solid line is computed following Eq. (4.128), while the dashed line is based on the approximate expression for the cavity frequency shift given by Eq. (4.129). We have assumed a refractive index of  $n = 2$ , cavity length  $L = 2.5$  mm, and  $z_m = 500$   $\mu\text{m}$ .

cavity into two parts, the membrane experiences a radiation pressure force from both sides. The strength of the interaction will depend on the amount of light in each sub-cavity. Here, we use the fact that the radiation pressure force in a canonical optomechanical system can be expressed in terms of the rate of photon momentum transfer [147]

$$\langle \hat{F}_{\text{rp}} \rangle = -2\hbar k \bar{n}_{\text{cav}} \tau_c^{-1}, \quad (4.130)$$

where  $\tau_c$  is the round-trip time of the photons inside the cavity, and  $k$  is the wavenumber. For our configuration, the differential radiation pressure force can therefore be expressed as follows

$$\langle \hat{F}_{\text{rp}} \rangle = 2\hbar k \left( \frac{\bar{n}_1}{\tau_1} - \frac{\bar{n}_2}{\tau_2} \right), \quad (4.131)$$

where  $\tau_i$  are the round-trip times for each sub-cavity, given by  $\tau_1 = 2(L - z_m)/c$  and  $\tau_2 = 2z_m/c$ , while the  $\bar{n}_i$  are the mean photon occupancies of each sub-cavity

$$\bar{n}_1 = (|A_1|^2 + |A_2|^2)\tau_1, \quad \bar{n}_2 = (|A_3|^2 + |A_4|^2)\tau_2. \quad (4.132)$$

Combined with the expression for the radiation pressure force in an end-mirror configuration (cf. Eq. (4.5)), we arrive at the following expression for

the single-photon optomechanical coupling rate

$$g_0 = 2kx_{\text{zpf}} \frac{(|A_1|^2 + |A_2|^2) - (|A_3|^2 + |A_4|^2)}{\tau_1(|A_1|^2 + |A_2|^2) + \tau_2(|A_3|^2 + |A_4|^2)}. \quad (4.133)$$

Finally, we consider the overcoupling parameter (i.e. outcoupling efficiency) for our optomechanical system. As one might anticipate, the amount of overcoupling will be largest when the mean photon number is concentrated in the sub-cavity facing the output mirror. We can estimate the outcoupling efficiency by the ratio of light leaving through the output port (in this case port 2), as compared to the total loss through the mirrors

$$\eta_c = \frac{|t_2|^2 |A_3|^2}{|t_2|^2 |A_3|^2 + |t_1|^2 |A_2|^2}, \quad (4.134)$$

where  $t_i$  are the transmissivities of the mirrors.

With this, we now consider the dependence of all discussed parameters as a function of modulo  $2kz_m$ , assuming experimentally relevant parameters. In Fig. 4.14 an overview of the parameter dependencies is shown. Since the calculated modulations are for a thin ( $h = 15$  nm) membrane, the modulation of the parameters is modest. The input mirror (see Fig. 4.10 for overview) is here assumed to have a low transmissivity ( $|t_1|^2 = 50$  ppm), while the output mirror is set to have a transmissivity of  $|t_2|^2 = 230$  ppm.

As can be seen, the cavity linewidth and the outcoupling efficiency are at their largest at the same position in  $2kz$ . This is due to the fact that for this relative membrane position the sub-cavity facing the output mirror has a larger photon population than elsewhere in  $2kz$ . Importantly, this coincides with the negative slope of the frequency shift, offering an experimentally convening way to identify the cavity resonance with the largest outcoupling efficiency. The cavity linewidth modulation demonstrates one of the attractive features of our system – whether one is interested in a large(r) detection efficiency and quadrature rotations, or better sideband resolution (at the expense of a slightly reduced detection efficiency), a simple change from one cavity resonance to another will do the job.

### 4.5.1 Modal overlap

Separate and apart from the transfer matrix model, yet important in assessing the optomechanical coupling rate, is the question of spatial modal overlap between the optical and the mechanical modes. Thus far we have treated the intracavity field in more general terms, disregarding its spatial

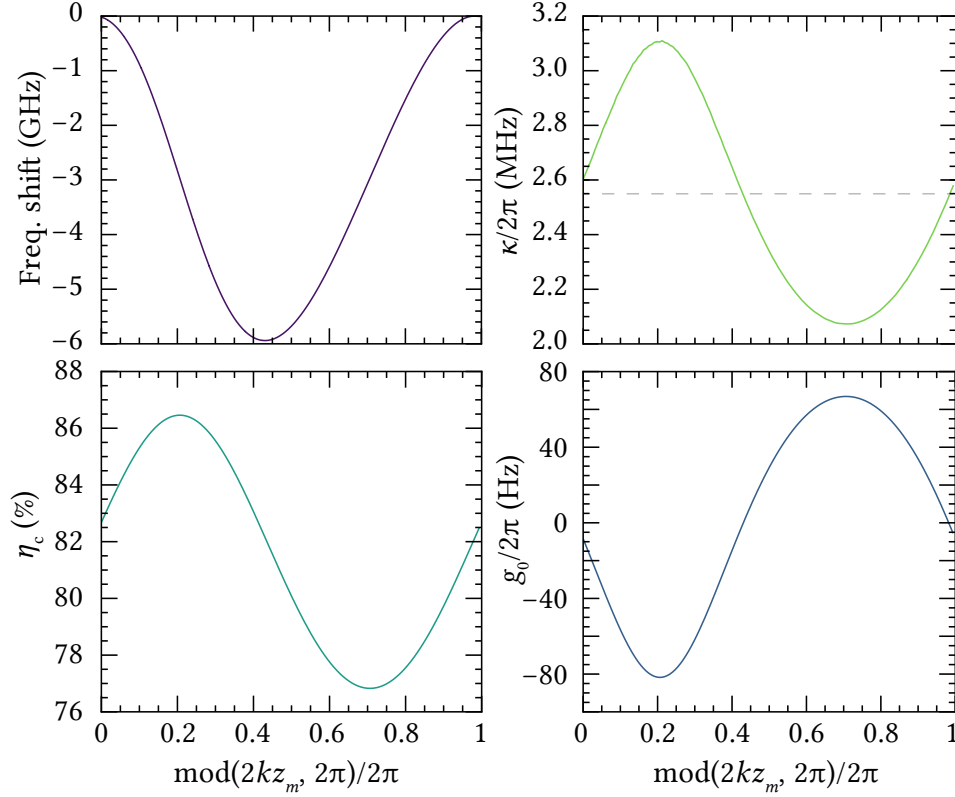


Figure 4.14: Modulation of membrane-in-the-middle cavity parameters, as a function of  $\text{mod}(2kz_m, 2\pi)$  (normalised to  $2\pi$ ). Here, the total cavity length  $L_{\text{cav}} = L_1 + L_2$  is assumed to be 2.62 mm, while  $z_m = 0.5$  mm. Furthermore, the following parameters are assumed in these calculations:  $h = 15$  nm,  $n_{\text{SiN}} = 2$ ,  $|t_1|^2 = 50$  ppm,  $|t_2|^2 = 230$  ppm,  $\Omega_m = 2\pi \times 1.475$  MHz,  $m_{\text{eff}} = 2$  ng (the latter two are used in estimating the zero-point motion of the membrane). The dashed line in the top-right figure indicates the bare cavity linewidth,  $\kappa_0 = 2\pi \times (c/2L_{\text{cav}})/(|t_1|^2 + |t_2|^2)$ , where we have used the definitions of finesse following Eq. (4.9).

form. However, the intracavity field has a transverse distribution, which can be described by a Gaussian distribution [177]

$$I(x, y, z_m) = P \underbrace{\frac{2}{\pi w^2(z_m)} e^{-2(x^2+y^2)/w^2(z_m)}}_{\phi(x,y)}, \quad (4.135)$$

where  $w(z_m)$  is the beam waist (radius) at the membrane position,  $P$  is the total optical power through the plane, and  $\phi(x, y)$  is the normalised intensity profile. As one might anticipate, the finite extent of the optical beam results

in a spatial averaging of the membrane displacement field. Hence, the average displacement, as “seen” by the light, is smaller, as compared to a point-like probe, focused on a position of the membrane with the largest transverse displacement.

We can cast this intuition into a formula, following our definition of the effective mass

$$m_{\text{eff}} = \rho \int \left( \frac{|\mathbf{Q}|}{|\mathbf{Q}|_{\text{max}}} \right)^2 dV, \quad (4.136)$$

where  $|\mathbf{Q}|$  is the displacement field of a particular vibration mode of the membrane. In reality, our optical beam doesn’t sample a single point on the membrane, indicated above with  $|\mathbf{Q}|_{\text{max}}$ , but a weighted average over the area of the optical beam. Naturally, the weighting is described by the Gaussian distribution of the optical intensity profile, which motivates the following re-definition of the effective mass

$$\tilde{m}_{\text{eff}} = \rho \int \frac{|\mathbf{Q}|^2}{\left( \int_A |\mathbf{Q}(x, y)| \phi(x, y) dA \right)^2} dV, \quad (4.137)$$

$$= \rho \int \frac{|\mathbf{Q}|^2}{|\mathbf{Q}|_{\text{max}}^2 \left( \int_A |\psi(x, y)| \phi(x, y) dA \right)^2} dV, \quad (4.138)$$

$$= \left( \int_A |\psi(x, y)| \phi(x, y) dA \right)^{-2} \rho \int \left( \frac{|\mathbf{Q}|}{|\mathbf{Q}|_{\text{max}}} \right)^2 dV, \quad (4.139)$$

$$=: \eta_{\text{om}}^{-2} m_{\text{eff}}, \quad (4.140)$$

where  $\psi(x, y) = |\mathbf{Q}|/|\mathbf{Q}|_{\text{max}}$  is the normalised displacement field of the membrane mode, and  $\eta_{\text{om}}$  is defined as the overlap integral between the normalised optical and mechanical modes. Since the effective mass appears in the definition of the zero point motion, this result furthermore suggests that the optomechanical coupling rate will have the following dependence on the spatial overlap

$$\tilde{g}_0 = \eta_{\text{om}} g_0. \quad (4.141)$$

As an example, we consider the magnitude of this effect for our membrane-in-the-middle system. First, a few general points regarding the optical part of this story. For a plano-concave cavity configuration, which this work is based on, the beam waist (on the flat mirror) is given by the following expression [177]

$$w_0 = \sqrt{\frac{\lambda L_{\text{cav}}}{\pi}} \left( \frac{R}{L_{\text{cav}}} - 1 \right)^{1/4}, \quad (4.142)$$

Frequency (MHz)	$\eta_{\text{om}}$ (%)	$m_{\text{eff}}$ (ng)	$\tilde{m}_{\text{eff}}$ (ng)
1.668	81.96	2.00	2.98
1.699	$1.90 \times 10^{-3}$	2.78	$7.67 \times 10^9$
1.787	$1.07 \times 10^{-3}$	2.61	$2.26 \times 10^{10}$
1.787	$4.31 \times 10^{-3}$	1.97	$1.06 \times 10^9$
1.798	$1.21 \times 10^{-4}$	2.50	$1.72 \times 10^{12}$

Table 4.1: Modal overlaps for the five localised modes of a third generation soft clamped membrane resonator, assuming a Gaussian beam centred on the defect. The parameters used in this calculation are:  $w_0 \approx 45.644 \mu\text{m}$ ,  $\lambda = 852 \text{ nm}$ ,  $h = 15 \text{ nm}$ ,  $a = \sqrt{3} \times 90.125 \mu\text{m}$ ,  $\sigma = 1.17 \text{ GPa}$ .

where  $R$  is the radius of curvature of the concave mirror, while  $L_{\text{cav}}$  is the total cavity length. In our case, the radius of curvature of the concave mirror is 25 mm, and the cavity length is approximately 2.64 mm in length, amounting to a beam waist of  $w_0 \approx 45.6 \mu\text{m}$  at a wavelength of 852 nm. The position dependence of the beam waist is described in terms of the Rayleigh length (which is related to the divergence angle of the beam) as follows

$$w(z) = w_0 \sqrt{1 + (z/z_R)^2}, \quad (4.143)$$

where the Rayleigh length is expressed in terms of the beam waist and the last wavelength,  $z_R = \pi w_0^2/\lambda$ . For our cavity parameters, the Rayleigh length is approximately 7.5 mm. With the membrane located 500  $\mu\text{m}$  from the flat mirror, we find that the beam waist at the membrane position is only  $\sim 0.2\%$  larger than on the flat mirror.

We are now in a position to calculate the mode overlap for a soft clamped resonator, assuming a beam waist of  $w_0 \approx 45.6 \mu\text{m}$ . In Table 4.1 the results for the five localised vibrational modes are shown. As anticipated, the fundamental-like mode has the largest overlap with the Gaussian beam (which is placed at the centre of the defect), while the other vibrational modes have a negligible overlap, since their respective mode shapes has a nodal line at the centre. According to Eq. (4.141) an  $\sim 82\%$  overlap would lead to a  $\sim 20\%$  decrease in the single photon coupling rate. Comparing to Fig. 4.14 this means that the largest optomechanical coupling rate would be reduced from  $g_0 \sim 2\pi \times 80 \text{ Hz}$  to  $\tilde{g}_0 \sim 2\pi \times 65 \text{ Hz}$ .

### Limits on quantum cooperativity

With the above insight, we now look back at the discussion regarding static bistability, in particular Eq. (4.48). The question we wish to answer is the

Frequency (kHz)	$\eta_{\text{om}}$ (%)	$m_{\text{eff}}$ (ng)	$\tilde{m}_{\text{eff}}$ (ng)
104.75	99.92	82.48	82.62
165.07	$1.56 \times 10^{-4}$	83.50	$3.45 \times 10^{13}$
165.77	$3.14 \times 10^{-3}$	83.41	$8.45 \times 10^{10}$
209.39	$6.41 \times 10^{-3}$	83.68	$2.04 \times 10^{10}$
233.30	99.61	68.63	69.17

Table 4.2: Modal overlaps for the five lowest vibrational modes of a third generation soft clamped membrane, assuming a Gaussian beam centred on the defect. The parameters used in this calculation are:  $w_0 \approx 45.644 \mu\text{m}$ ,  $\lambda = 852 \text{ nm}$ ,  $h = 15 \text{ nm}$ ,  $a = \sqrt{3} \times 90.125 \mu\text{m}$ ,  $\sigma = 1.17 \text{ GPa}$ .

following – what are the “limitations” on the highest attainable quantum cooperativity for our system<sup>11</sup>? Similar to the discussion above, we now compute the overlap integrals for the low-frequency (drum) modes of the entire membrane structure. For simplicity, we only consider the lowest five vibrational modes. In Table 4.2 the results of this simulation are presented. Recalling that the maximum quantum cooperativity can be estimated by the ratio of the spring constants (cf. Eq. (4.48))

$$C_q^{\text{onset}} = \frac{2}{\sqrt{3}} \frac{\tilde{k}_{\text{eff}}}{k_{\text{eff}}} \frac{\hbar}{k_{\text{B}}T} Q \times \Omega_{\text{m}}, \quad (4.144)$$

we can now estimate the ratio of the spring constants. Following the estimates in Table 4.2, we predominantly care about the effective spring constant of the first drum mode of the entire membrane structure. We find that  $\tilde{k}_{\text{eff}} = \tilde{m}_{\text{eff}} \tilde{\Omega}_{\text{m}}^2 \approx 35.79 \text{ N/m}$ , while the effective spring constant of the fundamental-like localised mode is  $k_{\text{eff}} \approx 436.17 \text{ N/m}$ . This clearly suggests that the lowest order vibrational mode of our mechanical resonator ultimately sets the limit on how much light can be injected into the system, before static bistability sets in. Assuming a mechanical quality factor of  $Q = 10^9$ , the highest attainable quantum cooperativity at 10 K is  $C_q^{\text{onset}} \approx 759$ . This is an encouraging result, which suggests that a MIM system based on soft clamped membranes can be operated deep within the backaction dominated regime, despite the “floppy” low-frequency modes of the membrane structure.

With this final piece of the puzzle in place, we are now ready to consider the experimental realisation of such a system.

<sup>11</sup>In this paragraph, “maximum quantum cooperativity” rather indicates the quantum cooperativity at the onset of static bistability.

## 4.6 Experimental realisation

At a first glance, the membrane-in-the-middle configuration is rather straightforward and merely requires “sandwiching” two high-reflective mirrors, alongside a pristine mechanical resonator. However, as it turns out, the devil is in the detail, and seemingly minor differences in cavity assembly can have a profound effect on the stability and reproducibility of the system. In the following, we discuss the particularities of our cavity realisation and the underlying reasons for these choices.

We then proceed to describing how we perform basic characterisation of our optomechanical system, which involves identifying the most favourable position in  $2kz_m$  and assessing key system parameters at said  $2kz_m$  position (cavity linewidth, detuning, light-enhanced coupling rate).

### 4.6.1 Optomechanical cavity

Within the sub-field in optomechanics that deals with membrane-in-the-middle systems, one can find a handful of modalities as it pertains to cavity assembly. In a majority of cases, the membrane resonator is mounted on a motorised stage, allowing for a complete control of the membrane position, as well as its tilt. Such an approach has been initially adapted by the group of Jack Harris [176, 178] and has the advantage of large tuneability. However, since the vast majority of quantum optomechanical systems operate in cryogenic settings, having a bulky motorised stage inside a cryostat can be problematic, both from the standpoint of thermalisation, as well as vibration stability.

In order to reduce the amount of material that needs to be thermalised within the cryostat, several groups have adapted the option of gluing the membrane resonator chip to a ring piezo, which is subsequently placed between the cavity mirrors (see for instance [179]). While this reduces the amount of material within the cryostat that requires cooling, it re-surfaces the issues of membrane alignment and, importantly, tilt. As reported by Jack Sankey and colleagues [180], tilting the membrane within the cavity has the effect of shifting higher-order Hermite-Gaussian modes of the cavity in wavelength, which can lead to mode crossings between the  $\text{TEM}_{00}$  mode of the cavity and the higher order optical modes. These avoided crossings can lead to additional optical losses of the  $\text{TEM}_{00}$  mode, which, as we saw in the section on ponderomotive squeezing, washes out hard-earned quantum correlations. This issue can be addressed to some extent by using low-CTE materials (e.g. invar) in constructing the cavity assembly. With that, one can in principle align away membrane tilt at room temperature, before cooling

it down, relying on the low expansion coefficient of the underlying structure to preserve said alignment. This, unfortunately, re-surfaces the previous problem of thermalisation, since materials with a low coefficient of thermal expansion tend to have a poor thermal conductivity.

This brings us to the experimental realisation of a MIM cavity adapted by the groups of Eugene S. Polzik and Albert Schliesser, the idea of which originates from Dalziel Wilson, a former postdoc in Eugene Polzik’s lab. Our cavity assembly is designed to address both of the above mentioned issues. By mechanically clamping the flat (output) mirror to the membrane chip, with a single silicon spacer between, we address the issue of parallelity and its thermal stability. Here, we rely on the fact that the mirror surface, as well as the silicon substrates, are flat, and misalignment only originates from specs of dust or other contaminants trapped between these surfaces. This sandwich of spacers, membrane chip and mirror is mechanically clamped inside a copper sample holder. This choice of material provides us with a strong thermal link between the cold finger of the cryostat and the membrane resonator. A cross-sectional view of the sampleholder is shown in Fig. 4.15. The continued parallelity between the flat mirror and the silicon substrate can be achieved by a spring-like object underneath the flat mirror (here, shown as an o-ring). This is particularly important for cryogenic cycling, since the surrounding copper does deform as we cool down from room temperature to 4.2 K. For further details regarding our “monolithic” cavity assembly, see the PhD thesis of William H. P. Nielsen [108].

The mirrors used in our cavity are super-polished mirrors from Advanced Thin Films (ATF), where the curved mirror has a radius of curvature of 25 mm. As for the flat mirror, our starting point was a 1 mm thick 4” glass wafer with the high reflective coating on one side, specified to have transmission of  $250 \pm 50$  ppm, and an anti-reflection (AR) coating on the opposite side. Since assembling a cavity with a 100 mm large glass wafer is impractical, to say the least, we first need to mill out smaller mirrors from the wafer. To avoid damaging the mirror coating, we spin coated a thick layer of photoresist on both sides of the wafer, and use crystalbond to attach the mirror wafer to a carrier glass wafer. The latter is subsequently glued to a metal carrier, compatible with the milling machine, where circular disks are carved out of the mirror wafer (see Fig. 4.16). Once the individual mirrors have been removed from the carrier wafer, we follow a combination of cleaning procedures described in Chapter 3. First, the mirrors are rinsed in deionised water, to remove larger contaminants. We proceed by cleaning the mirrors in NMP, followed by a rinse in isopropanol and deionised water. Since the capping (top) layer of the mirror coating is  $\text{SiO}_2$  (specified by ATF), we

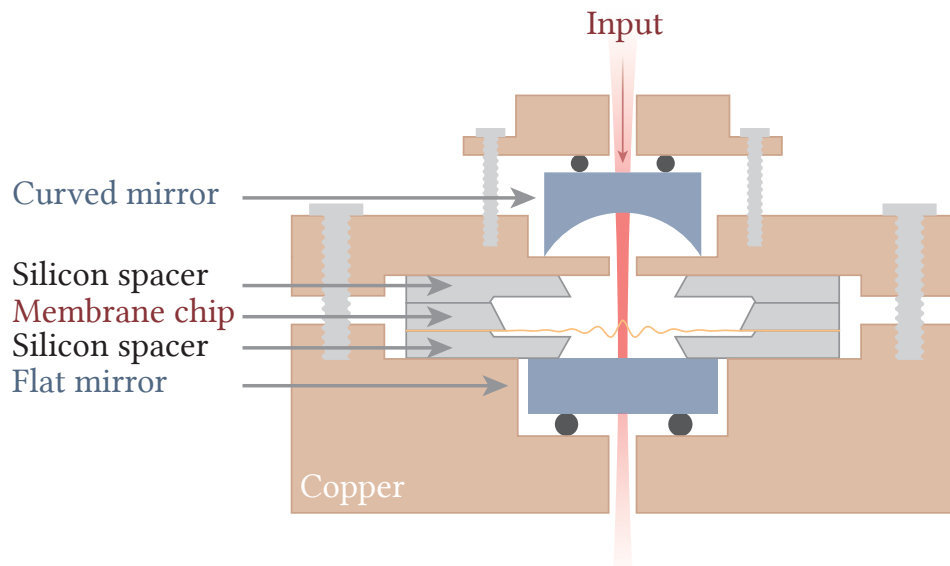


Figure 4.15: Cross sectional view of the “monolithic” cavity assembly. The flat (output) mirror is pressed against a silicon spacer, which, in turn, is pressed against the membrane chip. The sandwich of spacers is rigidly clamped with the surrounding copper sample holder. The copper sample holder is subsequently mounted to the cryostat cold finger.

clean the mirrors in a piranha solution, to remove all photoresist and milling related residues.



Figure 4.16: Flat high reflective mirrors, carved out from a 4” glass wafer with a mirror coating. On the left is shown the mirror immediately after milling, and on the right is the mirror following a cleaning procedure involving NMP and piranha solution. The mirrors are  $\sim 8$  mm in diameter and 1 mm in thickness.

After cleaning the mirrors, we perform transmission measurements for different wavelengths in order to verify that the cleaning procedure has not

damaged the coating quality. Seeing that the specified transmissivity is  $250 \pm 50$  ppm, we perform said measurement using a powermeter<sup>12</sup>. The light source used for all our measurements is a Ti-Sapphire laser<sup>13</sup>, which provides wide wavelength tuneability (from 740 nm to 920 nm), as well as low phase- and amplitude noise, which we will touch upon towards the end of this chapter. For different laser wavelengths we measure the mirror transmissivity, immediately followed by a reference measurement where the flat mirror is removed. The result of this measurement is shown in Fig. 4.17, alongside the transmissivities provided by ATF, indicative of the quality of this coating run. Our measurement suggests that the mirror transmission at 852 nm wavelength is  $252 \pm 5$  ppm, whereas the datasheet suggests a value of  $\sim 241$  ppm. While our data deviates appreciably from the datasheet for wavelengths between 815 nm and 850 nm, it remains within the specified tolerance level of  $\pm 50$  ppm. We thus conclude that our milling and cleaning procedure introduces (little to) no additional optical losses.

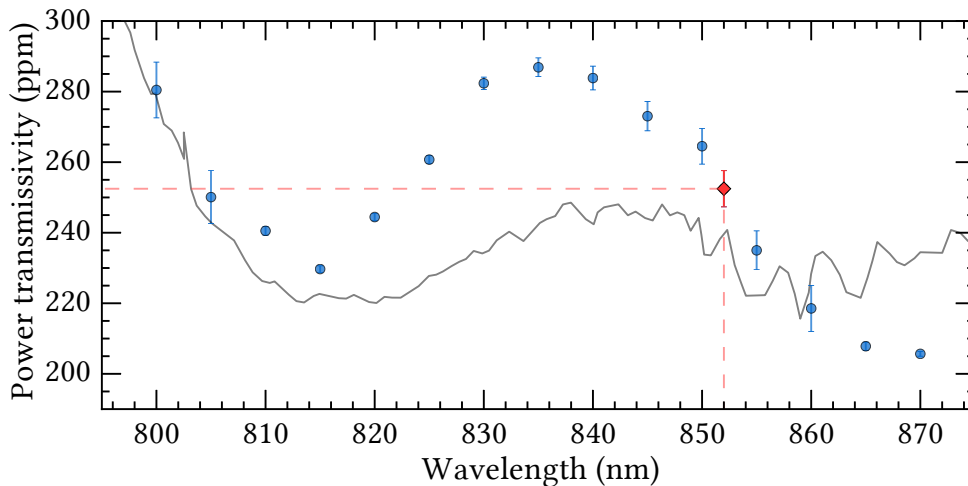


Figure 4.17: Measured power transmissivity of a flat ATF mirror after cleaning with NMP and piranha. The red (diamond) point corresponds to the operational wavelength of our experiment (852 nm), with the dashed line as a guide to the eye. The solid line is extracted from the datasheet provided by ATF.

Once the membrane chip and the spacers have been stacked on top of the flat mirror and clamped down, we can verify that the membrane is in-

<sup>12</sup>Thorlabs PM100A.

<sup>13</sup>MSquared SolsTiS SA PSX-R.

deed parallel to the mirror by imaging the membrane, upon illuminating the etalon formed by the membrane and the flat mirror with a wide laser beam. Averaging over several wavelengths, we indeed find negligible tilt in our assembly. Based on the interference pattern shown in Fig. 4.18b, indicating a single interference fringe over a distance of  $\sim 2$  mm, we estimate a tilt of  $\sim 0.5$  mrad between the membrane surface and the flat mirror.

Finally, we position the curved mirror such that the beam spot of the  $\text{TEM}_{00}$  mode is centred on the defect. Once the mirror has been clamped down, the cavity alignment can be maintained over a prolonged period of time. In Fig. 4.18c an image of the membrane is shown, alongside the  $\text{TEM}_{00}$  mode.

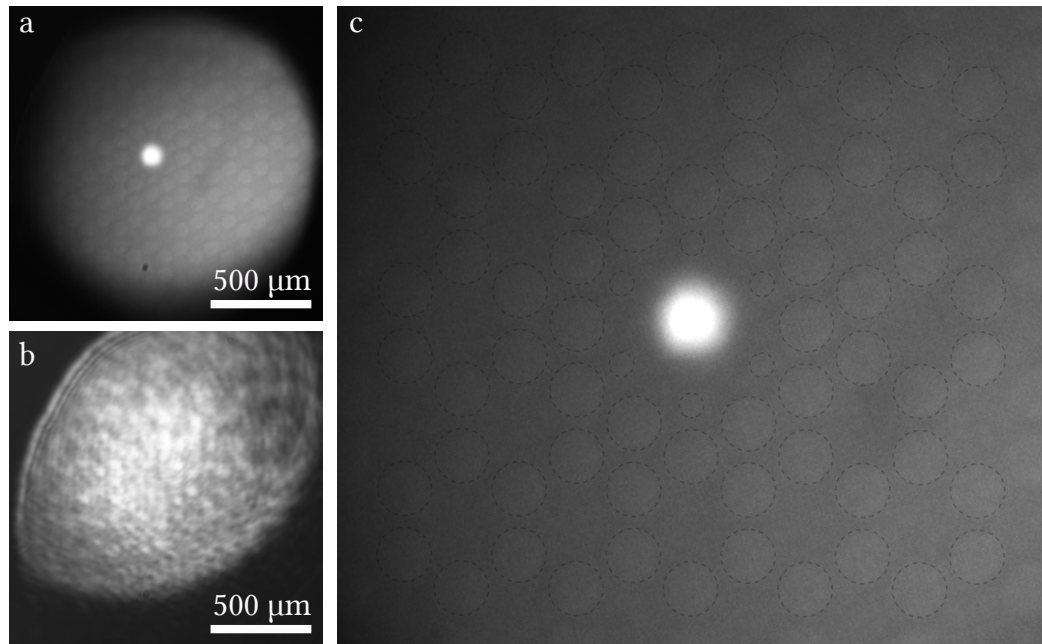


Figure 4.18: a) Direct image of the membrane stacked on top of the flat mirror (without the curved mirror in place). b) Interference pattern as a result of tilt between the flat mirror and the membrane along each diagonal of the image. The center brightness is the anti-node of fringes along both diagonals. The image is an average of 21 individual images acquired over a wavelength span of 1 nm. c) Image of the membrane after completed assembly, with the  $\text{TEM}_{00}$  seen in the centre. Dashed circles have been added as a guide to the eye.

### Clipping losses

As Fig. 4.18c suggests (despite the saturation), our optical beam spot is in fact appreciably large compared to the overall defect size. We therefore wish to estimate the optical losses associated with the overlap of our Gaussian mode with the phononic crystal holes. Following Eq. (4.135) we can estimate the transmitted power through an aperture of area  $A$ , oriented in the  $xy$  plane at the membrane position  $z = z_m$ , as

$$P_{\text{out}} = \int_A I(x, y, z_m) dA. \quad (4.145)$$

Now, we treat the phononic crystal holes as apertures (i.e. any fraction of light overlapping with a hole is forever lost) and calculate the single pass optical loss, as well as the associated finesse (see Eq. (4.9)), assuming the losses due to clipping are the only losses in the cavity. While the assuming that that light is permanently lost when it overlaps with a hole results in a conservative estimate, it can nevertheless give us a rough sense of the potential limitations for a given assembly. Fig. 4.19 shows the result of such a simulation. Evidently, for our combination of device and beam spot size we can anticipate  $\lesssim 30$  ppm single-pass losses in our cavity due to clipping of the optical beam. It goes without saying that this is not a desirable scenario for a quantum optician, who desperately counts every iota of optical loss and tries to eliminate it. However, the cavity parameters and its performance as they are presented in this work should rather be perceived as a “status update” towards a bigger goal (which we will return to later), rather than the end destination. For now it suffices to say that the current choice of membrane dimensions have largely been dictated by a dense spectrum of mirror modes.

### 4.6.2 Measurement of optomechanically induced transparency

As previously mentioned, one of the more convenient diagnostic tools within our toolkit is that of optomechanically induced transparency, which we use in measuring cavity linewidth  $\kappa$ , cavity detuning  $\bar{\Delta}$  and light enhanced coupling rate  $g$ . From the theoretical treatment of OMIT in Section 4.4.2, recall that the cavity response to an input field with a weak phase modulation consists of two components – the overall cavity response, described by the function  $C(\Omega)$  (cf. Eq. (4.93)), and a narrow-band feature associated with mechanical resonances described by the function  $M(\Omega)$  (cf. Eq. (4.94)). The cavity response does, however, depend on the incoupling cavity rate,  $\kappa_R$ . However, as we discussed in Section 4.5, the outcoupling efficiency, and

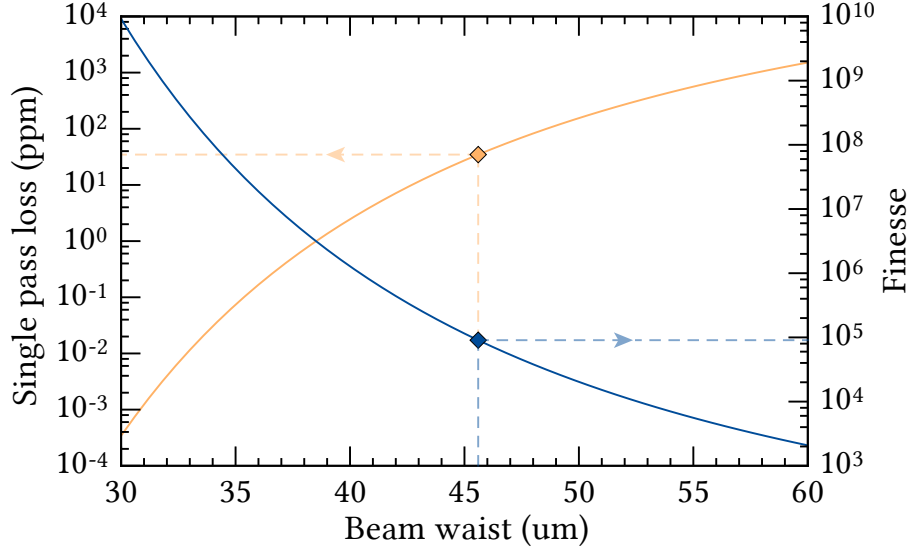


Figure 4.19: Upper bound single pass optical losses (and resultant maximum cavity finesse) for a cavity mode of varying beam waist passing through a membrane aperture.

therefore also the incoupling efficiency, of our cavity depends on the  $2kz_m$  position of the particular optical resonance. Fortunately, we can render this lack of information redundant by a simple normalisation. Seeing that the overall response of the cavity is largely dominated by the envelope function  $C(\Omega)$  (see Fig. 4.8 as a reference), we normalise the response, before fitting said function to the cavity response with two unknowns – the cavity linewidth and laser detuning.

In practice, the measurement is performed as follows. Light from our Ti:Sapphire laser is passed through a fiber EOM (phase modulator), before it is coupled into the optomechanical cavity. The transmitted light is collected at the cavity output using an avalanche photodetector<sup>14</sup>, while a small percentage ( $\ll 1\%$ ) of the light is used for imaging of the cavity modes, helping us in identifying the TEM<sub>00</sub> resonances. The photodetector signal is split between our acquisition system (i.e. oscilloscope, data acquisition (DAQ) card and/or network analyser) and a high-speed proportional integral controller<sup>15</sup>, the output of which is fed to the piezo of our laser resonator. All results presented in this chapter are based on a wide (with respect to the mechanical frequency) cavity resonances, and hence a simple transmission

<sup>14</sup>Thorlabs APD430A/M.

<sup>15</sup>New Focus LB1005-S.

lock is used in stabilising the laser to our cavity<sup>16</sup>. Once the cavity is locked, part of the photodetector signal is sent to a network analyser, the output of which is fed into the RF input of the EOM. We then apply a weak ( $-20$  dBm or lower) RF tone to the EOM, thus generating sidebands at  $\omega_L \pm \omega_p$ . The RF tone is swept, while demodulating the signal from the photodetector. Finally, the acquired cavity response is normalised to the integrated response and fitted to the envelope function,  $C(\Omega)$ .

The outcome of such a measurement is shown in Fig. 4.20a for three different laser detunings. While the envelope function seemingly fits all three curves equally well, a closer look at the linewidths extracted from our fits in Fig. 4.20b strongly suggests that for detunings larger than the cavity linewidth this approach is unreliable. For detunings smaller than  $-2.5$  MHz the relative error in the estimated linewidths is  $\sim 1.6\%$ .

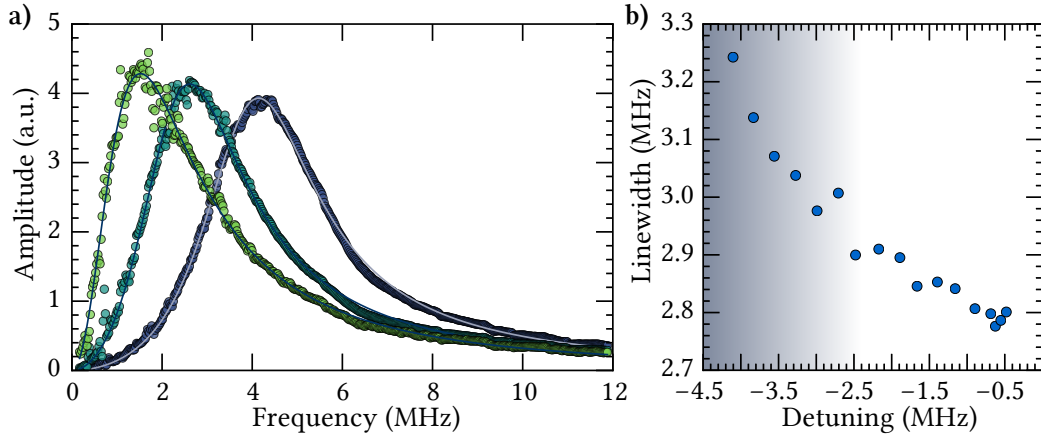


Figure 4.20: (a) Cavity detuning and linewidth from broadband driven cavity response for three different detunings. (b) Extracted cavity linewidth versus the fitted detuning. The overall systematic tendency is suspected to be due to the non-flat frequency response of the detector.

Once the cavity detuning and linewidth have been determined, the same measurement can be repeated in the vicinity of the mechanical mode. Having fixed two of the parameters associated with an OMIT feature, namely  $\kappa$  and  $\bar{\Delta}$ , the narrow-band measurement can be modelled by Eq. (4.94), yielding the light-enhanced coupling rate  $g$ . This will be of importance for the following section.

<sup>16</sup>Typical bandwidth of our feedback loop is  $\lesssim 10$  kHz

### 4.6.3 Modulation in $2kz_m$ and measurement of $g_0$

The measurements presented above were taken for a cavity resonance, disregarding the relative position of the membrane with respect to the optical standing wave. However, since our system parameters depend strongly on the position in  $2kz_m$ , it is important to identify the most favourable optical resonance. Here, we rely on the theory and intuition described in Section 4.5. Since the membrane associated with this measurement is on the order of 15 nm thin<sup>17</sup>, we can reliably use the approximate solution for the resonance frequency shift (see Eq. (4.129)) as our starting point. Let us first rewrite said expression, in order to motivate our measurement procedure. Multiplying both sides of Eq. (4.129) with  $c/2\pi$  and using our definition of FSR (cf. Eq. (4.6)) yields

$$f_{\text{res}} = f_{0,n} + |r_m| \frac{\text{FSR}}{\pi} \sin(2k_{0,n}z_m). \quad (4.146)$$

Using the fact that the (bare) cavity resonances are to evenly spaced with an FSR, implying that  $f_{0,n+m} = f_{0,n} + m \times \text{FSR}$ , we make the substitution  $f_{0,n} \rightarrow \tilde{f}_{0,n} + m_{\text{res}}\text{FSR}$ , as well as  $k_{0,n} \rightarrow (c/2\pi) \times (\tilde{f}_{0,n} + m_{\text{res}}\text{FSR})$ , where  $m_{\text{res}}$  is an integer number, signifying the  $m$ 'th resonance from an arbitrary reference point,  $\tilde{f}_{0,n}$ . Eq. (4.146) can therefore be expressed as follows

$$f_{\text{res}} = \tilde{f}_{0,n} + m_{\text{res}}\text{FSR} + |r_m| \frac{\text{FSR}}{\pi} \sin(2\pi\tilde{z}_m m_{\text{res}} + \phi_0), \quad (4.147)$$

where  $\tilde{z}_m = z_m/L_{\text{cav}}$ , and  $\phi_0$  is a constant phase associated with our starting resonance point. For all intents and purposes this phase can be ignored in the process of folding.

The above expression suggests a pathway for measuring the relative position of our membrane within the cavity. Record the wavelength of successive cavity resonances, followed by a least square fit of Eq. (4.147) to said data, provides us with estimates of  $\tilde{z}_m$  and FSR. The combination of these quantities gives us an accurate estimate of the membrane position within the cavity. Folding the  $2kz_m$  values back into  $2\pi$ , as described in Section 4.5, provides us with a convenient representation of the relative membrane positions for each recorded wavelength. The result of such a measurement is shown in Fig. 4.21, alongside the underlying fit.

Equation (4.147) furthermore provides us with an estimate of the membrane reflectivity. From the fit in Fig. 4.21 we extract an amplitude reflectivity of  $|r_m| = (13.3 \pm 0.5) \%$ , which according to Eq. (4.122) corresponds to a membrane thickness of  $h = (12.0 \pm 0.4) \text{ nm}$ .

<sup>17</sup>This is estimated from etch rate of silicon nitride and initial film thickness.

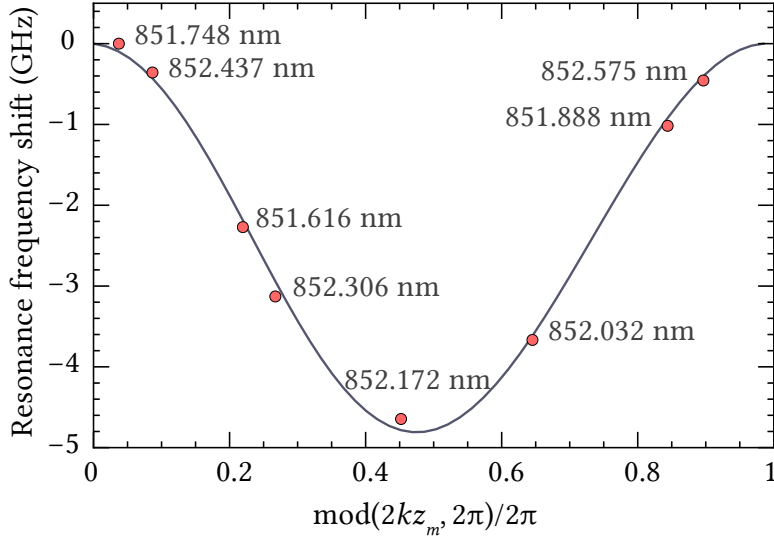


Figure 4.21: Cavity resonance wavelength measurements, alongside a sinusoidal fit following Eq. (4.147), folded back into  $2\pi$ . From the fit we find  $L_{\text{cav}} = 2.64$  mm and  $\tilde{z}_m/L_{\text{cav}} = 0.19$ .

We now perform OMIT measurements for all cavity resonances listed in Fig. 4.21. At each  $2kz_m$  position we perform two consecutive OMIT measurements – one of the broad cavity response, immediately followed by a narrow-band measurement in the vicinity of the membrane mode of interest (here, the fundamental-like localised mode). As previously mentioned, the broadband response provides us with the  $\kappa$  and  $\bar{\Delta}$ . With these parameters fixed, we can now extract the light-enhanced coupling rate through a fit of the narrowband OMIT feature. In Fig. 4.22 the result of one such measurement is shown.

Importantly, at each  $2kz_m$  position we also record the DC-voltage at the output of our detector and hence the optical power at the output of our optomechanical cavity. At each position we optimize the input cavity mode-matching and fix the optical power. The transmission, in conjunction with the cavity linewidth and the outcoupling efficiency, allows us to estimate the amount of intracavity power and hence the single photon coupling rate. However, in order to do so, we need to estimate the outcoupling efficiency at the respective  $2kz_m$  positions. With the above estimate of the membrane thickness, as well as the measured transmissivity of our input<sup>18</sup> and output mirror (see Fig. 4.17), we return to the transfer matrix model in order to

<sup>18</sup>The transmissivity of the input mirror has been estimated to be  $|t_{\text{in}}|^2 = 20$  ppm based on finesse measurements of an empty cavity consisting of two high-reflective mirrors.

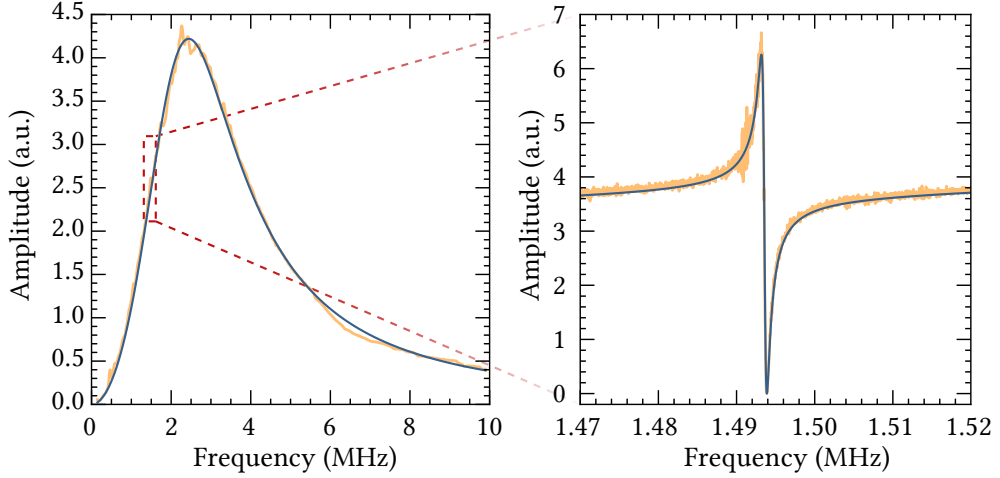


Figure 4.22: OMIT measurements at the  $2kz_m$  position corresponding to 851.616 nm. The broadband response (left) yields  $\bar{\Delta} = 2\pi \times -1.935$  MHz and  $\kappa = 2\pi \times 2.977$  MHz. From the narrowband response (right) we extract  $\Omega_m = 2\pi \times 1.494$  MHz and  $g = 2\pi \times 26.02$  kHz.

calculate the outcoupling efficiencies. Note that we do not assume additional optical losses due to clipping (cf. Section 4.6.1). Finally, to account for an overall phase-shift in  $2kz_m$ , we perform a least-square minimisation using the simulated and measured resonance frequency shifts, as well as cavity linewidths. With this in place, we can extract the relevant outcoupling efficiencies from our simulations. Using these values, combined with our OMIT measurements, we can estimate the mean intracavity photon number and thus  $g_0$ . Finally, we apply a correction factor to our simulated single photon coupling rates following our discussion on modal overlaps (cf. Table 4.1). The result of this analysis is shown in Fig. 4.23. The simulated resonance frequency shift and cavity linewidth show good agreement with measured values. The agreement between the measured and simulated linewidths is particularly notable, since it suggests that our estimate regarding clipping losses in Section 4.6.1 was somewhat pessimistic. With the exception of a single resonance, the agreement between our measurements and simulation is better than 10% across the board.

As for the outlier in terms of the cavity linewidth, we consider the optical modeshapes of two cavity resonances – the outlier, and its neighbour with comparable optomechanical coupling (see Fig. 4.24). The lossy optical mode shows a larger amount of speckles, which could be indicative of scattering into higher order optical modes. Since these modes are typically larger in terms of spatial extent, they are more likely to overlap with a larger fraction of

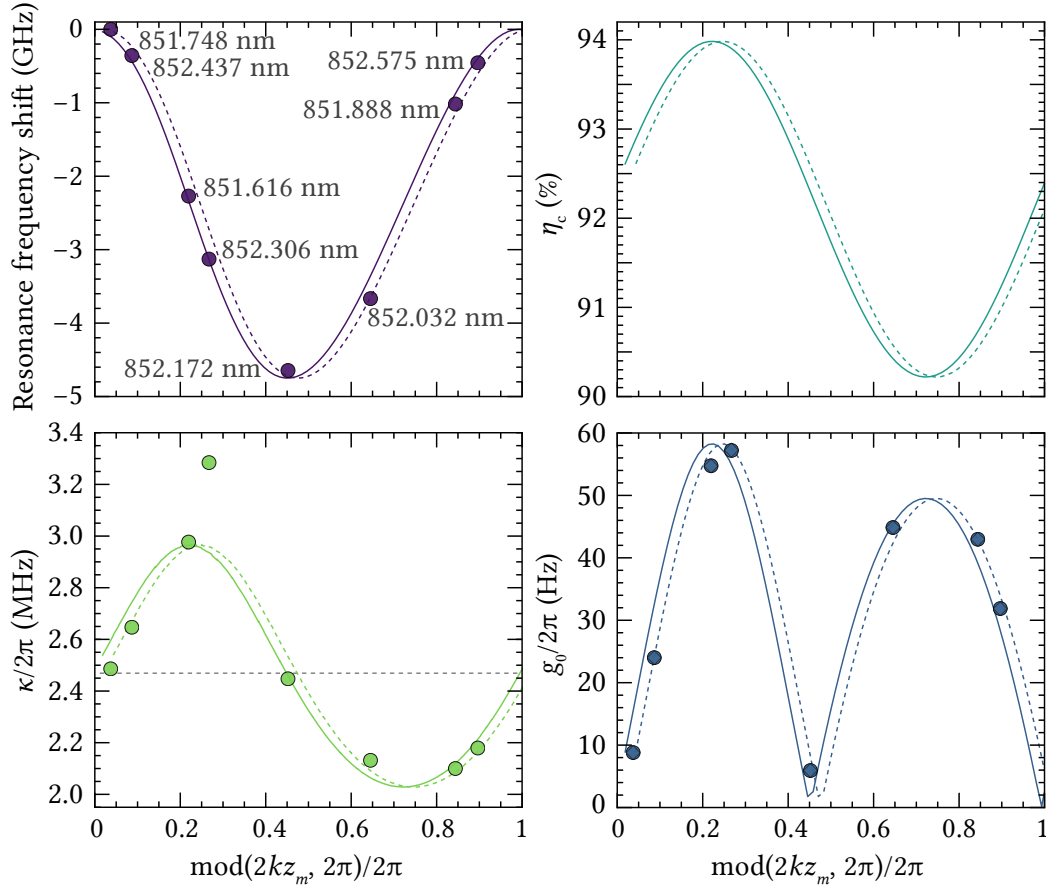


Figure 4.23: Measured and simulated values of resonance frequency shift, cavity linewidth, outcoupling efficiency and single photon coupling rate. Here we assume  $h = 12$  nm,  $|t_{\text{out}}|^2 = 252$  ppm,  $|t_{\text{in}}|^2 = 20$  ppm,  $L_{\text{cav}} = 2.64$  mm and  $z_m = 0.50$  mm, where the cavity length and membrane position are extracted from the fit shown in Fig. 4.21. The simulated curves have been shifted along the  $x$ -axis following a least square minimisation of either the resonance frequency shifts (solid) or cavity linewidths (dashed).

the perforated membrane region, as compared to the  $\text{TEM}_{00}$  mode. Further measurement and analysis would be required to test this hypothesis.

The analysis presented here suggests that we can indeed trust the system parameters estimated through OMIT. This is consistent with previous studies conducted in our research groups [14, 17].

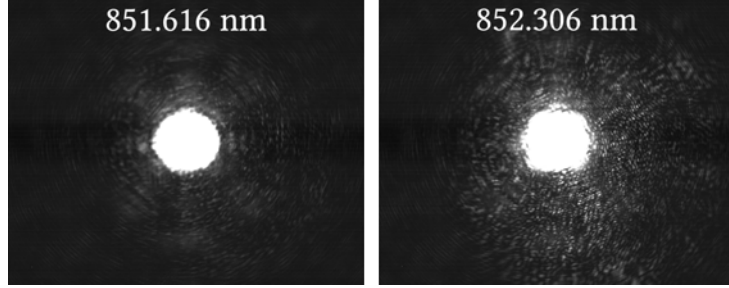


Figure 4.24: Images of optical mode shapes at the cavity output. Both cavity resonances represent a high-coupling point in  $2kz_m$  (cf. Fig. 4.23), with the main difference being in a  $\sim 300$  kHz additional optical loss associated with the mode on the right, which could be associated with the more pronounced patterns of speckles.

#### 4.6.4 Role of low-frequency membrane modes

As the reader might already suspect, for the most part we do not bother to think of the low-frequency vibrational modes of the entire membrane, and rather focus on the fundamental-like localised mode. However, there are a few instances where this is important. An example of this was discussed in Section 4.5.1, where we concluded that the largest attainable quantum cooperativity in our system is in fact limited by the fundamental mode of the perforated membrane structure. Here, we touch upon two additional instances where paying attention to these modes can be of importance.

First, we consider the output cavity fluctuations for varying laser detunings. As described above, light is injected into the cavity from the high-reflective port (i.e. through the curved mirror) and detected in transmission using an avalanche photodetector. Part of the output signal is sent to a DAQ card<sup>19</sup>, whereafter the power spectral density (i.e. the periodogram) is computed. Repeating this measurement for detunings ranging from  $-4.1$  MHz to  $-0.48$  MHz provides with a broadband map of spectral noise evolution. In Fig. 4.25 we show the result of such a measurement, where we highlight the bandgap region, as well as the frequency region in the vicinity of the fundamental mode of the entire membrane structure. We notice that for  $\bar{\Delta} < -\kappa/2$  the bandgap is populated by a forrest of peaks. However, past a certain detuning, these peaks seem to disappear. Interestingly, this coincides with a similar trend at lower frequencies. Upon a closer inspection we find that this is correlated with a reduction in the amplitudes of the low frequency modes (see Fig. 4.26). The abrupt change in the spectral composition

<sup>19</sup>Spectrum M2i.4931-exp.

within the bandgap suggests that the spurious peaks are a result of nonlinear mixing processes (optical or mechanical), involving the low frequency vibrational modes, and can be mitigated by reducing their amplitudes through backaction cooling.

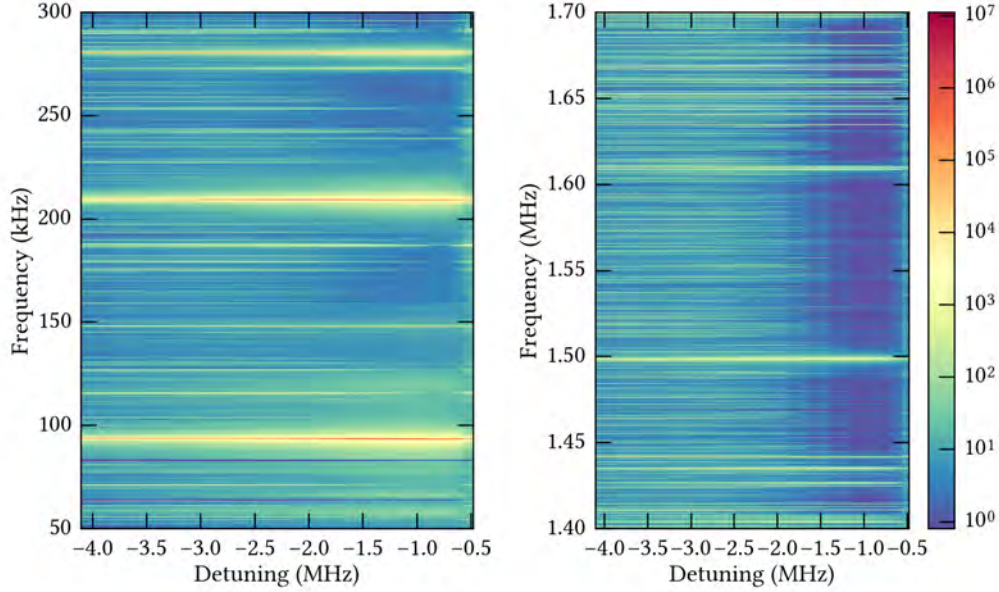


Figure 4.25: Normalised power spectral densities of the output cavity fluctuations, for varying cavity detunings. On the left is shown the “spectrogram” near the lowest order modes of the entire membrane structure (where the fundamental mode is  $\sim 100$  kHz), while the figure on the right shows the frequency regions near the phononic bandgap. As the detuning is decreased, we see a distinct reduction of spurious peaks inside the phononic bandgap. This coincides with a similar reduction in the number of noise peaks in the lower frequency band (left).

A second consideration is concerned with the optical spring effect of the lowest order membrane mode. Given its frequency, the mode is evidently in the unresolved sideband regime,  $\Omega_m \ll \kappa$ , where  $\Omega_m$  is the resonance frequency of the fundamental mode. A Taylor expansion of Eq. (4.63) in  $\Omega_m/\kappa$  yields

$$\delta\Omega_m \approx g^2 \frac{2\bar{\Delta}}{\bar{\Delta}^2 + (\kappa/2)^2}. \quad (4.148)$$

Combining this result with Eq. (4.46) for the maximum intracavity photon

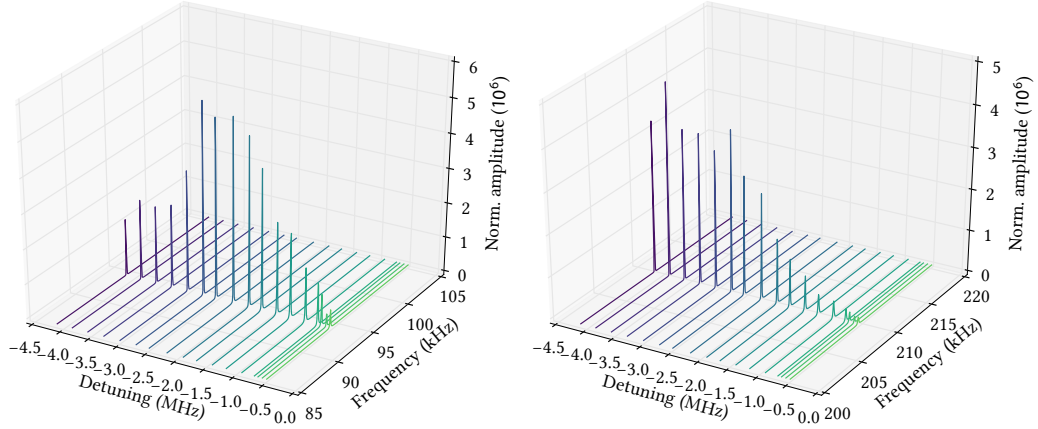


Figure 4.26: Normalised displacement spectra in the vicinity of the fundamental (left) and the third harmonic (right), as a function of cavity detuning. For detunings above  $\sim \kappa/2$  we see a clear reduction in the peak amplitude of the modes.

number, evaluated at the optimal detuning following Eq. (4.68), we find that

$$\delta\Omega_m^{\max} \approx -\Omega_m/2. \quad (4.149)$$

Hence we can anticipate an appreciate optical spring effect for measurements performed with high optical powers. Seeing that our starting point is typically a fundamental resonance frequency of  $\sim 100$  kHz or lower, the optical spring effect can shift the mode down to  $\sim 50$  kHz. Combined with the fact that the mode is broadened as a result of dynamical backaction, one must choose a feedback loop bandwidth for laser stabilisation which is sufficiently distant from the mode.

### 4.6.5 Cryogenic operation

With helium shortage being one of the hot topics these days within scientific circles, operating our optomechanical experiments in room temperature settings would be the preferred option. Unfortunately, the thermal noise of our cavity mirrors is too severe at room temperature to allow for quantum correlations to emerge, let alone survive. This is simply because the thermal fluctuations of the mirrors are written onto the phase of the intracavity light field, which, upon conversion to amplitude fluctuations, drives the membrane mode of interest. Hence, our experiments require cryogenic cooling. To this end we use a liquid helium flow cryostat<sup>20</sup> with a free-space optical

<sup>20</sup>Janis ST-100.

access. The low vibration levels of flow cryostats is the primary reason for this choice. To further reduce vibrations in our system, we maintain the helium flow by ensuring that the helium dewar is pressurised. In this regime we have consistently observed thermalisation of our membrane devices around  $\sim 10$  K [14, 17, 18, 18, 108, 175, 181]. Importantly, this was observed for membrane thicknesses between  $\sim 15$  nm and  $\sim 60$  nm. It is yet unclear why the thermalisation temperature is not closer to the cryostat base temperature of  $\sim 4.2$  K, but seeing that our assembly consists of two relatively large pieces of glass with poor thermal conductivity at cryogenic temperatures, it is conceivable that this is the culprit of the problem.

As for the specifics of our system, in particular when dealing with extremely thin samples (such as the one discussed in the previous section), a gentle cooldown rate of  $\sim 10$  K/min or lower is chosen, in order to avoid thermal shocks, which in most extreme cases can lead to rupture of the perforated membranes. Once the cavity resonances stop drifting over time, indicative of completed thermalisation, we maintain a moderate helium flow, in order to avoid additional vibrations [108], and begin cryogenic measurements.

#### 4.6.6 Cavity mirror noise

Reducing the temperature of our cavity inevitably reduces the thermal noise of our mirrors. But while the overall spectral weight is reduced, the individual vibrational modes of the mirrors can nevertheless be problematic. Similar to our discussion leading to the conclusion that a phononic crystal shield is important from the standpoint of spectral clarity, the same line of thought applies here. Our experiments typically require  $C_q \gg 1$ , which in practice involves broadening of the membrane mode. Therefore a clear spectral window of  $\gtrsim 50$  kHz is needed in our mirror vibrational spectrum.

Unfortunately, the dissimilar dimensions of our cavity mirrors results in a denser than usual mode spectrum. To illustrate this, we consider a cryogenic measurement of the same cavity previously described, but with the membrane removed, in order to see the cavity fluctuations only. Fig. 4.27 shows a calibrated spectrum of these fluctuations. Due to the monolithic nature of our assembly, we anticipate some degree of hybridisation between the mirrors and the silicon spacers (cf. Fig. 4.15), which can explain the observed bunching of vibrational modes.

Let us first get a sense for how large these fluctuations are, by considering their effect on the membrane mode of interest and how its minimum occupancy depends on these mirror noise induced phase fluctuations. For a given amount of intracavity phase noise the final occupancy of the resonator

(in the resolved sideband regime) can be expressed as follows [147, 182]

$$n_f \approx 2\pi \sqrt{\frac{\bar{n}_{\text{th}} \Gamma_m}{g_0^2} \bar{S}_{ff}(\Omega_m)}, \quad (4.150)$$

where  $\bar{S}_{ff}(\Omega_m)$  is the symmetrised power spectral density of frequency fluctuations evaluated at the resonance frequency of the membrane mode. Since the frequency fluctuations originate from the thermal motion of the mirrors, let us consider the scaling of the above expression with cavity. The spectral density scales quadratically with the optomechanical coupling rate of the mirrors [183], which means that  $\bar{S}_{ff}(\Omega_m) \propto g_{0,\text{mirror}}^2 \propto L_{\text{cav}}^{-2}$ . Of course, the optomechanical coupling rate of the membrane mode exhibits the same scaling with the cavity length, which suggests that the relative contribution of the mirror noise is unchanged upon cavity length change<sup>21</sup> Seeing that an increase in the cavity length results in a smaller free spectral range and hence cavity linewidth, bringing us to the resolved sideband regime, one could argue that using it for our cavity parameters is fair for a rough estimate. Now, assuming  $\bar{n}_{\text{th}} = 10^5$ ,  $\Gamma_m = 2\pi \times 1$  mHz and  $g_0 = 2\pi \times 10$  Hz, we find that  $2\pi \sqrt{\bar{n}_{\text{th}} \Gamma_m / g_0^2} = 0.5$ , suggesting that ground state cooling requires  $\bar{S}_{ff}(\Omega_m) \ll 4 \text{ Hz}^2/\text{Hz}$ . Looking at the scale of cavity fluctuations in Fig. 4.27 we therefore conclude that the valleys between the mirror modes is where our membrane mode should be placed.

At a first glance, the frequency window between  $\sim 1.05$  MHz and  $\sim 1.15$  MHz lends itself as a promising candidate. However, as we have previously reported [14, 17] (and will touch upon later in this chapter), our laser source has a non-negligible amount of classical noise at these frequencies, which would result in heating of the membrane mode of interest. With the current combination of cavity mirrors our choices are therefore quite limited. For now, we begrudgingly settle for the frequency window between  $\sim 1.45$  MHz and  $\sim 1.5$  MHz, but will return to the issue of mirror noise later in this chapter, offering a robust solution to the problem.

An example of an unfortunate frequency positioning of the membrane mode is shown in Fig. 4.28. Here, cryogenic performance of a third generation soft clamped membrane resonator is shown. While the mechanical quality factor of the two radial modes are perfectly suited for optomechanical experiments, a quick look at the vibrational mode spectrum reveals the mode perfectly overlaps with a forrest of mirror modes, rendering the membrane largely unusable for quantum optomechanical measurements. However, we

---

<sup>21</sup>This is strictly speaking not completely true, since the cavity acts as a low-pass filter. This means that in the resolved sideband regime the phase fluctuations are further suppressed due to the low-pass characteristic of the cavity.

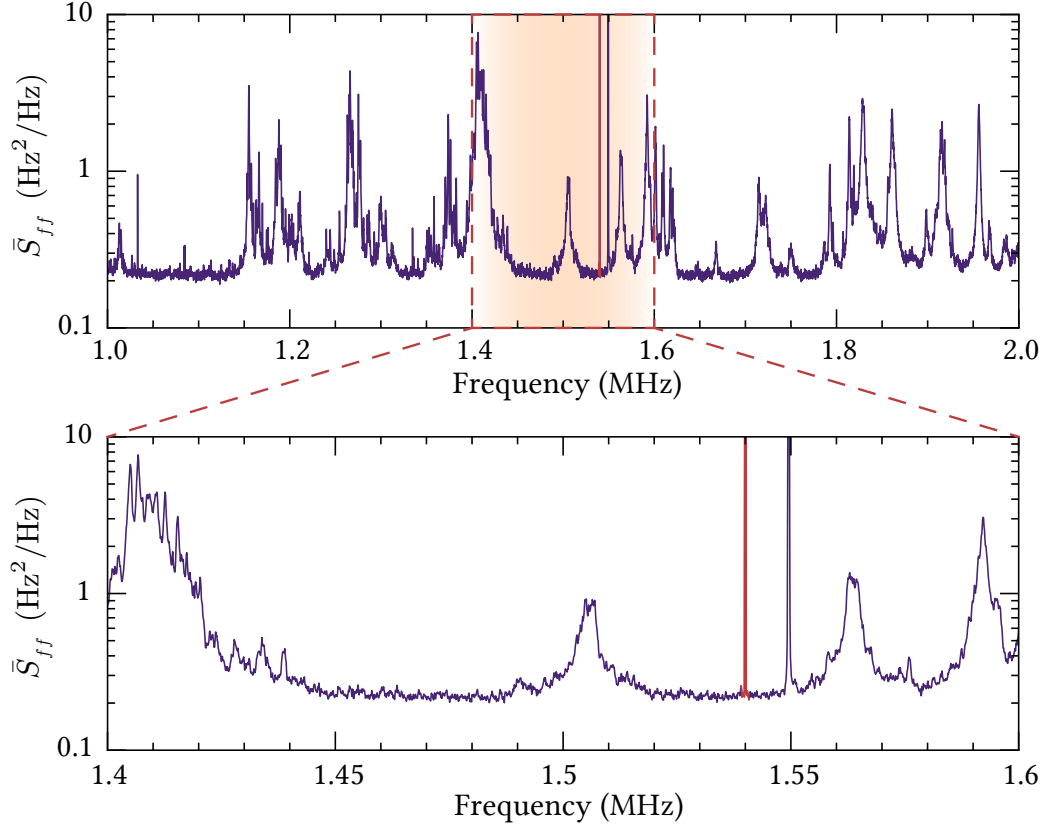


Figure 4.27: Vibrational spectrum of an empty cavity, calibrated using a known modulation depth of an electro-optic modulator (calibration tone at 1.54 MHz is highlighted in red). The highlighted portion of the spectrum represents our target region for the resonance frequency of the fundamental-like membrane mode.

note that this is in fact the highest mechanical quality factor measured to date with soft clamped membrane resonators. Furthermore, the measured quality factor agrees well with the predicted  $\sim 50\%$  improvement over second generation devices (see previous chapter), for which we have measured mechanical quality factors around  $10^9$  at cryogenic temperatures [17]. A device of comparable performance is characterised later in this chapter.

## 4.7 Ponderomotive squeezing

We now turn our attention to measurements of ponderomotive squeezing with soft clamped membranes. The main objective here is to compare the

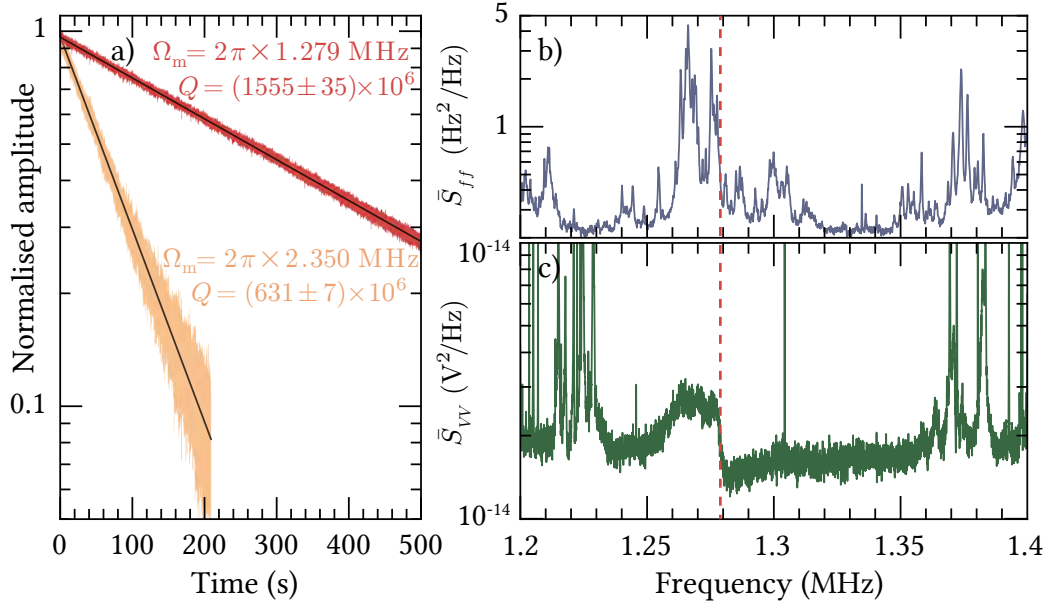


Figure 4.28: Cryogenic characterisation of a third generation soft clamped resonator. a) Ringdown measurements of the two radial localised modes are shown (left), alongside the respective mechanical frequencies and quality factors. b) Vibrational spectrum of an empty cavity in the vicinity of the first radial mode (cf. Fig. 4.27). c) Measured amplitude fluctuations at the output of the optomechanical cavity. The spectrum shows the first radial mode at  $\sim 1.28$  MHz, with a noise peak on its left wing.

performances of a second and a third generation membrane resonators, while operating in a high quantum cooperativity regime.

Our measurements are performed in cavity transmission using a home-built high-efficiency photodetector<sup>22</sup> based on Hamamatsu S5971 PIN photodiodes. Less than a percent of the transmitted light is picked off and directed to an APD, which is used for OMIT measurements. For each measured spectrum we perform an OMIT measurement immediately after, in order to determine  $\kappa$ ,  $\bar{\Delta}$  and  $g$ . Alongside a ringdown measurement, yielding  $\Gamma_m$ , all but two of the parameters in our squeezing model (cf. Eq. (4.116)) are fixed – the detection efficiency and the bath occupancy. The former we can typically estimate based on the outcoupling efficiency of our optomechanical cavity, optical losses between the cavity and the detector, as well as the detection efficiency of the detector.

It should be noted that our optomechanical system is placed separately

<sup>22</sup>We acknowledge J. Appel for help with the photodetector design.

from the Michelson interferometer used in the previous chapter for all characterisation measurements. Instead, we change the wavelength of our Ti-Sapphire laser by approximately 100 nm (typically down to  $\sim 740$  nm), where the cavity mirror coating are no longer high reflective<sup>23</sup>. Here, we have an effective interferometer, albeit with a poor sensitivity. This typically requires excitation of the mechanical mode to large amplitudes, in order to initially identify the mode of interest in a ringdown measurement. At these amplitudes the amplitude decay is initially nonlinear, due to non-negligible elongation losses within the resonator. To accurately determine the mechanical quality factor, we cross check the fit results of a simple exponential decay curve and a modified decay curve for the amplitude, which captures the initial nonlinear decay [184]

$$A(t) = \frac{A_0 e^{-\Gamma_m t/2}}{\sqrt{1 + \frac{\gamma_{\text{NL}}}{2\Gamma_m} A_0^2 (1 - e^{-\Gamma_m t})}}, \quad (4.151)$$

where  $A_0$  is the initial amplitude and  $\gamma_{\text{NL}}$  is the nonlinear decay rate. The result of such a decay curve is shown in Fig. 4.29.

### 4.7.1 Third generation device

We now consider the spectral density of detected amplitude fluctuations, in units of shot noise. For each recorded cavity spectrum we note the DC voltage at the output of our photodetector, and subsequently use a shot noise limited light source (e.g. a thermal light source) to acquire a reference spectrum with the same (or comparable) DC voltage. These shot noise spectra are rescaled with the voltage ratio<sup>24</sup>, to account for discrepancies between the optical powers used.

From the transfer matrix model we estimate an outcoupling efficiency of approximately 94% (see Fig. 4.23). Combined with  $\sim 95\%$  collection efficiency of light (i.e. optical losses between the cavity and the detector), as well as an estimated home-built detector detection efficiency of  $\sim 85\%$ , we anticipate an overall efficiency of  $\sim 76\%$ . This leaves us with the thermal occupancy as the only free parameters for our model given by Eq. (4.116). However, as can be seen in Fig. 4.30, the single free parameter fit (red dashed

---

<sup>23</sup>We ensure that there is no appreciable residual backaction damping the mechanical mode by comparing ringdown measurements performed on both sides of the broad ‘‘cavity’’ resonance.

<sup>24</sup>More specifically, we subtract the electronic noise contribution from the cavity and shot noise spectra, before rescaling with the ratio of DC voltages.

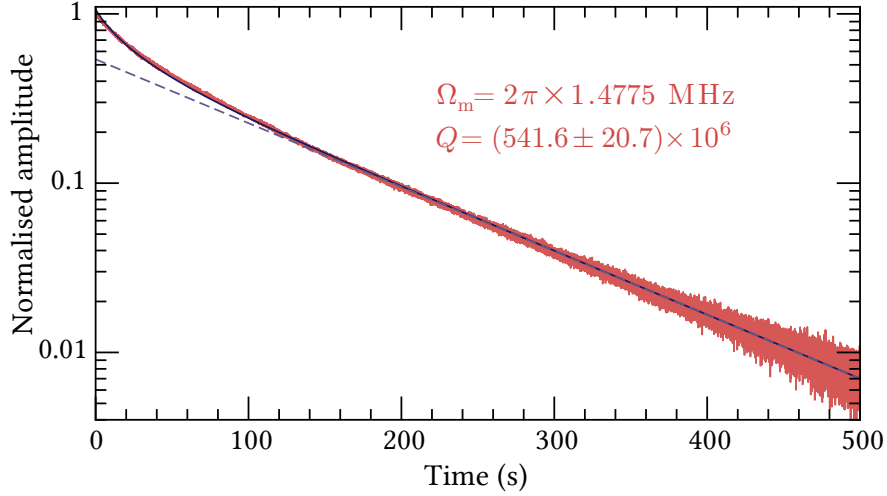


Figure 4.29: Cryogenic ringdown of a third generation soft clamped membrane resonator (same device as in Sections 4.6.3 and 4.6.4). The quality factor is based on 8 ringdown measurements. The solid line is a fit of a non-linear ringdown curve, while the dashed line correspond to a linear ringdown curve, extrapolated from the regime dominated by linear damping.

line) does not agree with our measurement<sup>25</sup>. With Fig. 4.9 as a reference, we see that this can be explained by a lower than anticipated detection efficiency.

In fact, OMIT measurements suggest that the cavity linewidth is  $\kappa \approx 2\pi \times 3.7$  MHz, indicative of additional optical losses within the cavity. Assuming that these losses lead to added inefficiency, we estimate a modified out-coupling efficiency of  $\tilde{\eta}_c = \eta_c \kappa_{\text{TMM}} / \kappa_{\text{meas}}$ . With a simulated cavity linewidth of  $\sim 3$  MHz, this amounts to an additional inefficiency of  $\sim 81\%$ , and a combined detection efficiency of  $\sim 58\%$ . In fact, allowing our model to fit two parameters, namely the bath temperature and the efficiency, yields  $\eta = 55.2\%$ . For a better estimate of both parameters, we perform a least square optimisation using four squeezing traces, similar to Fig. 4.30, where the detuning is varied between  $\bar{\Delta}/\kappa = -0.33$  and  $\bar{\Delta}/\kappa = -0.41$ . With the two free parameters shared between the four traces we find  $T_{\text{bath}} = (9.2 \pm 0.8)$  K and  $\eta = (55.5 \pm 0.3)\%$ .

We note a few things in relation to Fig. 4.30. Following the simulated ratio between the first and second localised modes of our defect (see Table 4.1) we recognise the sharp peak at  $\sim 1.51$  MHz as the second localised mode. In agreement with our calculated values of optical-mechanical mode overlaps, the second mode shows no discernible signs of dynamical backaction.

<sup>25</sup>The fit predicts a bath temperature of 4.2 K, which was set as the lower bound.

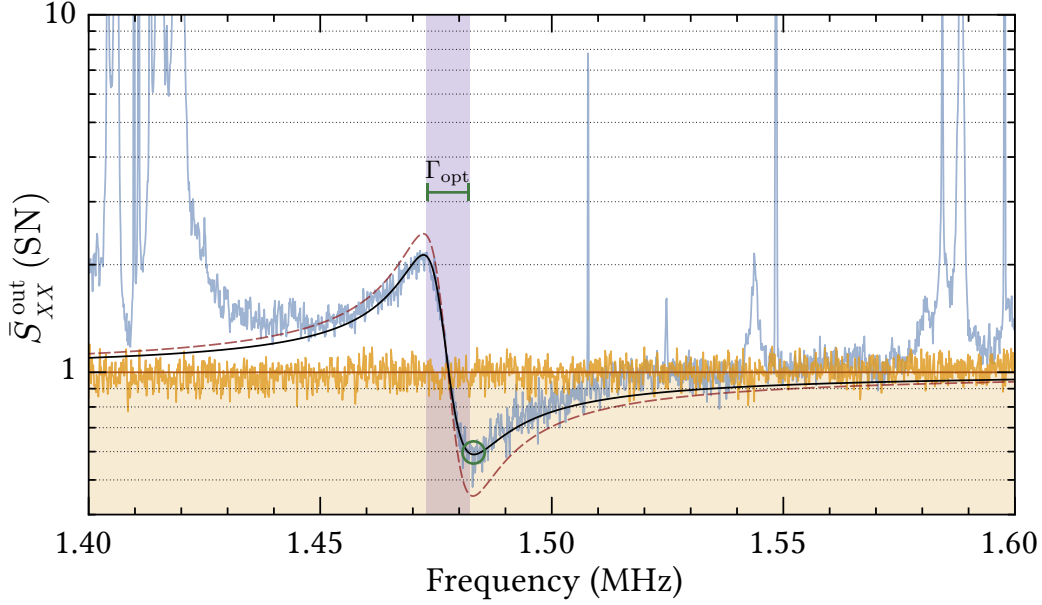


Figure 4.30: Power spectral density of output cavity fluctuations, showing squeezing below the shot noise level. The red dashed line is a fit of Eq. (4.116), assuming a detection efficiency of  $\sim 76\%$ , with the mean phonon occupancy as the only free parameter. With two free parameters, the detection efficiency and the mean thermal occupancy, we find a significantly better agreement between the measured data and the model. We find  $T_{\text{bath}} = (9.2 \pm 0.8)$  K and  $\eta = (55.5 \pm 0.3)\%$ . From OMIT measurements we find that  $\bar{\Delta} = -2\pi \times 1.199$  MHz,  $\kappa = 2\pi \times 3.63$  MHz and  $g = 2\pi \times 114.8$  kHz.

Below the resonance frequency of the fundamental-like mode we see the anti-squeezed part of the spectrum is bleeding out of the bandgap and exciting the edge modes. However, seeing that these are more than five linewidths away (where  $\Gamma_{\text{eff}} = 2\pi \times 9.6$  kHz in Fig. 4.30), we do not anticipate that the mechanical mode temperature changes significantly as a result thereof. With all parameters fixed in our model, we can therefore estimate the mean occupancy of the mode by inferring  $\bar{S}_{QQ}(\Omega)$  from measurement of  $\bar{S}_{XX}^{\text{out}}(\Omega)$  and integrating in the vicinity of the mechanical mode. We find that the mean occupancy of the mode in Fig. 4.30 is  $\bar{n} = (0.516 \pm 0.03)$ , with  $n_{\text{min}} = 0.477$ .

As for the elephant in the room, namely the amount of ponderomotive squeezing, we calculate the mean and standard deviation of the data in a bandwidth of  $10 \times \bar{n}_{\text{th}}\Gamma_{\text{m}} \approx 2\pi \times 3.5$  kHz. This is evaluated around the frequency of largest amount of squeezing predicted by our model. For the data in Fig. 4.30 we evaluate  $(-2.29 \pm 0.27)$  dB squeezing below shot noise.

With all parameters fixed, we consider the effect of increased intracavity power for a detuning of approximately  $-1.4$  MHz. In Fig. 4.31 we see spectra with quantum cooperativities ranging between  $C_q \approx 37$  and  $C_q \approx 80$ . We notice a slight deviation between the theoretical prediction and the measurement for the highest optical power, particularly in the peak amplitude of the mode. Whether this is due to additional excitation as a result of classical laser noise (i.e. amplitude and phase) or the fact that the out-of-bandgap mode is driven stronger for larger values of  $C_q$ , is not obvious from these measurements. While the amount of squeezing is essentially constant for values between  $C_q \approx 37$  and  $C_q \approx 80$ , the mechanical mode is significantly broadened for the highest intracavity power ( $\Gamma_{\text{eff}} = 2\pi \times 19.85$  kHz), and thus a non-negligible portion of the mode bleeds outside the bandgap. Even for a different method of thermometry than the one employed earlier this would pose a challenge.

Finally, we take a brief look at the vibrational spectrum near the second radial mode. As one might anticipate, the mirror mode spectrum becomes denser for higher frequencies, and this is indeed seen in Fig. 4.32. While there is some amount of ponderomotive squeezing, the spectrum is largely contaminated with mirror modes. Therefore, a cleaner mode spectrum in the vicinity of the second radial mode is imperative to harness the multimode nature of these structures.

### 4.7.2 Second generation device

For the second generation devices, we assemble a similar cavity as already described. In contrast to the assembly for the third generation device, here we measure a cavity linewidth of  $\kappa = 2\pi \times 3.11$  MHz, which is in close agreement with the simulated value from the transfer matrix model at the high-coupling point in  $2kz_m$ . The membrane device itself has a resonance frequency of  $\Omega_m = 2\pi \times 1.274$  MHz with a measured quality factor of  $(979.52 \pm 29.77) \times 10^6$  (based on 7 ringdown measurements). Assuming a detection efficiency of 76% and a temperature of 9.2 K, we consider measurements of ponderomotive squeezing for three different cavity detunings ( $\bar{\Delta}/\kappa = -0.58$ ,  $\bar{\Delta}/\kappa = -0.43$  and  $\bar{\Delta}/\kappa = -0.29$ ) in Fig. 4.33a-c. Consistent with theoretical predictions (see Fig. 4.9) we see a steady increase in the amount of squeezing, going from  $(-1.36 \pm 0.16)$  dB, to  $(-1.90 \pm 0.20)$  dB, and finally  $(-2.89 \pm 0.31)$  dB. As before, we evaluate the degree of squeezing in a frequency window of  $10 \times \bar{n}_{\text{th}}\Gamma_m \approx 2\pi \times 1.95$  kHz. Note that besides the fundamental-like mode, one of the higher order localised modes also produces squeezing, albeit to a lower degree. This suggests that our optical beam is not perfectly centred on the defect.

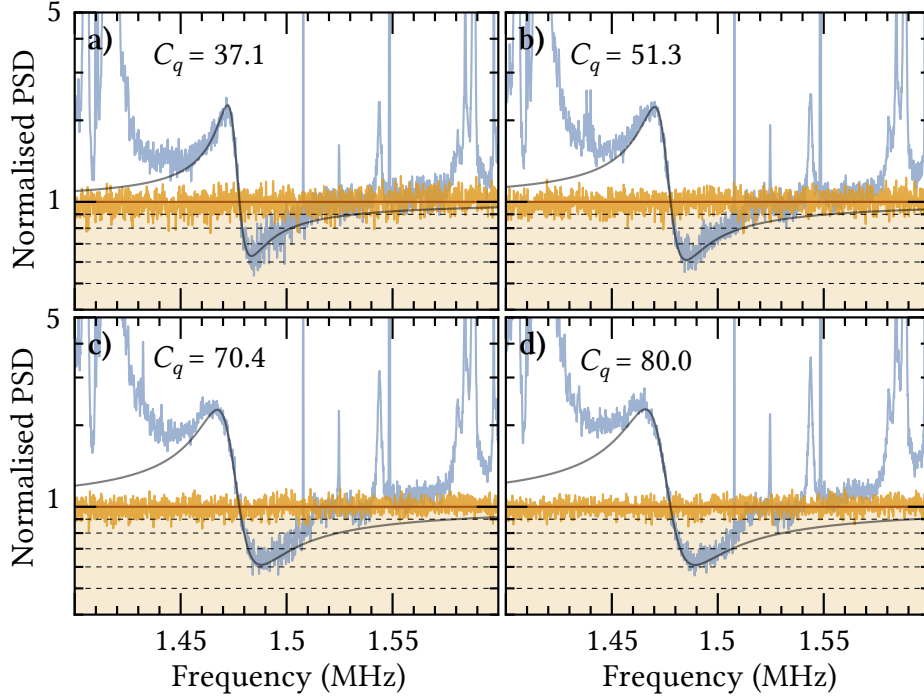


Figure 4.31: Ponderomotive squeezing for varying intracavity powers. The measured power spectral densities are normalised to shot noise and a zero-free parameter plot of the theoretical prediction is shown alongside each spectrum. The amount of squeezing for each measurement, evaluated in a frequency windows of  $\sim 3.5$  kHz centred around the minimum value according to the theoretical prediction, is: a)  $-(1.94 \pm 0.34)$  dB, b)  $-(1.84 \pm 0.34)$  dB, c)  $-(1.93 \pm 0.27)$  dB and d)  $-(2.04 \pm 0.18)$  dB. For the theoretical model we assume  $\eta = 55.5\%$ ,  $T_{\text{bath}} = 9.2$  K and  $\Gamma_m = 2\pi \times 2.686$  mHz. All other parameters are found via OMIT measurements.

Despite the appreciable amount of squeezing, our theoretical model predicts a larger degree of noise reduction for all three measurements. In order to fit the model to our measurements, one would have to increase the assumed bath temperature (the effect of which is increasing the overall excitation) and reduce the detection efficiency (which results in a reduction of the “visibility” of the curve – the maximum amplitude is reduced, and so is the amount of squeezing, as a result of lower detection efficiency). However, allowing our model to fit both of these parameters yields a bath temperature of  $\sim 45$  K, which is incompatible with estimated bath temperature from the previous section, as well as previous observations in our system. However, upon in-

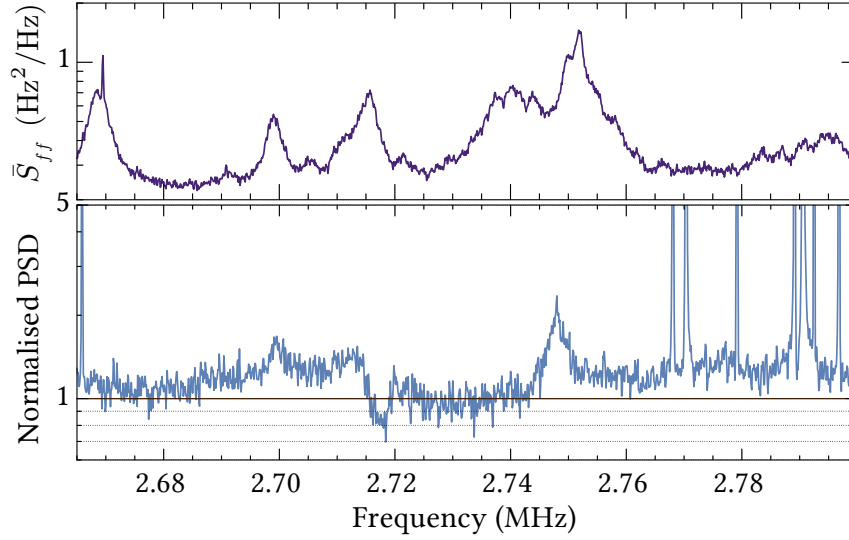


Figure 4.32: Calibrated mirror mode spectrum of a bare cavity (top, originating from the same measurement as Fig. 4.27), and normalised power spectral density (bottom) in the vicinity of the second radial mode ( $\Omega_m \approx 2\pi \times 2.715$  MHz).

creasing the intracavity power we notice the tips of spurious resonances show up on top of our mechanical mode (see Fig. 4.33d around 1.24 MHz and 1.3 MHz). Seeing that this coincides with a dense region within our mirror mode spectrum (cf. Fig. 4.27) it is therefore more likely that the lack of agreement between our model and the measurements is due to additional noise, origination from the thermal motion of the cavity mirrors.

It is furthermore worth noting that for the spectrum in Fig. 4.27 the light enhanced coupling rate is  $g = 2\pi \times 176$  kHz ( $\Gamma_m = 2\pi \times 22.6$  kHz), based on OMIT measurements, which amounts to a quantum cooperativity of 193.

In this section we have used ponderomotive squeezing as a probe for the potential shortcomings in cavity assemblies involving second and third generation soft clamped devices. As we have seen, both devices can provide appreciable amount of squeezing, as well as high quantum cooperativities, thus overwhelming the thermal Langevin noise with backaction.

While it might seem that the second generation devices are superior due to a larger absolute frequency separation between the first localised mode and the band edge, a more relevant figure of merit for a number of applications is the frequency separation in units of decoherence rate,  $\Gamma_{\text{dec}} = \bar{n}_{\text{th}}\Gamma_m$ . Seeing that the highest measured quality factor for a third generation soft clamped device is approximately  $1.5\times$  larger than for a second generation device (see Fig. 4.28), and recalling that  $C_q \approx \Gamma_{\text{opt}}/\bar{n}_{\text{th}}\Gamma_m$ , one could achieve

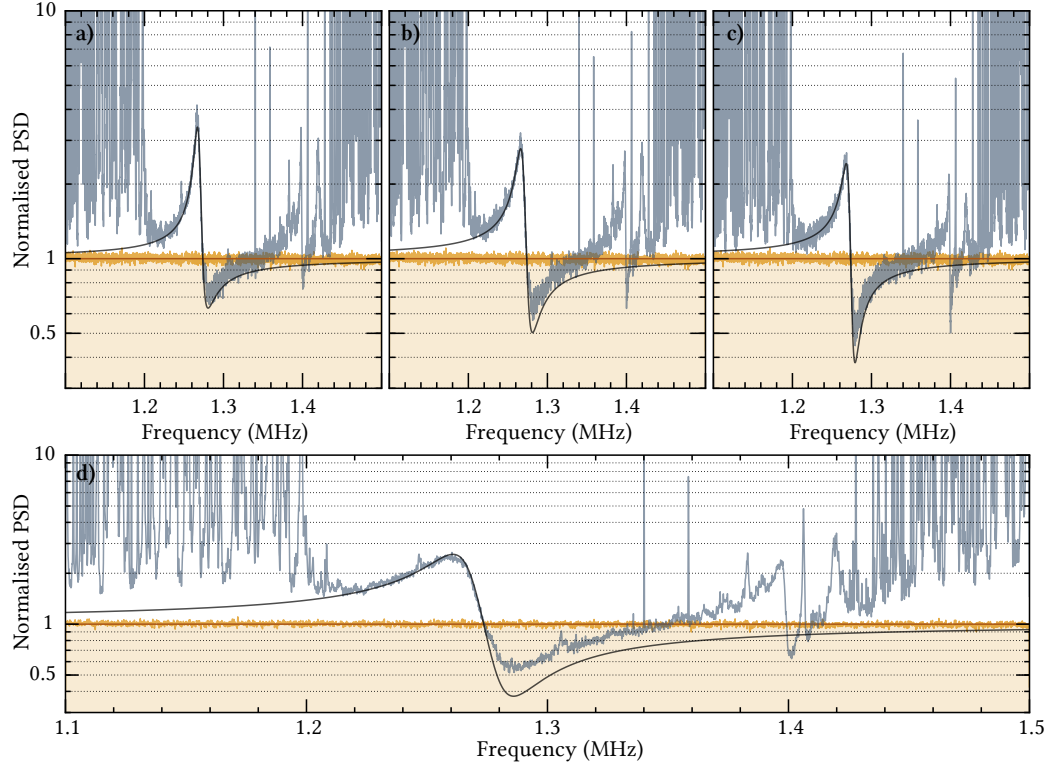


Figure 4.33: Ponderomotive squeezing spectra for a second generation soft clamped resonator. Top row: power spectral densities for varying cavity detunings. From left to right, we have  $\bar{\Delta}/\kappa = -0.58$ ,  $\bar{\Delta}/\kappa = -0.43$  and  $\bar{\Delta}/\kappa = -0.29$ , where  $\kappa = 2\pi \times \approx 3.11$  MHz. The theoretical curves are based on an estimated detection efficiency of 76% and a bath temperature of 9.2 K. The amount of ponderomotive squeezing is evaluated in a frequency window of  $\approx 1.95$  kHz, finding  $(-2.89 \pm 0.31)$  dB squeezing for the right-most measurement.

the same quantum cooperativity as for a second generation device using a third generation resonator for  $1.5\times$  smaller optical broadening. This relaxes the requirements on absolute frequency separation between the band edge and the membrane mode. Of course, this is only a relevant figure of merit if the sole requirement involving a particular experiment is to achieve a certain ratio between quantum backaction noise and thermal noise. If the amount of broadening for the mechanical mode is dictated by external factors, such as matching of bandwidths in a hybrid system, this argument is invalid and one has to resort to considerations based on absolute frequencies (in which case, the second generation devices are superior).

## 4.8 Summary and outlook

The primary purpose of this chapter has been to describe our implementation of the membrane-in-the-middle system involving soft clamped resonators, and demonstrate their performance at moderate cryogenic temperatures. Despite technical limitations we have observed strong ponderomotive squeezing with two types of soft clamped devices, which is an unambiguous sign that our system is indeed quantum limited. Our system combines coherence times in excess of 1 ms, high detection efficiency and can be operated in a regime where the backaction noise is almost 200 times larger than the thermal noise contribution. This combination is highly versatile and can be beneficial in a number of quantum optomechanical experiments. In the following I will outline one such effort in the group of Eugene Polzik, which I have been involved in, as well as present a potential solution to one of the most persistent sources of technical noise in relation to this work, namely that of mirror noise.

### 4.8.1 Towards generation of mechanical Fock states

The theoretical description of optomechanics presented in this chapter has been squarely within the linearised domain, where the intrinsic nonlinearity associated with the radiation pressure interaction was omitted. This is the consequence of the fact that for the vast majority of optomechanical systems, including our own, the single-photon optomechanical interaction strength (i.e.  $g_0$ ) is significantly smaller than other rates in the system ( $g_0 \ll \kappa, \Omega_m$ ), requiring the experimenter to inject a strong coherent field to ensure a non-negligible radiation pressure force. This allows us to realise non-classical Gaussian states, such as squeezed states of light or motion, motional ground state and entangled states. Extending our portfolio of quantum states into the non-Gaussian domain requires, however, the introduction or enhancement of a nonlinearity. A plethora of schemes have been proposed along these directions, ranging from enhancement of the single-photon interaction strength<sup>26</sup> by coupling to an ensemble of mechanical resonators [186] or through hybridisation with nonlinear components, such as a Josephson junction [187] or an optical parametric amplifier [188, 189], to dissipative schemes combining linear and quadratic optomechanical coupling [190, 191], injection of single photon states into the optomechanical system [6, 192, 193], and, finally, nonlinear detection [194, 195]. Among the various approaches, the latter and the former are arguably the least “invasive” methods for our system, since

---

<sup>26</sup>More specifically, the “granularity” parameter [185], defined as  $g_0/\kappa$ .

the additional requirements are largely extrinsic, and little to no alternation of the optomechanical system itself is needed. Coincidentally, the approach involving injection of a single photon is pursued by Albert Schliesser, in collaboration with the groups of Peter Lodahl and Anders Sørensen, while the approach involving nonlinearity through detection is pursued by Eugene Polzik. The experimental results presented in this chapter are part of the larger effort to prepare our membrane resonators in the first energy eigenstate, and in the following I outline progress and challenges towards this goal.

Due to the fact that our mechanical devices are quite devoid of any appreciable degree of anharmonicity, the Raman scattered photons within our cavity are effectively degenerate in frequency, preventing us from distinguishing between the different energy transitions of our resonator mode. Conversely, this prevents us from addressing a particular level transition. Hence, in order to prepare our vibration mode of choice in a specific energy eigenstate, we need to excite the mechanical mode probabilistically, and use single photon detection to herald the preparation of a single-phonon Fock state. More concretely, we seek to implement the scheme proposed by C. Galland et al. [195]. In short, the scheme involves state initialisation (i.e. ground state cooling of the vibrational mode), followed by a blue-detuned ( $\bar{\Delta} = +\Omega_m$ ) “write” pulse, which probabilistically scatters a single photon resonant with the cavity. Upon spectral filtering of the photon from the large drive field, the photon is detected with a single photon detector, where a “click” from the detector heralds the motional Fock state. To verify the generation of the first excited state, a red-detuned ( $\bar{\Delta} = -\Omega_m$ ) “read” pulse is sent onto the optomechanical cavity, which maps the single excitation onto the light field via an anti-Stokes scattering process. The emerging photon is once again resonant with the cavity and is passed through the spectral filtering system, before impinging onto the single photon detector. The single-photon nature of the read out state can be verified by computing the second-order autocorrelation (conditioned on the detection of a herald photon) in a Hanbury-Brown-Twiss (HBT) setup. For an ideal single-photon source  $g_{\text{cond}}^{(2)}(\tau = 0) = 0$ , where  $\tau$  is the time delay between the recorded photon counts of the two detectors in the HBT setup. The measurement of  $g^{(2)}$  essentially quantifies the purity of the single photon source.

Such a scheme was recently realised in the group of Simon Gröblacher [196], where a second-order intensity correlation of  $g_{\text{cond}}^{(2)}(\tau = 0) = 0.65$  was measured in a silicon optomechanical crystal based system. The high mechanical frequency of this system is particularly favourable with respect to spectral filtering of pump photons, where commercial optical filters can

be employed to achieve  $> 80$  dB rejection, as well as state initialisation, since at the base temperature of the dilution refrigerator ( $T = 35$  mK) the mechanical mode  $\Omega_m \approx 2\pi \times 5.25$  GHz has a mean phonon occupancy of  $\bar{n} \approx 0.75 \times 10^{-3}$ . However, the silicon optomechanical crystals are known to suffer from two-photon absorption at low temperatures, which limits the observed non-classicality in this system. Furthermore, despite the estimated coherence time of  $\sim 15$  ms (assuming  $Q = 3.8 \times 10^5$  [196] and thermalisation to 35 mK), the absorption heating also leads to a reduced coherence time due to appreciable frequency jitter of the mode, as described by MacCabe and colleagues [117].

While our system does not suffer from this issue, the low mechanical frequency poses two additional challenges – deep ground state cooling and filtering of the resonant (single) photons from the pump photons associated with the write/read pulses. Let us first consider the former of the two.

First and foremost, it is important to remind ourselves that laser cooling of the mechanical motion results in a *thermal* state with a certain mean occupation where the probability of finding the mode in a particular energy eigenstate  $|n\rangle$  is  $P_n = \bar{n}^n / (1 + \bar{n})^{n+1}$ , rather than a pure state. And while performing a measurement akin to the heralding scheme described above would yield non-Gaussian motional states<sup>27</sup>, even for non-negligible mean occupancies of the mechanical mode, one would have to resort to optical quantum-state tomography of the mechanical mode, in order to verify the nonclassicality. With this in mind, it is therefore not surprising that observing a second-order autocorrelation below unity demands a low initial mean phonon occupancy. Assuming  $\bar{n} \ll 1$ , Galland et al. [195] found that  $g_{\text{cond}}^{(2)}(\tau = 0) \approx 4\bar{n}$ , which suggests that a mean occupancy below  $\sim 1/4$  is required to observe  $g_{\text{cond}}^{(2)}(\tau = 0) < 1$  in a HBT experiment.

The most straightforward path forward for our system is to increase the cavity length, such that we operate in the resolved sideband, with a significantly lower backaction limit, as compared to our cavity assembly. In order to maintain (and preferably decrease) the optical beam spot size, which would increase the optomechanical coupling rate and reduce potential losses due to clipping, a cavity length of 24.2 mm or longer is needed with the current mirrors, amounting to a near ten-fold increase in cavity length. This assembly has already been successfully tested, and a (bare) cavity linewidth of  $(309 \pm 41)$  kHz has been measured<sup>28</sup>, consistent with the prediction based on

---

<sup>27</sup>Roughly speaking one could say that since  $\bar{n} = 1$  implies that the vibrational mode is found in the  $|0\rangle$  eigenstate 50% of the time and 25% in  $|1\rangle$ , with similar probabilities one would generate the energy eigenstates  $|1\rangle$  and  $|2\rangle$ , respectively.

<sup>28</sup>This was done by sweeping the laser frequency across the cavity resonance, while

mirror transmissivities. An advantage of a longer cavity is the fact that the free spectral range is significantly reduced, which would allow us to address multiple cavity resonances using the sidebands of an EOM. In practice, this could allow us to use one cavity resonance for locking and state preparation (i.e. sideband cooling), and another for write and read pulses. The advantage of this approach is that the cavity can be maintained locked while the pulses are injected into the cavity<sup>29</sup>.

Assuming a cavity linewidth of 300 kHz and mechanical resonance frequency of  $\Omega_m = 2\pi \times 1.5$  MHz, the backaction limit (cf. Eq. 4.80) is  $\bar{n}_{\min} = 2.5 \times 10^{-3}$  and the final occupancy is instead dictated by the quantum cooperativity and additional sources of noise. As we have seen in Section 4.7, we can reach quantum cooperativities in excess of  $10^2$  in our system, which, in the resolved sideband regime and in the absence of additional sources of heating, would amount to a final occupancy of  $\bar{n}_{\text{final}} \approx 10^{-2}$  (cf. Eq. (4.81)).

Besides excess phase noise due to the thermal motion of our mirror, the most obvious source of heating is our laser source. To this end, we have characterised the classical amplitude and phase noise of our Ti-Sapphire laser, using a cavity transduction technique similar to [197, 198]. Here, the idea is to use a Fabry-Pérot cavity to rotate the input light quadratures, thus converting classical phase noise to amplitude noise. These amplitude fluctuations are subsequently detected in cavity transmission by direct detection. As for the amplitude noise, we shine the laser directly onto a photodetector, acquiring spectra for varying input powers. Normalising each recorded PSD to the shot noise level and consider the scaling of the variance as a function of input power, we are able to quantify the classical amplitude noise (in units of shot noise). Following the definitions by Jayich et al. [199], the input field is defined as  $\hat{s}_{\text{in}} = \bar{s}_{\text{in}} + \delta\hat{s}_{\text{in}} + (\delta X + \delta Y)/2$ , where  $\delta X$  and  $\delta Y$  are the laser amplitude and phase noise, respectively. Assuming a white noise model (i.e.  $\langle \delta X(t)\delta X(t') \rangle = C_{xx}\delta(t-t')$  and  $\langle \delta Y(t)\delta Y(t') \rangle = C_{yy}\delta(t-t')$ ), we quantify the excess amplitude and phase noise by the real numbers  $C_{xx}$  and  $C_{yy}$ , which are proportional to the optical power. Our measurements suggest that the amount of excess classical noise at the Fourier frequency 1.475 MHz is  $C_{xx} \approx 3 \times 10^{-5} \mu\text{W}^{-1}$  and  $C_{yy} \approx 3 \times 10^{-3} \mu\text{W}^{-1}$ , consistent with similar measurements reported for a similar laser system in [17]<sup>30</sup>. A detailed

---

applying a weak modulation tone to the EOM. The latter introduces sidebands around the cavity resonance (separated by twice the modulation frequency). The spacing between the sidebands is used as a reference in estimating the cavity linewidth.

<sup>29</sup>Here we assume that the cavity resonance used for locking is not resonant with the filter cavities, and is thus strongly suppressed by the filtering system.

<sup>30</sup>It should be noted that the definition of  $C_{xx}$  and  $C_{yy}$  differs by a factor of 4 between Jayich et al. [199] and Rossi et al. [17].

summary of our measurements can be found in the master's thesis of Timo Zwickler [200]. Assuming a cavity linewidth of 300 kHz, a single-photon coupling rate of  $g_0 = 2\pi \times 6$  Hz,  $T_{\text{bath}} = 10$  K, as well as  $C_{xx} \approx 3 \times 10^{-5} \mu\text{W}^{-1}$  and  $C_{yy} \approx 3 \times 10^{-3} \mu\text{W}^{-1}$ , and using the theoretical framework from Jayich et al. [199], we find that the minimum occupation is approximately 0.232. Importantly, simulations suggest that it is indeed limited by the classical phase noise of the laser. To address this issue we recently implemented a filter cavity with a FWHM of  $\sim 130$  kHz, which suppresses classical laser noise at the relevant Fourier frequencies. We have measured more than a five-fold reduction of  $C_{yy}$  at the Fourier frequency of  $\Omega_{\text{m}} = 2\pi \times 1.5$  MHz (see [200]), bringing the predicted mean occupancy down to  $\sim 0.11$ . While this figure can be improved further, for initial studies of Fock state generation and, eventually, optical state tomography, this is a reasonable starting point. Finally, it should be noted for  $C_{xx} \approx 3 \times 10^{-5} \mu\text{W}^{-1}$  and  $C_{yy} \approx 3 \times 10^{-3} \mu\text{W}^{-1}$ , the estimated contribution of classical laser noise to the total phonon occupancy for the ponderomotive squeezing measurements is approximately 5% and is therefore negligible. This would also suggest that the additional heating seen in Fig. 4.31 is due to excitation of the band edge modes, rather than classical laser noise at high optical powers. The contribution of various heating mechanisms will be the subject of experimental study in our group moving forward.

Moving towards optical filtering, it is first and foremost worth acknowledging some of the advantages associated with an optomechanical system with a long coherence time, as it pertains to Fock state generation. Firstly, one could envision heralding the single-excitation state, and instead of reading it out immediately hereafter, storing it until need be. This is a desirable feature in the context of quantum repeaters and quantum networks more broadly, where not all parts of the network are ready at any given time, which calls for means to store single excitations. Second, the fact that our photons are spectrally narrow (and hence temporally broad), suggests that experiments involving two-photon interference, akin to the Hong-Ou-Mandel effect, would have more relaxed requirements on interferometric stability. These, among others, are some of the motivating aspects of our system.

Once the system has been initialised and a write pulse has resulted in a Stokes scattering event, our next task is to isolate that single photon from the pump field (i.e. the pulse). For a generic system, estimating the degree of suppression can be done using the light-mediated scattering rates (cf. Eq. (4.76)). Assuming operation in the resolved sideband regime (and  $\bar{\Delta} = -\Omega_{\text{m}}$ ), the scattering rate can be expressed as  $A^+ = \bar{n}_{\text{cav}} 4g_0^2/\kappa$ , and with an output photon flux of  $\bar{n}_{\text{cav}}\kappa$ , the ratio between scattered photons and total number of photons escaping the cavity is  $4g_0^2/\kappa^2$ . Assuming the resolved

parameters similar to those in the preceding paragraphs, this suggests a ratio of  $10^{-9}$ . This estimate suggests that our system requires a filter system which can provide  $10^9$  rejection at megahertz frequencies. Unfortunately, this estimate neglects an important detail, namely the fact that not only do we need to suppress the pump photons, but equally important is it to suppress the scattered photons originating from the mechanical modes outside the phononic bandgap. After all, as we have seen in Section 4.7, the edge of the bandgap is less than 100 kHz away from the mode of interest. Accounting for the presence of the edge modes, in actuality, a rejection of  $\sim 10^{14}$  is required by our filter cavities. The latter can be achieved using a system consisting of four cascaded Fabry-Pérot cavities with FWHM of  $\sim 30$  kHz. While a daunting task, such a system has been brought to life by Ivan Galinskiy, a PhD student in Eugene Polzik’s group. With this ingredient in place, we are therefore hopeful of exciting results to emerge in the near future.

Looking ahead, one of the prospects in our system is making use of the fact that our third generation membrane devices have two highly coherent radial localised vibrational modes. Following a proposal by Weaver et al. [201], one could implement a heralded scheme involving multiple input pulses, which would result in an entangled state between the two vibrational modes. Secondly, seeing that our system has the potential of achieving very detection efficiencies (values approaching 80% were integral to our work on quantum feedback cooling reported in [17]), the prospects of optical quantum-state tomography [202] of the non-Gaussian mechanical states are encouraging. Lastly, seeing that the atomic equivalent of the single-excitation experiment has been developed in the group of Eugene Polzik [203], using the DLCZ protocol to create entanglement between the our optomechanical system and the collective spin excitation of a Cesium atomic ensemble seems like a happy marriage waiting to happen.

### 4.8.2 Exoskeleton mirrors

A common thread throughout this chapter has been the issue of mirror modes, which ultimately prevented us from using the best performing device to date (cf. Fig. 4.28). Therefore, we seek to find a solution to this technical challenge. One path forward is to reduce mirror size, which will result in an increase of the eigenfrequencies of the mirror modes, thus reducing the mode density at megahertz frequencies. However, hybridisation can still be an issue in such a scenario.

An alternative and more robust solution includes phononic crystal structuring. However, structuring of glass, akin to the silicon phononic crystal devices considered in the previous chapter, can be technically challenging –

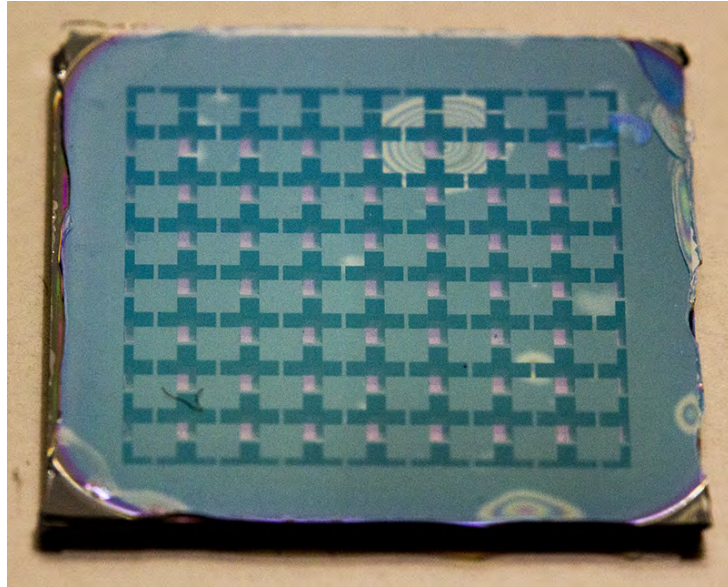


Figure 4.34: Exoskeleton mirror, consisting of a thick phononic crystal exoskeleton structure, with a thin ( $100\ \mu\text{m}$ ) pyrex glass anodically bonded to the silicon phononic crystal structure. The glass surface is coated with a mirror coating.

there is no DRIE equivalent for glass, and other techniques, such as wet etching or laser micromachining, have their respective issues. Since one would have to realise through-holes in glass of hundreds of micrometer thickness, wet etching would require highly resistant masking materials, which can withstand a hydrofluoric acid etch for several hours. As for laser micromachining, it can be a challenge to define structures with small critical dimensions (and, importantly, large aspect ratios), since cracking of the glass due to thermal shocks is a known issue.

The technique presented here addresses both of those issues, but separating the shielding structure from the glass structure. An important realisation with respect to phononic crystal structures is that full thickness modulation is not a necessity for a complete phononic bandgap to emerge, insofar the modulation is a significant fraction of the device thickness. On the same note, if a thin plate is glued to a phononic crystal perforated slab, the stack will exhibit a complete bandgap as long as the underlying phononic crystal is significantly thicker than the thin plate attached to it. This constitutes the core of the idea on how to address the issue of mirror noise.

Our approach is largely based on the silicon phononic crystal structures presented in the previous chapter, with the main difference that we do not

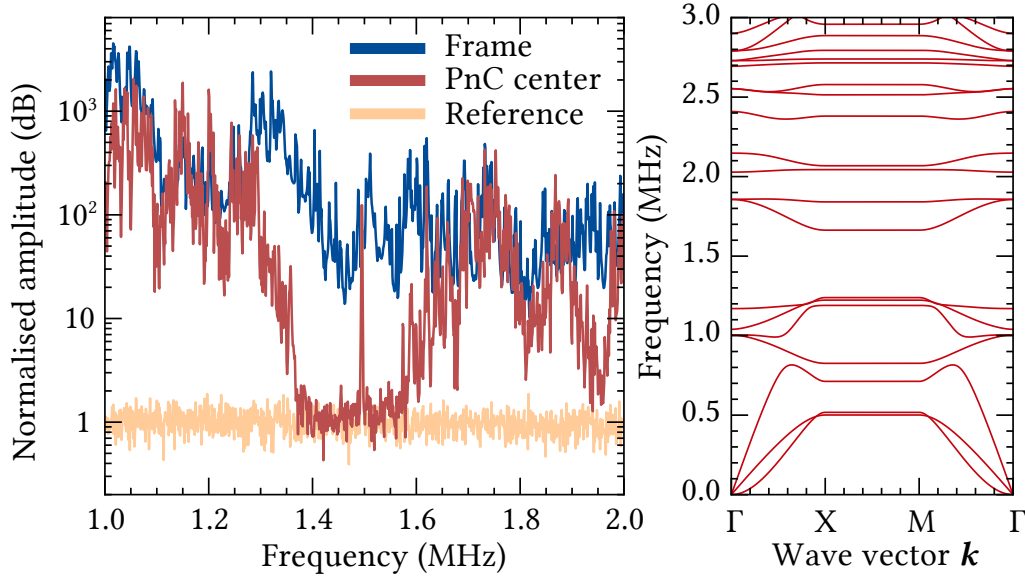


Figure 4.35: (Left) Driven response measurement of the exoskeleton structure of Fig. 4.34. Each trace consists of an average of 5 different sampled locations on the structure. The traces are normalised to the reference noise floor. The sharp peak at 1.5 MHz is an added calibration tone. (Right) The bandgap associated with the same crystal structure is shown.

introduce a geometric defect, as we did in relation to shielding of membrane resonators. Instead, we process base silicon wafers and, following a thorough cleaning procedure, use anodic bonding to attach a thin ( $100\ \mu\text{m}$ ) piece of pyrex glass. In Fig. 4.34 a photograph of the final product is shown.

With a target frequency is 1.5 MHz, we find a complete phononic bandgap for a silicon substrate thickness  $775\ \mu\text{m}$  and pyrex thickness  $100\ \mu\text{m}$ . Akin to the characterisation of silicon phononic crystal structures, we performed a piezo driven measurements, while monitoring the displacement outside of crystal structure (i.e. the frame) and subsequently in the central part of the exoskeleton structure. In Fig. 4.35 we see such a driven measurement, alongside the simulated band diagram. As we can see, the exoskeleton structure provides more than a ten-fold suppression of vibrations within the phononic bandgap. Furthermore, as it so happens, the higher order bandgaps placed such that both radial modes of the third generation soft clamped devices can be placed inside a bandgap, thus ensuring a clean mirror mode spectrum.

The exoskeleton structure shown here is still a work in progress, but preliminary measurements – optical, as well as mechanical – suggest that this approach could indeed resolve issues related to mirror noise in cavity

optomechanical experiments. Finally, simulations of phase noise fluctuations originating from the exoskeleton mirror have been performed within the framework of Levin's direct approach [204], finding that for a 2.5 mm cavity the phase noise from the exoskeleton structure is on order of  $\sim 2 \times 10^{-3} \text{ Hz}^2/\text{Hz}$  in room temperature settings. If proven to be correct, this suggests that the exoskeleton mirrors, in conjunction with our best performing soft clamped devices, could allow us to perform quantum optomechanical measurements, without the need of cryogenic cooling. The future does, indeed, look brighter towards the end.

## 4.9 Concluding remarks

On that note, we reach the conclusion of this thesis. Hence, a brief summary of the presented results and future prospects is in place. As we have seen, a careful analysis, design and subsequent implementation of phononic engineered mechanical resonators can result in devices with an exceptionally low degree of dissipation. Looking ahead, a number of potential improvements and alternations come to mind. First and foremost, given the fact that two-level systems are particularly prominent in amorphous materials, the possibility of replacing silicon nitride with a crystalline material is certainly one worth exploring. Measurements of high mechanical quality factors involving single-crystal diamond [68], as well as crystalline silicon [117], provide a clear incentive to explore microfabrication techniques allowing for tensioning of these materials. Next, electromechanical integration of soft-clamped resonators can provide a versatile platform for not only optomechanical studies, but also as a means of modifying the phononic properties in situ [205]. In extension, one could also envision realising electrostatically defined defects, in resemblance to [206], which could allow to tuneable coupling between multiple geometric defects within a soft clamped resonator. Finally, inspiration can be drawn from recent work on soft-clamped resonators, including strain-engineered strings [207], as well as low effective mass membrane resonators [208]. The possibility of combining our technique with the findings in these studies could potentially yield further improvements of the device performance.

As it pertains to the use of our devices in cavity optomechanics, the possibilities are numerous. Beyond the experiment described in Section 4.8.1, a related experiment is currently under way in the groups of Peter Lodahl and Albert Schliesser, involving the use of soft clamped resonators as a storage of single photons. Other potential trajectories include that of embedding multiple membrane resonators within an optical cavity. This would, for ex-

ample, allow for entanglement generation between multiple mechanical resonators [209] and studies of synchronisation effects [210]. Finally, with the potential improvements provided by the exoskeleton mirrors, one could furthermore hope to see some of these experimental endeavours move towards operation at liquid nitrogen or even room temperatures. I hope that the reader will join me in eagerly awaiting for these results to materialise.



# Bibliography

- [1] Yeghishe Tsaturyan. *Ultra-high Q micromechanical resonators for cavity optomechanics*. Master's thesis, University of Copenhagen, 2016.
- [2] K. Stannigel, P. Rabl, A. S. Sørensen, P. Zoller, and M. D. Lukin. Optomechanical transducers for long-distance quantum communication. *Physical Review Letters*, 105(22):1–4, 2010.
- [3] Changqiu Yu, Jiri Janousek, Eoin Sheridan, David L. McAuslan, Halina Rubinsztein-Dunlop, Ping Koy Lam, Yundong Zhang, and Warwick P. Bowen. Optomechanical Magnetometry with a Macroscopic Resonator. *Physical Review Applied*, 5(4):1–6, 2016.
- [4] Anders Simonsen, Sampo Antero Saarinen, Juan Diego Sanchez, Jan Henrik Ardenkjær-Larsen, Albert Schliesser, and Eugene Simon Polzik. Sensitive optomechanical transduction of electric and magnetic signals to the optical domain. *Optics Express*, 27(13):18561, 2019.
- [5] S. Bose, K. Jacobs, and P. L. Knight. Scheme to probe the decoherence of a macroscopic object. *Physical Review A - Atomic, Molecular, and Optical Physics*, 59(5):3204–3210, 1999.
- [6] William Marshall, Christoph Simon, Roger Penrose, and Dik Bouwmeester. Towards Quantum Superpositions of a Mirror. *Physical Review Letters*, 91(13):130401, 2003.
- [7] V. B. Braginsky and F. Ya Khalili. *Quantum Measurement*. Cambridge University Press, 1st edition, 1992.
- [8] J. D. Thompson, B. M. Zwickl, A. M. Jayich, Florian Marquardt, S. M. Girvin, and J. G.E. Harris. Strong dispersive coupling of a high-finesse cavity to a micromechanical membrane. *Nature*, 452(7183):72–75, 2008.
- [9] Scott S. Verbridge, Jeevak M. Parpia, Robert B. Reichenbach, Leon M. Bellan, and H. G. Craighead. High quality factor resonance at room

- temperature with nanostrings under high tensile stress. *Journal of Applied Physics*, 99(12), 2006.
- [10] L. Sekaric, D. W. Carr, S. Evoy, J. M. Parpia, and H. G. Craighead. Nanomechanical resonant structures in silicon nitride: Fabrication, operation and dissipation issues. *Sensors and Actuators, A: Physical*, 101(1-2):215–219, 2002.
- [11] M. D. LaHaye, O. Buu, B. Camarota, and K. C. Schwab. Approaching the Quantum Limit of a Nanomechanical Resonator. *Science*, 304(5667):74–77, apr 2004.
- [12] B. M. Zwickl, W. E. Shanks, a. M. Jayich, C. Yang, a. C Bleszynski Jayich, J. D. Thompson, and J. G E Harris. High quality mechanical and optical properties of commercial silicon nitride membranes. *Applied Physics Letters*, 92(10):130–132, 2008.
- [13] T. P. Purdy, P.-L. Yu, R. W. Peterson, N. S. Kampel, and C. a. Regal. Strong Optomechanical Squeezing of Light. *Physical Review X*, 3(3):031012, sep 2013.
- [14] William Hvidtfelt Padkær Nielsen, Yeghishe Tsaturyan, Christoffer Bo Møller, Eugene S. Polzik, and Albert Schliesser. Multimode optomechanical system in the quantum regime. *Proceedings of the National Academy of Sciences*, 114(1):62–66, jan 2017.
- [15] M. Underwood, D. Mason, D. Lee, H. Xu, L. Jiang, A. B. Shkarin, K. Børkje, S. M. Girvin, and J. G. E. Harris. Measurement of the motional sidebands of a nanogram-scale oscillator in the quantum regime. *Physical Review A*, 92(6):061801, dec 2015.
- [16] R. W. Peterson, T. P. Purdy, N. S. Kampel, R. W. Andrews, P. L. Yu, K. W. Lehnert, and C. A. Regal. Laser Cooling of a Micromechanical Membrane to the Quantum Backaction Limit. *Physical Review Letters*, 116(6):1–6, 2016.
- [17] Massimiliano Rossi, David Mason, Junxin Chen, Yeghishe Tsaturyan, and Albert Schliesser. Measurement-based quantum control of mechanical motion. *Nature*, 563(7729):53–58, nov 2018.
- [18] Christoffer B. Møller, Rodrigo A. Thomas, Georgios Vasilakis, Emil Zeuthen, Yeghishe Tsaturyan, Mikhail Balabas, Kasper Jensen, Albert

- Schliesser, Klemens Hammerer, and Eugene S. Polzik. Quantum back-action-evading measurement of motion in a negative mass reference frame. *Nature*, 547(7662):191–195, jul 2017.
- [19] David Mason, Junxin Chen, Massimiliano Rossi, Yeghishe Tsaturyan, and Albert Schliesser. Continuous force and displacement measurement below the standard quantum limit. *Nature Physics*, 15(8):745–749, aug 2019.
- [20] A. W. Leissa. *Vibration of plates*. NASA, Washington, D.C., 1969.
- [21] P.-L. Yu, T P Purdy, and C A Regal. Control of Material Damping in High-Q Membrane Microresonators. *Phys. Rev. Lett.*, 083603(8):1–5, 2012.
- [22] A. Bokaian. Natural frequencies of beams under tensile axial loads. *Journal of Sound and Vibration*, 142(3):481–498, 1990.
- [23] S. Schmid, L. G. Villanueva, and M. L. Roukes. *Fundamentals of Nanomechanical Resonators*. Springer International Publishing, 2016.
- [24] Ali H. Nayfeh and P. Frank Pai. *Linear and Nonlinear Structural Mechanics*. Wiley, 2004.
- [25] Walter Lacarbonara, Alih Nayfeh, and Wayne Kreider. Experimental Validation of Reduction Methods for Nonlinear Vibrations of Distributed-Parameter Systems: Analysis of a Buckled Beam. *Nonlinear Dynamics*, 17(2):95–117, 1998.
- [26] I. Wilson-Rae. Intrinsic dissipation in nanomechanical resonators due to phonon tunneling. *Physical Review B*, 77(24):1–31, jun 2008.
- [27] O. Ergincan, G. Palasantzas, and B. J. Kooi. Viscous damping of microcantilevers with modified surfaces and geometries. *Applied Physics Letters*, 101(6):061908, aug 2012.
- [28] K. L. Ekinci, D. M. Karabacak, and V. Yakhot. Universality in oscillating flows. *Physical Review Letters*, 101(26):1–4, 2008.
- [29] V Kaaajakari. *Practical MEMS*. Small Gear Pub., 2009.
- [30] A. F. Ismail, K. C. Khulbe, and T. Matsuura. *Gas separation membranes: Polymeric and inorganic*. 2015.

- [31] M. Bao, H. Yang, H. Yin, and Y. Sun. Energy transfer model for squeeze-film air damping in low vacuum. *J. Micromech. Microeng.*, 12:341–346, 2002.
- [32] Minhang Bao and Heng Yang. Squeeze film air damping in MEMS. *Sensors and Actuators, A: Physical*, 136(1):3–27, 2007.
- [33] I. Wilson-Rae, R. A. Barton, S. S. Verbridge, D. R. Southworth, B. Ilic, H. G. Craighead, and J. M. Parpia. High-Q Nanomechanics via Destructive Interference of Elastic Waves. *Physical Review Letters*, 106(4):047205, jan 2011.
- [34] C. Zener. Internal Friction in Solids. I. Theory of Internal Friction in Reeds. *Physical Review*, 52(3):230–235, aug 1937.
- [35] VK Kinra and A Wolfenden, editors. *M3D: Mechanics and Mechanisms of Material Damping*. ASTM International, 100 Barr Harbor Drive, PO Box C700, West Conshohocken, PA 19428-2959, jan 1992.
- [36] C. Zener. Internal friction in solids II. General theory of thermoelastic internal friction. *Physical Review*, 53(1):90–99, 1938.
- [37] Ron Lifshitz and M. Roukes. Thermoelastic damping in micro- and nanomechanical systems. *Physical Review B*, 61(8):5600–5609, 2000.
- [38] Clarence Zener. *Elasticity and anelasticity of metals*. Chicago, Illinois, 1948.
- [39] B Lautrup. *Physics of continuous matter, exotic and everyday phenomena in the macroscopic world*. Boca Raton, CRC Press, 2nd. ed. edition, 2011.
- [40] Clarence Zener. Internal Friction of Wires. *Nature*, 140(3551):895–895, nov 1937.
- [41] P. Linsay, P. Saulson, and R. Weiss. A Study of a Long Baseline Gravitational Wave Antenna System, 1983.
- [42] Gabriela I. Gonzalez and P. Saulson. Brownian motion of a mass suspended by an anelastic wire. *The Journal of the Acoustical Society of America*, 96(1):207, 1994.
- [43] YL Huang and PR Saulson. Dissipation mechanisms in pendulums and their implications for gravitational wave interferometers. *Review of scientific instruments*, 69(2):544, 1998.

- [44] S. Schmid and C. Hierold. Damping mechanisms of single-clamped and prestressed double-clamped resonant polymer microbeams. *Journal of Applied Physics*, 104(9), 2008.
- [45] Quirin P. Unterreithmeier, Thomas Faust, and Jörg P. Kotthaus. Damping of nanomechanical resonators. *Physical Review Letters*, 105(2):1–4, 2010.
- [46] S. Schmid, K. D. Jensen, K. H. Nielsen, and A. Boisen. Damping mechanisms in high-Q micro and nanomechanical string resonators. *Physical Review B - Condensed Matter and Materials Physics*, 84(16):1–6, 2011.
- [47] Ansel C. Ugural. *Plates and Shells*. CRC Press, Fourth edition. — Boca Raton : CRC Press, [2018] — Series: Applied and computational mechanics — Original edition published under the title: Stresses in plates and shells / Ansel C. Ugural. —Includes bibliographical references and index., 2017.
- [48] T.V. Roszhart. The effect of thermoelastic internal friction on the Q of micromachined silicon resonators. In *IEEE 4th Technical Digest on Solid-State Sensor and Actuator Workshop*, pages 13–16. IEEE, 1990.
- [49] A N Cleland. *Foundations of Nanomechanics: From Solid-State Theory to Device Applications*. Advanced Texts in Physics. Springer Berlin Heidelberg, 2002.
- [50] L D Landau, E M Lifshitz, A M Kosevich, J B Sykes, L P Pitaevskii, and W H Reid. *Theory of Elasticity*. Elsevier Science, 1986.
- [51] J. B. Alblas. On the general theory of thermo-elastic friction. *Applied Scientific Research*, 10(1):349–362, jan 1961.
- [52] Andrew N Norris and Douglas M Photiadis. Thermoelastic relaxation in elastic structures with applications to thin plates. *The Quarterly Journal of Mechanics and Applied Mathematics*, 58(1):22, 2004.
- [53] Ali H Nayfeh and Mohammad I Younis. Modeling and simulations of thermoelastic damping in microplates. *Journal of Micromechanics and Microengineering*, 14(12):1711–1717, dec 2004.
- [54] Scott S. Verbridge, Daniel Finkelstein Shapiro, Harold G. Craighead, and Jeevak M. Parpia. Macroscopic tuning of nanomechanics: Substrate bending for Reversible control of frequency and quality factor of nanostring resonators. *Nano Letters*, 7(6):1728–1735, 2007.

- [55] D. J. Wilson. *Cavity Optomechanics with High-Stress Silicon Nitride Films*. PhD thesis, 2012.
- [56] Benjamin Michael Zwickl. *Progress Toward Observation of Radiation Pressure Shot Noise*. PhD thesis, 2011.
- [57] S. Chakram, Y. S. Patil, L. Chang, and M. Vengalattore. Dissipation in Ultrahigh Quality Factor SiN Membrane Resonators. *Physical Review Letters*, 112(12):127201, mar 2014.
- [58] D.M Photiadis, B.H Houston, Xiao Liu, J.A Bucaro, and M.H Marcus. Thermoelastic loss observed in a high Q mechanical oscillator. *Physica B: Condensed Matter*, 316-317:408–410, 2002.
- [59] Hossein Ftouni, Christophe Blanc, Dimitri Tainoff, Andrew D. Fefferman, Martial Defoort, Kunal J. Lulla, Jacques Richard, Eddy Collin, and Olivier Bourgeois. Thermal conductivity of silicon nitride membranes is not sensitive to stress. *Physical Review B - Condensed Matter and Materials Physics*, 92(12):1–7, 2015.
- [60] A. A. Kiselev and G. J. Iafrate. Phonon dynamics and phonon assisted losses in Euler-Bernoulli nanobeams. *Physical Review B - Condensed Matter and Materials Physics*, 77(20):1–9, 2008.
- [61] Chengyun Hua, Lucas Lindsay, Xiangwen Chen, and Austin J. Minnich. Generalized Fourier’s law for nondiffusive thermal transport: Theory and experiment. *Physical Review B*, 100(8):085203, aug 2019.
- [62] K.Y. Yasumura, T.D. Stowe, E.M. Chow, Timothy Pfafman, T.W. Kenny, B.C. Stipe, and Daniel Rugar. Quality factors in micron- and submicron-thick cantilevers. *Journal of Microelectromechanical Systems*, 9(1):117–125, mar 2000.
- [63] K. L. Ekinici and M. L. Roukes. Nanoelectromechanical systems. *Review of Scientific Instruments*, 76(6), 2005.
- [64] L. G. Villanueva and Silvan Schmid. Evidence of Surface Loss as Ubiquitous Limiting Damping Mechanism in SiN Micro- and Nanomechanical Resonators. *Physical Review Letters*, 113(22):227201, nov 2014.
- [65] Kevin Luke, Avik Dutt, Carl B. Poitras, and Michal Lipson. Overcoming Si<sub>3</sub>N<sub>4</sub> film stress limitations for high quality factor ring resonators. *Optics Express*, 21(19):22829, 2013.

- [66] Jinling Yang, Takahito Ono, and Masayoshi Esashi. Surface effects and high quality factors in ultrathin single-crystal silicon cantilevers. *Applied Physics Letters*, 77(23):3860–3862, dec 2000.
- [67] Jinling Yang, Takahito Ono, and Masayoshi Esashi. Energy dissipation in submicrometer thick single-crystal silicon cantilevers. *Journal of Microelectromechanical Systems*, 11(6):775–783, dec 2002.
- [68] Y Tao, J M Boss, B a Moores, and C L Degen. Single-crystal diamond nanomechanical resonators with quality factors exceeding one million. *Nature communications*, 5:3638, 2014.
- [69] Niklas Luhmann, Artur Jachimowicz, Johannes Schalko, Pedram Sadeghi, Markus Sauer, Annette Foelske-Schmitz, and Silvan Schmid. Effect of oxygen plasma on nanomechanical silicon nitride resonators. *Applied Physics Letters*, 111(6):063103, aug 2017.
- [70] R O Pohl, Xiao Liu, and E Thompson. Low-temperature thermal conductivity and acoustic attenuation in amorphous solids. *Reviews of Modern Physics*, 74(October):991, 2002.
- [71] R. C. Zeller and R. O. Pohl. Thermal Conductivity and Specific Heat of Noncrystalline Solids. *Physical Review B*, 4(6):2029–2041, sep 1971.
- [72] W A Phillips. Tunneling states in amorphous solids. *Journal of Low Temperature Physics*, 7(3-4):351–360, may 1972.
- [73] P. w. Anderson, B I Halperin, and C M Varma. Anomalous low-temperature thermal properties of glasses and spin glasses. *Philosophical Magazine*, 25(1):1–9, jan 1972.
- [74] J. Jäckle. On the ultrasonic attenuation in glasses at low temperatures. *Zeitschrift für Physik*, 257(3):212–223, 1972.
- [75] S Hunklinger, W Arnold, and S Stein. Anomalous ultrasonic attenuation in vitreous silica at low temperatures. *Physics Letters A*, 45(4):311–312, oct 1973.
- [76] D. Tielbürger, R. Merz, R. Ehrenfels, and S. Hunklinger. Thermally activated relaxation processes in vitreous silica: An investigation by Brillouin scattering at high pressures. *Physical Review B*, 45(6), 1992.
- [77] R. Vacher, E. Courtens, and M. Foret. Anharmonic versus relaxational sound damping in glasses. II. Vitreous silica. *Physical Review B*, 72(21):214205, dec 2005.

- [78] T. Faust, J. Rieger, M. J. Seitner, J. P. Kotthaus, and E. M. Weig. Signatures of two-level defects in the temperature-dependent damping of nanomechanical silicon nitride resonators. *Physical Review B*, 89(10):100102, mar 2014.
- [79] Jiansheng Wu and Clare C. Yu. How stress can reduce dissipation in glasses. *Physical Review B*, 84(17):174109, nov 2011.
- [80] R Kubo. The fluctuation-dissipation theorem. *Reports on Progress in Physics*, 29(1):306, jan 1966.
- [81] Kun Wang, Ark-Chew Wong, and C.T.-C. Nguyen. VHF free-free beam high-Q micromechanical resonators. *Journal of Microelectromechanical Systems*, 9(3):347–360, sep 2000.
- [82] Garrett D Cole, Ignacio Wilson-Rae, Katharina Werbach, Michael R Vanner, and Markus Aspelmeyer. Phonon-tunnelling dissipation in mechanical resonators. *Nature communications*, 2:231, jan 2011.
- [83] Manoj Pandey, Robert B. Reichenbach, Alan T. Zehnder, Amit Lal, and Harold G. Craighead. Reducing anchor loss in MEMS resonators using mesa isolation. *Journal of Microelectromechanical Systems*, 18(4):836–844, 2009.
- [84] B. P. Harrington and R. Abdolvand. In-plane acoustic reflectors for reducing effective anchor loss in lateral-extensional MEMS resonators. *Journal of Micromechanics and Microengineering*, 21(8), 2011.
- [85] Enrico Serra, Bruno Morana, Antonio Borrielli, Francesco Marin, Gregory Pandraud, Antonio Pontin, Giovanni Andrea Prodi, Pasqualina M. Sarro, and Michele Bonaldi. Silicon nitride MOMS oscillator for room temperature quantum optomechanics. *Journal of Microelectromechanical Systems*, 27(6):1193–1203, 2018.
- [86] R. A. Buser and N. F. De Rooij. Very high Q-factor resonators in monocrystalline silicon. *Sensors and Actuators: A. Physical*, 21(1-3):323–327, 1990.
- [87] Baptiste Le Foulgoc, Tarik Bourouina, Olivier Le Traon, Alain Bosseboeuf, Frédéric Marty, Cédric Breluzeau, Jean Paul Grandchamp, and Stève Masson. Highly decoupled single-crystal silicon resonators: An approach for the intrinsic quality factor. *Journal of Micromechanics and Microengineering*, 16(6), 2006.

- [88] M. J. Weaver, B. Pepper, F. Luna, F. M. Buters, H. J. Eerkens, G. Welker, B. Perock, K. Heeck, S. De Man, and D. Bouwmeester. Nested trampoline resonators for optomechanics. *Applied Physics Letters*, 108(3), 2016.
- [89] Sheng-Shian Li, Yu-Wei Lin, Yuan Xie, Zeying Ren, and C.T.-C. Nguyen. Micromechanical "hollow-disk" ring resonators. In *17th IEEE International Conference on Micro Electro Mechanical Systems. Maastricht MEMS 2004 Technical Digest*, pages 821–824. IEEE, 2004.
- [90] G. Anetsberger, R. Rivière, A. Schliesser, O. Arcizet, and T. J. Kippenberg. Ultralow-dissipation optomechanical resonators on a chip. *Nature Photonics*, 2(10):627–633, 2008.
- [91] E. Yablonovitch, T. J. Gmitter, and K. M. Leung. Photonic band structure: The face-centered-cubic case employing nonspherical atoms. *Physical Review Letters*, 67(17):2295–2298, 1991.
- [92] M. S. Kushwaha, P. Halevi, L. Dobrzynski, and B. Djafari-Rouhani. Acoustic band structure of periodic elastic composites. *Physical Review Letters*, 71(13):2022–2025, sep 1993.
- [93] M Sigalas and E.N. Economou. Band structure of elastic waves in two dimensional systems. *Solid State Communications*, 86(3):141–143, apr 1993.
- [94] N W Ashcroft and N D Mermin. *Solid State Physics*. HRW international editions. Holt, Rinehart and Winston, 1976.
- [95] Zhengyou Liu, Zhengyou Liu, Xixiang Zhang, Yiwei Mao, and Y Y Zhu. Locally Resonant Sonic Materials. *Science*, 289(September):1734–1736, 2000.
- [96] Matt Eichenfield, Jasper Chan, Ryan M. Camacho, Kerry J. Vahala, and Oskar Painter. Optomechanical crystals. *Nature*, 462(7269):78–82, 2009.
- [97] Martin Maldovan and Edwin L. Thomas. Simultaneous localization of photons and phonons in two-dimensional periodic structures. *Applied Physics Letters*, 88(25):20–23, 2006.
- [98] D. J. Wilson, C. A. Regal, S. B. Papp, and H. J. Kimble. Cavity optomechanics with stoichiometric SiN films. *Physical Review Letters*, 103(20):3–6, 2009.

- [99] P. L. Yu, K. Cicak, N. S. Kampel, Y. Tsaturyan, T. P. Purdy, R. W. Simmonds, and C. A. Regal. A phononic bandgap shield for high-Q membrane microresonators. *Applied Physics Letters*, 104(2):2–6, 2014.
- [100] Y. Tsaturyan, A. Barg, A. Simonsen, L. G. Villanueva, S. Schmid, A. Schliesser, and E. S. Polzik. Demonstration of suppressed phonon tunneling losses in phononic bandgap shielded membrane resonators for high-Q optomechanics. *Optics Express*, 22(6):6810, mar 2014.
- [101] Laude Vincent. *Phononic Crystals, Artificial Crystals for Sonic, Acoustic, and Elastic Waves*, 2015.
- [102] M P Marder. *Condensed Matter Physics*. Wiley, 2010.
- [103] Matthew A. Hopcroft, William D. Nix, and Thomas W. Kenny. What is the Young’s modulus of silicon? *Journal of Microelectromechanical Systems*, 19(2):229–238, 2010.
- [104] L. E. Kinsler, A. R. Frey, A. B. Coppens, and J.V. Sanders. *Fundamentals of Acoustics*. New York Chichester, Wiley, 4th edition, 2000.
- [105] A Khelif, B Aoubiza, S Mohammadi, A Adibi, and V Laude. Complete band gaps in two-dimensional phononic crystal slabs. *Physical Review E*, 74(4):046610, oct 2006.
- [106] S. Mohammadi, A.A. Eftekhar, A. Khelif, H. Moubchir, R. Westafer, W.D. Hunt, and A. Adibi. Complete phononic bandgaps and bandgap maps in two-dimensional silicon phononic crystal plates. *Electronics Letters*, 43(16):898, 2007.
- [107] Junghoon Yeom, Yan Wu, John C Selby, and Mark A Shannon. Maximum achievable aspect ratio in deep reactive ion etching of silicon due to aspect ratio dependent transport and the microloading effect. *Journal of Vacuum Science and Technology B: Microelectronics and Nanometer Structures*, 23(6):2319, 2005.
- [108] William Hvidtfelt Padkær Nielsen. *Quantum Cavity Optomechanics with Phononic Bandgap Shielded Silicon Nitride Membranes*. PhD thesis, University of Copenhagen, 2016.
- [109] Amir H. Safavi-Naeini and Oskar Painter. Design of optomechanical cavities and waveguides on a simultaneous bandgap phononic-photonic crystal slab. *Optics Express*, 18(14):14926, jul 2010.

- [110] Thiago P. Mayer Alegre, Amir Safavi-Naeini, Martin Winger, and Oskar Painter. Quasi-two-dimensional optomechanical crystals with a complete phononic bandgap. *Optics Express*, 19(6):5658, 2011.
- [111] Nagi Elabbasi. Modeling Phononic Band Gap Materials and Structures, 2016.
- [112] Björn Bretz. Improved Capabilities for Meshing with Tetrahedral Elements, 2016.
- [113] Jonathan Richard Shewchuk. What is a Good Linear Element? Interpolation, Conditioning, and Quality Measures. *Eleventh International Meshing Roundtable*, pages 115–126, 2002.
- [114] Bethany Nine. How to Implement a Mesh Refinement Study, 2013.
- [115] A. Frangi, A. Bugada, M. Martello, and P.T. Savadkoohi. Validation of PML-based models for the evaluation of anchor dissipation in MEMS resonators. *European Journal of Mechanics - A/Solids*, 37:256–265, jan 2013.
- [116] David S. Bindel and Sanjay Govindjee. Elastic PMLs for resonator anchor loss simulation. *International Journal for Numerical Methods in Engineering*, 64(6):789–818, oct 2005.
- [117] Gregory S. MacCabe, Hengjiang Ren, Jie Luo, Justin D. Cohen, Hengyun Zhou, Alp Sipahigil, Mohammad Mirhosseini, and Oskar Painter. Phononic bandgap nano-acoustic cavity with ultralong phonon lifetime. *arXiv*, 2019.
- [118] J D Plummer. *Silicon VLSI Technology: Fundamentals, Practice and Modeling*. Pearson Education, 2009.
- [119] M. Stadtmueller. Mechanical Stress of CVD-Dielectrics. *Journal of The Electrochemical Society*, 139(12):3669, 1992.
- [120] Yasumasa Okada and Yozo Tokumaru. Precise determination of lattice parameter and thermal expansion coefficient of silicon between 300 and 1500 K. *Journal of Applied Physics*, 56(2):314–320, 1984.
- [121] Amit Kaushik, Harold Kahn, and A.H. Heuer. Wafer-level mechanical characterization of silicon nitride MEMS. *Journal of Microelectromechanical Systems*, 14(2):359–367, 2005.

- [122] S. Linas, Y. Magnin, B. Poinso, O. Boisron, G. D. Förster, V. Martínez, R. Fulcrand, F. Tournus, V. Dupuis, F. Rabilloud, L. Bardotti, Z. Han, D. Kalita, V. Bouchiat, and F. Calvo. Interplay between Raman shift and thermal expansion in graphene: Temperature-dependent measurements and analysis of substrate corrections. *Physical Review B*, 91(7):075426, feb 2015.
- [123] P. Temple-Boyer, C. Rossi, E. Saint-Etienne, and E. Scheid. Residual stress in low pressure chemical vapor deposition SiNx films deposited from silane and ammonia. *Journal of Vacuum Science and Technology*, A 16(4):2003–2007, 1998.
- [124] Ankit Rohatgi. <https://automeris.io/WebPlotDigitizer>.
- [125] M. Zecchino and T. Cunningham. Thin Film Stress Measurement Using Dektat Stylus Profilers, 2010.
- [126] Grégory Abadias, Eric Chason, Jozef Keckes, Marco Sebastiani, Gregory B Thompson, Etienne Barthel, Gary L. Doll, Conal E Murray, Chris H Stoessel, and Ludvik Martinu. Review Article: Stress in thin films and coatings: Current status, challenges, and prospects. *Journal of Vacuum Science and Technology A: Vacuum, Surfaces, and Films*, 36(2):020801, mar 2018.
- [127] W. D. Nix and B. M. Clemens. Crystallite coalescence: A mechanism for intrinsic tensile stresses in thin films. *Journal of Materials Research*, 14(08):3467–3473, 1999.
- [128] Andreas Barg, Yeghishe Tsaturyan, Erik Belhage, William H. P. Nielsen, Christoffer B. Møller, and Albert Schliesser. Measuring and imaging nanomechanical motion with laser light. *Applied Physics B*, 123(1):8, 2017.
- [129] Wanli Jiang, Dehui Xu, Bin Xiong, and Yuelin Wang. Effects of rapid thermal annealing on LPCVD silicon nitride. *Ceramics International*, 42(1):1217–1224, jan 2016.
- [130] T Faust, P Krenn, S Manus, J.P. Kotthaus, and E.M. Weig. Microwave cavity-enhanced transduction for plug and play nanomechanics at room temperature. *Nature Communications*, 3(1):728, jan 2012.
- [131] A. Kaushik, H. Kahn, and A. H. Heuer. Wafer-level mechanical characterization of silicon nitride MEMS. *Journal Of Microelectromechanical Systems*, 14(2):359–367, 2005.

- [132] Yeghishe Tsaturyan, Andreas Barg, Eugene S. Polzik, and Albert Schliesser. Ultracoherent nanomechanical resonators via soft clamping and dissipation dilution. *Nature Nanotechnology*, 12(8):776–783, aug 2017.
- [133] R. v. Mises. Mechanik der festen Körper im plastisch- deformablen Zustand. *Nachrichten von der Gesellschaft der Wissenschaften zu Göttingen, Mathematisch-Physikalische Klasse*, 4:582–592, 1913.
- [134] Paul Doru Barsanescu and Ana Maria Comanici. von Mises hypothesis revised. *Acta Mechanica*, 228(2):433–446, feb 2017.
- [135] MicroChemicals GmbH. [www.microchemicals.com/downloads/application\\_notes](http://www.microchemicals.com/downloads/application_notes).
- [136] C. Gerry and P. L. Knight. *Introductory Quantum Optics*. Cambridge University Press, 2005.
- [137] C. Law. Interaction between a moving mirror and radiation pressure: A Hamiltonian formulation. *Physical Review A*, 51(3):2537–2541, mar 1995.
- [138] Warwick P. Bowen and Gerard J. Milburn. *Quantum Optomechanics*. CRC Press, 2015.
- [139] Stefano Zippilli, Giovanni Di Giuseppe, and David Vitali. Entanglement and squeezing of continuous-wave stationary light. *New Journal of Physics*, 17, 2015.
- [140] J J Sakurai and J Napolitano. *Modern Quantum Mechanics*. Addison-Wesley, 2011.
- [141] Cw Gardiner and Mj Collett. Input and output in damped quantum systems: Quantum stochastic differential equations and the master equation. *Physical Review A*, 31(6):3761–3774, 1985.
- [142] C. Gardiner and P. Zoller. *Quantum Noise: A Handbook of Markovian and Non-Markovian Quantum Stochastic Methods with Applications to Quantum Optics*. Springer Series in Synergetics. Springer, 2004.
- [143] G. W. Ford, J. T. Lewis, and R. F. Oconnell. Quantum Langevin equation. *Physical Review A*, 37(11):4419–4428, 1988.
- [144] A. Dorsel, J. D. McCullen, P. Meystre, E. Vignes, and H. Walther. Optical Bistability and Mirror Confinement Induced by Radiation Pressure. *Physical Review Letters*, 51(17):1550–1553, oct 1983.

- [145] Cheng Yang. *Progress Toward Observing Quantum Effects in an Optomechanical System in Cryogenics*. PhD thesis, Yale University, 2011.
- [146] A. Clerk, M. H. Devoret, S. M. Girvin, F. Marquardt, and R. J. Schoelkopf. Introduction to quantum noise, measurement, and amplification. *Reviews of Modern Physics*, 82(2):1155–1208, apr 2010.
- [147] Markus Aspelmeyer, Tobias J. Kippenberg, and Florian Marquardt. Cavity optomechanics. *Reviews of Modern Physics*, 86(December), 2014.
- [148] Jeremy B. Clark, Florent Lecocq, Raymond W. Simmonds, José Aumentado, and John D. Teufel. Sideband cooling beyond the quantum backaction limit with squeezed light. *Nature*, 541(7636):191–195, 2017.
- [149] M. R. Vanner, I. Pikovski, G. D. Cole, M. S. Kim, Č Brukner, K. Hammerer, G. J. Milburn, and M. Aspelmeyer. Pulsed quantum optomechanics. *Proceedings of the National Academy of Sciences of the United States of America*, 108(39):16182–16187, 2011.
- [150] M. R. Vanner, J. Hofer, G. D. Cole, and M. Aspelmeyer. Cooling-by-measurement and mechanical state tomography via pulsed optomechanics. *Nature Communications*, 4(May):1–8, 2013.
- [151] Teemu Ojanen and Kjetil Børkje. Ground-state cooling of mechanical motion in the unresolved sideband regime by use of optomechanically induced transparency. *Physical Review A*, 90(1):013824, jul 2014.
- [152] K. Hammerer, M. Aspelmeyer, E. Polzik, and P. Zoller. Establishing Einstein-Poldosky-Rosen Channels between Nanomechanics and Atomic Ensembles. *Physical Review Letters*, 102(2):020501, jan 2009.
- [153] Stephen E Harris. Electromagnetically Induced Transparency. *Physics Today*, 50(7):36–42, jul 1997.
- [154] C. S. Roos, D. Leibfried, A. Mundt, F. Schmidt-Kaler, J. Eschner, and R. Blatt. Experimental Demonstration of Ground State Laser Cooling with Electromagnetically Induced Transparency. *Physical Review Letters*, 85(26):5547–5550, 2000.
- [155] Giovanna Morigi, Jürgen Eschner, and Christoph H. Keitel. Ground state laser cooling using electromagnetically induced transparency. *Physical Review Letters*, 85(21):4458–4461, 2000.

- [156] Lene Vestergaard Hau, S. E. Harris, Zachary Dutton, and Cyrus H. Behroozi. Light speed reduction to 17 metres per second in an ultracold atomic gas. *Nature*, 397(6720):594–598, feb 1999.
- [157] Chien Liu, Zachary Dutton, Cyrus H. Behroozi, and Lene Vestergaard Hau. Observation of coherent optical information storage in an atomic medium using halted light pulses. *Nature*, 409(6819):490–493, jan 2001.
- [158] Martin Mücke, Eden Figueroa, Joerg Bochmann, Carolin Hahn, Karim Murr, Stephan Ritter, Celso J. Villas-Boas, and Gerhard Rempe. Electromagnetically induced transparency with single atoms in a cavity. *Nature*, 465(7299):755–758, 2010.
- [159] Albert Schliesser. *Cavity Optomechanics and Optical Frequency Comb Generation with Silica Whispering-Gallery-Mode Microresonators*. PhD thesis, Max Planck Institute of Quantum Optics, 2009.
- [160] Stefan Weis, Rémi Rivière, Samuel Deléglise, Emanuel Gavartin, Olivier Arcizet, Albert Schliesser, and Tobias J. Kippenberg. Optomechanically Induced Transparency. *Science*, 330(6010):1520–1523, dec 2010.
- [161] Andrey E. Miroshnichenko, Sergej Flach, and Yuri S. Kivshar. Fano resonances in nanoscale structures. *Reviews of Modern Physics*, 82(3):2257–2298, 2010.
- [162] P. Meystre, E. M. Wright, J. D. McCullen, and E. Vignes. Theory of radiation-pressure-driven interferometers. *Journal of the Optical Society of America B*, 2(11):1830, 1985.
- [163] R. E. Slusher, L. W. Hollberg, B. Yurke, J. C. Mertz, and J. F. Valley. Observation of squeezed states generated by four-wave mixing in an optical cavity. *Physical Review Letters*, 55(22):2409–2412, 1985.
- [164] Horace P. Yuen and Jeffrey H. Shapiro. Generation and detection of two-photon coherent states in degenerate four-wave mixing. *Optics Letters*, 4(10):334, oct 1979.
- [165] Carlton M. Caves. Quantum-mechanical noise in an interferometer. *Physical Review D*, 23(8):1693–1708, apr 1981.
- [166] T W Hänsch and Y R Shen. *Laser Spectroscopy VII: Proceedings of the Seventh International Conference, Hawaii, June 24–28, 1985*. Springer Series in Optical Sciences. Springer Berlin Heidelberg, 2013.

- [167] D. F. Walls. Squeezed states of light. *Nature*, 306(5939):141–146, nov 1983.
- [168] Henning Vahlbruch, Moritz Mehmet, Karsten Danzmann, and Roman Schnabel. Detection of 15 dB Squeezed States of Light and their Application for the Absolute Calibration of Photoelectric Quantum Efficiency. *Physical Review Letters*, 117(11):110801, sep 2016.
- [169] L Hilico, J M Courty, C Fabre, E Giacobino, I Abram, and J. L. Oudar. Squeezing with  $\chi(3)$  materials. *Applied Physics B Photophysics and Laser Chemistry*, 55(3):202–209, 1992.
- [170] C. Fabre, M. Pinard, S. Bourzeix, A. Heidmann, E. Giacobino, and S. Reynaud. Quantum-noise reduction using a cavity with a movable mirror. *Physical Review A*, 49(2):1337–1343, 1994.
- [171] S. Mancini and P. Tombesi. Quantum noise reduction by radiation pressure. *Physical Review A*, 49(5):4055–4065, may 1994.
- [172] V. B. Braginsky and A. B. Manukin. Ponderomotive Effects of Electromagnetic Radiation. *Journal of Experimental and Theoretical Physics*, 25(4):653–655, 1967.
- [173] Daniel W C Brooks, Thierry Botter, Sydney Schreppler, Thomas P. Purdy, Nathan Brahms, and Dan M. Stamper-Kurn. Non-classical light generated by quantum-noise-driven cavity optomechanics. *Nature*, 488(7412):476–480, 2012.
- [174] Amir H Safavi-Naeini, Jasper Chan, Jeff T Hill, Simon Gröblacher, Haixing Miao, Yanbei Chen, Markus Aspelmeyer, and Oskar Painter. Laser noise in cavity-optomechanical cooling and thermometry. *New Journal of Physics*, 15, 2013.
- [175] Christoffer Bo Møller. *Quantum Back-Action Evasion in a Hybrid Spin-Optomechanical System*. PhD thesis, University of Copenhagen, 2018.
- [176] A M Jayich, J C Sankey, B M Zwickl, C Yang, J D Thompson, S M Girvin, a a Clerk, F Marquardt, and J G E Harris. Dispersive optomechanics: a membrane inside a cavity. *New Journal of Physics*, 10(9):095008, sep 2008.
- [177] P W Milonni and J H Eberly. *Laser Physics*. Wiley, 2010.

- [178] J C Sankey, C Yang, B M Zwickl, A M Jayich, and J G E Harris. Strong and tunable nonlinear optomechanical coupling in a low-loss system. *Nature Physics*, 6(9):707–712, 2010.
- [179] T. P. Purdy, P.-L. Yu, N. S. Kampel, R. W. Peterson, K. Cicak, R. W. Simmonds, and C. A. Regal. Optomechanical Raman-ratio thermometry. *Physical Review A*, 92(3):031802, 2015.
- [180] Jack C. Sankey, Andrew M. Jayich, Benjamin M. Zwickl, Cheng Yang, and Jack G. E. Harris. Improved "Position Squared" Readout of a Mechanical Resonator in an Optical Cavity Using Degenerate Optical Modes. pages 1–12, 2008.
- [181] Andreas Barg. *Optomechanics with soft-clamped silicon nitride membranes and carrier-mediated forces in coupled quantum wells*. PhD thesis, University of Copenhagen, 2018.
- [182] P. Rabl and M. Aspelmeyer. Phase-noise induced limitations on cooling and coherent evolution in optomechanical systems. *Physical Review A - Atomic, Molecular, and Optical Physics*, 80(6):1–10, 2009.
- [183] M. L. Gorodetsky, Albert Schliesser, G. Anetsberger, S. Deleglise, and Tobias J. Kippenberg. Determination of the vacuum optomechanical coupling rate using frequency noise calibration. *Optics Express*, 18(22):23236, oct 2010.
- [184] Stav Zaitsev, Oleg Shtempluck, Eyal Buks, and Oded Gottlieb. Non-linear damping in a micromechanical oscillator. *Nonlinear Dynamics*, 67(1):859–883, jan 2012.
- [185] Kater W. Murch, Kevin L. Moore, Subhadeep Gupta, and Dan M. Stamper-Kurn. Observation of quantum-measurement backaction with an ultracold atomic gas. *Nature Physics*, 4(7):561–564, jul 2008.
- [186] André Xuereb, Claudiu Genes, and Aurélien Dantan. Strong Coupling and Long-Range Collective Interactions in Optomechanical Arrays. *Physical Review Letters*, 109(22):223601, nov 2012.
- [187] T. T. Heikkilä, F. Massel, J. Tuorila, R. Khan, and M. A. Sillanpää. Enhancing optomechanical coupling via the Josephson effect. *Physical Review Letters*, 112(20):1–6, 2014.
- [188] Sumei Huang and G. S. Agarwal. Normal-mode splitting in a coupled system of a nanomechanical oscillator and a parametric amplifier cavity. *Physical Review A*, 80(3):033807, sep 2009.

- [189] Xin-You Lü, Ying Wu, J. R. Johansson, Hui Jing, Jing Zhang, and Franco Nori. Squeezed Optomechanics with Phase-Matched Amplification and Dissipation. *Physical Review Letters*, 114(March):1–6, 2015.
- [190] Matteo Brunelli, Oussama Houhou, Darren W. Moore, Andreas Nunnenkamp, Mauro Paternostro, and Alessandro Ferraro. Unconditional preparation of nonclassical states via linear-and-quadratic optomechanics. *Physical Review A*, 98(6):063801, dec 2018.
- [191] Matteo Brunelli and Oussama Houhou. Linear and quadratic reservoir engineering of non-Gaussian states. *Physical Review A*, 100(1):1–17, 2019.
- [192] Farid Khalili, Stefan Danilishin, Haixing Miao, Helge Müller-Ebhardt, Huan Yang, and Yanbei Chen. Preparing a mechanical oscillator in non-Gaussian quantum states. *Physical Review Letters*, 105(7):1–4, 2010.
- [193] U. Akram, N. Kiesel, M. Aspelmeyer, and G. J. Milburn. Single-photon opto-mechanics in the strong coupling regime. *New Journal of Physics*, 12, 2010.
- [194] M. R. Vanner, M. Aspelmeyer, and M. S. Kim. Quantum State Orthogonalization and a Toolset for Quantum Optomechanical Phonon Control. *Physical Review Letters*, 110(1):1–5, 2013.
- [195] Christophe Galland, Nicolas Sangouard, Nicolas Piro, Nicolas Gisin, and Tobias J. Kippenberg. Heralded single-phonon preparation, storage, and readout in cavity optomechanics. *Physical Review Letters*, 112(14):1–6, 2014.
- [196] Sungkun Hong, Ralf Riedinger, Igor Marinković, Andreas Wallucks, Sebastian G. Hofer, Richard A. Norte, Markus Aspelmeyer, and Simon Gröblacher. Hanbury Brown and Twiss interferometry of single phonons from an optomechanical resonator. *Science*, 358(6360):203–206, 2017.
- [197] P. Galatola, L. A. Lugiato, M. G. Porreca, P. Tombesi, and G. Leuchs. System control by variation of the squeezing phase. *Optics Communications*, 85(1):95–103, 1991.
- [198] T. C. Zhang, J. P. Poizat, P. Grelu, J. F. Roch, P. Grangier, F. Marin, A. Bramati, V. Jost, M. D. Levenson, and E. Giacobino. Quantum noise of free-running and externally-stabilized laser diodes. *Quantum*

and *Semiclassical Optics: Journal of the European Optical Society Part B*, 7(4):601–613, 1995.

- [199] A. M. Jayich, J. C. Sankey, K. Borkje, D. Lee, C. Yang, M. Underwood, L. Childress, A. Petrenko, S. M. Girvin, and J. G.E. Harris. Cryogenic optomechanics with a Si<sub>3</sub>N<sub>4</sub> membrane and classical laser noise. *New Journal of Physics*, 14, 2012.
- [200] Timo Zwickler. *Suppression of Heating Mechanisms for Deep Optomechanical Ground State Cooling*. Master thesis, University of Copenhagen, 2019.
- [201] M. J. Weaver, D. Newsom, F. Luna, W. Löffler, and D. Bouwmeester. Phonon interferometry for measuring quantum decoherence. *Physical Review A*, 97(6):063832, jun 2018.
- [202] A I Lvovsky and M G Raymer. Continuous-variable optical quantum-state tomography. *Reviews of Modern Physics*, 81(1):299–332, mar 2009.
- [203] Michael Zugenmaier, Karsten B. Dideriksen, Anders S. Sørensen, Boris Albrecht, and Eugene S. Polzik. Long-lived non-classical correlations towards quantum communication at room temperature. *Communications Physics*, 1(1):76, 2018.
- [204] Yu Levin. Internal thermal noise in the LIGO test masses: A direct approach. *Physical Review D - Particles, Fields, Gravitation and Cosmology*, 57(2):659–663, 1998.
- [205] D. Hatanaka, A. Bachtold, and H. Yamaguchi. Electrostatically Induced Phononic Crystal. *Physical Review Applied*, 11(2):1, 2019.
- [206] Abeer Z. Barasheed, Tina Müller, and Jack C. Sankey. Optically defined mechanical geometry. *Physical Review A*, 93(5):1–6, 2016.
- [207] Amir H Ghadimi, Sergey A Fedorov, Nils J Engelsen, Mohammad J Bereyhi, Ryan Schilling, Dalziel J Wilson, and Tobias J. Kippenberg. Elastic strain engineering for ultralow mechanical dissipation. *Science*, 360(6390):764–768, may 2018.
- [208] Chris Reetz, Ran Fischer, Gabriel G. T. Assumpcao, Dylan P. McNally, Peter S. Burns, Jack C. Sankey, and Cindy A. Regal. Analysis of membrane phononic crystals with wide bandgaps and low-mass defects. pages 1–12, 2019.

- [209] L. F. Buchmann and D. M. Stamper-Kurn. Nondegenerate multimode optomechanics. *Physical Review A*, 92(1):013851, 2015.
- [210] Mian Zhang, Gustavo S. Wiederhecker, Sasikanth Manipatruni, Arthur Barnard, Paul McEuen, and Michal Lipson. Synchronization of Micromechanical Oscillators Using Light. *Physical Review Letters*, 109(23):233906, dec 2012.
- [211] P R Saulson. *Fundamentals of Interferometric Gravitational Wave Detectors*. World Scientific, 1994.

# Appendices



# Appendix A

## Fourier analysis

This appendix covers the basics of Fourier analysis, which is used throughout the thesis in describing the spectral composition of signals emerging from our experimental setups. Here, we draw broadly from [138, 211].

### A.1 Fourier transforms

We begin by define the Fourier transform of an arbitrary time-varying signal  $s(t)$  as

$$s(\Omega) = \mathcal{F}[s(t)](\Omega) := \int_{-\infty}^{\infty} s(t)e^{i\Omega t} dt. \quad (\text{A.1.1})$$

Similarly, the inverse Fourier transform of a signal in the Fourier domain is defined as

$$s(t) = \mathcal{F}^{-1}[s(\Omega)](t) := \int_{-\infty}^{\infty} s(\Omega)e^{-i\Omega t} \frac{d\Omega}{2\pi}. \quad (\text{A.1.2})$$

Since we rely on Fourier analysis in deriving the power spectral densities of quantum operators, we note that the Hermitian conjugate of a quantum operator  $\hat{X}(\Omega)$  is

$$(\hat{X}(\Omega))^\dagger = \hat{X}^\dagger(-\Omega), \quad (\text{A.1.3})$$

which follows directly from the definition of the Fourier transform. Evidently, for a Hermitian operator it holds that  $(\hat{X}(\Omega))^\dagger = \hat{X}(-\Omega)$ .

Finally, we often use the Fourier transform in order to solve a time-domain differential equation by transforming to the Fourier domain. Following the definitions of the Fourier transform and it's inverse, it can be shown that

$$\mathcal{F} \left[ \frac{d}{dt} X(t) \right] = -i\Omega X(\Omega). \quad (\text{A.1.4})$$

## A.2 Power spectral densities

In our experimental endeavours we are often interested in the spectral composition of time-domain signals emerging from a photodetector, particularly around the resonance frequency of our mechanical resonator. This is done by computing the *power spectral density* (PSD) of the signal. Here, we consider stationary and ergodic stochastic signals, where the former implies statistical properties constant in time, while the latter implies that the ensemble average of several experimental realisations is equivalent to the long time time-average of a single realisation.

The power spectral density for a stationary signal  $X(t)$ , defined for all times  $t$ , is defined as

$$S_{XX}(\Omega) := \lim_{T \rightarrow \infty} \frac{1}{T} |X_T(\Omega)|^2, \quad (\text{A.2.5})$$

where  $X_T(\Omega)$  is the finite-time Fourier transform of  $X(t)$ , defined as

$$X_T(\Omega) := \int_{-T/2}^{T/2} X(t) e^{i\Omega t} dt. \quad (\text{A.2.6})$$

Evidently, we can never measure the actual power spectral density, due to the fact that in practice we will be working with signals acquired over a finite period of time in discrete steps. Instead the power spectral density is estimated, and the estimator of choice in our case in the so-called periodogram<sup>1</sup>.

Here, we use the discrete version of the Fourier transform (DFT)

$$\text{DFT}[X](m) := \sum_{n=0}^{N-1} X_n e^{2\pi i m n / N}, \quad (\text{A.2.7})$$

where  $X$  is an array of length  $N = F_S T$ , representing a time-signal sampled at a rate  $F_S$  over a time period  $T$ . The integer  $m$ , running from 0 to  $N - 1$ , is mapped to an specific frequency component  $f_m$  following

$$f_m = m \frac{F_S}{N}. \quad (\text{A.2.8})$$

Using the definition of the DFT (A.2.7), the periodogram as an estimator for the power spectral density (A.2.5) of signal  $X$  can be expressed as

$$P_{XX} = \frac{1}{T} |\text{DFT}[X](m) \Delta t|^2, \quad (\text{A.2.9})$$

where  $\Delta t = 1/F_S$ .

---

<sup>1</sup>Modern spectrum analysers similarly use the periodogram as the estimator for the power spectral density.

### A.3 Cross spectral densities

We define the *cross-correlation* function of two time-signals,  $X(t)$  and  $Y(t)$ , as follows

$$(X \star Y)(\tau) := \lim_{T \rightarrow \infty} \frac{1}{T} \int_{-T/2}^{T/2} X^*(t)Y(t + \tau) d\tau, \quad (\text{A.3.10})$$

where  $\tau$  is the time-lag between the two signals. The cross-correlation can be expressed as

$$(X \star Y)(\tau) = \langle X^*(t)Y(t + \tau) \rangle = \langle X^*(0)Y(\tau) \rangle, \quad (\text{A.3.11})$$

where, from left to right, we assume ergodicity, and that the signals are stationary (allowing us to set  $t = 0$ ). Here,  $\langle \cdot \rangle$  indicates an ensemble average. Invoking the Wiener-Khinchin theorem, we can now write the cross power spectral density as

$$S_{XY}(\Omega) = \int_{-\infty}^{\infty} \langle X^*(t)Y(t + \tau) \rangle_{t=0} e^{i\Omega\tau} d\tau \quad (\text{A.3.12})$$

$$= \int_{-\infty}^{\infty} \langle X^*(\Omega)Y(\Omega') \rangle \frac{d\Omega'}{2\pi}, \quad (\text{A.3.13})$$

where the first equality is due to the Wiener-Khinchin theorem, while the second is obtained via the definition of the inverse Fourier transform (cf. eq. (A.1.2)). Replacing the complex conjugate with a Hermitian conjugate, the expression above can be used directly to compute quantum power spectral densities. In doing so,  $\langle \cdot \rangle$  now represents an expectation value, rather than an ensemble average.